

# **Dissertation**

submitted to the

Combined Faculty of Mathematics, Engineering and Natural Sciences

of Heidelberg University, Germany

for the degree of

Doctor of Natural Sciences

Put forward by

M.Sc. Hannes Pahl

born in: Göttingen, Germany

Oral examination: 17.12.2024



**Advances in the design, modelling and operation of  
high-performance Electron Beam Ion Sources**

Referees: Apl. Prof. Dr. José R. Crespo López-Urrutia  
Apl. Prof. Dr. Yury Litvinov



---

## Advances in the design, modelling and operation of high-performance Electron Beam Ion Sources

**Abstract** Highly charged ions see widespread use in fundamental research, medicine, and industry. This thesis describes development work carried out to improve on the charge breeding performance of electron beam ion sources (EBIS) and to advance their modelling in computer simulations. Established expressions for the mathematical modelling of the charge breeding of trapped ions are reviewed and the implementation of a modern software package for the simulation of charge breeding dynamics is put forward. Simulation results are compared to experimental data containing signatures of dielectronic recombination reflected in the emerging charge state distribution. REXEBIS, processing rare isotope beams at the ISOLDE facility, has been upgraded with a new, weakly-immersed electron gun to increase its reliability and raise the available electron current density. Here, a passive magnetic element is used to dampen radial electron beam oscillations resulting from space charge defocusing. The damping technique is investigated and results of extensive commissioning experiments characterising the efficiency of the upgraded EBIS are presented. MEDeGUN, a prototype for a 1 A Brillouin-type electron gun for medical charge breeding applications, has been characterised at the TwinEBIS test stand. The measurement campaign reveals multiple critical performance limitations, such as a stagnation of charge breeding and large ion losses, warranting further investigations. The design study for a dedicated ion beamline which will support future experiments is summarised.

## Fortschritte bei Entwurf, Modellierung und Betrieb von Hochleistungs-Elektronenstrahl-Ionenquellen

**Zusammenfassung** Hochgeladene Ionen finden eine breite Anwendung in der Grundlagenforschung, Medizin und Industrie. Diese Dissertation beschreibt Entwicklungsarbeiten, die durchgeführt wurden, um die Leistung der Ladungsbrütung in Elektronenstrahl-Ionenquellen (EBIS) zu verbessern und deren Modellierung in Computersimulationen voranzutreiben. Etablierte Ausdrücke zur mathematischen Modellierung des Ladungsbrütens gefangener Ionen werden besprochen und die Implementierung eines modernen Softwarepaketes für die Simulation von Ladungsbrütern wird vorgestellt. Simulationsergebnisse werden mit experimentellen Daten verglichen, die Signaturen von dielektronischer Rekombination enthalten, welche sich in der entstehenden Ladungszustandsverteilung widerspiegeln. REXEBIS, welche an der ISOLDE Anlage Strahlen seltener Isotope verarbeitet, wurde mit einer neuen, schwachen Magnetfeldern ausgesetzten, Elektronenkanone aufgerüstet, um ihre Zuverlässigkeit zu erhöhen und höhere Elektronenstromdichten verfügbar zu machen. Dabei wird ein passives magnetisches Element verwendet, um radiale Oszillationen des Elektronenstrahls zu dämpfen, die in Folge der raumladungsgetriebenen Defokussierung auftreten. Die Dämpfungstechnik wird erkundet und die Ergeb-

---

nisse umfangreicher Experimente zur Inbetriebnahme der aufgerüsteten EBIS werden präsentiert. MEDeGUN, ein Prototyp für eine 1 A Brillouin-artige Elektronenkanone für medizinische Ladungsbrütungsanwendungen, wurde am TwinEBIS Teststand charakterisiert. Die Messkampagne zeigt verschiedene kritische Leistungslimitierungen auf, wie zum Beispiel ein Stagnieren des Ladungsbrütungsprozesses und starke Ionenverluste, und motiviert so weitergehende Untersuchungen. Die Entwurfsstudie für ein dediziertes Ionenstrahltransportsystem, das zukünftige Messungen unterstützen soll, wird zusammengefasst.

# CONTENTS

<b>1</b>	<b>Introduction</b>	<b>1</b>
<b>2</b>	<b>Theory</b>	<b>5</b>
2.1	Electron beam ion sources . . . . .	5
2.2	Charge breeding . . . . .	7
2.2.1	Electron impact ionisation . . . . .	7
2.2.2	Radiative recombination . . . . .	9
2.2.3	Dielectronic recombination . . . . .	11
2.2.4	Charge exchange . . . . .	12
2.2.5	Charge state evolution . . . . .	13
2.3	Non-relativistic electron beam dynamics . . . . .	17
2.3.1	Electron gun . . . . .	18
2.3.2	Electron trajectories in crossed electric and magnetic fields . . . . .	20
2.3.3	Busch's theorem . . . . .	21
2.3.4	Beam induced space charge field . . . . .	22
2.3.5	Space charge balanced flow . . . . .	23
2.3.6	Electron beam radius . . . . .	24
2.3.7	Energy correction and virtual cathode formation . . . . .	25
<b>3</b>	<b>Charge Breeding Simulations</b>	<b>29</b>
3.1	Model overview . . . . .	29
3.2	Radial ion distribution and space charge compensation . . . . .	31
3.2.1	Poisson-Boltzmann equation . . . . .	31
3.2.2	Quantities derived from the radial ion distribution . . . . .	33
3.3	Charge state and temperature evolution . . . . .	36
3.3.1	Charge state changing interactions . . . . .	36
3.3.2	Heating and thermalisation . . . . .	40
3.3.3	Losses and evaporative cooling . . . . .	43
3.4	<i>Ebisim</i> package . . . . .	45
3.4.1	User interface . . . . .	46
3.4.2	Included resources . . . . .	49

3.4.3	Numerical solution of the radial space charge equation . . . . .	50
3.5	Example: Shifting of the charge state balance due to dielectronic recombinations	55
3.5.1	Experimental methods . . . . .	55
3.5.2	Simulation setup . . . . .	57
3.5.3	Experimental results . . . . .	57
3.5.4	Simulation results and comparison to the experimental data . . . . .	59
3.6	Conclusion . . . . .	65
<b>4</b>	<b>Nonadiabatic Electron Guns</b>	<b>67</b>
4.1	Reducing beam ripple with nonadiabatic magnetic fields . . . . .	67
4.1.1	Simulation setup . . . . .	68
4.1.2	Demonstration of ripple reduction with a passive element . . . . .	69
4.1.3	Matching the cyclotron motion with an active element . . . . .	71
4.1.4	Damping on later nodes . . . . .	72
4.1.5	Ripple amplitude . . . . .	74
4.1.6	Closing remarks . . . . .	77
4.2	A nonadiabatic electron gun for REXEBIS . . . . .	78
4.2.1	The need for an electron gun upgrade . . . . .	79
4.2.2	Electron gun design and simulation . . . . .	82
4.2.3	Mechanical design . . . . .	87
4.2.4	Experimental setup . . . . .	90
4.2.5	Experimental methods & results . . . . .	92
4.3	Conclusion . . . . .	114
<b>5</b>	<b>MEDeGUN &amp; TwinEBIS</b>	<b>119</b>
5.1	Description of MEDeGUN and the TwinEBIS test stand . . . . .	120
5.1.1	MEDeGUN . . . . .	120
5.1.2	TwinEBIS . . . . .	122
5.1.3	Ion extraction and the Time of Flight spectrometer . . . . .	125
5.2	Experimental methods . . . . .	131
5.2.1	Electron beam commissioning . . . . .	131
5.2.2	Charge breeding experiments . . . . .	133
5.3	Experimental results . . . . .	139
5.3.1	MEDeGUN perveance . . . . .	139
5.3.2	Beam energy reduction & Bursian limit . . . . .	141
5.3.3	Space-charge trap compensation . . . . .	142
5.3.4	Charge state spectrum evolution . . . . .	149

5.4	Discussion of experimental results . . . . .	154
5.4.1	Electron beam measurements . . . . .	154
5.4.2	Trap compensation and ion extraction . . . . .	157
5.4.3	Charge breeding performance . . . . .	162
5.5	Studies of a low energy ion transport and measurement beamline . . . . .	165
5.5.1	Overview . . . . .	168
5.5.2	Beam optics . . . . .	170
5.5.3	Three-way ion switchyard . . . . .	173
5.5.4	Gridded lenses . . . . .	175
5.6	Conclusion . . . . .	180
<b>6</b>	<b>Summary &amp; Outlook</b>	<b>185</b>
	<b>Publications</b>	<b>195</b>
	<b>References</b>	<b>197</b>
	<b>Acknowledgements</b>	<b>211</b>
	<b>Abbreviations &amp; Acronyms</b>	<b>I</b>
	<b>Symbols</b>	<b>III</b>



# CHAPTER 1

## INTRODUCTION

Much of modern physics and technology is concerned with or relies on the manipulation and investigation of matter on an atomic scale. Individual atoms and molecules, however, are difficult to hold in free space or move around at will for experimental or technological purposes. Ions, on the other hand, have a charge imbalance allowing them to directly interact with and be controlled by externally applied electromagnetic fields. Mastery of large parts of the electromagnetic spectrum as well as past and present advances in electronics have provided researchers and engineers with unique ways of manipulating charged particles with a high degree of precision and if necessary also power.

Ions are readily created under everyday environmental conditions, but their charge imbalance rarely exceeds a few elementary charges. Beyond that point, work has to be done in order to further increase the charge state of the ion. Once an ion's charge state is pushed beyond this point, one commonly speaks of Highly Charged Ions (HCI). For the remainder of this document the focus is going to be on positive atomic ions, i.e. atoms that had some of their electrons removed. Here, the term HCI shall refer to any ion that was artificially prepared to be missing a significant fraction or even all of its usual bound electrons.

HCI are of particular interest in the context of particle acceleration, as the accelerating force ions experience in a given electric field  $E_{\text{acc}}$  scales linearly with their charge state  $q_i$ :  $F_{\text{acc}} = -q_i e E_{\text{acc}}$ . This means that the same (often costly) accelerating structure can be exploited more efficiently if the charge state of the accelerated particle is maximised. With the widespread use of small- and mid-scale accelerators in modern industry (e.g. ion implantation [1]) and medicine (e.g. hadron therapy [2–4]), this extends the demand for HCI beyond the scope of high energy physics experiments.

Besides kinetic advantages to the high charge state, HCI themselves offer unique opportunities for research. Highly charged ions are usually only found in hot (astronomical / fusion) plasmas where the inter-particle collision energies are sufficiently high to break strongly bound electrons off of their ionic cores. These ions typically have their own distinct spectral signatures often featuring lines in the ultraviolet to x-ray range. Comparative laboratory measurements

are required to identify the spectral fingerprint of ion species within astronomical data or to determine the source of previously unexplainable lines as demonstrated in e.g. Refs. [5, 6]. While atoms are electrically neutral, they are much more susceptible to external perturbations than a highly charged ion with all its remaining electrons stuck close to the nucleus. Not only does this shield HCI from external influences, it also amplifies energy term corrections and shifts which are usually very weak when observed in neutral atoms. This makes HCI interesting candidates for high precision measurements, such as tests of quantum electro dynamics or clock applications [7, 8].

Electron Beam Ion Sources (EBIS), first developed by Donets et al. [9], are devices specialised in the production of HCI. This is achieved through the bombardment of a trapped ion cloud with an electron beam. Electrons from the beam successively knock bound electrons out of the ion orbitals to increase the ions' charge state, a process commonly referred to as charge breeding. Their ability to create short intense pulses of highly charged ions, makes EBIS devices particularly interesting as injectors for particle accelerators. An example for an ion collider fed by an EBIS is RHIC at BNL [10].

Electron Beam Ion Traps (EBIT) are closely related to electron beam ion sources. Introduced by Levine et al. [11, 12] in the 1980s, their development was driven by the desire to observe the hot plasma created in an EBIS in-situ. Of particular interest is the radiation – typically x-rays – that is emitted in the interaction of the HCI with the electron beam and residual neutral gas. An EBIT typically features a shorter ion trap and a device geometry that is optimised to provide visual or even mechanical access to the charge breeding region.

In this thesis, the primary subject will be the use of electron beam ion sources as beam preparation devices for particle accelerators. This work is aiming to improve on the state-of-the-art charge breeding performance and to better the understanding of the underlying dynamics of the breeding process. The investigations are therefore guided by an interest in key performance figures, such as the charge breeding speed, capacity and efficiency, the highest attainable charge state and accumulated ion charge, and the beam purity. Most of the discussed concepts should map closely to comparable scenarios in an EBIT nevertheless.

Chapter 2 provides a summary of the most important theoretical aspects of EBIS design and operation. It introduces the general operational principles of an EBIS and a description of the charge breeding process. This includes an overview of the relevant collision processes driving the charge state evolution during the charge breeding process as well as a high level model for describing the charge breeding dynamics. The performance of an EBIS is closely tied to the properties of the electron beam powering it. For this reason, the chapter contains some general concepts regarding electron gun design, lays out the relevant theoretical models for describing the electron beam propagation in the ion source, and provides some beam characterisation metrics such as the current density.

---

Owing to their primary design concerns, most ion sources provide poor to no in-situ access, hindering diagnostic measurements – EBIS devices are no exception to this. Modelling and simulating the charge breeding process can provide much needed additional insight into the dynamics and time evolution of the intrinsically transient charge breeding process. Chapter 3 contains a much more detailed literature review and discussion of the mathematical expressions that can be used to describe the effect that elastic and inelastic collision processes have on the trapped ion population. These are used to define a system of rate equations that can be integrated to predict the charge state and ion temperature evolution from a given set of initial conditions. The implementation of this model in the form of a *Python* package is presented. As a showcase example, this *ebisim* simulation tool is used to replicate the results of a number of charge breeding experiments which measured the impact of resonant recombination processes on the final charge state distribution, providing additional insight into the obscured breeding dynamics.

In the following it will become clear, that a well-behaved high current density electron beam is crucial for a performant EBIS charge breeder, which brings with it many practical challenges. One challenge is the radial defocusing of the electron beam due to its own space charge. This can trigger oscillations of the beam cross section which can act adversely on efficient EBIS operation. In Chapter 4 the design of a novel type of electron gun is presented, which employs a rapid non-adiabatic magnetic field modulation to dampen radial beam oscillations. The concept is explored in a number of simulation studies working towards the design of a new electron gun with increased current density for REXEBIS, which operates as a charge breeder for the post-acceleration of Rare Isotope Beams (RIB) at the ISOLDE facility at CERN. Extensive charge breeding experiments have been carried out with the new electron gun driving the EBIS to characterise the charge breeding performance of the upgraded system. Experimentally determined charge breeding and ion temperature dynamics are compared to simulations and models based on the material from the prior chapter.

Chapter 5 explores the use of an EBIS as an ion source for medical applications. A sufficiently powerful EBIS is theoretically able to provide a high rate of intense  $\mu\text{s}$  pulses of fully ionised  $\text{C}^{6+}$  ions, which could make it a suitable source for a linear accelerator based hadron therapy machine. Concepts for such facilities are being developed as an alternative to existing designs, looking at possibilities for treatment improvements and cost savings. The performance requirements have motivated the development of MEDeGUN, a Brillouin-type electron gun, that can focus a beam close to the smallest stable cross section or highest current density. The chapter describes electron beam commissioning and charge breeding experiments carried out with MEDeGUN installed in the TwinEBIS charge breeder test stand. Additionally, it contains a review of the design studies for an extension of the test bench with a dedicated ion beamline, which is to be installed in the future. A summary of the thesis and a brief outlook are given in Chapter 6.



# CHAPTER 2

## THEORY

This chapter contains the relevant theoretical concepts needed to understand the operation of an Electron Beam Ion Source (EBIS). A general introduction dealing with EBIS devices and their use at particle accelerators is followed by a summary of the most important plasma interactions surrounding the production of Highly Charged Ions (HCI). Finally, a theoretical description of the electron beam dynamics in an EBIS is presented.

### 2.1 Electron beam ion sources

The general operating principle of an EBIS is sketched out in Figure 2.1. In the electron gun, a beam is formed from electrons emitted by a hot cathode. The beam is compressed and guided through the centre of the machine with the help of a solenoidal magnetic field. At the far end, the beam follows the diverging magnetic field lines and the electrons hit the surface of the collector electrode. Positive ions are attracted by the negative charges in the electron beam and get trapped in its radial potential well. A series of hollow electrodes, so-called drift tubes, are used to create an axial trap by applying suitable electrical potentials to each of them. Owing to the high current density of the electron beam, there is a high likelihood for collisions between electrons and ions in the central trap region. These collisions drive the successive ionisation into high charge states. Once the target charge state is reached, the ions can be extracted from the EBIS by modifying the axial potential in such a way, that the ions are expelled through the open end of the collector.

There are two predominant ways to introduce particles into an EBIS; either as singly charged ions or as a neutral gas. Singly charged ions, created in an external source, can be injected into the EBIS from the collector side or through a hollow cathode on the gun side. The preferred injection method is to briefly open the axial trap and send a short ion bunch into the EBIS. The ions are reflected at the potential barrier on the gun-side, and before they leave the EBIS again the collector-side barrier is raised to trap the ion bunch. Alternatively, a small amount of neutral gas can be injected into the EBIS. If a neutral atom or molecule passes through the

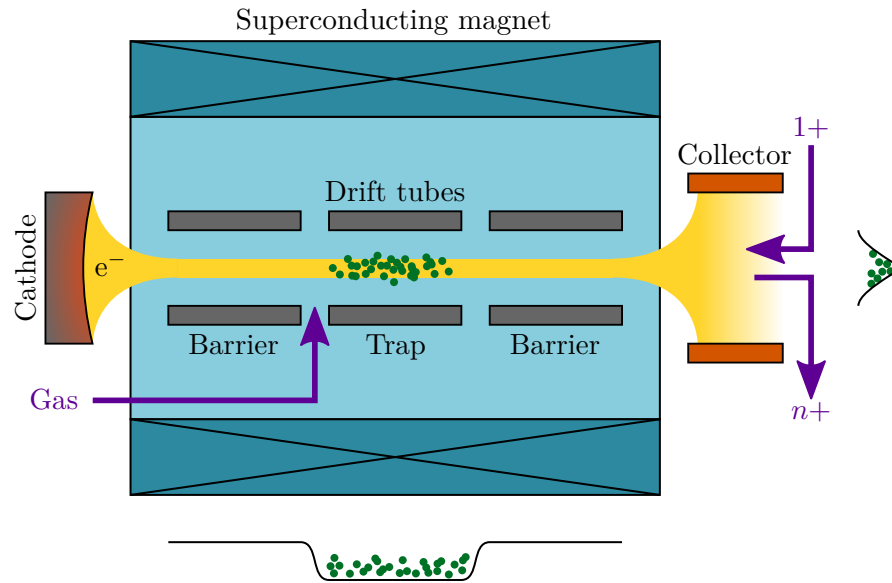


Figure 2.1: Conceptual design of an EBIS.

electron beam it can get ionised in a collision. The newly created ion is immediately trapped by the electrostatic potentials.

In the context of particle acceleration, EBIS devices can provide some advantages over the two other established methods for HCI production, i.e. the use of stripper foils and Electron Cyclotron Resonance Ion Sources (ECRIS). When stripping the remaining electrons of an ion with a foil, a pre-accelerator is needed to provide the required momentum to the lowly charged ions. The pre-accelerator typically has a higher initial investment cost and is usually less flexible than a dedicated charge breeder. In an ECRIS the electrons have a thermal distribution which impedes the production of very high ion charge states. Moreover, the geometry of an ECRIS can enhance ion losses and contamination if the generated plasma interacts with the walls. Compared to this, EBIS devices can be operated with very small losses and nearly contamination free. This has made them very popular for the preparation of highly charged Rare Isotope Beams (RIB) at facilities like ISOLDE and CARIBU [13–16] (with further projects in progress at TRIUMF and FRIB [17–21]), where both losses and background signals are major concerns due to the often miniscule abundance of the isotope of interest.

Additionally, a short ion bunch length is required in many applications, like e.g. LINAC-based hadron therapy [3, 4, 22]. An ECRIS can produce high beam currents, but is often limited by the length of the extracted ion pulse. In an EBIS ions are trapped during the charge breeding process and can be extracted within typically several  $\mu\text{s}$ . ECRIS produce much longer pulses ( $\sim \text{ms}$ ) or often even dc-beams that may have to be chopped before injecting the ions into the

accelerator. On the other hand, it has been demonstrated that slow extraction from an EBIS is still possible if this is preferred from an operational perspective [23, 24].

Electron beam ion traps are largely similar in design to an EBIS. In order to provide transverse optical access to the trapping region, the solenoid is usually replaced by a pair of Helmholtz coils. In comparison to an EBIS, an EBIT is usually much shorter, since the total ion storage capacity is not a primary concern. The shorter trap length is meant to reduce the susceptibility to collective instabilities which could develop in elongated highly compressed electron beams [25–27]. The trapping region is instead optimised for long storage times and efficient evaporative cooling of the ion population, in order to reach high charge states and observe the ions for an extended amount of time. Regardless of these differences, the theoretical EBIS concepts introduced below equally apply to EBIT devices.

## 2.2 Charge breeding

In an EBIS, electron bombardment drives the successive ionisation of the target population; in practice however, numerous processes take place simultaneously and determine the overall charge breeding dynamics. These are in principle the same effects as found in any hot multi-component plasma. In the interaction region, the ion cloud is radially confined to the proximity of the central electron beam. There, the ions are subject to collisions with the beam electrons which are streaming through the ion cloud with a given kinetic energy  $E_e$ . While elastic collisions primarily increase the temperature of the ion cloud - an effect commonly referred to as Spitzer heating [28] - inelastic collisions drive processes like excitation, ionisation, and recombination. Furthermore, the ions can interact and exchange electrons with neutral atoms composing the residual gas found in any real vacuum system. Together these charge state changing interactions determine the evolution of the charge state distribution over time.

### 2.2.1 Electron impact ionisation

The primary mechanism driving the successive ionisation to high charge states is Electron impact Ionisation (EI). If enough energy is transferred from a beam electron to a bound electron to overcome the binding energy, the target electron can detach from the ion  $A^{q+}$ , increasing its charge state by a single step



The cross section for electron impact ionisation at a given projectile energy  $E_e$  can be estimated using an empirical model developed and refined by Lotz [29–31], which expresses the total

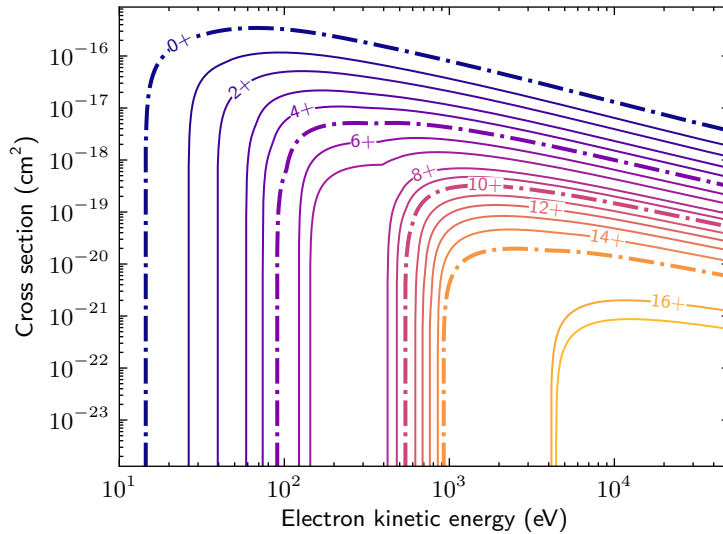


Figure 2.2: Electron ionisation cross sections for argon ions, modelled with the Lotz formula. The sharply rising flanks are located at the smallest binding energy of each charge state. The step-like features visible in some curves arise due to the contributions of more strongly bound states.

ionisation cross section as a sum over the contributions of individual subshells  $k$  as

$$\sigma^{\text{EI}} = \sum_{\forall k: E_e > I_k} a_k N_k \frac{\log(E_e/I_k)}{E_e I_k / \text{eV}^2} \left( 1 - b_k \exp \left[ -c_k \left\{ \frac{E_e}{I_k} - 1 \right\} \right] \right). \quad (2.2)$$

Here,  $N_k$  denotes the number of electrons in a subshell with the associated binding energy  $I_k$ . The coefficients  $a_k$ ,  $b_k$ , and  $c_k$  have been tabulated by Lotz for neutrals and low charge states, for all other cases they can be approximated as  $a_k = 4.5 \cdot 10^{-14} \text{ cm}^2$  and  $b_k = c_k = 0$ . In Figure 2.2 the cross sections for argon are provided as an example.

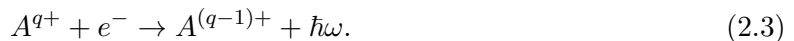
Typically, the dominant contribution to the total cross section is given by the outermost shell with the ionisation energy  $I$ . Using this assumption, one can approximate that  $\sigma^{\text{EI}}$  has its maximum value when  $E_e \approx 2.7I$ . Considering that the cross section decreases rapidly with increasing charge state, the charge breeding time is mostly spent on the final ionisation step. In order to accelerate the charge breeding process, the electron beam energy can therefore be set such that it is approximately 2.7 times larger than the ionisation energy required to reach the target charge state. Ultimately, the electron beam energy sets a practical limit on the highest attainable charge state, since electron impact ionisation halts once all binding energies exceed the beam energy.

An energetic projectile can also cause double or even multiple ionisation in a collision, but the effect is commonly ignored. Data for multiple ionisation cross sections is rarely available and while some models exist (e.g. [32]), their accuracy suffers from the difficulty to describe the

contributing interactions. Since the associated cross sections appear to be significantly smaller than those for single ionisation, neglecting their contribution to the charge state evolution is usually justified.

### 2.2.2 Radiative recombination

Instead of triggering an ionisation process, beam electrons can also be captured into bound states of the target ions; in its simplest form this process is referred to as direct Radiative Recombination (RR). The released energy, which comprises the kinetic energy  $E_e$  and the binding energy  $I$  of the capturing state is carried away through the emission of a photon with  $\hbar\omega = E_e + I$ . This means that RR is the inverse process to photoionisation, and can be expressed as



The process is illustrated in the left part of Figure 2.3. If the light emitted from the interaction region of an EBIS is analysed with a suitable detector, photons linked to RR are readily identified due to the direct linear dependence of their energy on the electron beam energy.

Kim and Pratt have developed a model to estimate the RR cross sections by fitting a modified Kramers formula to known cross sections [33] which can be expressed as

$$\sigma^{\text{RR}} = \frac{8\pi\alpha}{3\sqrt{3}} \left( \frac{\hbar}{m_e c} \right)^2 \chi \log \left( 1 + \frac{\chi}{2n_{\text{eff}}^2} \right). \quad (2.4)$$

In this expression,  $\alpha$  is the fine structure constant. The factor  $\chi$  depends on the effective charge  $Z_{\text{eff}} = (Z + q)/2$ , where  $Z$  is the nuclear charge, and on the electron beam energy

$$\chi = Z_{\text{eff}}^2 \frac{2 \text{Ry}}{E_e}. \quad (2.5)$$

Here,  $\text{Ry} \approx 13.6 \text{ eV}$  denotes the Rydberg energy. The factor  $n_{\text{eff}}$  describes an effective principal quantum number

$$n_{\text{eff}} = n + (1 - w_n) - 0.3, \quad (2.6)$$

where  $w_n$  is the fraction of unoccupied states in the valance shell  $n$ . Due to the dependency of  $\sigma^{\text{RR}}$  on  $E_e$  and  $Z_{\text{eff}}$ , the charge state evolution is typically only affected by radiative recombination once very high charge states are reached and the cross sections become sufficiently large to compete with ionisation cross sections. The radiative cross sections of argon are shown in Figure 2.4.

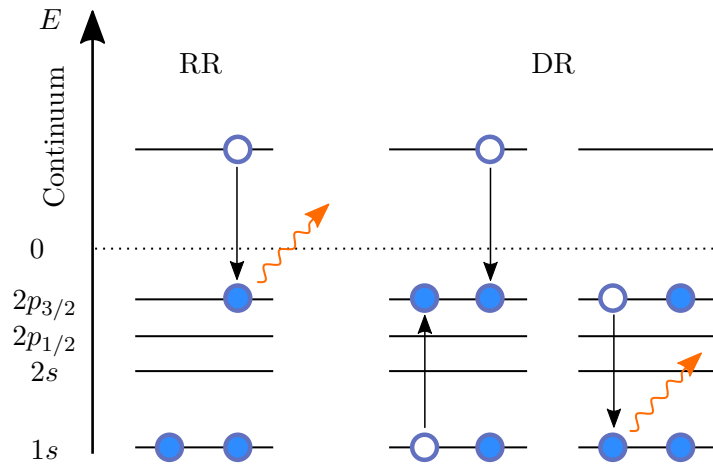


Figure 2.3: Illustration of radiative recombination process (left) and dielectronic recombination process (right). The DR process is split into electron capture and radiative decay steps.

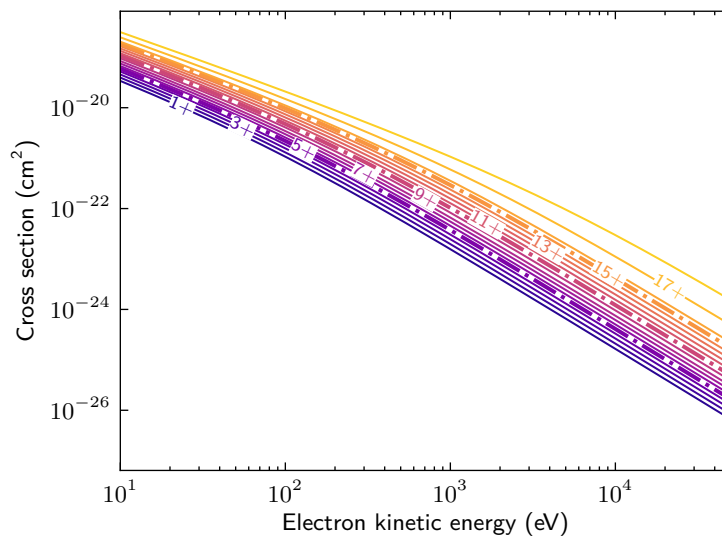
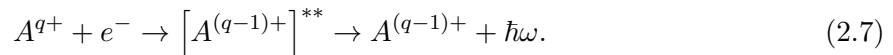


Figure 2.4: Radiative recombination cross sections for argon ions, according to the Kim & Pratt model.

### 2.2.3 Dielectronic recombination

The recombination of beam electrons with ions can also occur in a resonant fashion. Instead of emitting the energy released in the recombination event as a photon, one or more inner shell electrons are transferred into an excited state, which subsequently decays. Here, the sum of kinetic energy and binding energy released during the recombination have to match the energy required for the excitation of the inner shell electrons.

The simplest form of resonant recombination is referred to as Dielectronic Recombination (DR), which can be written as



This process can be interpreted as the inverse process to the Auger-Meitner effect [34]. An illustration of the two-step process is given in the right part of Figure 2.3. Higher order versions of resonant recombination (e.g. trielectronic) exist, but are not discussed here.

After capturing the electron, the ion is left in an intermediate doubly-excited state, which can decay radiatively through the emission of a photon with a characteristic wavelength. The intermediate state can also decay in an auto-ionising fashion; in this case there is no net change in the charge state of the ion. The branching ratio depends on the transition strengths of all possible auto-ionising and radiative decay channels.

Dielectronic recombination transitions are categorised based on the initial and final electronic state of the ion, which is in the direct accordance to the names of the corresponding Auger decays. This is best explained by giving an example. An ion is initially configured with an electron in the K shell. After the recombination event, the old and the recombined electron are found in the L shell. In this case one speaks of a KLL transition. Similarly, the configuration could change from an electron occupying the L shell to one in the M and one in the N shell, this would be an LMN transition.

There is no generalised model to compute or estimate the effective cross sections  $\sigma^{\text{DR}}$  for dielectronic recombination. Usually, the transition strengths and resonance energies have to be determined with the help of computation-intensive atomic structure calculations using tools like the Flexible Atomic Code FAC [35, 36]. Since the energy spread of the electron beam typically greatly exceeds the natural line width of the DR transitions, the effective cross section profile is dominated by the required convolution with the energy distribution of the projectile electrons. A more detailed explanation of this follows in Section 3.3.1.2. An example is provided in Figure 2.5, in the form of the KLL transitions of argon.

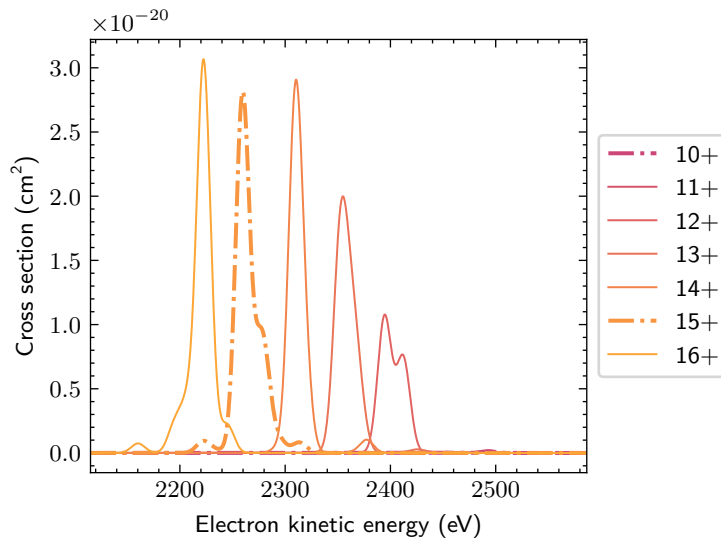
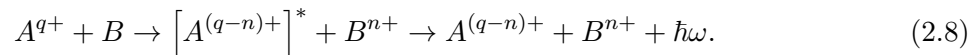


Figure 2.5: KLL-type dielectronic recombination cross sections for argon ions. The resonance energies and transition strengths were determined using FAC. The energy spread of the electron beam is typically much larger than the natural line width of the transition. In this plot it is incorporated through the convolution of the resonance lines with a Gaussian distribution with a FWHM of 15 eV.

### 2.2.4 Charge exchange

Charge exchange (CX) describes the process in which electrons are transferred from a neutral particle to an ion during collisions of the ion population  $A$  with the residual background gas  $B$ . In simplified terms this phenomenon can be explained through the formation of a quasi-molecule when the highly charged ion approaches the gas particle. During the close encounter, the potentials of the collision partners are superimposed and the coupling of their energy levels allows for the transfer of one or more electrons. Generally, the stronger coupling between states with similar binding energies lead to a preferred capture into high-lying states of the ion. Subsequently, the ion is de-excited predominantly through radiative decay. The reaction equation for the transfer of  $n$  electrons can be written as



The cross section for charge exchange is commonly estimated using a scaling formula, fitted to experimentally determined cross sections by Müller and Salzborn [37]. For the case of single electron capture the cross section is given as

$$\sigma^{\text{CX}} = 1.43 \cdot 10^{-12} \text{ cm}^2 q^{1.17} \left( \frac{I}{\text{eV}} \right)^{-2.76}, \quad (2.9)$$

where  $q$  denotes the initial ion charge state and  $I$  is the ionisation potential of the neutral target species. Similar scaling laws are provided for up to fourfold charge exchange, but single charge exchange is generally understood to be the dominant effect. Furthermore, the authors advocate against extrapolating the scaling laws for multiple charge exchange to cases where  $q > 8$  because the scaling would eventually contradict the observed dominance of single charge exchange.

In a more general sense, charge exchange also occurs between lowly and highly charged ions. In this case the electron is transferred from the lowly to the highly charged ion. The cross section for this process can be approximated by inserting the ionisation energy of the lowly charged ion into the Müller Salzborn formula.

### 2.2.5 Charge state evolution

Equipped with the cross sections for the different processes taking place in the EBIS, it is possible to develop a simple model describing the evolution of the charge state spectrum over time. The model presented here is simplified and takes into account only ionisation and recombination effects, to illustrate the general charge breeding behaviour. It is going to show the importance of having a high current density electron beam and can be used to derive relations between the interaction cross sections and the emerging steady state of the charge state distribution. A more extensive view on the topic of charge breeding simulations is found in Chapter 3. In addition to the charge state changing processes, it also deals with effects of the increasing ion cloud temperature like losses from the trap and a reduction of the ion density.

#### 2.2.5.1 The simplified rate equations

The charge breeding process in an EBIS can be modelled through a set of rate equations which follow from straight forward assumptions. Let the electron beam be cylindrical with a uniform current density  $j = I/(\pi r^2)$  and a given kinetic energy  $E_e$ . Furthermore, assume that all ions are evenly spread across the electron beam cross section. Due to the large mass of the ions, they are practically at rest compared to the electron beam streaming through the ion cloud. In this configuration, the rate of interactions between any ion of charge state  $q_i$  and the electron beam can be written as

$$\Gamma_i^P = \frac{j}{e} \sigma_i^P(E_e), \quad (2.10)$$

where  $\sigma_i^P$  is the cross section of process P for the charge state in question.

This form of reaction rate is sufficient to write down the simplified rate equations. Let  $N_i$  reflect the number of ions in charge state  $q_i$ . Then its rate of change can be expressed as

$$\frac{dN_i}{dt} = \frac{j}{e} \left[ - \left( \sigma_i^{\text{EI}} + \sigma_i^{\text{RR}} + \sigma_i^{\text{DR}} \right) N_i + \sigma_{i-1}^{\text{EI}} N_{i-1} + \left( \sigma_{i+1}^{\text{RR}} + \sigma_{i+1}^{\text{DR}} \right) N_{i+1} \right], \quad i \in \{0, 1, \dots, Z\}, \quad (2.11)$$

where the dependence of the cross sections on the electron energy has been omitted. This equation represents a reduction in abundance of charge state  $q_i$  due to charge state changing reactions, while the same processes cause particles from neighbouring charge states to get transferred into charge state  $q_i$ . Only single ionisation and recombination are taken into account. Charge exchange is not included in this model because it requires a notion of ion temperature which is deferred to Chapter 3. Similar rate equations form the base of most charge breeding simulation efforts, starting with Penetrante et al. [38].

### 2.2.5.2 Charge breeding example: argon

The system of coupled linear ordinary differential equations defined by Equation 2.11 is readily solvable through numerical integration techniques. Sticking to the example of argon, Figure 2.6 shows the charge state evolution under several conditions.

Figure 2.6a shows the charge breeding process for reasonably conventional parameters. As time passes, the ions are bred into higher and higher charge states. Since the cross sections for ionisation are significantly larger than those for recombination at the chosen beam energy of  $E_e = 2100$  eV, the dynamics are dominated by  $\sigma_i^{\text{EI}}$ . Because  $\sigma_i^{\text{EI}}$  decreases strongly with increasing charge state, an ever-increasing amount of time is needed to reach each subsequent charge state. Eventually the distribution approaches an equilibrium with most ions occupying charge state 16+, because the electron beam is not energetic enough to break open the K-shell and remove the remaining two electrons of the argon ion. This, so called, closed-shell breeding is sometimes used to artificially increase the yield of certain charge states [39].

The resonant nature of dielectronic recombination cross sections is illustrated in Figure 2.6b.  $E_e = 2220$  eV is slightly increased with respect to the previous scenario to match a KLL-DR resonance of  $\text{Ar}^{16+}$  ( $\text{FWHM}(E_e) = 15$  eV, cf. Figure 2.5). Close to the resonance energy,  $\sigma^{\text{DR}}$  grows quickly, and in this specific case the DR cross section for charge state 16+ slightly exceeds the EI cross section of charge state 15, i.e.  $\sigma_{16+}^{\text{DR}} > \sigma_{15+}^{\text{EI}}$ . This tips the emerging equilibrium distribution in favour of the 15+ charge state. The relative abundance is linked to the ratio of the relevant cross sections as will be shown in the next section.

In the first two scenarios, the argon was initialised in the 1+ charge state; Figure 2.6c shows argon ions continuously being injected from a neutral background population. These two modes correspond to pulsed singly charged ion injection and continuous neutral gas injection, respectively. In order to model a constant supply of neutral particles, the model equations can simply be adjusted to read

$$\frac{dN_0}{dt} = 0 \Rightarrow N_0(t) = \text{const.} \quad (2.12)$$

Because this generates a constant source term, the particle number increases over time. Figure 2.6c shows the abundance normalised by the total particle number. The charge state curves

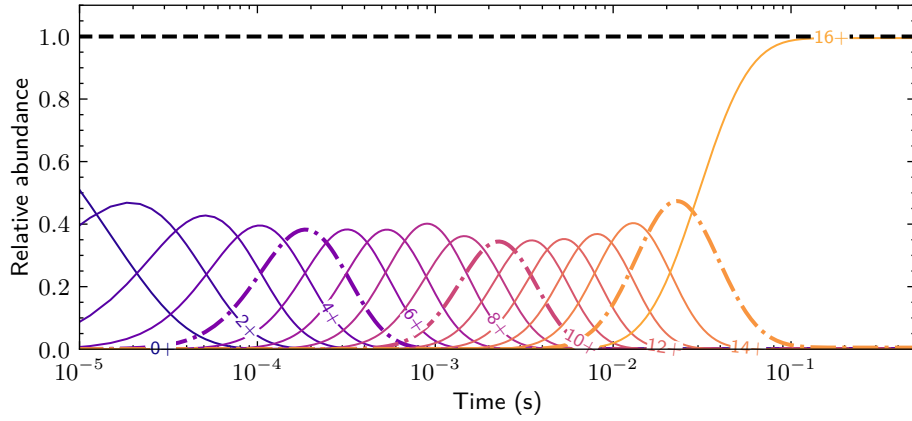
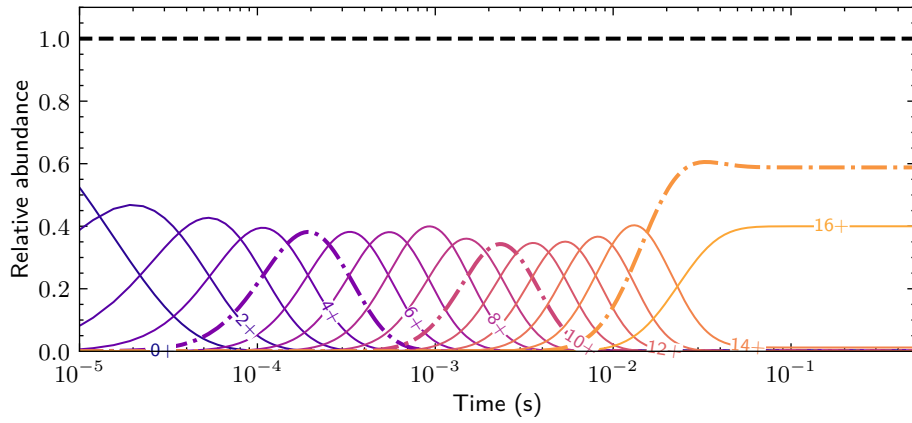
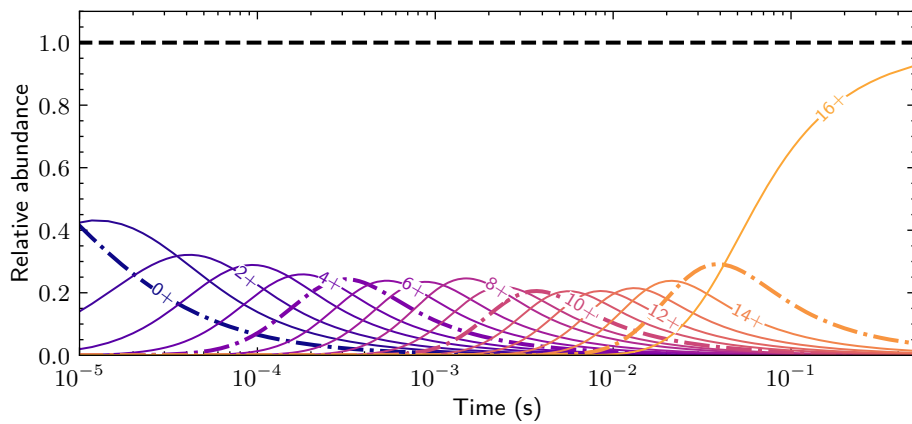
(a)  $\text{Ar}^{1+}$  ions,  $j = 500 \text{ A/cm}^2$ ,  $E_e = 2100 \text{ eV}$ .(b)  $\text{Ar}^{1+}$  ions,  $j = 500 \text{ A/cm}^2$ ,  $E_e = 2220 \text{ eV}$ ,  $\text{FWHM}(E_e) = 15 \text{ eV}$ . The electron beam energy falls onto a resonance for DR of  $\text{Ar}^{16+}$ , cf. Figure 2.5.(c) Injection of neutral Ar,  $j = 500 \text{ A/cm}^2$ ,  $E_e = 2100 \text{ eV}$ . The abundance is normalised with the total ion count at any given time.

Figure 2.6: Charge state evolution of argon under differing breeding conditions.

appear smeared out towards longer times compared to the pulsed injection case. Due to the permanent influx of lowly charged ions, intermediate charge states are not depleted, but their relative weight decreases over time as more ions are injected and evolve towards the highest attainable charge state.

### 2.2.5.3 Steady state

After a sufficiently long time (exceeding the time constants of the slowest relevant processes) the charge state distribution tends towards an equilibrium or steady state. This is not strictly true, if the particle number is not constant. In steady state the rate of change in abundance for a given charge state is perfectly balanced, i.e.  $dN_i/dt = 0$ . For the highest attainable charge state  $\hat{q}$  (e.g.  $\text{Ar}^{16+}$  in Figure 2.6), the ionisation cross section  $\sigma_{\hat{q}}^{\text{EI}} = 0$ , and the equilibrium condition yields

$$N_{\hat{q}} \left( \sigma_{\hat{q}}^{\text{DR}} + \sigma_{\hat{q}}^{\text{RR}} \right) = N_{\hat{q}-1} \sigma_{\hat{q}-1}^{\text{EI}}. \quad (2.13)$$

Far off DR resonances  $\sigma^{\text{DR}} = 0$ , and the charge state equilibrium is determined by RR and EI cross sections

$$\frac{N_{\hat{q}}}{N_{\hat{q}-1}} = \frac{\sigma_{\hat{q}-1}^{\text{EI}}}{\sigma_{\hat{q}}^{\text{RR}}}. \quad (2.14)$$

This relation puts a limit on the largest achievable abundance of the highest charge state  $N_{\hat{q}}$ .

Compared to DR transitions, the cross sections of EI and RR typically vary slowly with the electron energy. Therefore, steady state abundance modulations close to DR resonance energies can be related to the (widened) line profile of the corresponding transition

$$\sigma_{\hat{q}}^{\text{DR}}(E_e) = \sigma_{\hat{q}-1}^{\text{EI}} \frac{N_{\hat{q}-1}(E_e)}{N_{\hat{q}}(E_e)} - \sigma_{\hat{q}}^{\text{RR}}. \quad (2.15)$$

Assuming knowledge of  $\sigma_{\hat{q}-1}^{\text{EI}}$  and  $\sigma_{\hat{q}}^{\text{RR}}$ , this means that  $\sigma_{\hat{q}}^{\text{DR}}(E_e)$  can be measured by scanning the electron beam energy and observing the abundance ratio.

### 2.2.5.4 Exact solution

Equation 2.11 can be cast into a different form by introducing the abundance vector  $\mathbf{N} = (N_0, N_1, \dots, N_Z)$  (where  $Z$  represents the bare nucleus) and the cross section matrix  $\mathbf{\Sigma}$ , where

$$\Sigma_{ij} = \begin{cases} -\sigma_i^{\text{EI}} - \sigma_i^{\text{RR}} - \sigma_i^{\text{DR}} & \text{if } j = i \\ \sigma_{i-1}^{\text{EI}} & \text{if } j = i - 1 \geq 0 \\ \sigma_{i+1}^{\text{RR}} + \sigma_{i+1}^{\text{DR}} & \text{if } j = i + 1 \leq Z \end{cases}. \quad (2.16)$$

The new system of equations reads

$$\frac{d\mathbf{N}}{dt} = \frac{j}{e}\boldsymbol{\Sigma}\mathbf{N}. \quad (2.17)$$

In analogy to one dimensional linear differential equations the solution of this system can be written in a matrix exponential form as

$$\mathbf{N}(t) = \exp\left(\frac{j}{e}\boldsymbol{\Sigma}t\right)\mathbf{N}_0. \quad (2.18)$$

Here,  $\mathbf{N}_0$  describes the initial charge state distribution.

This result underlines the importance of the current density  $j$  which acts as a direct scaling factor for the speed of the evolution.  $\boldsymbol{\Sigma}$  is relatively constrained and offers little freedom for optimising the charge breeding speed, whereas doubling  $j$  should in theory cut the required breeding time in half.

## 2.3 Non-relativistic electron beam dynamics

The electron beam is the core component of any EBIS. It is responsible for charge breeding the ions through inelastic collisions and confining the ions radially through its negative space charge potential. As was shown in Section 2.2.5, the electron beam current density  $j$  determines the collision rate and hence directly affects the charge breeding time. High current densities are therefore desirable but the provision and long-distance transport of high current density beams is generally challenging. Typical target values for  $j$  are in the range of hundreds to thousands A/cm<sup>2</sup> and greatly exceed the current densities which can be extracted from known cathode materials under dc-conditions. Furthermore, the mutual repulsion of the electrons in the beam creates a space charge field that causes the beam to diverge quickly.

These problems are mitigated through the use of a focusing magnetic field. A common choice for this application is either a solenoid magnet or a pair of Helmholtz coils. The electron gun is usually located in the magnetic fringe field where the flux density is small or even zero. Launched along the symmetry axis of the magnetic field, the beam experiences an increase in magnetic flux density as it enters the full field region. The Lorentz force causes the electrons to spiral around the magnetic flux lines and can be thought of confining their movement to the vicinity of the flux line. These flux lines converge towards the axis along the magnetic field gradient and force the electrons comprising the beam into a smaller radius. In this fashion the beam is compressed and the current density increases. The focusing forces exerted by the magnetic field also stop the beam from diverging due to space charge forces.

### 2.3.1 Electron gun

Electron beam devices generally rely on a so-called electron gun as the primary beam source. In principle an electron gun consists of an electron emitting cathode and a positively biased anode towards which the electrons are accelerated before they escape through a dedicated aperture. This is in principle very similar to the operation of a thermionic planar diode, or electric valve.

**Space charge limited flow in thermionic diodes** In an ideal diode, an infinitely large cathode located in the  $z = 0$  plane is heated which results in the emission of electrons, cf. Figure 2.7a. Applying a positive bias to the anode located at  $z = d$  causes the electrons to drift towards it. In a conventional capacitor this arrangement of the electrodes is known to result in a homogeneous electric field, but in a diode the charge density created by the drifting electrons needs to be taken into account. Without loss of generality, we can assume a cathode potential of  $\Phi_C = \Phi(z = 0) = 0$  and an anode potential  $\Phi_a = \Phi(z = d)$ . Under stationary conditions, the electron distribution will work to shield the externally applied field, and just above the cathode where the electrons are virtually at rest we obtain the field free boundary condition  $\Phi'(z = 0) = 0$ . This problem was analysed by Child and Langmuir [40] who found that it is readily solved by a total potential obeying  $\Phi \propto z^{4/3}$ . In this situation, the current density in the diode scales with the applied voltage and electrode spacing as  $j \propto \Phi_a^{3/2} d^{-2}$ . This functional relationship between current and acceleration potential turns out to be universally useful, and for a beam with total current  $I$  it is often expressed as the perveance  $P = I/\Phi^{3/2}$ .

Here, we have quietly assumed that the cathode is able to emit sufficiently many electrons to sustain the flow regardless of the applied voltage. This is referred to as space charge limited emission or Child-Langmuir emission. Real cathodes have an emission limit of typically a few A/cm<sup>2</sup>, and if the anode voltage is increased such that the flow exceeds this limit, the flow is referred to as thermionically limited and in general the field at the cathode no longer vanishes. In this regime the beam current increases more slowly than predicted by the perveance law. If the field strength at the cathode raises to extreme levels (which can be encouraged with dedicated geometric features like emission tips), the cathode may begin to break down and field emission may be achieved.

**Planar Pierce gun** Conceptually, a planar gun could be designed simply by choosing a finite size for the cathode and anode, and providing an aperture through which the formed beam can escape. In practice however, one needs to account for the now inhomogeneous charge density, which causes a deformation of the electric field. For beams of increasing perveance, the excess of electrons in the beam creates a defocusing field that causes the beam to diverge. The radius of a beam with a perveance of  $1 \cdot 10^{-6}$  A/V<sup>3/2</sup> for example would double over an axial distance equivalent to just about ten times its initial radius [41].

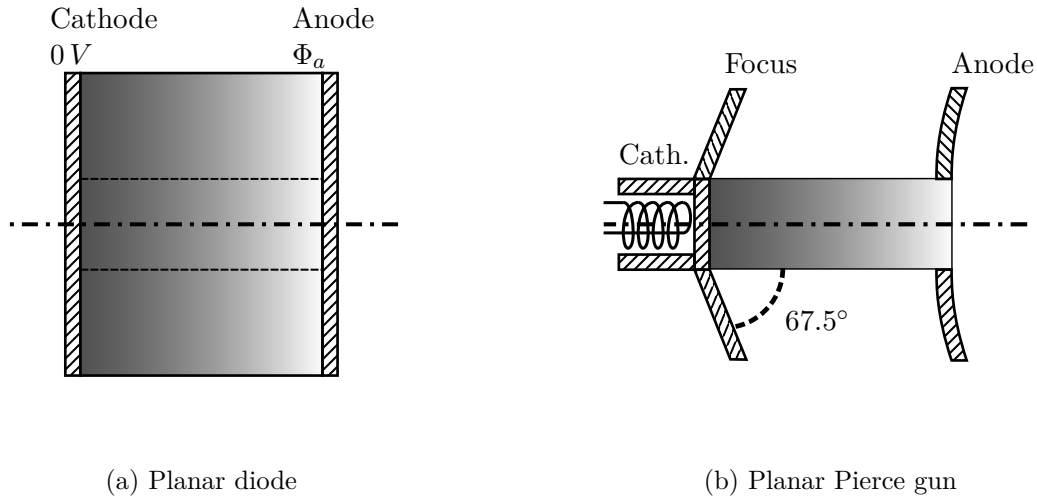


Figure 2.7: Schematic representations of the principal design of a planar diode and the derived Pierce gun geometry.

Pierce observed that the parallel electron flow inside the beam could be maintained by restoring the conditions for vanishing transverse fields at the beam boundary and reproducing on the beam axis the potential gradient previously found in the planar diode. After extending the Laplace equation into the complex domain, Pierce found that this was possible by surrounding the cathode with a planar non-emissive surface angled at exactly  $67.5^\circ$  with respect to the beam edge [42]; this is regularly dubbed the focus electrode or Wehnelt. The anode obtains a curved shape, where the exact profile follows the equipotential contours of Pierce's solution which vary as a function of  $z$ . This geometry is illustrated in Figure 2.7b.

Strictly speaking this gun geometry is only applicable for a one dimensional ribbon beam, but even for more complex geometries as e.g. a cylindrical one, the region close to the cathode can be considered planar, such that the focus electrode follows the same profile adjacent to the cathode, but may have its profile adapted at larger radii. Electron guns of this type are common, and in the scope of this thesis have been used at REXEBIS, as described in Chapter 4.

**Spherical Pierce gun** A geometry that lends itself particularly well to high current density applications is a spherical design. This type of gun was explored by Langmuir and Blodgett based on the electron flow in a diode consisting of concentric sphere segments [43]. Here the cathode has the larger radius, and the emergent beam is focused and accelerated towards the anode which has a smaller radius of curvature and an appropriate aperture for the beam to escape. Such a design is attractive because it naturally compresses the beam to a focal point which is generally located outside the gun. This facilitates the injection of the convergent beam into a magnetic focusing field.

The derivation of the gun perveance and the potential inside the gun follows the ideas for

the planar geometry and yields expressions of similar forms, however an analytical solution is no longer possible, and the results rely on polynomial approximations. To first order the perveance of a cylindrical electron gun scales  $\propto (\sin \theta/2)^2 (\ln r_a/r_c)^{-2}$ , where  $\theta$  is the half opening angle of the spherical cathode, and  $r_a$  and  $r_c$  are the curvature radii of the anode and cathode, respectively. In the context of EBIS/T devices, spherical guns are often combined with magnetic shielding to produce a Brillouin beam, which will be introduced in more detail below. In this thesis, MEDeGUN installed at TwinEBIS follows this principle, cf. Chapter 5.

**Anode aperture defocusing** The discussion above neglects the influence of the anode aperture on the fields in the electron gun. A strong accelerating field is formed between the cathode and the anode, whereas the fields downstream of the gun is typically much smaller or even zero. Such a configuration is known as an aperture lens and has a defocusing effect on a traversing particle beam [44]. This becomes particularly relevant for high perveance guns, as these typically feature the highest field strengths in the gun volume and may require large anode apertures to prevent scraping the edge of the high current beam [41]. For a planar gun this essentially dictates the emergence of a divergent beam from the gun; a spherical gun may still have sufficient focusing to overcome the defocusing from the anode aperture and only suffer from a shifted focal point and possible aberrations. With increasing perveance, this means more design effort is needed to adjust the electrode shapes in an attempt to mitigate the defocusing or accommodate for its consequences.

### 2.3.2 Electron trajectories in crossed electric and magnetic fields

Exactly describing the motion of charged particles in mixed magnetic and electric fields is generally difficult. But using the cylindrical symmetry of the problem and a few simplifying assumptions, a theoretical description of the electron beam in the EBIS is possible. In this framework the behaviour of the electron beam traversing the focusing structure can be understood and expressions for the expected beam radius can be derived.

Due to the symmetry of the problem it is advisable to choose a cylindrical coordinate system  $(r, \theta, z)$ . Let the electric field  $\mathbf{E}$  and the magnetic field  $\mathbf{B}$  be symmetric about the  $z$ -axis and the azimuthal field components  $E_\theta = B_\theta = 0$ ; then the equations of motion follow from the Lorentz force as

$$\ddot{r} - r\dot{\theta}^2 = -\eta (E_r + r\dot{\theta}B_z) \quad (2.19)$$

$$\frac{1}{r} \frac{d}{dt} (r^2\dot{\theta}) = -\eta (\dot{z}B_r - \dot{r}B_z) \quad (2.20)$$

$$\ddot{z} = -\eta (E_z - r\dot{\theta}B_r). \quad (2.21)$$

Here  $\eta = e/m_e$  denotes the electron's (positive) charge to mass ratio. The magnetic field is

assumed to be purely external, whereas the electric field includes the space charge field generated by the beam itself.

If laminar flow is assumed, a particle located on the edge of the beam will never dive into the centre, as such layer crossing is forbidden. In this case the beam envelope can be described through a single on-edge particle. Provided the right initial conditions, the equations of motion then describe the evolution of the beam envelope. These conditions are usually determined for a particle emitted on the edge of the cathode.

### 2.3.3 Busch's theorem

In the common case that the external magnetic field does not change over time, Equation 2.20 can be used to derive a conservation law also known as Busch's theorem [45]. By rewriting the magnetic field in terms of its vector potential  $\mathbf{A}$  and exploiting that  $\partial_t \mathbf{A} = 0$ , it is straight forward to show [46] that

$$\frac{1}{r} \frac{d}{dt} (r^2 \dot{\theta}) = \eta \left( \dot{r} \frac{\partial(rA_\theta)}{\partial r} + \dot{z} \frac{\partial A_\theta}{\partial z} \right) = \frac{1}{r} \eta \frac{d}{dt} (rA_\theta). \quad (2.22)$$

Adding that the magnetic flux threading the area encompassed by  $r$  is given by  $\psi = 2\pi rA_\theta$ , which follows from Stokes' theorem, the conservation law for the canonical angular momentum reads

$$\frac{d}{dt} \left( m_e r^2 \dot{\theta} - e \frac{\psi}{2\pi} \right) = 0. \quad (2.23)$$

This expression shows a direct relation between the classical angular momentum of the particle and the magnetic flux that it is currently encircling. In this manner, the conservation law automatically accounts for any torque created by radial magnetic fields that the electron is crossing. For a particle that was emitted with no initial velocity, i.e.  $\dot{\theta}_0 = 0$ , at the edge of a cathode with radius  $r_0$  and enclosing a magnetic flux  $\psi_0$  the angular velocity is

$$\dot{\theta} = \frac{\eta}{2\pi r^2} (\psi - \psi_0). \quad (2.24)$$

It will become clear later that the cathode flux plays a major role for the achievable beam compression.

For a sufficiently uniform magnetic field, one can identify  $\psi = \pi r^2 B_z$ . If the electron beam is launched in a field free region where  $\psi_0 = 0$ , the angular velocity loses the radial dependence and the whole beam performs a rigid rotation at the so called Larmor frequency  $\omega_L$

$$\dot{\theta} = \frac{\eta B_z}{2} = \omega_L. \quad (2.25)$$

### 2.3.4 Beam induced space charge field

The electric field generated by the negative space charge density of the electron beam is significant and has to be accounted for in describing the electron beam behaviour. As will be demonstrated, the space charge creates a radial electric field that exerts defocusing forces on the electron beam. This divergence inherently limits the achievable current density and adequately countering these forces is key to ensure smooth transport of the beam through the focusing magnetic field. On the other hand, the potential well created by the beam is also responsible for radially confining the ion population.

In order to describe the radial space charge field, a simple model is used. The electron beam is assumed to be an infinitely long cylinder with a uniform charge density  $\rho$  across its radius  $r_e$ . It is surrounded by a hollow electrode of inner radius  $r_{DT}$  - typically a drift tube - which acts as a boundary surface. The charge density is determined by the current density  $j = I/\pi r_e^2$  and the velocity  $u_e$  of the beam. In cylindrical coordinates, the Poisson equation for the electrostatic potential  $\Phi$  reads

$$\frac{1}{r} \frac{\partial}{\partial r} \left( r \frac{\partial \Phi(r)}{\partial r} \right) = -\frac{\rho(r)}{\varepsilon_0} \quad \text{where} \quad \rho(r) = \begin{cases} -I/(u_e \pi r_e^2) & \text{if } r \leq r_e \\ 0 & \text{if } r > r_e \end{cases}. \quad (2.26)$$

From symmetry considerations it follows that  $\Phi'(0) = 0$  and to describe the space charge potential with respect to the surrounding electrode the boundary potential is chosen as  $\Phi(r_{DT}) = 0$ . In this model, the space charge field does not have any axial components. This is justified if the beam radius does not vary strongly along the beam.

The solution for  $\Phi$  is readily obtained through the application of Gauss's theorem and can be written as

$$\Phi_{SC}(r) = \begin{cases} \Phi_0 \left[ \left( \frac{r}{r_e} \right)^2 + 2 \ln \frac{r_e}{r_{DT}} - 1 \right] & \text{if } r \leq r_e \\ \Phi_0 2 \ln \frac{r}{r_{DT}} & \text{if } r > r_e \end{cases}. \quad (2.27)$$

Here  $\Phi_0$  is equivalent to the potential drop between the edge and the centre of the beam

$$\Phi_0 = \Phi_{SC}(r_e) - \Phi_{SC}(0) = \frac{I}{4\pi\varepsilon_0 u_e}. \quad (2.28)$$

Figure 2.8 shows an example of a typical radial space charge profile. For the further analysis of the beam envelope, the electric field on the edge of the beam is required. It can be derived from Equation 2.27 as

$$E_r^{SC}(r_e) = -\frac{I}{2\pi\varepsilon_0 u_e r_e} = -\frac{\omega_p^2}{2\eta} r_e, \quad (2.29)$$

where  $\omega_p^2 = \eta|\rho(r_e)|/\varepsilon_0$  defines the plasma frequency.

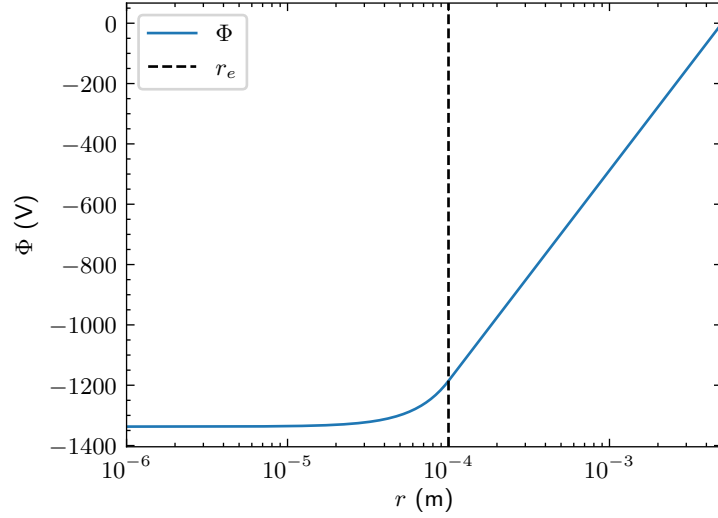


Figure 2.8: Typical radial potential well created by an electron beam ( $I = 1$  A,  $E_e = 10$  keV,  $r_e = 0.1$  mm) travelling through a hollow cylindrical electrode (with inner radius  $r_{DT} = 5$  mm).

### 2.3.5 Space charge balanced flow

Using the preceding derivations one can now set up the equation of motion for the beam envelope. In doing so, external radial electric fields will be neglected and the magnetic flux density is assumed to be constant across the beam. Inserting Equations 2.24 and 2.29 into Equation 2.19 yields

$$\ddot{r} = \frac{\eta I}{2\pi\epsilon_0 u_e} \frac{1}{r} - \left(\frac{\eta B_z}{2}\right)^2 r + \left(\frac{\eta\psi_0}{2\pi}\right)^2 \frac{1}{r^3}. \quad (2.30)$$

Letting  $\psi$  and  $\omega_p$  be defined in terms of a newly introduced equilibrium beam radius  $r_a$ , this equation can be restated in a more convenient form [46]

$$\frac{1}{\omega_p^2} \frac{d^2}{dt^2} \left(\frac{r}{r_a}\right) = \frac{1}{2} \left(\frac{r}{r_a}\right)^{-1} - \left(\frac{\omega_L}{\omega_p}\right)^2 \left(\frac{r}{r_a}\right) + \left(\frac{\omega_L}{\omega_p}\right)^2 \left(\frac{\psi_0}{\psi}\right)^2 \left(\frac{r}{r_a}\right)^{-3}. \quad (2.31)$$

It can be seen that all forces are balanced and the beam radius is constant if and only if the conditions

$$r = r_a \quad \wedge \quad \frac{1}{2} = \left(\frac{\omega_L}{\omega_p}\right)^2 \left[1 - \left(\frac{\psi_0}{\psi}\right)^2\right] \quad (2.32)$$

are fulfilled. This is called space charge balanced flow and describes the situation in which the focusing forces exerted by the external magnetic field perfectly cancel the sum of space charges forces and centrifugal forces. If  $\psi_0 = 0$ , one also speaks of Brillouin flow [47].

If the above conditions are violated or if the beam envelope is initially converging or diverging, i.e.  $\dot{r}(t=0) \neq 0$ , the beam radius will oscillate around the equilibrium value  $r_a$ . Weak

oscillations of the envelope are practically unavoidable and generally not an issue. Large amplitude oscillations are problematic, since the varying radius could introduce a strong periodic modulation of the space charge potential along the beam and lead to a less stable operation of the EBIS.

### 2.3.6 Electron beam radius

By substituting the quantities in Equation 2.32 with their definitions, the equation can be solved for a formula for the equilibrium beam radius

$$r_a = r_B \sqrt{\frac{1}{2} + \frac{1}{2} \sqrt{1 + 4 \frac{r_0^4 B_0^2}{r_B^4 B^2}}}. \quad (2.33)$$

Here,  $r_B$  denotes the so called Brillouin radius [47] which is the beam radius if there is no initial enclosed flux, i.e.  $\psi_0 = \pi r_0^2 B_0 = 0$ ,

$$r_B = \sqrt{\frac{2I}{\eta \pi B^2 \epsilon_0 u_e}}. \quad (2.34)$$

To accelerate the charge breeding process it is often desirable to optimise the current density of the beam. The primary way to achieve this is to reduce the beam radius. The Brillouin radius can be thought of as the smallest equilibrium radius achievable for a beam with a given current and energy in a given magnetic field. In the context of an EBIS,  $\psi_0$  can be understood as the magnetic flux threading the cathode inside the electron gun. Equation 2.33 shows the importance of reducing the cathode flux in order to maximise the achievable current density.

Driven by experiments that had shown the formation of cathode images along the electron beam in elongated focusing systems, Herrmann developed a new “optical theory” to describe the beam propagation [48]. Since this theory does not rely on laminarity but explicitly deals with trajectory crossings, thermal effects can be included naturally. In reality the cathode surface is hot, and the electrons are emitted with a finite momentum in random directions. Similar to cathode flux this is a source of initial canonical angular momentum. In this situation the beam can no longer be pictured as performing coherent radial oscillations but has a more diffuse nature due to the randomised momentum distribution of all electrons. The effective beam radius accounting for thermal effects can be derived from the original work as

$$r_H = r_B \sqrt{\frac{1}{2} + \frac{1}{2} \sqrt{1 + 4 \left( \frac{r_0^4 B_0^2}{r_B^4 B^2} + \frac{8m_e k_B T_0 r_0^2}{e^2 r_B^4 B^2} \right)}}, \quad (2.35)$$

where  $T_0$  is the emitter temperature. This result is often referred to as the Herrmann formula,

and provides the standard way of estimating the beam radius in an EBIS.

The thermal contribution to the radius is based on evaluating a trajectory which encloses  $\pm\sqrt{2}$  standard deviations ( $\doteq 84\%$ ) of the thermal velocity distribution; this may be the reason that the Herrmann radius is often claimed to enclose approximately 80% of the total beam current. If  $T_0 = 0$ , Equation 2.35 is equivalent to Equation 2.33 and therefore agrees with the prior result. The Herrmann radius could in fact be derived analogous to Equation 2.33, by assigning an initial angular momentum  $L_0 = m_e r_0 v_{th} = m_e r_0 \sqrt{2k_B T/m_e}$  to the beam edge particle.

Even for relatively small residual cathode fields, the expression for the beam radius is quickly dominated by the  $r_0^4 B_0^2 / r_B^4 B^2$  term. Disregarding the remaining terms under the square roots, the radius formula simplifies to

$$r_I = r_0 \sqrt{\frac{B_0}{B}}, \quad (2.36)$$

which presents a widely used approximation for the compression of a strongly immersed beam. Conveniently, the beam radius depends only on the cathode radius and magnetic field ratio in this case.

Before closing this section, it is worth noting that the current density associated with the Brillouin radius, does not directly depend on the beam current:

$$j_B = \frac{I}{\pi r_B^2} = \frac{\eta B^2 \varepsilon_0 u_e}{2}. \quad (2.37)$$

Instead, the current density is determined by the magnetic field and the electron velocity which needs to be tuned such that a perfect force balance is achieved for the chosen electron current. In analogy to the previous expression, the current density associated with the Herrmann radius can be written as

$$j_H = \frac{I}{\pi r_H^2} = \frac{j_B}{\frac{1}{2} + \frac{1}{2} \sqrt{1 + 4 \left( \frac{r_0^4 B_0^2}{r_B^4 B^2} + \frac{8m_e k_B T_0 r_0^2}{e^2 r_B^4 B^2} \right)}}. \quad (2.38)$$

As the electron current is increased, the value of the Brillouin radius grows and consequently the denominator approaches a value of 1. Hence, the current density in a real beam would be expected to approach the theoretical Brillouin optimum for very high currents. In practice however, the transmittable current is naturally limited by the design of the electron gun and the EBIS electrodes.

### 2.3.7 Energy correction and virtual cathode formation

Up to this point, the electron beam energy  $E_e$  and the closely related forward beam velocity  $u_e$  have not been paid much attention. Nonetheless, they are critical quantities:  $u_e$  has a direct impact on the electron charge density and the emerging space charge forces, whereas  $E_e$  is closely

linked to the charge breeding cross sections as shown in Section 2.2.

Because of the energy conserving properties of static electric fields, the kinetic energy of the electrons is simply given by the local potential, measured with respect to the cathode where the electrons were emitted  $\Phi_C$ . In practice, the local electric potential is dominated by the voltage applied to the surrounding electrode – or drift tube –  $\Phi_{DT}$  and by the electron beam’s space charge  $\Phi_{SC}$ . The kinetic energy is hence

$$E_e = e (\Phi_{DT} + \Phi_{SC} - \Phi_C). \quad (2.39)$$

Commonly the energy spread, caused by the space charge gradient across the beam, can be ignored and the kinetic energy is determined using the on-axis space charge potential (cf. Equation 2.27).

Often it is assumed, that the forward momentum  $p_z$  carries the majority of the kinetic energy. In this case, the (non-relativistic) forward velocity of the beam can simply be estimated as

$$u_e = \sqrt{\frac{2E_e}{m_e}}. \quad (2.40)$$

Yet caution is necessary since a significant fraction of the kinetic energy  $E_\perp$  may be stored in the transverse motion of the electron. If this is the case, a correction is required

$$u_e = \sqrt{\frac{2(E_e - E_\perp)}{m_e}}. \quad (2.41)$$

As the electrons travel from the gun into the full field region of the EBIS, they gather angular momentum and an increasing amount of kinetic energy is drawn from the forward motion. In extreme cases this can force the electron to turn around, comparable to the reflections found in magnetic mirrors or bottles [49].

A closer look at Equations 2.27, 2.39 and 2.40 reveals that  $E_e$  and  $u_e$  are mutually dependent on each other through the space charge potential. This is because the space charge field decelerates the beam, which in turn causes an increase of the charge density and so forth. Usually it is possible to find a self-consistent solution for  $E_e$  and  $u_e$  by iteratively computing the space charge correction until convergence is reached.

If the externally applied acceleration gradient is too small, the beam can become unstable. Taking an on-axis particle and letting the beam velocity  $u_e = \sqrt{2e(\Phi_{ext} + \Phi_{SC})/m_e}$ , Equation 2.27 can be rewritten as

$$\Phi_{SC} = \frac{I}{4\pi\epsilon_0} \sqrt{\frac{m_e}{2e(\Phi_{ext} + \Phi_{SC})}} \left( 2 \ln \frac{r_e}{r_{DT}} - 1 \right). \quad (2.42)$$

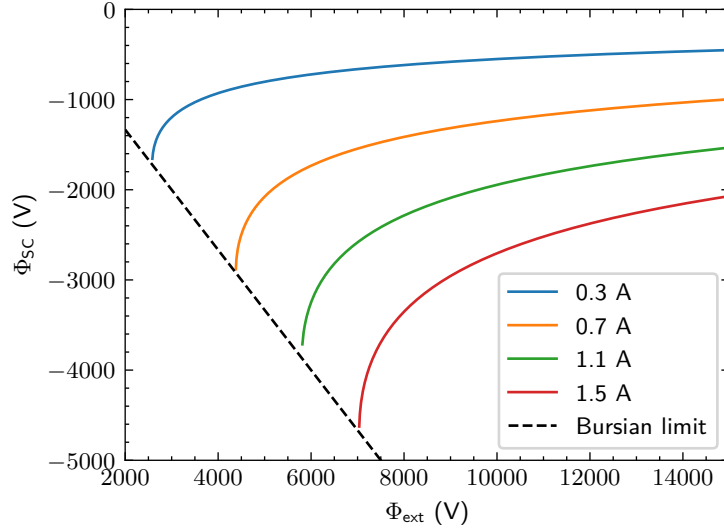


Figure 2.9: On-axis space charge corrections  $\Phi_{\text{SC}}$  for different electron beam currents. The beam energy is determined by the externally applied voltage  $\Phi_{\text{ext}}$  and the space charge correction as  $E_e = e(\Phi_{\text{ext}} + \Phi_{\text{SC}})$ . Electron beam radii have been computed using the Brillouin formula for a magnetic field of 2 T and a drift tube radius of 5 mm. Underneath the black dashed line, the beam is unstable.

Here,  $r_e$  and  $r_{\text{DT}}$  are the radii of the electron beam and the drift tube, respectively. From this expression a limit for the maximum transmissible current can be derived by evaluating  $\partial I / \partial (\Phi_{\text{ext}} + \Phi_{\text{SC}}) = 0$  [50, 51]. The so called Bursian limit can be written as

$$\frac{I}{\Phi_{\text{ext}}^{3/2}} = \frac{8\pi\epsilon_0}{3} \sqrt{\frac{2e}{3m_e}} \frac{1}{1 + 2 \ln r_{\text{DT}}/r_e} \approx \frac{25.4 \mu\text{A}/\text{V}^{3/2}}{1 + 2 \ln r_{\text{DT}}/r_e}. \quad (2.43)$$

It presents the largest perveance achievable for a given beam size and drift tube radius. If this current limit is exceeded (or the applied potential falls below a critical value), the beam is unstable and losses will occur. It is interesting to note that, when the Bursian limit is reached, the external acceleration potential has not yet been fully compensated by space charge but instead  $\Phi_{\text{SC}} = -2/3 \cdot \Phi_{\text{ext}}$ . At this point even a small fluctuation in beam energy can cause an avalanche effect, where the interaction of beam velocity and space charge causes the beam to come to a sudden halt and the beam is essentially reflected by its own space charge barrier [52]. This is often interpreted as the formation of a virtual cathode. Figure 2.9 presents the solution of Equation 2.42 for a number of different currents and externally applied potentials. The plot also shows a line marking the limiting relation between  $\Phi_{\text{ext}}$  and  $\Phi_{\text{SC}}$ .



## CHAPTER 3

# CHARGE BREEDING SIMULATIONS

This chapter takes a closer look at simulations of the charge breeding dynamics in an EBIS. A *Python* package for charge breeding simulations, named *ebisim*, has been developed in the framework of this thesis. This package implements the simulation on two complexity levels. The basic simulation model is largely equivalent to the equations presented in Section 2.2.5. The effects composing the advanced simulation model are covered in this chapter. Most importantly, the advanced model adds the concept of ion temperature and introduces related phenomena, like elastic collision heating, ion cloud expansion around the electron beam, and thermal losses from the central trap. The chapter opens with a discussion of the physics model, followed by remarks concerning the specific implementation of the simulation code. Finally, the capabilities of the simulation tool are illustrated in an example dealing with charge breeding of potassium around its KLL dielectronic recombination resonances.

### 3.1 Model overview

The earliest simulations of the charge breeding process in an EBIS were performed by Penetrante et al. [38] through the integration a set of rate equations. These rate equations offer a relative simplicity and thanks to the comprehensive research on numerical methods for solving ordinary differential equations (e.g. [53, 54]) there is a wide range of stable and efficient solvers available, enabling rather fast simulations. While there are attempts to simulate charge breeding through more involved means as for example particle in cell simulations [55], rate equations remain the primary method for describing the charge breeding dynamics. The general building blocks composing the overall model have largely remained the same since the early work by Penetrante et al.; numerous modifications and improvements to the contributing terms have been proposed throughout the years, among others by Liu et al. [56], Fussmann et al. [57], Radtke et al. [58], Kalagin et al. [59], and Currell and Fussmann [28].

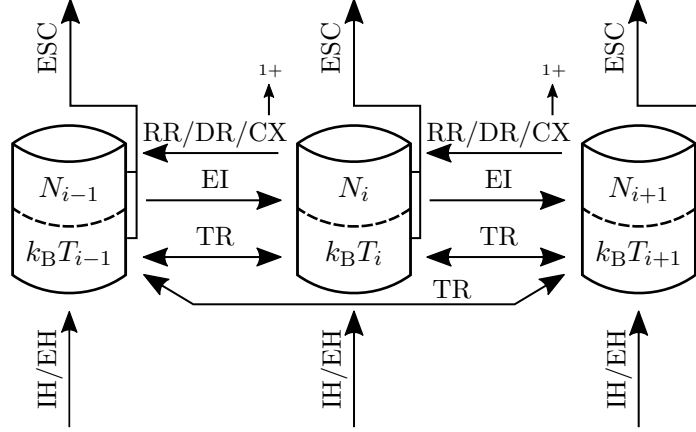


Figure 3.1: Diagram of the particle and heat flow described by the rate equations (3.1) and (3.2).

The rate equations for the particle number are an extension on Equation 2.11

$$\frac{dN_i}{dt} = - \left( R_i^{\text{EI}} + R_i^{\text{RR}} + R_i^{\text{DR}} + R_i^{\text{CX}} \right) + R_{i-1}^{\text{EI}} + R_{i+1}^{\text{RR}} + R_{i+1}^{\text{DR}} + R_{i+1}^{\text{CX}} - R_i^{\text{ESC}}. \quad (3.1)$$

Besides the familiar terms for electron ionisation (EI) and radiative (RR) and dielectronic recombination (DR), there are new terms for charge exchange (CX) and particles escaping the trapping region (ESC). Figure 3.1 shows a coarse graphical representation of the interactions between different charge states. The actual expressions for these terms will be introduced throughout this chapter. For the simulations it will be assumed, that the axial trap is flat, and the ions are evenly distributed along the axis of the trap. It is therefore suitable to interpret  $N_i$  as the linear ion density, i.e. the amount of ions per unit length. The volumetric ion density resulting from the radial spread of the ion population will be identified with a small letter  $n_i$ .

In addition to the rate equations for the particle numbers, a second set of equations is needed to describe the temperature evolution of the ions

$$\frac{d(k_B T_i)}{dt} = \left( S_i^{\text{EI}} + S_i^{\text{RR}} + S_i^{\text{DR}} + S_i^{\text{CX}} \right) + S_i^{\text{EH}} + S_i^{\text{IH}} - S_i^{\text{ESC}} + S_i^{\text{TR}}. \quad (3.2)$$

Here, it should be clarified that the bracketed terms describe the temperature change due to ions being added to the population  $N_i$  from neighbouring charge states  $N_{i-1, i+1}$  through EI / RR / DR / CX interactions. Ions randomly drawn and removed from the energy distribution described by  $T_i$  do not change the temperature. This is not true for the escape term  $S^{\text{ESC}}$ , since the hottest particles escape from the trap first and do not form a representative sample of the total population.  $S^{\text{EH}}$  describes heating caused by elastic collisions between the ions and the beam electrons. The term  $S^{\text{IH}}$  denotes so-called ionisation heating which is related to the sudden change in potential energy that an ion experiences when its charge state is changing.

The final term  $S^{\text{TR}}$  covers the thermalisation resulting from collisional energy transfer between ions of different charge states and species.

A fundamental assumption underlying this description is that the ions belonging to a distinct population  $N_i$  are in thermal equilibrium with each other. Especially when ion densities are low this may not always strictly reflect reality; collisions become less likely and the relaxation times can be longer than the typical time scales of other interactions and processes. To make things worse, the radial ion density distribution can add a spatial dependency to this effect. However, describing non-thermal distributions would add severe complexity to the model, since it would be necessary to evolve not just a scalar temperature but in the worst case an entire distribution over time, comparable to approaches taken in Vlasov solvers [60] or particle in cell codes [61]. One therefore sticks to the assumption of a well-defined temperature. By computing the collision rate which will be introduced later, typical relaxation times can be estimated and compared to other timescales to develop a qualitative judgement on the meaningfulness of the temperature.

Before proceeding to the next section, it should be pointed out that, due to the thermal interaction and due to space charge considerations, this new model can yield interesting results when mixing different ion species. One can therefore think of the index  $i$  as describing not only different charge states but possibly also iterating over different elements. A second index for the species was omitted here to improve readability. Clearly, ionisation and recombination processes as in Equation 3.1 are still limited to occurring within the same species.

## 3.2 Radial ion distribution and space charge compensation

Before proceeding with the description of the time evolution it is helpful to consider the radial extent of the ion distribution. Due to their finite energy, the ions are moving throughout the trapping region. If this motion causes the ions to leave the electron beam, they will no longer be ionised or undergo recombination, which slows down the charge breeding process. Therefore, the radial extent of the ion cloud is of importance.

### 3.2.1 Poisson-Boltzmann equation

As discussed in Section 2.3.4, the negative space charge of the electron beam creates a potential trough within the drift tube which is responsible for the radial confinement of the ion cloud. Technically, the magnetic field impedes the radial movement of the ions since they are forced onto cyclotron trajectories, analogous to the focusing effect of the magnetic field on the electron beam. Through collisions however, the ions can diffuse across the axial magnetic field lines. Since the magnetic field does not contribute the potential energy of the ions, the radial distribution of the ion cloud is dominated by the space charge potential and the ion temperature. If the collision

rate is sufficiently high, the ion density profile will therefore follow a Boltzmann distribution in the potential well created by the electron beam. For an ion of charge state  $q_i$  this is given by the expression

$$n_i(r) = n_i^0 \mathcal{B}_i(r), \quad (3.3)$$

where shorthand notations for the on-axis ion density and the Boltzmann shape factor have been defined to reduce visual clutter

$$n_i^0 = n_i(0) \quad (3.4)$$

$$\mathcal{B}_i(r) = \exp\left(\frac{-q_i e (\Phi(r) - \Phi(0))}{k_B T_i}\right). \quad (3.5)$$

If the total ionic charge is insignificant compared to the electronic charge of the beam, then Equation 2.29 is sufficient to describe the radial ion cloud profile. In practice however, the ionic charge grows over time as higher charge states are reached and in the case of neutral gas injection more ions are created continuously. This causes the ions to compensate the negative space charge of the electron beam, reducing the overall potential depth. Early studies either ignored the varying space charge [38, 62] or tried to tackle the problem with the help of simplified effective models [63].

Lu et al. were the first to include a fully self-consistent solution of the radial space charge problem in the framework of charge breeding simulations [64, 65]. For this purpose the Poisson equation introduced earlier (Equation 2.26) needs to be extended to account for the positive ion charge contribution. The *ebisim* code assumes the following model

$$\frac{1}{r} \frac{\partial}{\partial r} \left( r \frac{\partial \Phi(r)}{\partial r} \right) = -\frac{\rho_e(r) + \rho_{ion}(r)}{\epsilon_0} \quad (3.6)$$

$$\rho_e(r) = \begin{cases} -I / (u_e(r) \pi r_e^2) & \text{if } r \leq r_e \\ 0 & \text{if } r > r_e \end{cases} \quad (3.7)$$

$$\rho_{ion}(r) = \sum_i n_i^0 q_i e \mathcal{B}_i(r) \quad (3.8)$$

where the electron beam velocity is given by

$$u_e(r) = \sqrt{2 [E_{e,0} + e\Phi(r)] / m_e}. \quad (3.9)$$

$E_{e,0}$  is the externally applied axial beam energy, not considering space charge corrections. Possible variations of the electron beam radius due to the varying space charge potential are neglected. The 3D ion densities relate to the linear densities in the rate equation as

$$N_i = 2\pi \int_0^{r_{DT}} n_i(r) r dr, \quad (3.10)$$

where  $r_{\text{DT}}$  is the drift tube radius. The problem defined in this way is nonlinear and a general closed form solution to the Poisson-Boltzmann equation does not exist. Instead, the potential and the ion density profiles have to be computed numerically. This procedure is explained in Section 3.4.3. For now, the solution is assumed to be known.

A couple of example solutions for a trap filled with singly charged ions are shown in Figure 3.2. The solutions nicely illustrate the importance of ion temperature for the compensated trapping potential. If the same amount of ions is brought into the trap at a higher temperature, the ions spread out further. Somewhat counter-intuitively, this results in a less significant overall change of the potential than for a cold ion cloud. Even if the total amount of charges is balanced ( $\xi = 1$ ) the radial potential does not vanish, because it is still dominated by the large negative charge density of the electron beam.

The approach taken in the simulation code presented here differs from the earlier work by Lu et al. in how the problem of particle number conservation is handled. As the ion cloud spreads out, the density has to decrease to maintain a constant number of ions. In Ref. [65] the rate equations are formulated for the 3D ion density. This requires an adjustment of the density in between time steps of the integration routine to account for any volume change. Opposed to that, the rate equations (3.1) are formulated in terms of the linear densities of ions. Due to the axial symmetry the linear density carries an equivalent meaning to the particle number. The volumetric densities are computed in the beginning of every time step by solving the Poisson-Boltzmann equation. This offers advantages with respect to the integration of the rate equation since advanced solvers may employ so-called multistep methods [54] which rely on information from previous time steps. Inter-time step adjustments to the state of the system would require a reinitialisation of such solvers, effectively rendering their advantages useless.

### 3.2.2 Quantities derived from the radial ion distribution

The solution of the Boltzmann-Poisson equation provides access to important quantities describing the properties and dynamics of the ion cloud inside the trapping region of the EBIS. Both, the radial electric potential  $\Phi(r)$  and the radial density profile for all ion species  $n_i(r)$  follow directly from the iterative solution algorithm. With these at hand, a number of effective quantities can be defined to aid with forthcoming computations.

As the electron beam traverses the drift tube structure its kinetic energy is modified due to the combined ion and electron space charge potential. Generally, the cross sections for processes playing out during charge breeding vary only weakly over the energy intervals typically covered by the electron beam. Nevertheless, these variations can be very large close to ionisation thresholds and resonant recombination lines as shown in Figure 2.2 and Figure 2.5, respectively. In these situations variations of the beam energy should be taken into account.

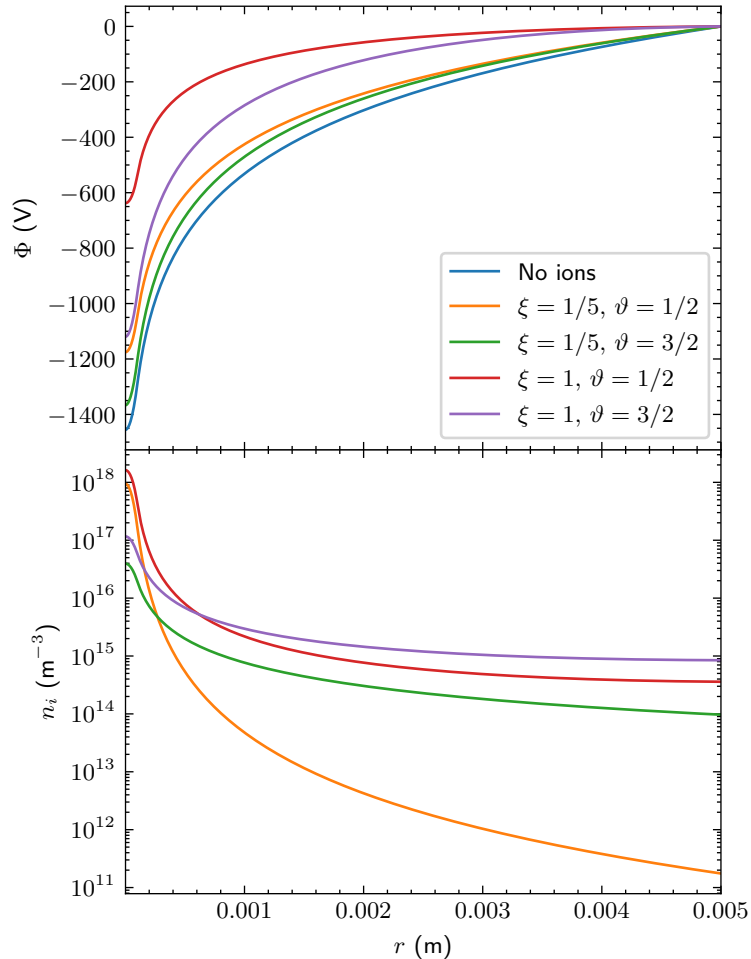


Figure 3.2: Radial potential and ion distribution for various ion densities and temperatures as self-consistent solutions to the Poisson-Boltzmann equation. The electron beam parameters are  $I = 1$  A,  $E_e = 10$  keV,  $r_e = 0.1$  mm,  $r_{DT} = 5$  mm. Singly charged ions fill the potential created by the electron beam and compensate it partially. The ion clouds are defined by  $\xi = N_i/N_e$  and  $\vartheta = k_B T_i / (e\Phi_0)$ , where  $N_e$  is the linear electron density and  $\Phi_0$  is the potential drop within the electron beam as defined in (2.28). The values of  $N_e$  and  $\Phi_0$  correspond to the nominal beam energy, ignoring space charge corrections.

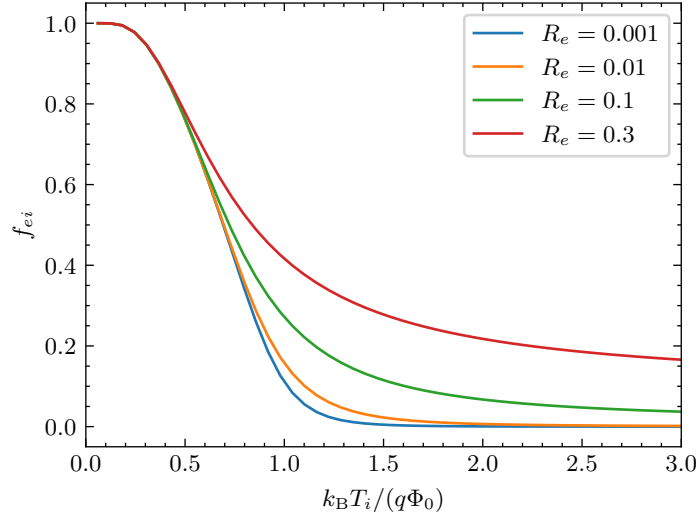


Figure 3.3: Plot of the electron ion overlap factors for a non-compensated uniform electron beam. The beam radii (legend) are given in units of the drift tube radius  $r_{DT}$ .

The average value of the space charge field across the electron beam radius can be written as

$$\langle \Phi \rangle_{r_e} = \frac{2}{r_e^2} \int_0^{r_e} \Phi(r) r dr. \quad (3.11)$$

To avoid confusion it should be stressed that  $\Phi$  carries a negative sign. It follows that the corrected beam energy is given by

$$E_e = E_{e,0} + e \langle \Phi \rangle_{r_e}. \quad (3.12)$$

Moreover, the emerging beam energy spread, which is of particular interest for narrow dielectric resonances, can be estimated as

$$\delta E_e = e \sqrt{\frac{2}{r_e^2} \int_0^{r_e} [\Phi(r) - \langle \Phi \rangle_{r_e}]^2 r dr}. \quad (3.13)$$

Owing to the Boltzmann distribution, ions of different charge state and temperature occupy different volumes around the trap axis. Since only ions within the electron beam experience inelastic collisions causing EI/RR/DR interactions, it is common to introduce overlap factors

$$f_{ei} = \frac{\int_0^{r_e} \mathcal{B}_i(r) r dr}{\int_0^{r_{DT}} \mathcal{B}_i(r) r dr}, \quad (3.14)$$

which describe the fraction of each ion species that overlaps with the electron beam cross section [63]. Using the definitions from Section 2.3.4 the overlap factors for a non-compensated uniform

electron beam can be calculated exactly as

$$\frac{1}{f_{ei}^{\text{UNI}}} = 1 + \frac{\theta}{1 - \theta} \frac{1 - (r_e/r_{\text{DT}})^{2-2\theta}}{(r_e/r_{\text{DT}})^{2-2\theta}(\exp(\theta) - 1)}, \quad (3.15)$$

where  $\theta = q\Phi_0/(k_B T)$  relates the ion temperature to the potential well depth inside the electron beam. A plot of the overlap factors for various electron beam radii is provided in Figure 3.3.

Similar overlap considerations arise when evaluating the collision rates between different ion species [38]. The effective radius of an ion cloud is computed as [65]

$$r_i = \frac{\int_0^{r_{\text{DT}}} r \mathcal{B}_i(r) r dr}{\int_0^{r_{\text{DT}}} \mathcal{B}_i(r) r dr}. \quad (3.16)$$

With this radius, the factor for ions  $i$  overlapping with a second population  $j$  can be defined as

$$f_{ij} = \min \left\{ \left( \frac{r_j}{r_i} \right)^2, 1 \right\} \neq f_{ji}. \quad (3.17)$$

This expression can be understood by imagining two ion species with different radial extent. A tightly confined ion cloud within a large cloud of background ions will effectively experience a homogeneous background density. When the roles are reversed, only a minor fraction of the large ion cloud will interact with the small ion cloud in its own centre.

### 3.3 Charge state and temperature evolution

The central piece of the charge breeding simulations are the rate equations for the charge state evolution (3.1) and the temperature flow (3.2). With the solution to the space charge problem at hand, one can write down the individual rates composing these model equations.

#### 3.3.1 Charge state changing interactions

The rates for EI/RR/DR interactions in the advanced model are very similar to those presented in Section 2.2 (and implemented in the basic simulation model). In addition to these effects, the advanced model introduces a term for CX. The rate expressions and additional information on the computation of the relevant cross sections are detailed in the following paragraphs.

As ions change their charge state, they join a different population which generally has a different temperature. This creates the need to introduce temperature rates associated with the charge breeding rates in order to accurately model the ion temperature. It is assumed that the affected ions form a representative sample of the thermal distribution of their original family. In this case removing ions from the original population will not affect its temperature. Therefore, the temperature of each ion population is only modified by ions pouring in from neighbouring

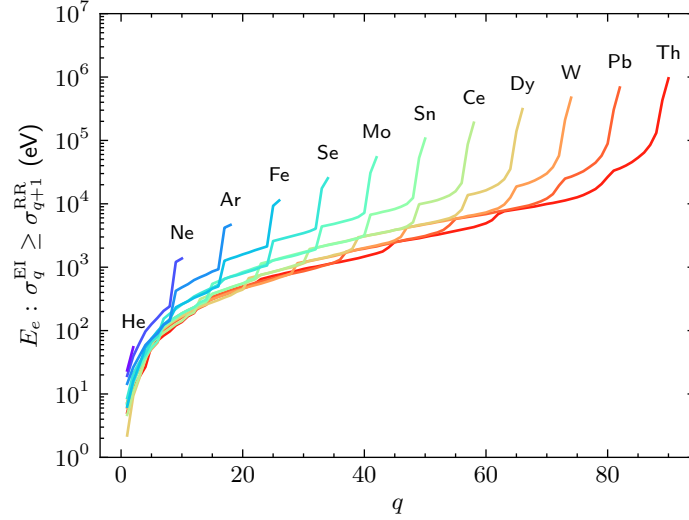


Figure 3.4: Plot of the minimum electron energy at which the electron ionisation cross section exceeds the radiative recombination cross section as a function of charge state for selected elements.

charge states. The actual rates are given below.

### 3.3.1.1 Electron ionisation and radiative recombination

In order to make use of the additional information in the advanced model, the rates for EI and RR can simply be extended by the newly introduced electron ion overlap factor

$$R_i^{\text{EI}} = \int_e \sigma_i^{\text{EI}}(E_e) f_{ei} N_i \quad (3.18)$$

$$R_i^{\text{RR}} = \int_e \sigma_i^{\text{RR}}(E_e) f_{ei} N_i. \quad (3.19)$$

This reflects the fact that ions located outside the electron beam do not participate in EI and RR processes. The cross sections  $\sigma^{\text{EI}}$  and  $\sigma^{\text{RR}}$  are computed according to Equation 2.2 and Equation 2.4, respectively.<sup>1</sup> Section 3.4.2.1 contains some additional *ebisim* specific information concerning the atomic data needed for cross section computations.

For sufficiently high charge states, the recombination cross section can exceed the ionisation cross section which results in a stalling of the charge breeding process. Due to the monotonically decreasing nature of the recombination cross section (cf. Section 2.2.2), this can be mitigated by increasing the electron beam energy. Figure 3.4 shows which beam energy is required for the ionisation process to dominate over recombination for selected elements.

<sup>1</sup>To aid future development, the *ebisim* implementation for the EI cross section also includes a relativistic correction factor developed by Gryziński [66, 67] as previously demonstrated in Ref. [65].

It is assumed that ions within a given population thermalise immediately. As ions of a different temperature join this population the difference in thermal energy is balanced out over the entire population until a new thermal equilibrium is established. The rate of temperature change can therefore be written as

$$S_i^{\text{EI}} = \frac{R_{i-1}^{\text{EI}}}{N_i} (k_{\text{B}}T_{i-1} - k_{\text{B}}T_i) \quad (3.20)$$

$$S_i^{\text{RR}} = \frac{R_{i+1}^{\text{RR}}}{N_i} (k_{\text{B}}T_{i+1} - k_{\text{B}}T_i). \quad (3.21)$$

In this context,  $i$  should be understood to represent purely the charge state of an ion. While several elements can be charge bred at the same time, there is no mixing between elements due to charge state changing processes.

### 3.3.1.2 Dielectronic recombination

The charge state evolution and temperature rates for DR are in direct analogy as those for RR

$$R_i^{\text{DR}} = \frac{j}{e} \sigma_i^{\text{DR}}(E_e) f_{ei} N_i \quad (3.22)$$

$$S_i^{\text{DR}} = \frac{R_{i+1}^{\text{DR}}}{N_i} (k_{\text{B}}T_{i+1} - k_{\text{B}}T_i). \quad (3.23)$$

But as previously stated a generally accepted scaling law for DR cross sections and resonance energies is not available. Instead, the cross sections are computed from supplied tables of resonance energies and transition strengths. More information on these tables is found in Section 3.4.2.2.

An additional quirk is the narrow width of DR transitions. Whereas RR/EI cross sections vary reasonably slowly with energy, such that the electron beam can safely be regarded as mono-energetic, the situation is turned on its head for the resonant nature of the DR process. The natural line width of DR transitions, which stems from the resonant excitation of the bound electron, is generally very small (commonly  $\ll 1$  eV) compared to the energy spread of the electron beam (several eV to hundreds of eV). Additionally, there is a collision energy spread introduced by the thermal energy of the ions, but due to their large mass, it can usually be neglected. In practice this means that only a fraction of all electrons have the correct kinetic energy to drive DR transitions.

An effective cross section could be determined by convoluting the natural line profile with the collision energy distribution. Yet, thanks to their small width, it is justified to treat the DR lines as  $\delta$ -distributions. In this case the convolution essentially corresponds to a scaling and shift of the beam energy distribution towards the resonance energy. In an attempt to find a good general model, the energy spread is assumed to be described by a normal distribution; the

cross section for a single transition  $\alpha$  can then be written as

$$\sigma_{i,\alpha}^{\text{DR}}(E_e) = \frac{A_{i,\alpha}}{\sqrt{2\pi}\sigma_E} \exp\left(-\frac{(E_e - E_{i,\alpha})^2}{2\sigma_E^2}\right). \quad (3.24)$$

Here,  $E_{i,\alpha}$  is the resonance energy of the transition and  $A_{i,\alpha}$  is the associated line strength (as defined in Section 3.4.2.2). The energy spread  $\sigma_E$  can either be set by the user or determined from Equation 3.13. Taking all possible transitions into account, the cross section profile for a given charge state is simply the total of all contributors

$$\sigma_i^{\text{DR}}(E_e) = \sum_{\alpha} \sigma_{i,\alpha}^{\text{DR}}(E_e). \quad (3.25)$$

Figure 2.5 contains an example covering KLL-type transitions of argon.

### 3.3.1.3 Charge exchange with neutrals

Charge exchange is implemented in the form of single electron transfer from a neutral particle to any ion of arbitrary charge state. Since this process is not driven by the electron beam the rate expression is a little different from that for EI/RR/DR. For the electron driven interactions the assumption was that the electrons stream through a cloud of essentially stationary ions. In the case of CX however, the collision partners are neutral atoms composing the residual background gas. Background gas will usually be at room temperature — corresponding to a thermal energy of approximately 25 meV — or below. Compared to this the ion temperature is usually ranging from several eV to keV. In this situation it is the ions which are streaming through a practically static field of neutral atoms. For a mixture of background gases  $b$  the charge exchange rate can be written as

$$R_i^{\text{CX}} = \sum_b n_b \sigma_{i,b}^{\text{CX}} v_{\text{th},i} N_i, \quad (3.26)$$

where the thermal velocity is defined as

$$v_{\text{th},i} = \sqrt{\frac{8k_B T_i}{\pi m_i}}. \quad (3.27)$$

The ion mass is denoted by  $m_i$ ,  $n_b$  is the gas particle density and  $\sigma_{i,b}^{\text{CX}}$  is the associated cross section as defined in Equation 2.9. There is no overlap factor here since the neutral particles, unaffected by electromagnetic fields, are expected to spread uniformly throughout the entire trapping region. The corresponding temperature rate is directly related to that of RR and DR

$$S_i^{\text{CX}} = \frac{R_{i+1}^{\text{CX}}}{N_i} (k_B T_{i+1} - k_B T_i). \quad (3.28)$$

In reality, every CX event brings with it the creation of a new singly charged ion. *Ebisim* offers a choice of defining pure background gases that simply act as a collision partner (neglecting the ion creation), or enabling CX with neutral particles belonging to any of the charge bred ion species. Both mechanisms can be combined freely.

### 3.3.2 Heating and thermalisation

Up to this point heat is only exchanged between ion populations through the conversion of the ions' charge states. This picture is obviously incomplete. Charged particles readily exchange momentum and kinetic energy through Coulomb collisions. This kind of interaction drives the collective thermalisation and isotropisation of all ions in the trapping region. Additionally, elastic collisions between beam electrons and ions act as a heating mechanism as the total amount of thermal energy in the ion cloud is increased. Without external heating (and cooling) mechanisms the ion temperature would hardly be of interest in the first place, since it would not change significantly during the charge breeding process.

#### 3.3.2.1 Spitzer heating

As the electron beam streams through the trapping region, individual electrons collide elastically with the captured ions. In such collisions they transfer some of their mostly forward directed momentum to the ion. Due to the random nature of repeated scattering events this leads to an increase of the thermal energy of the target ion. This electron beam heating mechanism is commonly referred to as Spitzer heating due to its relation to the Spitzer resistivity of a plasma [68, 69].

Assuming that the total energy loss of the beam as it crosses the ion cloud can be neglected, the heating rate can be written as [38]

$$S_i^{\text{EH}} = \frac{2}{3} n_e u_e \sigma_i 2 \frac{m_e}{m_i} E_e. \quad (3.29)$$

Here,  $n_e$  is the electron density and  $\sigma_i$  the Coulomb cross section. Identifying  $n_e u_e = j/e$ , the similarity between this expression and those for EI/RR/DR interactions is easily recognised.

The Coulomb collision cross section is given by [70]

$$\sigma_i = 4\pi \left( \frac{q_i e^2}{4\pi \epsilon_0 m_e} \right)^2 \frac{\ln \Lambda_{ei}}{u_e^4}, \quad (3.30)$$

where  $\ln \Lambda_{ei}$  is the so-called Coulomb logarithm. The Coulomb logarithm contains crucial plasma parameters and can be thought of as characterising the scattering angle distribution. It depends on the range of possible impact parameters, where the lower cut-off is presented by the closest

possible approach between two charged particles of a given temperature and the upper limit is determined by the Debye length, i.e. the length scale on which the surrounding plasma shields electromagnetic fields

$$\lambda_D = \sqrt{\frac{\varepsilon_0 k_B / e^2}{n_e / T_e + \sum_i q_i^2 n_i / T_i}}. \quad (3.31)$$

The value of the Coulomb logarithm is generally computed using approximations [71]

$$\ln \Lambda_{ei} \approx \begin{cases} 23 - \ln \left[ \left( \frac{n_e}{\text{cm}^{-3}} \right)^{1/2} \left( \frac{k_B T_e}{\text{eV}} \right)^{-3/2} q_i \right] & \text{if } T_i \frac{m_e}{m_i} < T_e < \frac{10 q_i^2 \text{eV}}{k_B} \\ 24 - \ln \left[ \left( \frac{n_e}{\text{cm}^{-3}} \right)^{1/2} \left( \frac{k_B T_e}{\text{eV}} \right)^{-1} \right] & \text{if } T_i \frac{m_e}{m_i} < \frac{10 q_i^2 \text{eV}}{k_B} < T_e. \\ 16 - \ln \left[ \left( \frac{n_i}{\text{cm}^{-3}} \right)^{1/2} \left( \frac{k_B T_i}{\text{eV}} \right)^{-3/2} q_i^2 \frac{m_i}{m_p} \right] & \text{if } T_e < T_i \frac{m_e}{m_i} \end{cases} \quad (3.32)$$

Here,  $m_p$  is the proton mass. Technically, these approximations have been derived for thermal electrons; for the EBIS simulation the thermal electron energy  $k_B T_e$  is replaced by the beam energy  $E_e$ .

### 3.3.2.2 Ionisation heating

Another heating mechanism that is caused by the presence of the electron beam, and closely linked to the presence of the radial trapping potential is so-called ionisation heating. During an ionisation or recombination event, the potential energy of an ion in the radial trapping field changes instantaneously because of the altered charge state. For processes driven by the electron beam, the mean change of potential energy per ion  $\Delta \mathcal{U}_i$  can be estimated using the thermal ion distribution as

$$\frac{\Delta \mathcal{U}_i}{\Delta q} = \frac{2}{r_e^2} \int_0^{r_e} (\Phi(r) - \Phi(0)) \mathcal{B}_i(r) r dr, \quad (3.33)$$

where  $\Delta q$  denotes the change in charge state associated with the observed process.

This effect creates an offset in potential energy compared to the ensemble formed by the remaining ions. Repeated collisions transform the potential energy into thermal energy leading to a net temperature increase for ionisation processes and a cooling effect for recombination processes. The combined ionisation heating rate for EI/RR/DR can be written as [65]

$$S_i^{\text{IH}} = \frac{2}{3} \frac{1}{N_i} \frac{2}{r_e^2} \int_0^{r_e} e (\Phi(r) - \Phi(0)) \left[ R_{i-1}^{\text{EI}} \mathcal{B}_{i-1}(r) - \left( R_{i+1}^{\text{RR}} + R_{i+1}^{\text{DR}} \right) \mathcal{B}_{i+1}(r) \right] r dr. \quad (3.34)$$

### 3.3.2.3 Collisional thermalisation

The rates for Spitzer heating and ionisation heating suggest a very distinct temperature evolution for each ion species and charge state. In practice of course, the ions are occupying the same

space and are going to exchange momentum through collisions. Through this mechanism their respective temperatures are driven towards a common value. Spitzer has derived an equation describing the temperature evolution of a population  $i$  thermalising with a background population  $j$  drawing from his earlier work on globular cluster mechanics [69, 72]

$$\frac{dT_i}{dt} = \frac{T_j - T_i}{t_{ij}^{\text{eq}}} \quad (3.35)$$

$$\text{where } t_{ij}^{\text{eq}} = \frac{3(4\pi\epsilon_0)^2 m_i m_j}{8\sqrt{2}\pi n_j q_i^2 q_j^2 e^4 \ln \Lambda_{ij}} \left( \frac{k_B T_i}{m_i} + \frac{k_B T_j}{m_j} \right)^{3/2}. \quad (3.36)$$

If the background temperature  $T_j$  is assumed to be constant, this equation describes an exponential approach of the test particle temperature  $T_i$  towards  $T_j$  on the timescale  $t_{ij}^{\text{eq}}$ , the so-called equipartition time. The ion-ion Coulomb logarithm can be approximated using [71]

$$\ln \Lambda_{ij} = \ln \Lambda_{ji} = 23 - \ln \left[ \frac{q_i q_j (m_i + m_j)}{m_i k_B T_j + m_j k_B T_i} \left( \frac{n_i q_i^2}{k_B T_i} + \frac{n_j q_j^2}{k_B T_j} \right)^{1/2} \left( \frac{\text{eV}^{3/2}}{\text{cm}^{-3/2}} \right) \right]. \quad (3.37)$$

In order to express the thermalisation rates in terms commonly used in the EBIS/T field, the Coulomb collision rate  $\nu_{ij}$  can be factored out of the expression for the equipartition time as [38]

$$\frac{1}{t_{ij}^{\text{eq}}} = \nu_{ij} \frac{m_i}{m_j} \frac{2}{\left( 1 + \frac{m_i k_B T_j}{m_j k_B T_i} \right)^{3/2}} \quad (3.38)$$

$$\text{where } \nu_{ij} = \frac{1}{(4\pi\epsilon_0)^2} \frac{4\sqrt{2}\pi}{3} n_j \left( \frac{q_i q_j e^2}{m_i} \right)^2 \left( \frac{m_i}{k_B T_i} \right)^{3/2} \ln \Lambda_{ij} \neq \nu_{ji}. \quad (3.39)$$

Here,  $\nu_{ij}$  should be interpreted as the collision rate of a single particle of species  $i$  with any background particle out of population  $j$ . To compute the temperature evolution for a given charge state  $i$  during the charge breeding process, the interaction with all possible collision partners  $j$  needs to be included yielding the rate expression [38, 62]

$$S_i^{\text{TR}} = \sum_j 2\nu_{ij} \frac{m_i}{m_j} \frac{k_B T_j - k_B T_i}{\left( 1 + \frac{m_i k_B T_j}{m_j k_B T_i} \right)^{3/2}}. \quad (3.40)$$

If ion overlap effects should be accounted for, the Coulomb collision rate can be multiplied by the overlap factor  $f_{ij}$  introduced in Equation 3.17

$$\nu_{ij} \rightarrow \nu_{ij} f_{ij}. \quad (3.41)$$

Collisional thermalisation is the main mechanism driving energy from hotter to colder ion populations, balancing out their temperature in the process. Since ions in lower charge states are experiencing smaller electrostatic trapping forces they will overcome the trapping field at lower temperatures than comparable ions in a high charge state. Combining this with the fact that highly charged ions are particularly affected by Spitzer heating, this can create a situation where energy is predominantly brought into the system through heavy highly charged ions and then transferred to lowly charged ions, which eventually heat up to the point where they can escape the trapping region. While this loss-driving effect can actually be exploited to actively cool the ion species of interest by injecting a lighter cooling gas, it serves to underline the importance of the heat transfer term.

### 3.3.3 Losses and evaporative cooling

Due to the finite depth of the electrostatic trapping potential, the ion temperature cannot grow indefinitely. All the rates that have been introduced up to this point either introduce more heat into the system or redistribute heat among different ion species and charge states. As the temperature is increasing, so is the average velocity of the ions. Eventually ions occupying the high energy tail of the Maxwell-Boltzmann distribution will acquire sufficient kinetic energy to escape from the trap. Obviously, the escaping ions have a much larger kinetic energy than the ensemble average, as one can imagine the tail of the particle speed distribution getting clipped. This clipping of the distribution causes a reduction of the average thermal energy per particle. Consequently, the remaining ions will through collisions establish a new equilibrium distribution at a slightly reduced temperature. Resembling the mechanism by which a hot drink cools down over time, this effect is referred to as evaporative cooling.

Evaporative cooling provides a balancing term to the various heat sources increasing the ion temperature and is of particular importance in electron beam ion traps, where ions are commonly stored over very long confinement times. Without a way to cool the ion populations, all ions would eventually boil out of the trap. A common technique is to inject a small amount of low-Z gas into the trap. Light ions tend to evaporate from the trap faster than the heavier ion species, since they develop lower charge states, effectively limiting their trapping potential. Secondly, the collision mechanics underlying Equation 3.40 imply that lighter ions will heat up faster when supplied with a given amount of thermal energy. In this manner, cooling gas injection provides a way to extract heat from the trap without sacrificing the ion species of interest.

Formulating the actual escape and cooling rates is a somewhat involved problem. While it is easy to determine the fraction of ions that can escape the trap for any given temperature, the difficulty lies in determining how this process acts out dynamically. In practice ions exceeding the escape velocity are essentially lost immediately, such that a high energy tail cannot emerge. The important question therefore becomes at which rate ions from a given population collide in

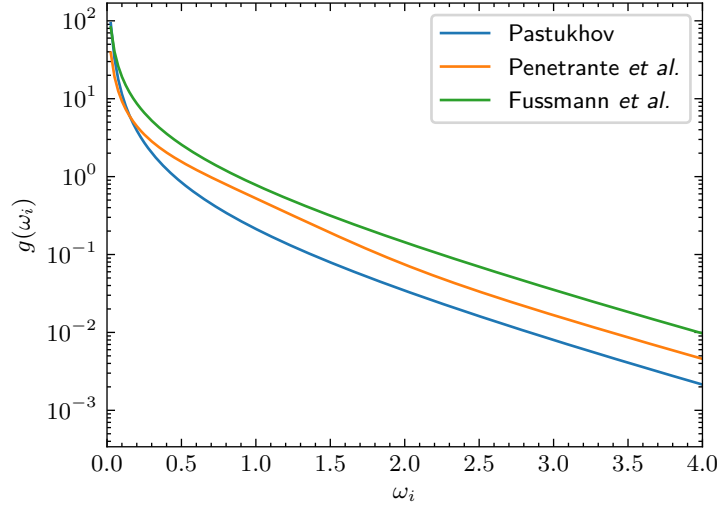


Figure 3.5: Comparison of the scaling of different escape rate models. On the vertical axis  $g(\omega_i) = R_i^{\text{ESC}} / (N_i \sum_j \nu_{ij})$  describes the distinct multipliers of the rate expressions given in the main text.

such a way that they pick up the momentum required to escape. This links the escape dynamics to the problem of collision driven velocity diffusion in a plasma [68, 73].

Loss rates typically used in the EBIS/T community can largely be traced back to earlier work by Pastukhov who developed a model for the loss rate from a magnetic mirror trap [74] starting from the Fokker-Planck equation [75]. As some assumptions and approximations are practically unavoidable when deriving the loss rate, several expressions have been used throughout the years, e.g. in Refs. [38, 56, 57, 76]. The particle loss rates, which conveniently link the ion loss rate with the Coulomb collision rate introduced in Equation 3.39, can be written as

$$\text{Pastukhov [74]:} \quad R_i^{\text{ESC}} = N_i \left( \sum_j \nu_{ij} \right) \frac{4}{3 \ln 6} \left[ \frac{\exp(-\omega_i)}{\sqrt{\pi} \omega_i} + \frac{\text{erfc}(\sqrt{\omega_i})}{2\omega_i^{3/2}} \right], \quad (3.42)$$

$$\text{Penetrante et al. [38]:} \quad R_i^{\text{ESC}} = N_i \left( \sum_j \nu_{ij} \right) \left[ \frac{\exp(-\omega_i)}{\omega_i} + \omega_i \text{erfc}(\omega_i) \right], \quad (3.43)$$

$$\text{Fussmann et al. [57]:} \quad R_i^{\text{ESC}} = N_i \left( \sum_j \nu_{ij} \right) \frac{3}{\sqrt{2}} \frac{\exp(-\omega_i)}{\omega_i}, \quad (3.44)$$

$$\text{where} \quad \omega_i = \frac{v_{\text{esc}}^2}{v_{\text{th}}^2} = \frac{q_i \Phi_{\text{T}}}{k_{\text{B}} T_i}. \quad (3.45)$$

Here,  $\text{erfc}$  denotes the complementary error function. A visual comparison of these rates is provided in Figure 3.5. *Ebisim* implements the loss rate model brought forward by Fussmann et al. [57, 58].

Here,  $\omega_i$  relates the thermal velocity  $v_{\text{th}}^2 = 2k_{\text{B}}T_i/m_i$  to the escape velocity  $v_{\text{esc}}^2 = 2q_i\Phi_{\text{T}}/m_i$  for a given trapping potential barrier height  $\Phi_{\text{T}}$ . In reality, there are two loss terms, to reflect the generally different depth of the potential trough in the axial and radial direction. Losses predominantly occur across the shallower barrier as that barrier puts a practical limit on the ion temperature. The axial trap depth  $\Phi_{\text{ax}}$  is determined by the voltage bias applied to the barrier drift tubes. In the radial direction the potential depth  $\Phi_{\text{ra}} = \Phi(r_{\text{DT}}) - \Phi(0)$  is given by the electron beam-induced voltage drop between the axis of the machine and the inner drift tube surface. If the trap is loaded heavily, compensation effects may cause the effective values of  $\Phi_{\text{T}}$  to drift over time.

While some authors argue that the magnetic field does not contribute to the total energy of ions and should therefore not affect losses in the long run, others have developed models to account for the fact that the axial field could impede radial ion escape by forcing trapped ions onto cyclotron trajectories [59, 62, 65]. *Ebisim* follows the approach of Lu and Currell who propose a modification of  $\Phi_{\text{ra}} \rightarrow \Phi_{\text{ra}} + B\sqrt{2k_{\text{B}}T_i/(3m_i)}r_{\text{DT}}$  to pay respect to the magnetic confinement [65].

The corresponding rate for the temperature evolution can be determined by observing that an escaping particle will carry a characteristic energy of  $q_i\Phi_{\text{T}} = \omega_i k_{\text{B}}T_i$ . This loss of energy is subsequently redistributed across the 3 degrees of freedom of the remaining ions, such that the temperature rate is

$$S_i^{\text{ESC}} = \frac{2}{3} \frac{R_i^{\text{ESC}} \omega_i k_{\text{B}}T_i}{N_i}. \quad (3.46)$$

Note that here  $R^{\text{ESC}}$  and  $S^{\text{ESC}}$  carry a positive sign to comply with the signs chosen in Equations 3.1 and 3.2. This completes the discussion of the individual components composing the charge breeding physics model implemented in *ebisim*.

### 3.4 *Ebisim* package

A software library for the simulation of electron beam driven charge breeding processes has been developed based on the presented physics model and published online [77]. As a fully qualified *Python* [78] package based on an established software stack, *ebisim* integrates well into the existing scientific *Python* universe and offers not just the simulation capabilities but an array of convenience functions for the inspection of simulation results and inquiry of charge breeding related phenomena.

*Python* was chosen as the implementation language since — owing to its simple syntax and mature ecosystem — it is growing ever more popular in the scientific community. In order to provide both maintainability and performance, the package aims to keep the use of custom data structures and algorithms to a minimum. Instead, it is built around the de facto standard

libraries *numpy* [79], *scipy* [80], and *matplotlib* [81], to benefit from their versatile and well-tested functionality.

Notably, the integration of the rate equations is based on *scipy*'s ordinary differential equation interface, which provides access to an increasing selection of different solvers that can easily be exchanged, if numerical stability issues demand it. Since the rate equations exhibit stiffness (a tendency for rapid variations) explicit solvers like Euler or Runge-Kutta methods tend to be unstable and crash or produce dubious results. Implicit algorithms, like RADAU IIA [54] or BDF [82], generally show a good performance and stability.

To overcome the performance limitations of an interpreted language, *numba* [83, 84], a just in time compiler for numerical *Python* functions, is used. With just very minor modifications to the source code, this package employs the heavily optimised *LLVM* compiler infrastructure [85] to translate numerical functions into native machine code on demand. This dramatically increases the performance of the simulations while preserving the simplicity of the *Python* language. Paired with the extensive documentation [86] of the *ebisim* code and examples shipped with the package, this modern architecture should facilitate not only the use of the package but also the modification of its source code by third parties if they wish to change or extend the physics model to their needs.

### 3.4.1 User interface

The package has been designed in a modular fashion, to provide a general toolbox to the user. As previously mentioned, *ebisim* offers two interfaces for basic and advanced simulations. Each of these interfaces provides a convenient way of launching simulations based on a set of simulation parameters. The simulation parameters are provided by the user in the form of basic immutable data structures which contain information like the electron beam and trap parameters, ion species, and initial densities and temperatures. These data structures do not need to be populated manually, but are created by a set of convenience functions that generate and fetch additional derived information in the background. The provided simulation parameters are used to set up the system of rate equations and solve it.

Upon successful completion of the simulation, a rich result object is returned. The result object contains the data describing the charge breeding and temperature evolution and may contain more in depth data like the individual transition rates or the space charge evolution depending on the simulation setup. Many convenience methods for facilitating further analysis and plotting the output data are provided.

Instead of running a full simulation, it is also possible to interact with most of the individual functions describing the underlying physics model directly. Examples of this are cross section and plasma parameter computations as well as the Poisson-Boltzmann solver. This can be useful if one wishes to investigate isolated effects.

### 3.4.1.1 Basic simulations

Basic simulations implement the much simplified model presented in Section 2.2.5. While this means that any temperature related effects cannot be taken into account, it makes the simulations light weight and very quickly running, typically finishing in fractions of a second on a modern computer. This makes the basic simulations particularly useful for parameter scans or fitting procedures which require many repeated runs. They are also a helpful tool for quick interactive work and estimates.

An example of this interactive work is a small web application that was built on top of the basic *ebisim* model and deployed at CERN. Accessible with any modern web browser, it provides a simple dashboard-style graphical user interface that exposes the basic simulation functionality. Simulation requests are sent to the web-server which returns the simulation results and related data in a set of interactive plots. This tool has proven to be very useful during EBIS operations and for measurement interpretation, since it provides the user with an approximate prediction of the charge breeding dynamics in an uncomplicated fashion and with virtually immediate feedback. Since the simulations are lightweight enough to run on a small virtualised web server, this makes such a tool easily accessible from anywhere without the need to install any additional software. Figure 3.6 shows a screenshot of the web application.

### 3.4.1.2 Advanced simulations

Advanced simulations closely follow the equations laid out in Sections 3.1, 3.2, and 3.3. The computation of the advanced rates and in particular solving the radial space charge problem on every time step make this model much more computationally demanding and simulations typically run from several seconds to minutes. Therefore, the advanced model is less suitable for large parameter scans, but it can instead provide much deeper insight into the dynamics of the charge breeding process.

The advanced simulation implementation is versatile and offers fine grain control to the user. As their input they take a definition of the trap and electron beam parameters, a collection of ionisation targets and background gases, and a set of simulation options. A simulation can include one or more target species, for which the charge breeding process will be simulated. Here, neutral gas injection and ion injection can be combined at will. The targets can be combined with any amount of background gases which act purely as additional charge exchange partners.

By passing specific simulation options, the user can enable and disable almost any effect individually. This includes EI/RR/DR/CX interactions as well as Spitzer heating, ionisation heating, collisional thermalisation, and axial and radial escape. Moreover, there are switches to override certain automatically determined values, as for example the beam energy spread used in DR cross sections. Through these switches the user can manipulate the physics model in an uncomplicated way and compare the results of different models. Other switches aim primarily

### ebisim dash.

A dashboard for basic ebisim simulations.

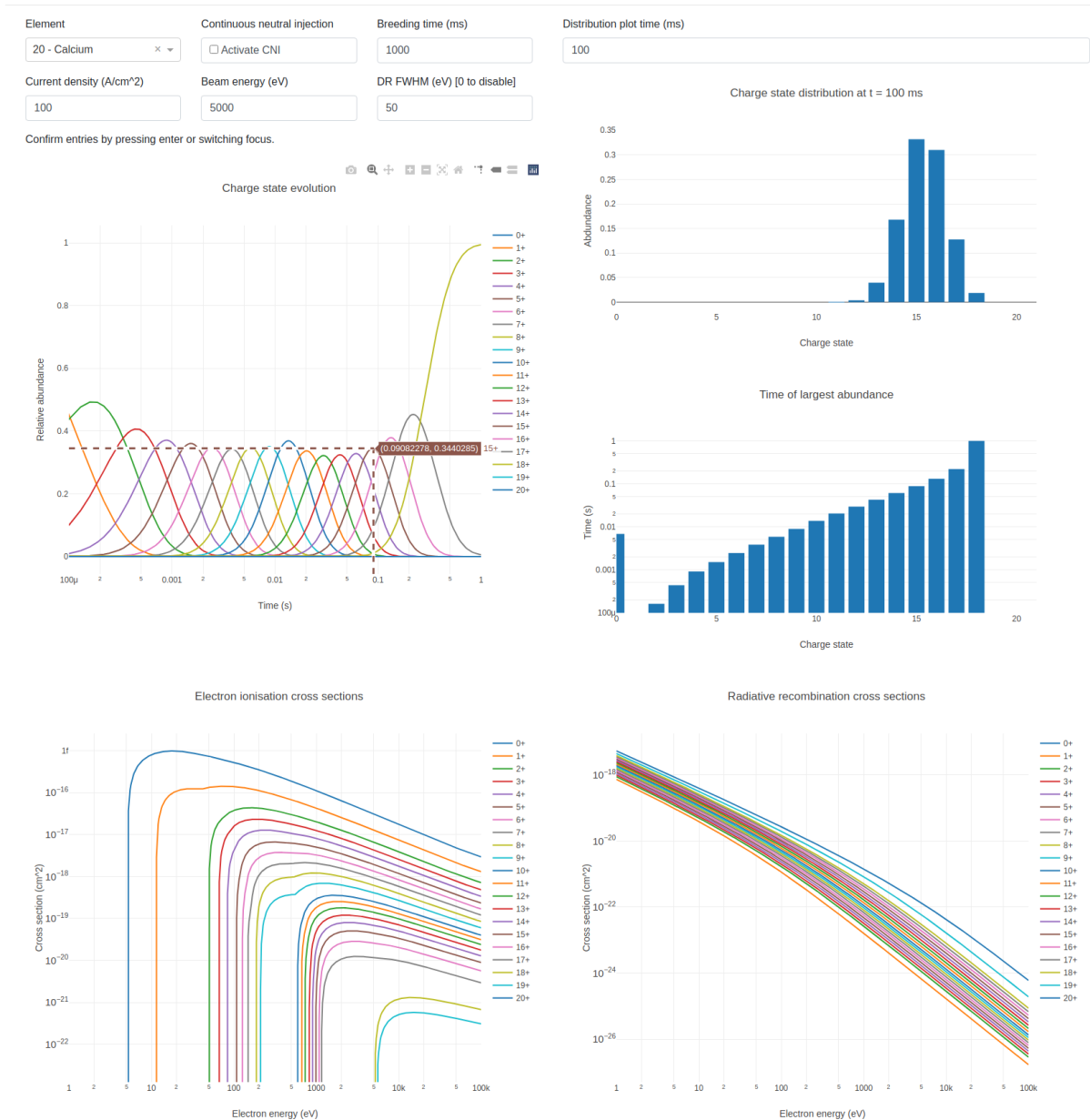


Figure 3.6: A screenshot of the *ebisim* based web application for basic simulations. Shown are the input mask on top of the page and several plots showing the computed charge state evolution (top left), the spectrum at a given time (top right), the approximate optimised breeding time for every charge state (middle right), and the electron impact ionisation and radiative recombination cross sections for the currently selected element (bottom row).

at performance optimisations. Interaction cross sections can either be recomputed dynamically based on the current value of the beam energy or only once in the beginning. The self-consistent radial space charge solution can be deactivated when compensation is insignificant. If the self-consistent solution is turned off, the radial trapping is based on the potential of the electron beam alone.

### 3.4.2 Included resources

In order to actually run the simulations, certain atomic physics data is required; for example to compute quantities like interaction cross sections. The *ebisim* package ships with both the needed data and some additional tables included for convenience. This data is saved in human-readable and easily editable tables that are read from disk during the package initialisation, providing a compromise between performance and the users' ability to extend the data for their needs. One such table is a rudimentary periodic table of elements that contains names, symbols, typical isotope masses, and approximate ionisation potentials to aid the user with defining target species for a simulation.

#### 3.4.2.1 Atomic shell data

For the computation of the EI and RR cross sections, information about the electron configuration and the binding energies of individual electrons for every individual charge state is required. The corresponding tables have been adapted from a catalogue created by Mertzig [87, 88], who used the Flexible Atomic Code (FAC) [35] to systematically compute the binding energies for elements up to  $Z=105$  in all their charge states. As such they are theoretical approximations and not experimentally confirmed values. However, the empirical scaling laws used for the EI and RR cross sections likely dominate the error.

Figure 3.7 contains an overview of the lowest binding energies for ions with a given charge state and nuclear charge, based on the binding energy tables used in *ebisim*. The neutral atom curve in this plot shows some deviations from experimentally measured binding energies, but it should be noted that these errors are not expected to have a big impact on the general simulation results. Firstly, the electron beam energy is typically much larger than typical ionisation energies of neutral elements; secondly, the ionisation rate for lowly charge ions is particularly high and the recombination rate small compared to the higher charge states. This diminishes their contribution to the dynamics on longer, more practically important timescales.

#### 3.4.2.2 Dielectronic transitions

As explained in Section 3.3.1.2 the DR cross sections are computed from a set of resonance energies and associated line strengths. *Ebisim* includes tables for KLL-type transitions which

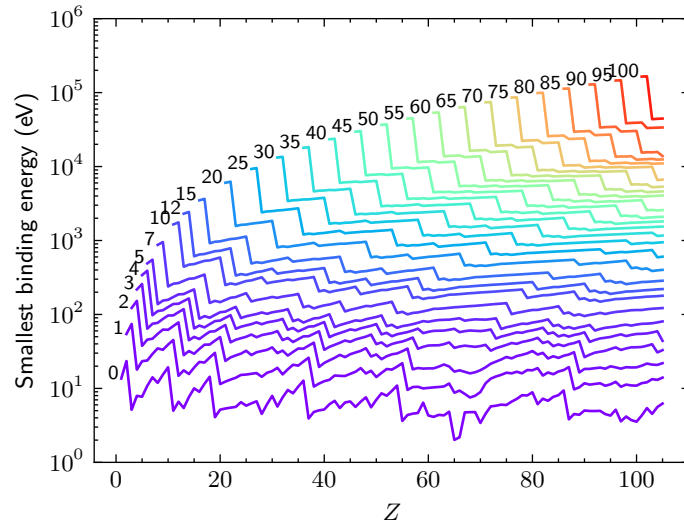


Figure 3.7: Plot of the smallest electron binding energies associated with selected charge states (curve labels) as a function of the nuclear charge. This data was extracted from the binding energy tables used in *ebisim*.

have been generated using FAC in a three step model. First, a set of initial states, transient excited states, and final states is computed. Afterwards, FAC produces the strength of the electron capture from the initial into the final states  $A_{i,\alpha}^{\text{EC}}$ , and the rates of all possible radiative decays  $\Gamma_{i,\alpha,\beta}^{\text{R}}$  from the transient into the final states. Since the transient states are auto-ionising, their auto-ionisation rates  $\Gamma_{i,\alpha}^{\text{AI}}$  are computed as well. The DR line strength then follows as the product of the electron capture strength and the radiative/auto-ionising branching ratio

$$A_{i,\alpha} = A_{i,\alpha}^{\text{EC}} \frac{\sum_{\beta} \Gamma_{i,\alpha,\beta}^{\text{R}}}{\Gamma_{i,\alpha}^{\text{AI}} + \sum_{\beta} \Gamma_{i,\alpha,\beta}^{\text{R}}}. \quad (3.47)$$

For the sake of rigour, it should be mentioned that the default tables include transient states with multiply excited L-shells; this strictly speaking makes them  $n$ -electronic transitions, but for brevity they are simply referred to as DR transitions.

### 3.4.3 Numerical solution of the radial space charge equation

Other than the time integration which is based on the *scipy* library, the solver for the Poisson-Boltzmann equation had to be implemented from scratch. The space charge problem will have to be solved on every time step of the charge breeding simulations. Since this could imply hundreds of thousands of evaluations, an efficient algorithm is essential. Equation 3.6 presents a boundary value problem, where, due to symmetry,  $\Phi'(0) = 0$  and, without loss of generality,  $\Phi(r_{\text{DT}}) = 0$ . Such equations are commonly solved with finite difference methods.

### 3.4.3.1 Finite difference scheme

Finite difference methods estimate derivatives through difference quotients and transform the differential equation into an algebraic problem which is highly adapted to being solved with a computer. For this purpose, Equation 3.6 has to be discretised in space

$$r \rightarrow r_k, \Phi \rightarrow \Phi_k = \Phi(r_k), \rho = \rho_e + \rho_{ion} \rightarrow \rho_k = \rho(r_k), \text{ where } r_0 = 0, r_K = r_{DT} \quad (3.48)$$

$$\Rightarrow \Phi_k'' + \frac{1}{r_k} \Phi_k' = -\frac{\rho_k}{\varepsilon_0}. \quad (3.49)$$

Before developing expressions for the derivatives of  $\Phi$ , it is advisable to look ahead to the solution for a moment. Since the radius of the electron beam is typically much smaller than that of the surrounding drift tube, variations in  $\Phi$  are typically the strongest close to the electron beam, as was shown in Figure 2.8. This localised variability should be reflected in the chosen discretisation scheme or grid. Uniform grids, where  $r_{k+1} - r_k = \text{const.}$ , are popular thanks to their simplicity and well-behaved errors but do not present an efficient choice for the problem at hand. Grids with a geometrically increasing distance between grid points are well suited to the typical length scales of the problem and the truncation error introduced in the discretisation of the derivatives is reasonably well-behaved [89].

To be able to use a geometric grid spacing, the difference quotients need to be determined for non-uniform grids. Let  $\Delta_k = r_{k+1} - r_k$  denote the distance between neighbouring grid points. The forward and backward Taylor expansion of  $\Phi$  can be written as

$$\Phi(r_k + \Delta_k) \approx \Phi(r_k) + \Phi'(r_k)\Delta_k + \frac{1}{2}\Phi''(r_k)\Delta_k^2 + \frac{1}{6}\Phi'''(r_k)\Delta_k^3 + \dots \quad (3.50)$$

$$\Phi(r_k - \Delta_{k-1}) \approx \Phi(r_k) - \Phi'(r_k)\Delta_{k-1} + \frac{1}{2}\Phi''(r_k)\Delta_{k-1}^2 - \frac{1}{6}\Phi'''(r_k)\Delta_{k-1}^3 + \dots \quad (3.51)$$

Appropriate linear combinations of these two expansions yield the expressions for the central finite differences. Terms including the third and higher order derivatives have been truncated [89].

$$\Phi_k' \approx \frac{\Delta_{k-1}^2 \Phi_{k+1} - \Delta_k^2 \Phi_{k-1} + (\Delta_k^2 - \Delta_{k-1}^2) \Phi_k}{\Delta_k^2 \Delta_{k-1} + \Delta_k \Delta_{k-1}^2} \quad (3.52)$$

$$\Phi_k'' \approx 2 \frac{\Delta_{k-1} \Phi_{k+1} + \Delta_k \Phi_{k-1} - (\Delta_k + \Delta_{k-1}) \Phi_k}{\Delta_k \Delta_{k-1} (\Delta_k + \Delta_{k-1})} \quad (3.53)$$

Substituting these expressions back into Equation 3.49 yields an algebraic expression for  $\Phi_k$ , now free of any explicit derivatives.

The central finite differences are only valid inside the problem domain, but not on the boundaries. On the outer radius, that is the drift tube surface, the potential is simply given by the

boundary condition

$$\Phi_K = \Phi(r_{\text{DT}}) = 0. \quad (3.54)$$

On the symmetry axis, the  $1/r$  term is divergent, but L'Hôpital's rule can be used to show that

$$\lim_{r \rightarrow 0} \left( \Phi''(r) + \frac{1}{r} \Phi'(r) \right) = 2\Phi''(r). \quad (3.55)$$

The difference quotient for  $\Phi_0''$  is derived using the forward Taylor approximation and noting that  $\Phi'(0) = 0$  due to the radial symmetry

$$\Phi_0'' \approx 2 \frac{\Phi_1 - \Phi_0}{\Delta_0^2}. \quad (3.56)$$

For further discussion it is helpful to recast Equation 3.49 as a vector equation.

$$\mathbf{M} \cdot \Phi = \mathbf{M} \cdot \begin{pmatrix} \Phi_0 \\ \Phi_1 \\ \vdots \\ \Phi_{K-1} \\ \Phi_K \end{pmatrix} = -\frac{1}{\varepsilon_0} \begin{pmatrix} \rho_0 \\ \rho_1 \\ \vdots \\ \rho_{K-1} \\ 0 \end{pmatrix} = -\frac{1}{\varepsilon_0} \boldsymbol{\rho} \quad (3.57)$$

Here, the elements of matrix  $\mathbf{M}$  are directly determined by the central finite differences and boundary conditions presented above. Because of the second order nature of the Poisson equation and the choice of finite difference scheme,  $\mathbf{M}$  has a tridiagonal structure. Such a system of equations can very efficiently be solved using the tridiagonal matrix algorithm, also called Thomas algorithm. The complexity of this algorithm scales linearly with the number of grid points  $\mathcal{O}(K)$ [90]. However, one must not forget that this system is still nonlinear due to the dependence  $\boldsymbol{\rho}(\Phi)$  introduced by the Boltzmann distribution of the ions.

### 3.4.3.2 Solution of the linear system

Before tackling the nonlinearity, it is advisable to test the finite difference solution for an ion-free electron beam with uniform current density and velocity as introduced in Section 2.3.4. For this purpose the numerical solution is compared to the analytical solution for a number of different discretisation grids. Three different grid types, uniform, geometric, and hybrid, were tested at two resolutions. The hybrid grid is a combination of a uniform grid extending from the axis out to two electron beam radii, followed by a geometric grid up to the drift tube radius. Approximately a third of the total nodes are part of the uniform grid; the remaining nodes are part of the geometric grid.

Figure 3.8 displays the numerical results and deviations from the analytical solution. The

advantage of the more advanced grids is clearly visible. The hybrid grid clearly yields the best results for a given number of grid points. While all grids have the ability to yield good results if the number of nodes is increased sufficiently, this would unnecessarily increase the computation time. For this reason *ebisim* defaults to the hybrid grid.

### 3.4.3.3 Solving the nonlinear system

The nonlinear problem can be solved iteratively using the n-dimensional equivalent of the Newton root finding algorithm [91]. Roots of a given objective function  $\mathbf{f}(\mathbf{x})$  can be approximated by repeatedly computing

$$\mathbf{x}^{s+1} = \mathbf{x}^s - \mathbf{J}^{-1}(\mathbf{x}^s) \cdot \mathbf{f}(\mathbf{x}^s) \quad (3.58)$$

for a given initial value  $\mathbf{x}^0$  until the solution converges. Here,  $J_{ij} = \partial f_i(\mathbf{x})/\partial x_j$  is the Jacobian of the objective function. Since a full inversion of  $\mathbf{J}$  is computationally expensive, it is usually more efficient to solve the expression

$$\mathbf{J}(\mathbf{x}^s) \cdot \mathbf{y}^s = \mathbf{f}(\mathbf{x}^s) \quad (3.59)$$

for  $\mathbf{y}^s$  and modify the update rule to  $\mathbf{x}^{s+1} = \mathbf{x}^s - \mathbf{y}^s$ . Before proceeding, it should be noted that attempts of improving the convergence rate by mixing the Newton-Raphson method with the method of successive over relaxation as proposed in Ref. [92] have not been successful for the problem presented here.

In the context of the space charge problem, one can identify  $\mathbf{x} = \Phi$  and obtain the target function and Jacobian by rearranging Equation 3.57 and inserting the definitions from Equations 3.7, 3.8, and 3.9

$$\mathbf{f}(\Phi) = \mathbf{M}\Phi + \frac{1}{\varepsilon_0} \rho(\Phi) \quad (3.60)$$

$$\begin{aligned} J_{kl} &= M_{kl} + \frac{\partial}{\partial \Phi_l} \frac{\rho_k(\Phi)}{\varepsilon_0} \\ &= M_{kl} + \frac{\delta_{kl}}{\varepsilon_0} \left[ -\frac{\eta}{u_{e,k}^2} \rho_{e,k} - \sum_i \frac{(q_i e)^2}{k_B T_i} n_i^0 \mathcal{B}_{i,k} \right]. \end{aligned} \quad (3.61)$$

Here,  $\delta_{kl}$  denotes the Kronecker symbol. The on-axis ion density is fixed by the normalisation condition (3.10)

$$n_i^0 = N_i \left[ 2\pi \int_0^{r_{\text{DT}}} \mathcal{B}_i(r) r dr \right]^{-1} \quad (3.62)$$

These equations maintain the tridiagonal structure of the finite difference scheme, such that the iterative correction term  $\mathbf{y}^s$  can be computed very efficiently.

With the quantities defined above, the solution algorithm for the Boltzmann-Poisson equation can be summarised in a couple of steps:

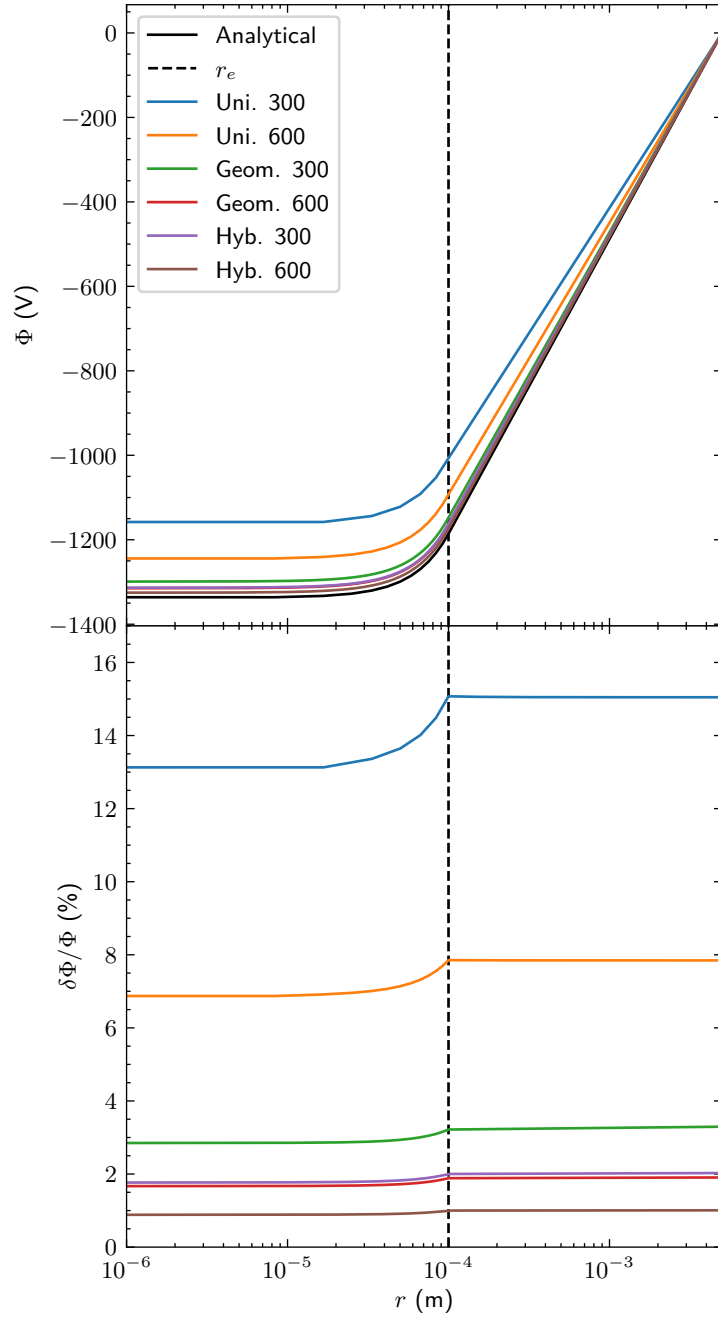


Figure 3.8: Effect of the chosen discretisation grid on the solution of the linear finite difference problem (defined in Equation 3.57) for an electron beam with  $I = 1 \text{ A}$ ,  $E_e = 10 \text{ keV}$ ,  $r_e = 0.1 \text{ mm}$ ,  $r_{DT} = 5 \text{ mm}$ . Shown are the numerical solution and the relative deviations from the analytical solution for uniform, geometrically spaced and hybrid grids with 300 or 600 nodes.

1. Make a first guess  $\Phi^0$  for the space charge potential, e.g. the analytical solution for an uncompensated electron beam.
2. Use the current solution  $\Phi^s$  to compute the ion distribution  $n_i^0$  and  $\mathcal{B}_i(r)$ .
3. Compute the charge density  $\rho^s$ , objective function  $\mathbf{f}^s$ , and Jacobian matrix  $\mathbf{J}^s$ .
4. Solve for the correction term  $\mathbf{y}^s$  (employing the tridiagonal matrix algorithm for optimal efficiency).
5. Update the potential  $\Phi^{s+1} = \Phi^s - \mathbf{y}^s$ .
6. Repeat steps 2. through 5. until  $\Phi$  has converged or a maximum number of iterations has been reached.

### 3.5 Example: Shifting of the charge state balance due to dielectronic recombinations

The capabilities of *ebisim* can best be illustrated by comparing simulation results to real experimental data. For this demonstration the following scenario was selected: By recording the charge state evolution for a range of electron beam energies, it is possible to observe how the emerging charge state balance is affected by the presence of dielectronic recombination resonances. This scenario offers the opportunity to use all the features included in the simulation tool. Here, we have scanned the electron beam energy over the energy range in which the strongest KLL-type resonances of highly charged  $^{39}\text{K}$  ions are expected, according to the pre-generated table of transitions included in *ebisim*, cf. Figure 3.9.

#### 3.5.1 Experimental methods

The experiments were carried out at the REXEBIS setup at the ISOLDE facility. Here, the focus is on the comparison of the experimental data with the simulation results, so the description of the experimental methods will be kept brief, and the reader is referred to Chapter 4 which contains a detailed description of the REXEBIS setup.

Potassium ions are available at the REX installation through an alkaline metal hot surface ion source. The beam of singly charged ions is first accumulated and cooled in REXTRAP, a Penning trap that acts as a cooler-buncher. The accumulated beam is then transferred into REXEBIS for charge breeding. A Faraday cup at the entrance of the EBIS was used to determine an injected pulse intensity of approximately 5 to 7 pC or  $3.1 \cdot 10^7$  to  $4.4 \cdot 10^7$  ions, neglecting losses. In addition to the injected ions, neon - used as a cooling gas in REXTRAP - is known to migrate into the EBIS in notable quantities. After the breeding cycle has ended, the highly

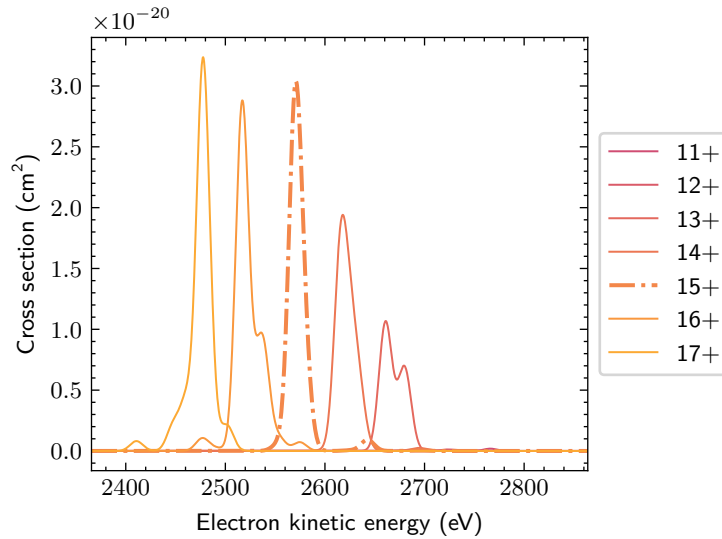


Figure 3.9: Dielectronic recombination cross sections of  $^{39}\text{K}$ , convoluted with an electron energy spread of 15 eV (FWHM), as assumed by *ebisim*.

charged ions are extracted from the EBIS and separated according to their charge-to-mass ratio in a magnetic spectrometer; finally the intensity of the filtered beam is measured with a Faraday cup.

The measurements were carried out prior to the upgrade of the electron gun described in Chapter 4, using the original REXEBIS electron gun configuration which was routinely operated with beam currents ranging from 200 to 300 mA. To increase the sensitivity to dielectronic resonances, the beam current was dropped to just 50 mA in an attempt to reduce the intrinsic energy spread in the electron beam, while maintaining a reasonable charge breeding time  $< 1$  s. The cathode of this gun had a radius of 0.8 mm, and is heated to approx. 1850 K; together with a cathode flux density of 200 mT, the Herrmann formula Equation 2.35 yields a beam radius prediction of 253  $\mu\text{m}$  in the full 2 T field.

To scan the electron beam energy, the high voltage bias of the electron gun was adjusted in between charge breeding cycles, in steps of 2.5 V, from  $-1900$  to  $-2400$  V. The drift tubes forming the trap were set to a constant bias of 500 V, resulting in an effective, uncorrected beam energy range of 2400 to 2900 eV. As the magnetic spectrometer allows for measuring just one charge state at a time, this scan had to be repeated multiple times to cover the charge states  $^{39}\text{K}^{13+}$  to  $^{39}\text{K}^{17+}$ . An additional reference measurement was taken, with suppressed potassium ion injection, to estimate the background signal and assert that the signal due to contaminants was insignificant. The whole procedure was then carried out for a number of breeding times (500 ms, 700 ms, 800 ms, 900 ms, and 995 ms) to determine the charge state evolution.

### 3.5.2 Simulation setup

The comparative simulations were carried out with the full advanced simulation model introduced in this chapter, with all interaction models enabled. That means, in addition to the pure charge state evolution, the thermal evolution of the ions was taken into account, and the self-consistent space charge solution was determined at every time-step (on a radial grid with 800 nodes) to compute beam energy corrections and overlap factors.

The electron beam is defined purely in terms of its current (50 mA), its uncorrected energy (2400 to 2900 eV) and beam radius (350  $\mu\text{m}$ ). The beam radius deviates from the theoretical prediction, since it was empirically determined that it produces better results, both in terms of charge breeding speed and space charge corrections to the beam energy. The remaining parameters are dynamically computed at every simulation step. Just as in the experiment, the axial barrier was set to 600 V above the trapping drift tubes.

Given a trap length of 0.8 m, the initial linear density of the potassium ions was estimated to be  $4.7 \cdot 10^7 \text{ m}^{-1}$ , at an initial temperature of 30 eV. In addition to the potassium ions, a background population of neutral neon atoms is added, assuming a partial pressure of approx.  $7 \cdot 10^{-12}$  mbar at room temperature (300 K). The neon can act as a coolant for the heavier potassium ions, but also contributes to space charge compensation, reducing the radial well depth over time.

In addition to the full simulation, two slightly modified runs were performed. In the first alternative run, neon was omitted, whereas the second alternative was performed with an assumed fixed electron energy spread of 26 eV.

### 3.5.3 Experimental results

The results of the experimental campaign are gathered in Figure 3.10. The curves in the plot show the charge-state separated ion current recorded as a function of the nominal electron beam energy for the individually sampled breeding times. For every curve, the current detected by the Faraday cup has been subtracted by the dark current measured without potassium injection, and subsequently normalised by the known charge state. This yields an effective particle current measured in particle pico Ampere (ppA).

The localised bumps visible in the charge state curves are the signatures of dielectronic recombination. When the electron beam energy approaches such a resonance, recombination is strongly enhanced, which effectively slows down the charge breeding into the highest charge states. Wherever charge state  $n + 1$  has a DR resonance, this increases the abundance in charge state  $n$  with respect to the immediate surrounding. For every peak, the successively higher charge states display a depression, as their positive ion number rate contributions are inhibited. By comparing the most prominent peaks to the cross sections presented in Figure 3.9, one may identify a discrepancy in the resonance energies. This is due to the fact that the energy axis

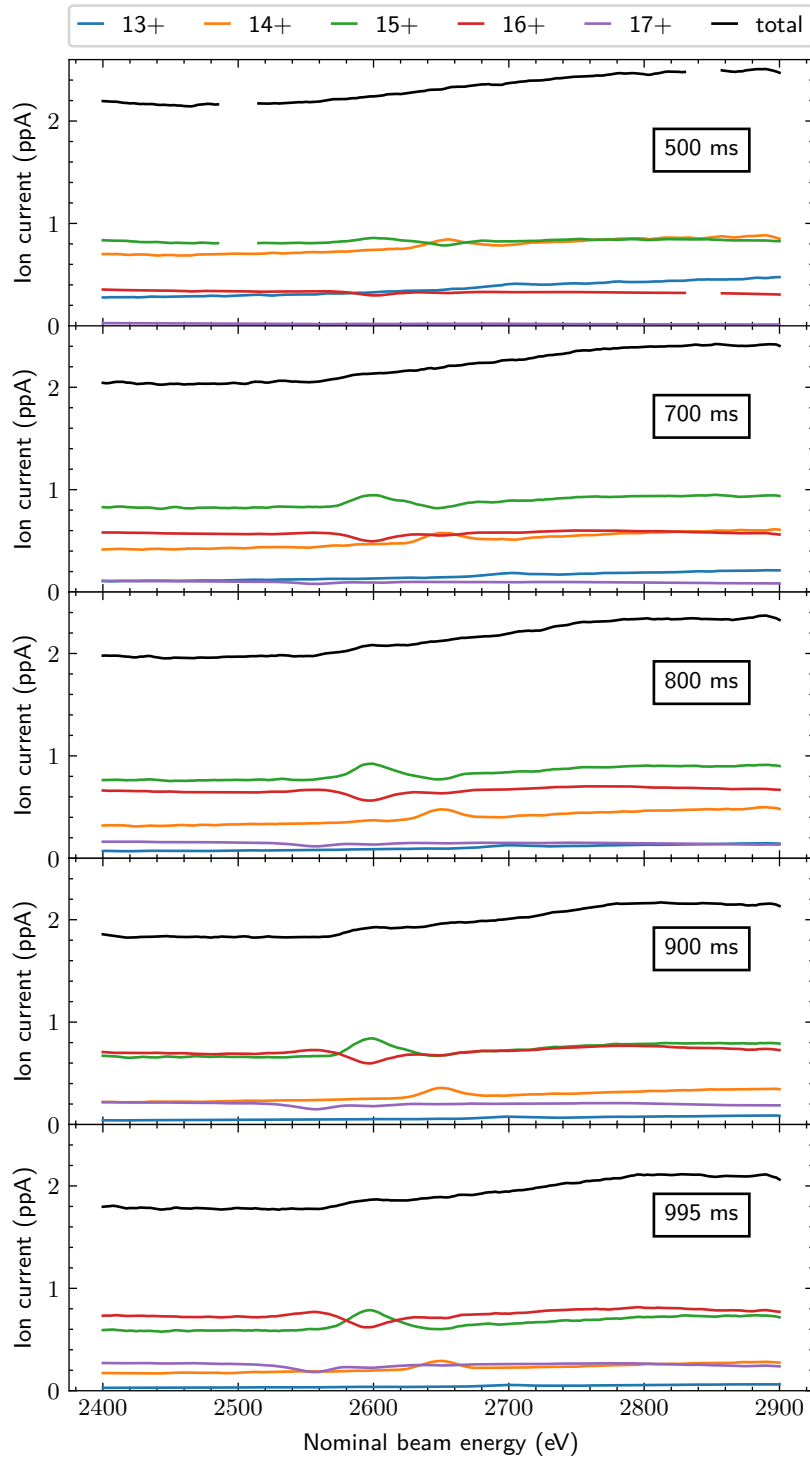


Figure 3.10: Data recorded in the dielectronic recombination-sensitive charge breeding experiments with  $^{39}\text{K}$ . Every trace depicts the detected current of a given charge state, measured in particle pico Ampere (ppA), for a distinct breeding time. The black curves represent the sum over the individual traces in every subplot.

does not take into account space charge corrections to the externally applied electron beam acceleration gradient.

For all breeding times presented here, the vast majority of the total potassium ion current extracted from the EBIS was detected in the presented charge states 13+ to 17+, with little to no detectable current in the lower charge states. The black curve in every subplot represents the accumulated particle current in all measured charge states, and provides a good estimate for the total extracted potassium particle current. The upwards trend observable on the black traces, is likely caused by changing ion injection efficiencies, as the beam energy is varied. Below, when comparing the measurement results to the simulation results, the particle current in every charge state is normalised by the total particle current determined in this manner, to provide the relative abundance.

### 3.5.4 Simulation results and comparison to the experimental data

**Baseline simulation** The relative charge state abundances for potassium computed with the charge breeding simulation toolkit are presented in Figure 3.11 (dashed lines) alongside the equivalent data from the experimental campaign (solid lines). For breeding times of 800 ms and longer in particular, a good agreement between both data sets can be observed. The overall abundance level, long range slopes, and the location of the resonance signatures follow each other closely. For the subplots representing breeding times of 500 ms and 700 ms, there is a more pronounced discrepancy in the relative charge state abundance, but the qualitative agreement of the corresponding traces is still recognisable.

The most striking difference between the simulation and the experiment are provided by the sharper dielectronic recombination peaks in the simulation. This indicates that the simulation, employing Equation 3.13, underestimates the energy spread in the electron beam. The computed FWHM energy spread in the simulation remained within  $(10 \pm 2)$  eV at all times. The peaks can appear a little wider, as the instantaneous energy spread is additionally superimposed by a drift of the mean beam energy, which is caused by an increasing space charge compensation as more and higher charged ions fill the electron beam, cf. Figure 3.14g.

**Fixed energy spread simulation** The effect of the electron energy spread is illustrated more clearly in the second simulation with a fixed FWHM of 26 eV. The results of this run are presented in Figure 3.12. Compared to the reference simulation the general peak shape is much closer to that recorded in the experiment. By spreading the beam energy distribution's overlap with the resonance lines, the characteristic DR signatures are widened and their amplitude is reduced. This comparison suggests that the tabulated transition strengths are close to the real values. The only distinct discrepancy can be seen in the abundance of the 13+ charge state where the prominence of the simulated DR peak is consistently overestimated. For the 14+

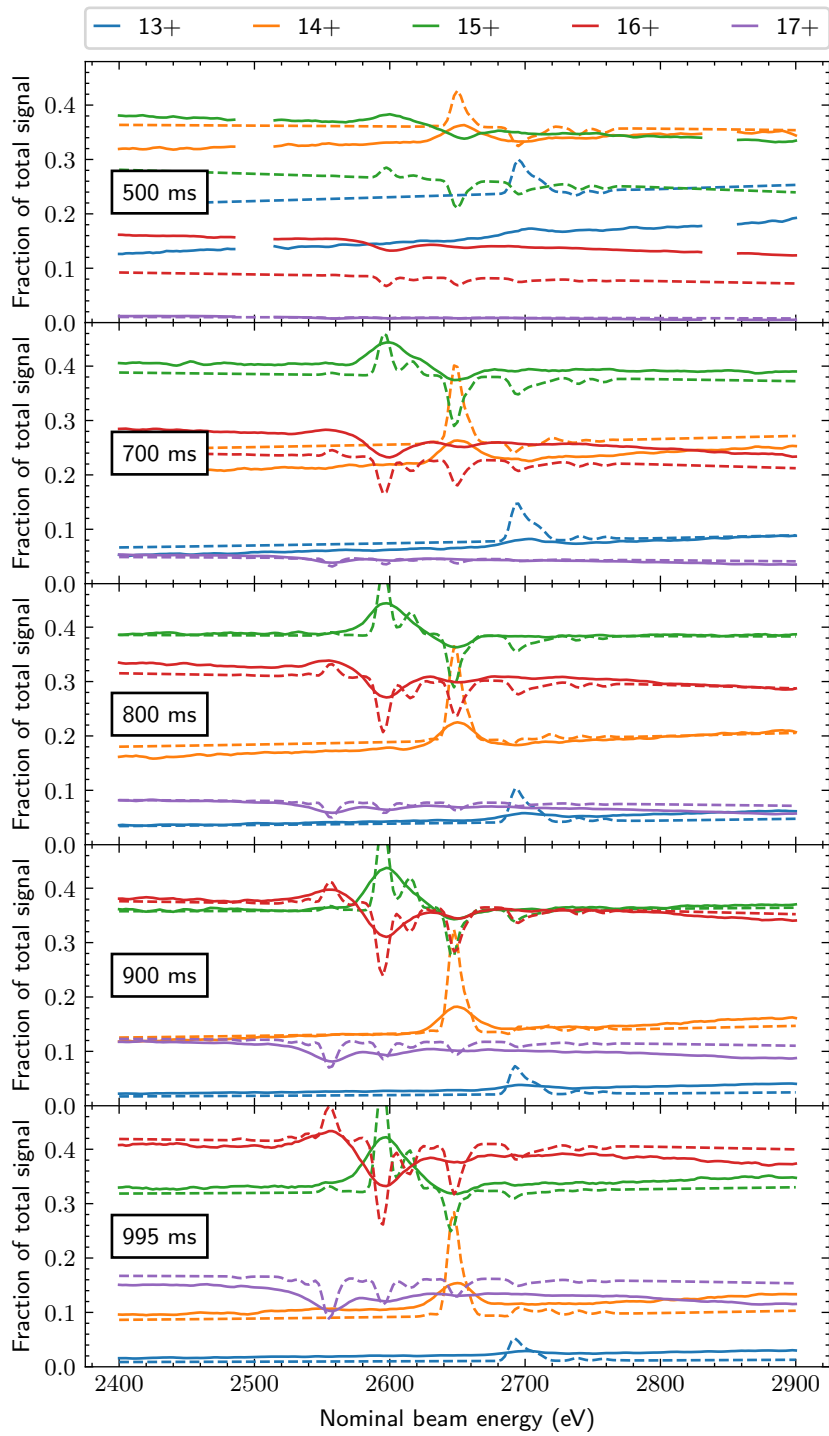


Figure 3.11: Comparison of the relative abundance of  $^{39}\text{K}^{13+}$  to  $^{39}\text{K}^{17+}$  as measured in the experiment (solid lines), and predicted by the fully dynamic simulation (dashed lines).

charge state a similar effect can only be clearly observed at longer breeding times, for shorter breeding times the agreement with the experimental profile is reasonable.

**Simulation without neon** Finally, it is of interest to illustrate the contribution of the neon background gas to the charge breeding dynamics. Figure 3.13 contains the comparison of the charge state abundance levels for the simulation run carried out without additional neon. Compared to the two prior cases, the overall agreement of the relative charge state abundance is quite poor for all sampled breeding times.

To understand this effect it is helpful to compare the charge breeding dynamics in both cases. Figure 3.14 contains a side-by-side comparison of the charge state evolution, ion temperature and overlap factors, as well as the mean beam energy in the simulations with and without neon presence.

Figure 3.14c contains the simulated temperature evolution of the potassium ions in the baseline simulation. It stabilises quickly at just around 60 eV. This is still quite hot for such a weak electron beam, which is why the overlap factors of the lower charge states are quite small (cf. Figure 3.14e), but as the charge state increases the potassium ions are more tightly confined and their overlap factors approach unity. It should be noted, that the higher temperatures observed below 50 ms arise mainly due to the finite initial conditions of the simulation, but the extremely low abundance of the affected high charge states, make them virtually meaningless. Once the high charge states are populated from below, their temperature evolution is quickly corrected to follow the general trend.

Without neon present on the other hand, the ion temperature can grow substantially (see Figure 3.14d), which eventually drives even the highest charge states out of the electron beam, as expressed by the decreasing overlap factors in Figure 3.14f. Consequently, the overall charge state evolution of potassium is slower when no neon is present to act as a collision partner and coolant. This change in charge breeding speed is the main reason for the poor abundance agreement with the experimental campaign, in which neon is known to be present.

Finally, it is interesting to note that the electron beam energy performs a larger sweep if neon is present. This is both because of an added source for highly charged ions that contribute to positive space charge, but also because the highly charged potassium ions are colder and therefore closer to the beam axis. As can be seen in Figure 3.14b, the mean charge state is clearly still increasing after 0.2s. Yet, the mean electron beam energy tapers off, because the ions move outside the electron beam while they are bred into higher charge states. This limits the growth of the positive charge density and hence the beam energy adjustment.

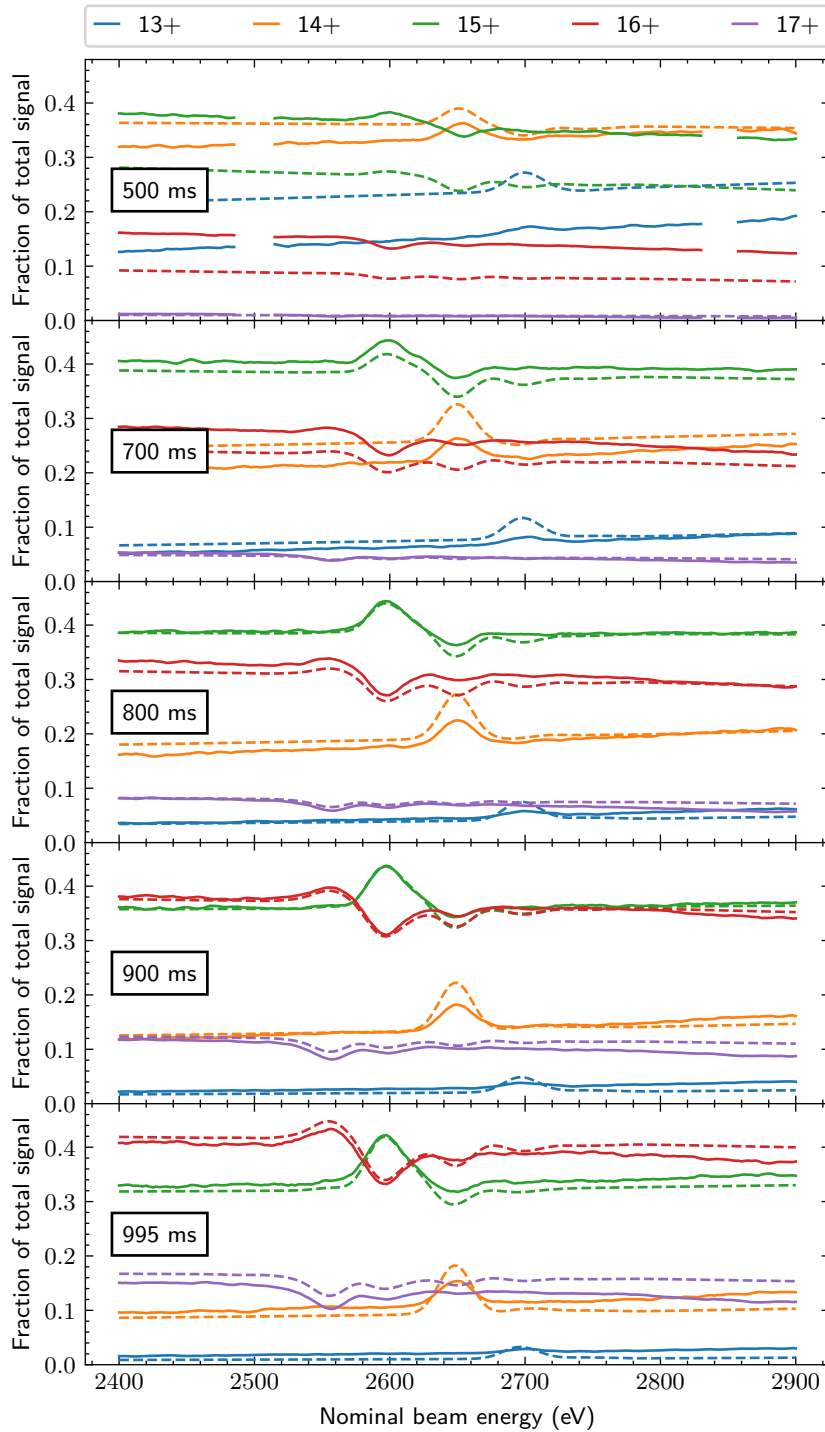


Figure 3.12: Comparison of the relative abundance of  $^{39}\text{K}^{13+}$  to  $^{39}\text{K}^{17+}$  as measured in the experiment (solid lines), and predicted by the simulation with a fixed beam energy spread (dashed lines).

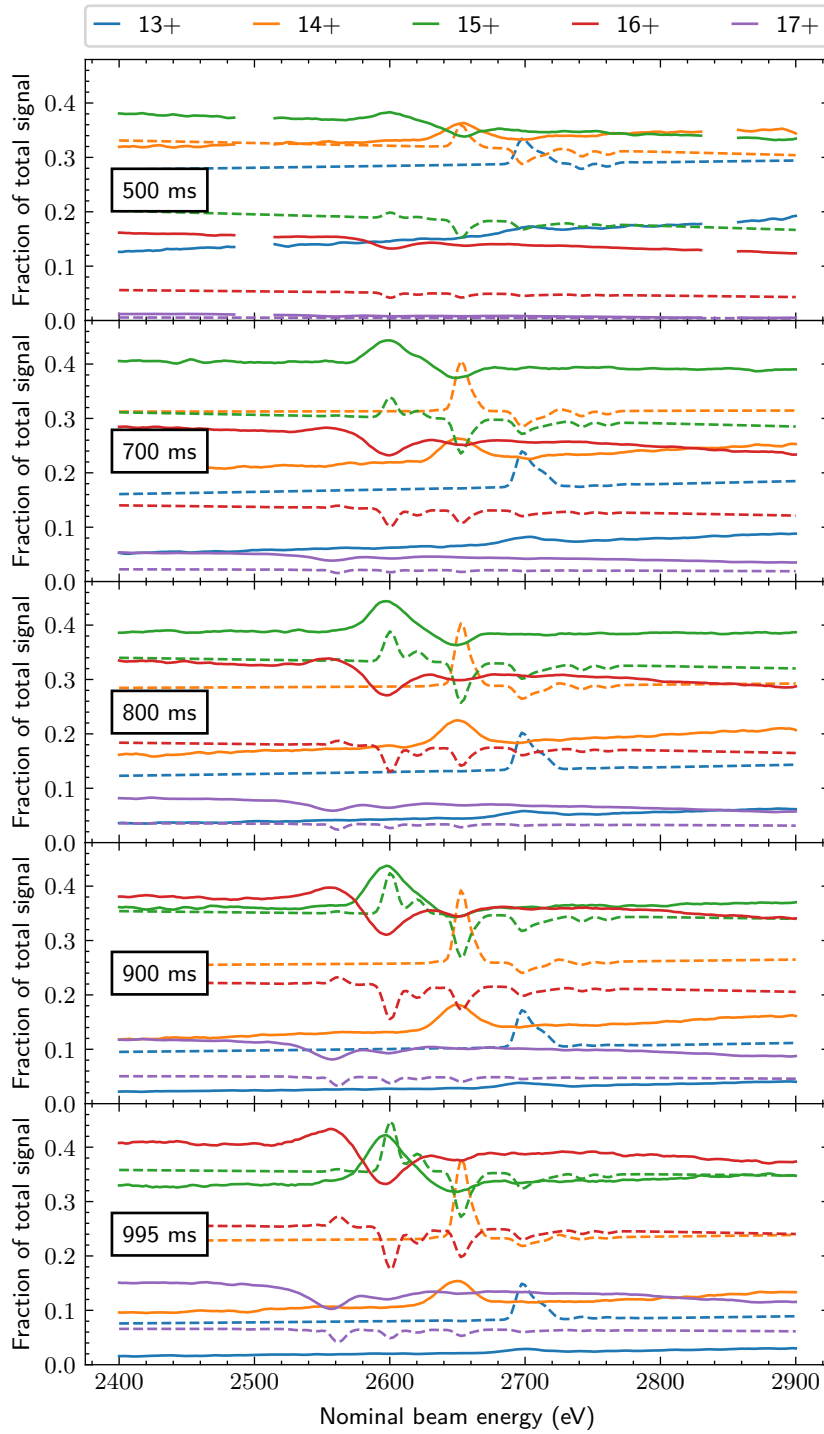


Figure 3.13: Comparison of the relative abundance of  $^{39}\text{K}^{13+}$  to  $^{39}\text{K}^{17+}$  as measured in the experiment (solid lines), and predicted by the simulation without a neon population (dashed lines).

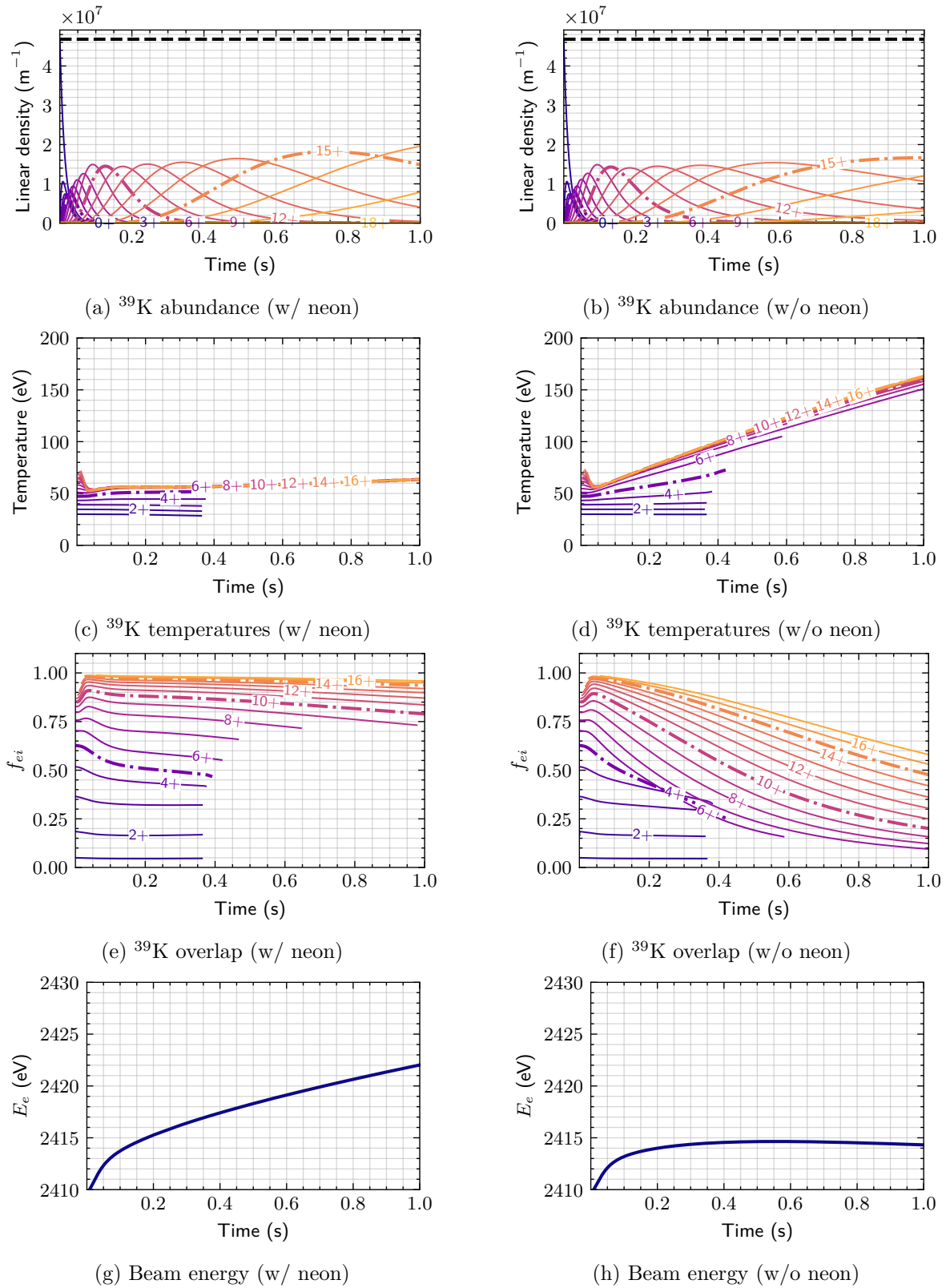


Figure 3.14: Simulated charge breeding dynamics with and without neon inclusion at a nominal beam energy of 2500 eV.

## 3.6 Conclusion

In this chapter the *ebisim* simulation tool has been introduced. For this purpose, a review of the established mathematical expressions used for the modelling of charge breeding dynamics in EBIS devices is provided. Notable differences between existing modelling approaches are discussed, as for example different ion escape loss terms.

The physics model has been implemented and extended in a dedicated *Python* package that ships with implementations of the relevant models, solvers and data resources. The whole package is freely distributed and easily modifiable by third parties. Additionally, a web-based tool for running simplified simulations without the need for installing the code locally has been developed and deployed.

To the best knowledge of the author, *ebisim* is the first public simulation tool that can solve the radial space charge problem on every time step, without the need for density corrections in between time-integration steps. Moreover, the thermal evolution is modelled in terms of temperature rate equations instead of the more commonly employed energy density rate equations, leading to a simplification of the rate equation system and providing improved numerical stability when the ion abundance approaches 0. In addition to the core simulation tooling, the package includes many options for flexible inspection and plotting of the generated results.

For demonstration purposes, a dielectronic recombination-sensitive charge breeding experiment has been carried out at ISOLDE's REXEBIS setup, and the results have been compared to the output of equivalent simulations generated with *ebisim*. The simulation code is able to provide an output that agrees well with the recorded measurement data over long timescales, without the need to adjust the simulation parameters. That means that the fully dynamically computed evolution of the mixed species ion cloud and electron beam system is capable of reproducing the charge state evolution observed in the experiments.

The option to flexibly modify the simulation scenario has proven helpful in illustrating the contributions of individual effects to the total result, as demonstrated with the fixed energy spread and neon-less simulations. In this manner, and by exposing the evolution of difficult-to-measure parameters, like e.g. the estimated overlap factors, simulations can grant additional insight into the charge breeding dynamics.

Naturally, some discrepancies between simulations and experiment remain visible, as for example slight differences in the exact charge state evolution or the inferred beam energy spread. Moreover, the theoretical limitations of the ion escape model for extremely shallow traps and non-thermal populations have been discussed in Section 3.2. As the simulation results are helpful in understanding and interpreting recorded measurements, these known limitations and issues should provide ample motivation for a continued development of improved models and simulation techniques for EBIS charge breeders.



## CHAPTER 4

# NONADIABATIC ELECTRON GUNS

For many typical EBIS applications, a higher electron beam current density is advantageous as it accelerates the charge breeding process. In practice however, increasing the current density of an EBIS presents a challenge, particularly when upgrading an existing system. While Equation 2.38 suggests that the Brillouin current density limit of an EBIS can be approached by increasing the electron current, this is usually not practical, due to constraints on thermal loads, beam-induced contaminant desorption, and operation limits of existing equipment.

To achieve a high current density in the charge breeding region, it is therefore desirable to maximise the initial current density and magnetic beam compression. A rather obvious way to achieve this, is to position a high emission density cathode in as weak a magnetic field as possible. High emission density cathodes ( $\gtrsim 20 \text{ A/cm}^2$ ) based on various materials are commercially available, but if they are installed in a weak magnetic field ( $\lesssim 100 \text{ mT}$ ), the Lorentz force is too weak to balance the space charge forces generated by the beam itself at conventional acceleration voltages of a few kV. As a result the beam will start to diverge strongly immediately upon leaving the cathode. Even a weak field will refocus the beam eventually, but the radial oscillation amplitude can reach excessive levels, up to the point where the electron beam is scraped by the surrounding electrodes. In less extreme cases, this imbalanced beam will continue to oscillate while it travels along the magnetic field. If the beam is injected into a compressing magnetic field – as usual for an EBIS – electrons with large pitch angles are at a risk of being reflected in the field gradient, akin to the mechanism of a magnetic bottle. Moreover, sufficiently strong oscillations create axial potential modulations that are a further risk to beam quality and ion source operation, as externally inaccessible micro-traps could be created in the waists of the scalloping beam.

### 4.1 Reducing beam ripple with nonadiabatic magnetic fields

Inspired by earlier work on creating calm hollow beams for gyrotron devices [93, 94], Pikin et al. looked into the possibility to dampen the ripple with the help of short-range field modulations.

They found that both electric and magnetic fields can in principle be used to guide the beam from an unbalanced oscillating state closer to an equilibrium state. Since the field modulations have typical scale lengths smaller than the cyclotron period of the electrons traversing them, they are dubbed nonadiabatic. In conditions like these, the magnetic moment is no longer generally conserved.

At BNL several designs were studied, that included in the gun geometry elements which would create the required modulations. One such gun, with an iron rim (shaping the external magnetic field) built into the anode electrode was built and tested extensively [95, 96]. Based on simulations and hardware tests it was determined that one of the limiting design factors was the inclusion of the nonadiabatic element into the gun assembly itself, as this leaves limited room for operational range and optimisation. Here, we continue the work started at BNL with the introduction of an independent nonadiabatic element. The studies summarised here have been adapted from Ref. [I].

#### 4.1.1 Simulation setup

Chapter 2 illustrates that an analytical treatment of the electron beam motion requires a couple of simplifying assumptions. The results of that discussion are not directly useful for understanding the motion of the beam and individual electrons while traversing nonadiabatic fields. Therefore, employing the help of particle tracking simulations is virtually unavoidable.

To explore the concept of separating the nonadiabatic element from the electron gun, various configurations have been tested with the help of the 2.5D simulation suite *TRAK Charged Particle Toolkit* [97]. *TRAK* features a “gun iteration” mode, for solving space charge dominated problems. The beam is tracked through the external fields and then its space charge field is computed. Afterwards the beam is tracked through the superimposed fields and the space charge field is refined based on the new trajectories. This process is repeated until it converges on a self-consistent solution [98].

For our studies a series of toy models were developed to verify the applicability of the nonadiabatic concept in a range of situations [I]. Here, the focus will be on two of the basic models. Their exact parameter values are not crucial for this conceptual introduction, but for completeness they are given below. Disregarding the field modulation introduced by the nonadiabatic element, the background magnetic field was kept uniform in order to suppress effects caused by adiabatic field gradients, like e.g. beam compression. Besides a brief check, temperature effects were ignored in these studies; the initial angular momentum of the electrons is absolutely dominated by the magnetic field as is easily verified by comparing their magnitudes with the expressions given in Section 2.3.5.

The first model features a conventional Pierce-style electron gun with strong transverse fields in the cathode anode gap, cf. Figure 4.1. A beam of 0.7 A and a nominal energy of 8.5 keV is

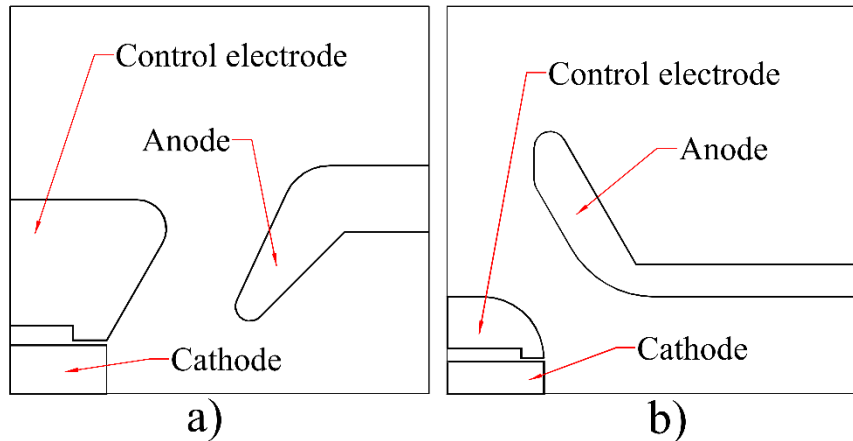


Figure 4.1: Sketches of the two gun geometries used to explore the concept of nonadiabatic electron beam injection. Figure (a) shows the Pierce type gun, (b) shows the overhanging anode gun. The cathode radius is 1 mm for the scenarios discussed in this chapter. Figure reproduced from Ref. [I].

injected into a drift tube with an internal radius of 5 mm. The cathode radius is 1 mm, implying an emission density in excess of  $22 \text{ A/cm}^2$ . The main magnetic field has a flux density of 50 mT. A soft iron ring is used as the nonadiabatic element. Its high permeability causes a rearrangement of the magnetic field lines, such that there is an on-axis flux density dip downstream of the gun.

The electron gun in the second model features a convex geometry with an anode overhanging the cathode / Wehnelt assembly, as shown in (b) of Figure 4.1. Such a geometry generates softer transverse fields than the Pierce geometry. The results presented here were generated for a 0.7 A beam with a nominal energy of 6 keV. As in the first model, the cathode radius is 1 mm. The background magnetic flux density is 100 mT, and the drift tubes had an internal radius of 3 mm. In contrast to the first model, a coil is used as the nonadiabatic element. Its polarity was chosen such that it opposes the main field and consequently creates a flux density depression similar to the ring.

#### 4.1.2 Demonstration of ripple reduction with a passive element

Before looking at the mitigation of beam scalloping it is helpful to demonstrate the issue. For this purpose a simulation of the first model with the Pierce gun was performed without the iron ring. This means that the magnetic field is uniform, and the beam should propagate in line with the theory introduced in Chapter 2. Figure 4.2 contains the resulting electron trajectories and clearly shows the strong radial oscillations. These arise because 50 mT is not sufficient to maintain a space charge balanced flow at the (cathode) radius of 1 mm. A careful look towards the region furthest away from the gun also reveals some phase slipping between central and

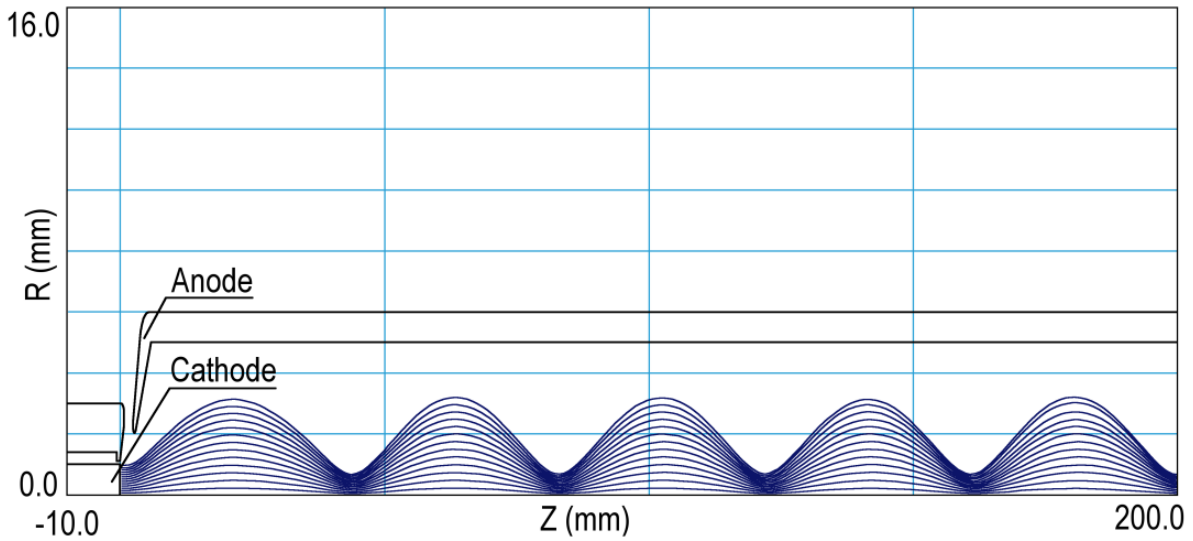


Figure 4.2: Outline of the model geometry based on the Pierce gun and the iron ring. Overlaid are the electron trajectories illustrating large amplitude radial oscillations of the beam cross section. The uniform magnetic field has a flux density of 50 mT. Figure reproduced from Ref. [I].

peripheral electrons, an effect that will be relevant later in Section 4.1.4.

Once the iron ring is added to the simulation model, the magnetic field lines (which are generated by a large solenoid not shown here) rearrange to preferably pass through the iron ring. This reduces the on-axis field strength and introduces transverse magnetic field components. It is these transverse fields that can exert a torque on the passing electrons and hence manipulate the gyrating motion. By shaping the iron ring, the field depression can be tuned to almost perfectly cancel out the beam ripple. This effect is demonstrated in Figure 4.3. Whereas the first radial excursion is largely similar to that observed in the model without the ring, the magnetic field dip located on the descending slope of the beam envelope acts to almost entirely eliminate the radial ripple observed before.

It is noteworthy that the beam radius downstream of the nonadiabatic modulation is larger than the cathode radius. This is absolutely necessary in order to allow for a balanced flow of the beam. Applying the Herrmann formula, cf. Equation 2.35, with the beam parameters given above yields a beam radius of 1.62 mm, which is in excellent agreement with the simulated envelope that is represented by the outermost trajectory.<sup>1</sup> A higher density beam with the given energy cannot possibly travel along this field without scalloping. This starts to paint a picture of the nonadiabatic dip as a kind of transition or matching region, a notion that will be reinforced in the following section where the transverse motion is examined.

<sup>1</sup>Due to the proximity between the cathode and the iron ring, the cathode-threading field is increased slightly from the initial 50 mT. This has been taken into account when computing the Herrmann radius.

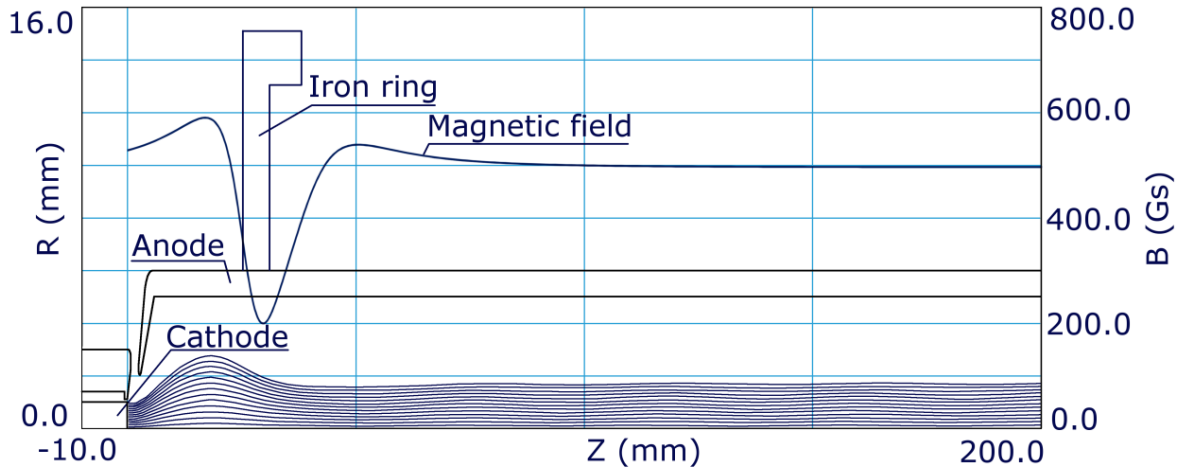


Figure 4.3: Simulation results for the same setup as in Figure 4.2, but now including a soft iron ring carefully designed to produce a nonadiabatic field modulation that dampens the envelope ripple. Figure reproduced from Ref. [I].

### 4.1.3 Matching the cyclotron motion with an active element

Whilst using an iron ring as a passive element is a very affordable option, it lacks in flexibility. Since the geometry of the ring cannot reasonably be changed during operation the field modulation is fixed and cannot be adjusted to match the beam parameters. A coil on the other hand offers a larger degree of tunability. Figure 4.4 demonstrates this model in action. Once again the radial motion of the beam is eliminated almost entirely.

By changing the current turns in the coil, the strength of the field depression can be adjusted easily. This makes the model well suited to demonstrating the transverse matching that occurs in this transition region, as illustrated in Figure 4.5. For an uncorrected beam (black line), the trajectory displays large self-intersecting lobes in the transverse trajectory. This motion is the result of unbalanced forces and in turn explains the radial oscillations. Since electrons with different initial radii are expected to oscillate in phase, unless the beam is too distorted, the characteristic motion depicted here for the outermost electron is indeed a collective behaviour. As the current in the coil is increased (red line) the average radius grows and the self-intersecting lobes begin to close. Eventually, as the perfect coil current is reached (blue line), the trajectory is smoothly transitioning into a circular motion while passing the field dip. The trajectory is no longer self-intersecting, and all particles perform a coherent drift around the common axis. If the coil current is increased further (green) the force balance is broken again, and the cyclotron motion emerges once more.

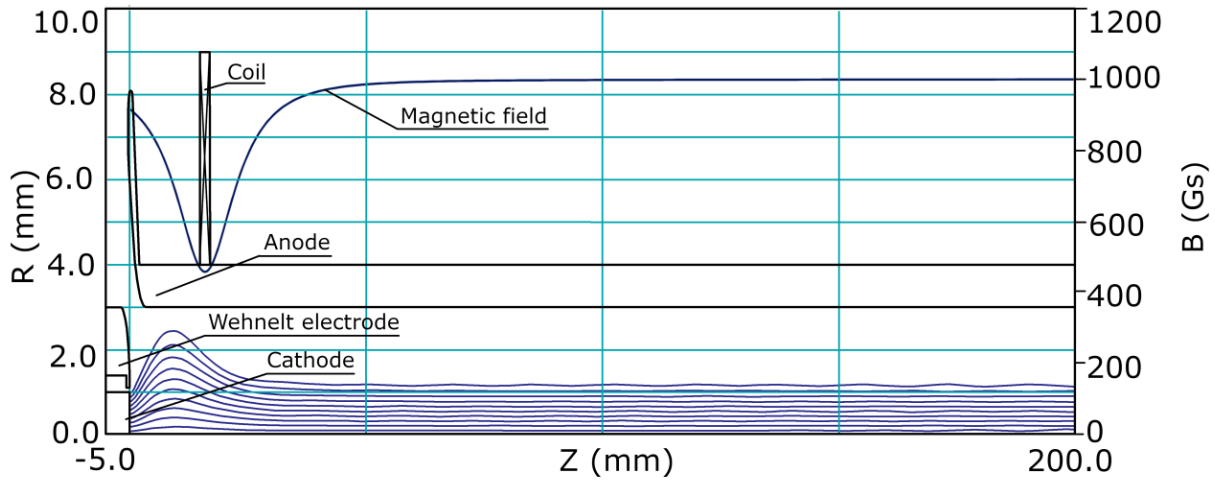


Figure 4.4: Simulation results for overlapping anode gun geometry in combination with a coil acting as an active nonadiabatic element. In this plot the coil was trimmed to 850 A turns, the almost optimal value. Figure reproduced from Ref. [I].

#### 4.1.4 Damping on later nodes

In the simulations presented so far, the nonadiabatic element was located as close to the electron gun as possible, since this is expected to be the most convenient position in an EBIS context, where one also needs to account for the main field gradient used for beam compression. Yet, this does not actually illustrate the initially claimed separation of gun and nonadiabatic damping very well. In Figure 4.6, the coil model is presented with the coil shifted downstream to the third descending slope. Here, the separation of electron gun fields and the magnetic field modulation is much more apparent.

One can see that damping the motion at a downstream position is generally possible. This also demonstrates that the technique of nonadiabatic damping is actually largely independent of the electron gun itself; it is the beam dynamics that dictate the tuning of the field modulation. A more careful look at Figure 4.6 reveals a slightly larger residual ripple than in the original scenario. As indicated above, the strong initial ripple of the beam causes a phase slipping of the concentric layers of the beam. This decoherence cannot easily be compensated for since this introduces individual damping requirements for electrons with different cyclotron phases. As a result, there is generally a slightly larger residual ripple for some radial positions. Hence, the possible placement options for the nonadiabatic element are practically limited by how quickly the trajectories de-phase with respect to each other.

We expect that practical concerns will typically encourage damping close to the electron gun. In many of those cases this will push the field modulation into the electron gun volume, such that their effects become more closely coupled. Whenever the nonadiabatic element can be placed

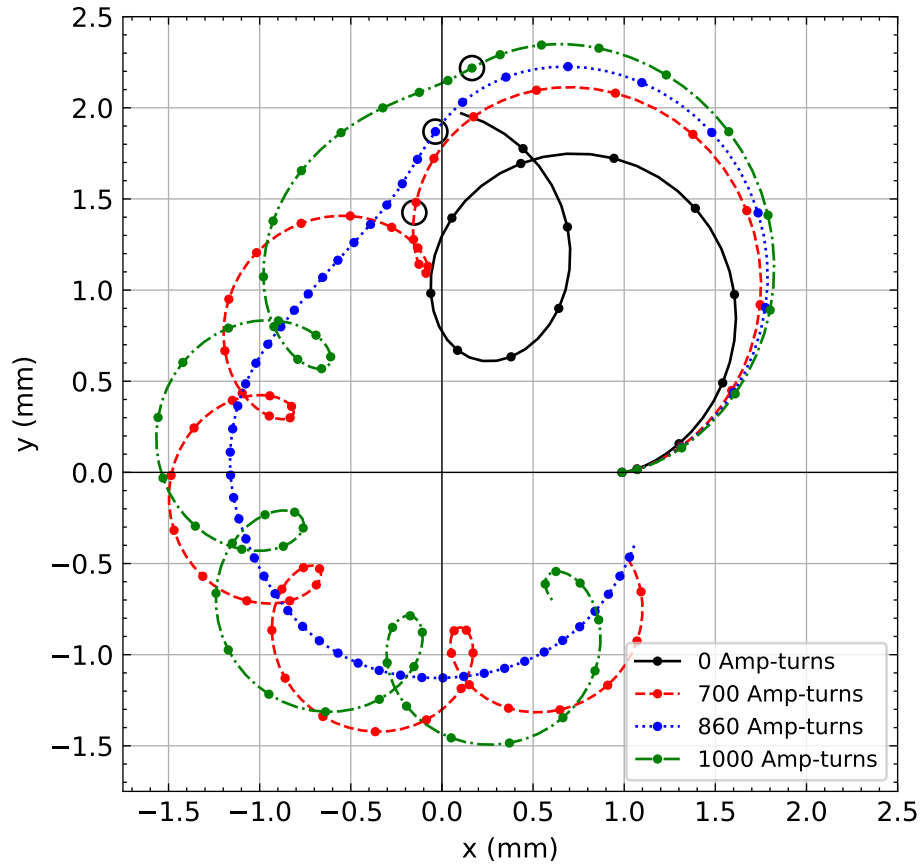


Figure 4.5: Plot of the outermost trajectory (envelope particle) for the simulation model shown in Figure 4.4 with different strengths of the nonadiabatic coil. The black line depicts the trajectory in a uniform field of 100 mT. The blue line is the trajectory for the optimised coil current with minimal beam ripple. Red and green show over- and under-compensated cases, respectively. The dot markers along the lines are spaced at even time intervals of 40 ps beginning on the x-axis, and the instant of passing the minimum field is marked with black circles. Figure reproduced from Ref. [I].

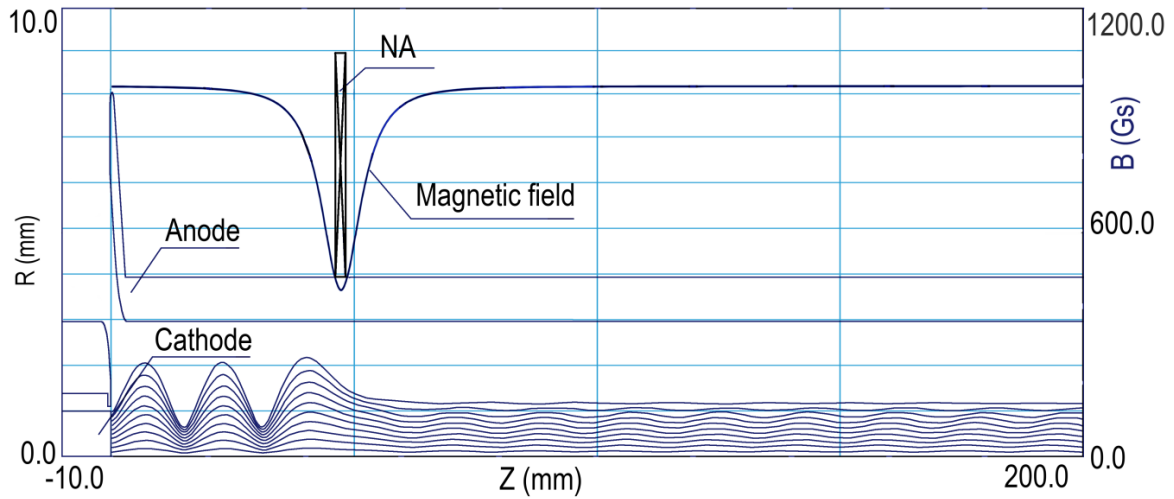


Figure 4.6: Plot of the trajectories for a model equivalent to Figure 4.4, but with the nonadiabatic element pushed downstream. Figure reproduced from Ref. [I].

further downstream though, this should make the design process much more straight forward as the gun and damping element can be optimised largely independent of each other.

#### 4.1.5 Ripple amplitude

At this point it is sensible to start looking at the ripple amplitude more quantitatively. Once again using the coil based model in its original configuration with the coil located right next to the electron gun, the ripple amplitude was determined from simulations for a range of coil currents and axial positions around their optimal values.

##### 4.1.5.1 Working range

The results of the tracking simulation are provided as the black curves in Figure 4.7. As already shown above, the coil is located so closely to the gun, that varying the current or position actually slightly changes the flux density at the cathode. Therefore, the ripple amplitude has been normalised by the average beam radius in each scenario.

Both curves show pronounced minima, indicating that an efficient damping requires careful tuning of the field modulation. Whereas the coil current is easily adjusted, positioning can be more challenging in practice. The margins may appear relatively small, but since they are tightly linked to the specific beam parameters, it is helpful to compare them to some relevant length scales, namely the wavelength of the beam ripple and the typical scale length of the magnetic depression.

The wavelength of the radial oscillations can be estimated using the cyclotron frequency

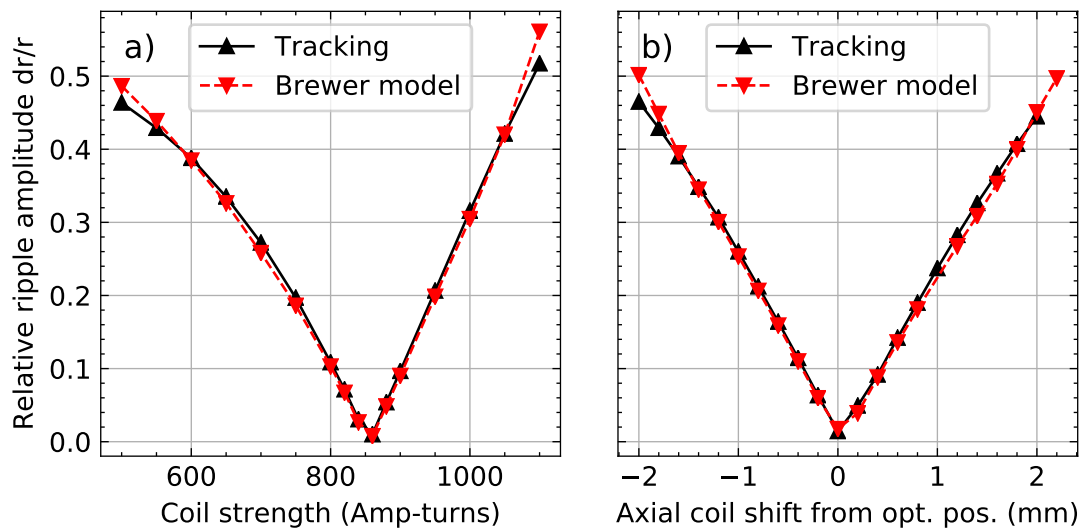


Figure 4.7: Plot of the dependence of the radial oscillation amplitude on the strength and position of the nonadiabatic field. The ripple amplitude is shown as normalised by the mean beam radius. In (a) the strength of the field depression is varied by adjusting the coil current while the coil is located at the optimal position. In contrast, the position was varied in (b) while the current was at the optimal value. The black curves show the direct results of the tracking simulations, whereas the red curves are based on a semi-analytical prediction detailed in the main text. Figure reproduced from Ref. [I].

$\omega_c = 2\omega_L$  and the beam velocity as introduced in Chapter 2

$$\lambda_c = \frac{u_e}{\omega_c/2\pi} = \sqrt{\frac{8\pi^2\Phi}{\eta B^2}} \approx 0.67 \text{ mm} \frac{\sqrt{\Phi/\text{kV}}}{B/\text{T}}. \quad (4.1)$$

In our simulations the unmodified magnetic field  $B = 0.1 \text{ T}$  and the acceleration potential  $\Phi = 6 \text{ kV}$  (neglecting space charge corrections). This yields a wavelength of  $\lambda_c = 16.4 \text{ mm}$ , a value that is in good agreement with the oscillations observed in Figure 4.6.

The exact shape of the field depression depends on the nonadiabatic element, but to give a more general estimate, one can assume a very short and compact coil. The field of such a coil is similar to that of single wire loop, for which the on-axis magnetic field can be written as [99]

$$B_o(z, r = 0) = \frac{\mu_0 I_o}{2} \frac{R_o^2}{(z^2 + R_o^2)^{3/2}}. \quad (4.2)$$

Here,  $R_o$  and  $I_o$  denote the loop radius and current respectively. From this equation one can determine that the magnetic field generated by the loop drops by 50% at an axial distance  $\Delta z = \sqrt{2^{2/3} - 1} R_o \approx 0.766 R_o$ . Approximating  $R_o = 7 \text{ mm}$  this corresponds to  $\Delta z \approx 5.36 \text{ mm}$ . In light of these characteristic length scales, the sensitivity of the damping efficiency to axial positioning is unsurprising, but nonetheless it remains important.

#### 4.1.5.2 Analytical amplitude estimation

The ripple amplitude offers an interesting opportunity to link the simulation results to the formalism introduced in Section 2.3.5. For this purpose it is possible to generalise a method initially suggested by Brewer [46], which links the ripple amplitude to the beam radius and divergence angle in a single arbitrary point.

This relation can be extracted from the equation of motion for the beam envelope (2.31). It shall be reproduced here with some convenient substitutions

$$\mathcal{R}'' = \frac{d^2\mathcal{R}}{d\mathcal{T}^2} = \frac{1}{2}\mathcal{R}^{-1} - \left(\frac{\omega_L}{\omega_p}\right)^2 (\mathcal{R} + K\mathcal{R}^{-3}) \quad (4.3)$$

$$\text{where } \mathcal{T} = \omega_p t, \quad \mathcal{R} = \frac{r}{r_a}, \quad K = \left(\frac{\psi_0}{\psi}\right)^2. \quad (4.4)$$

To obtain the required expression, the equation needs to be integrated over  $\mathcal{R}$ . This is trivial for the right-hand side, but the left-hand side requires a substitution and recursive partial

integration

$$\int_{\mathcal{R}_0}^{\mathcal{R}} \tilde{\mathcal{R}}'' d\tilde{\mathcal{R}} = \int_0^{\mathcal{T}} \tilde{\mathcal{R}}' \tilde{\mathcal{R}}'' d\tilde{\mathcal{T}} \quad (4.5)$$

$$= \tilde{\mathcal{R}}'^2 \Big|_0^{\mathcal{T}} - \int_0^{\mathcal{T}} \tilde{\mathcal{R}}' \tilde{\mathcal{R}}'' d\tilde{\mathcal{T}} \quad (4.6)$$

$$= \frac{1}{2} (\mathcal{R}'^2 - \mathcal{R}'_0^2). \quad (4.7)$$

Consequently, an expression for the normalised slope  $\mathcal{R}'$  emerges as

$$\mathcal{R}'^2 = \ln \left( \frac{\mathcal{R}}{\mathcal{R}_0} \right) - \left( \frac{\omega_L}{\omega_p} \right)^2 \left[ \mathcal{R}^2 - \mathcal{R}_0^2 + K \left( \frac{1}{\mathcal{R}^2} - \frac{1}{\mathcal{R}_0^2} \right) \right] + \mathcal{R}'_0^2. \quad (4.8)$$

The extrema of  $\mathcal{R}$  are the roots of this equation, which is parameterised by the radius  $\mathcal{R}_0$  and slope  $\mathcal{R}'_0$  at an arbitrary axial position.

To evaluate the simulation results with this formalism, the axial position was set to  $z_0 = 100$  mm, sufficiently far away from the coil, cf. Figure 4.4. The theoretical equilibrium radius  $r_a$ , the frequencies  $\omega_L$  and  $\omega_p$ , and the flux parameter  $K$  can easily be computed from the beam parameters. This includes some iteration to account for space charge retardation and a consideration of the slightly varying flux density at the cathode. In a second step  $\mathcal{R}_0$  and  $\mathcal{R}'_0$  can be extracted from the simulation output for the envelope electron at  $z_0$ .

With this information the roots, and hence the extrema of  $\mathcal{R}$ , can be computed numerically. Normalising the amplitude with the equilibrium radius yields the red curves in Figure 4.7. The agreement with the extrema extracted directly from the tracking data is virtually perfect. This increases the confidence in the correctness of the simulation results and also shows that – despite the unconventional transition through the nonadiabatic field modulation – the beam still adheres to the discussion in Chapter 2. Whereas an explicit description of the movement through the field modulation is not generally possible due to the fast changing fields, the generalised angular momentum remains conserved such that the derivations still hold.

#### 4.1.6 Closing remarks

The original publication [I] demonstrates a few other interesting scenarios, for example damping a hollow beam, and combining damping with subsequent compression. Additionally, we demonstrate that a nonadiabatic element can be used to excite cyclotron oscillations in a previously ripple-free beam, i.e. the process is reversible. For brevity these proofs of concept will be skipped here, but the reader is referred to paper [I] for more details. Here, we continue the discussion

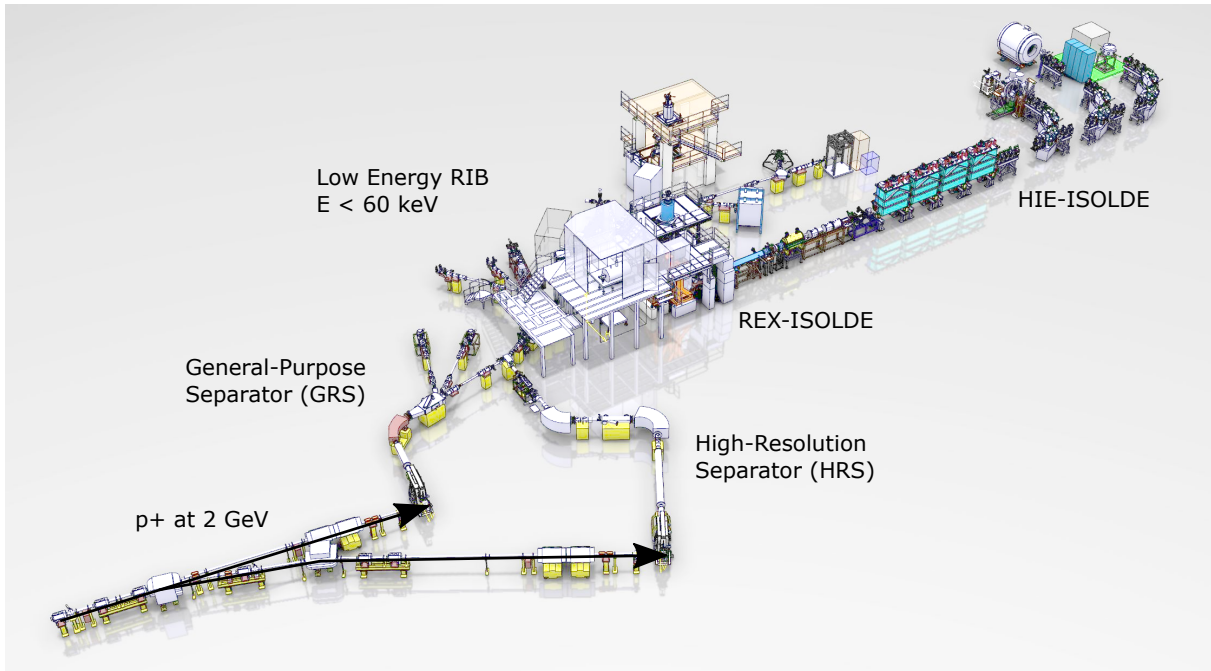


Figure 4.8: The ISOLDE facility. Figure kindly provided by Niels Bidault.

with experiments on a real electron gun based on the nonadiabatic technique.<sup>2</sup>

## 4.2 A nonadiabatic electron gun for REXEBIS

REXEBIS is a charge breeder for Rare Isotope Beams (RIB) at CERN’s ISOLDE facility [14, 100, 101]. At ISOLDE, cf. Figure 4.8, beams of radioactive isotopes are created through the irradiation of specialised targets with a 1.4 GeV proton beam originating from the Proton Synchrotron Booster. Fission-, fragmentation-, and spallation-processes create a wide range of isotopes, that are subsequently ionised and separated with the help of magnetic spectrometers [102]. This technique is known as Isotope Separation On-line (ISOL). In large parts of the ISOLDE complex, ions are accelerated to just 30 to 60 keV in order to transport them to one of the many experimental stations. Driven by the interest in nuclear reactions occurring at elevated centre-of-mass energies however, ISOLDE has been expanded with the Radioactive beam EXperiment (REX) [13, 103, 104], which later in turn saw the High Intensity and Energy upgrade (HIE) [105]. The centre piece of the REX/HIE setup is a linear post-accelerator designed to accelerate RIB to specific energies of up to 10 MeV/u for a charge-to-mass ratio  $A/Q \leq 4.5$ .

Injecting singly charged ions directly into the linear accelerator (LINAC) would be extremely inefficient and limiting, since the low charge makes poor use of the provided accelerating fields.

<sup>2</sup>While it was stressed that the nonadiabatic damping and the electron gun are separable, the term “nonadiabatic gun” will be used throughout this work for simplicity.

The acceleration ions experience inside the radio frequency (RF) cavities of the LINAC scales with their charge-to-mass ratio, which means that an increase in charge before entering the LINAC directly allows shortening the accelerating structure while maintaining the target energy. In practice, constraints of the RF hardware and the physical dimensions of the cavity define a certain  $A/Q$  acceptance, within which ions have to fall to enable their acceleration. Hence, there is a need to increase the charge state of the primary RIB originating from the ISOLDE target.

The REX accelerator has a dedicated beam preparation section consisting of two stages pictured in Figure 4.9. The primary beam is accumulated in REXTRAP, a Penning-Malmberg trap, and cooled with the help of neutral neon – acting as a buffer gas – to reduce the transverse emittance of the beam [106]. Subsequently, the ions are ejected and transferred to the REXEBIS charge breeder with the help of an electrostatic beam line. The ions are injected into the EBIS trapping region through the open-ended electron beam collector and ionised until the majority of the ions has been transferred into an appropriate charge state. After ejection from the EBIS, a single  $A/Q$  ratio is selected with the help of a Nier-type spectrometer and the ions are passed into an accelerating Radio Frequency Quadrupole (RFQ) forming the first stage of the post-accelerator. An EBIS was chosen as the charge breeder because of its comparatively high single charge state yield, low contamination degree and excellent emittance of the extracted beam. All these characteristics ensure that the valuable and often scarce ions of interest are neither lost nor drowned out by contaminants.

### 4.2.1 The need for an electron gun upgrade

Until 2020 REXEBIS has been operating with its original magneto-immersed electron gun. The gun was designed around commercially available flat-surfaced  $\text{LaB}_6$  cathodes with a radius of 0.8 mm, positioned in the fringe field of the main solenoid at a flux density of 200 mT. Typically operated at a current of 200 mA, the theoretical current density of the beam in the full field (2 T) breeding region was approximately 100 A/cm<sup>2</sup>, cf. Equation 2.36. With this electron beam, ions ranging from  ${}^6\text{He}$  to  ${}^{228}\text{Ra}$  have been charge breed and provided to users on around 200 occasions [107–110]. Despite this success, there were a number of arguments in favour of an upgrade. The remainder of this chapter closely follows our publication [II], which details the mechanical design of the new electron gun and describes measurements carried out during the commissioning run.

The cathodes have always posed a certain risk to the uninterrupted operation of REXEBIS. After months of operation the bonding of the  $\text{LaB}_6$  crystal to the heating element could weaken leading to sagging of the cathode; in other cases cracks would form in the crystal near the emission surface. Under those conditions, with degraded thermal contact, a stable electron beam can no longer be ensured, and occasionally the deterioration would be sufficiently bad to necessitate an exchange of the cathode in the middle of the operational year. In fact, REXEBIS

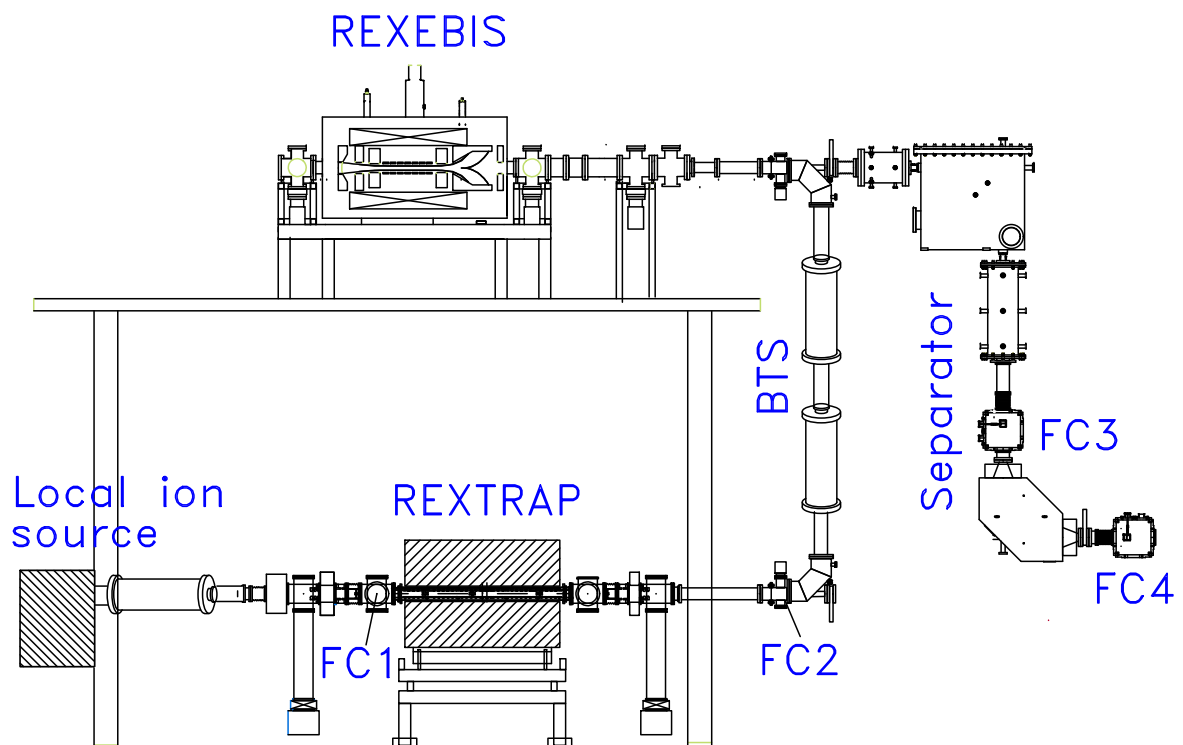


Figure 4.9: Overview of the REX low-energy beam preparation stage. Ions from ISOLDE (or a local source used for machine studies and set-up) are accumulated and cooled in REXTRAP and subsequently transferred to REXEBIS for charge breeding. Afterwards a specific  $A/Q$  ratio is selected in the spectrometer and the filtered beam is sent to the REX/HIE linac. Faraday cups (FC1-4) along the beam path can be used to monitor the throughput efficiency. Figure reproduced from Ref. [II].

and its gun had been designed to operate at current of up to 500 mA, but concerns about the cathode health made this goal unachievable.

Beyond that, there was a strong desire to improve the current density and hence accelerate the charge breeding process. This would improve access to very short-lived isotopes that are at a risk of decaying prior to reaching the experiment if they are held up in REXTRAP and REXEBIS for extended times. Moreover, it is possible to increase the repetition frequency of REX and reduce the number of particles in each pulse. For heavy elements, charge breeding times of up to 500 ms could be required, during which beam would be accumulated in REXTRAP. This leads to high instantaneous particle rates downstream, which can create problems for experiments that have to deal with the resulting detector dead-times and event pile-up, even when slow extraction schemes are employed [23, 111].

In the context of REXEBIS we had three crucial requirements for any upgrade of the electron gun. Firstly, the operation of the machine had to be ensured as soon as ISOLDE would go back into operation after CERN's long shutdown. This means severe modifications of the machine were not an option, in case a rollback would be needed. Secondly, the efficiency of REX as a whole should not be diminished compared to its previous performance. Here, efficiency describes the yield of highly charged ions in a selected charge state for a given input intensity. While the maximum single charge state yield is practically always limited by the successive ionisation dynamics introduced in Chapter 2 and Chapter 3, the overall survival rate depends heavily on a reliable injection into and extraction from the EBIS. A poor injection can also smear out the charge state spectrum if some ions initially encircle the electron beam and “fall” into the beam over an extended timeframe such that their charge breeding is delayed. Last but not least the excellent vacuum level (on the order of a few  $10^{-11}$  mbar at room temperature) should be maintained, and a low evaporation cathode is required to guarantee that the RIB is not contaminated with stable isotopes, or even worse, the space charge trap of the electron beam is compensated quickly by unwanted ions. These requirements translate into the demand of maintaining the acceptance – i.e. the size of the phase-space volume from which ions could be injected into the electron beam – while also not increasing the electron beam current recklessly.

Wenander provides an analytical expression for the maximum acceptance of an EBIS, which builds on the acceptance formula for ECR sources by taking into account the space charge well of the electron beam [112]

$$\alpha = \frac{r_e}{\sqrt{2\Phi_i}} \left[ Br_e \sqrt{\frac{q_i e}{m_i}} + \sqrt{\frac{q_i e B^2 r_e^2}{4m_i} + \frac{\lambda_e}{2\pi\epsilon_0}} \right]. \quad (4.9)$$

Here,  $r_e$  and  $\lambda_e$  denote the radius and linear charge density of the electron beam;  $\Phi_i$ ,  $q_i$ , and  $m_i$  are the ion injection potential, charge state and mass respectively. For mid-range mass  $^{39}\text{K}^+$  ions injected at an energy of 30 keV and the original 200 mA electron beam of radius 250  $\mu\text{m}$

and with an energy of 5400 eV this expression yields an acceptance of 10  $\mu\text{m}$ . Pre-empting the results of the next section, and assuming a beam radius of 187  $\mu\text{m}$  for the new electron beam, one can compute that a beam current of 500 mA at 6400 eV is required to match this value. This was judged to be an acceptable increase in beam current.

A Brillouin gun would have presented an interesting option to achieve a better beam compression. A geometry similar to MEDeGUN, under development in our team at the same time, cf. Chapter 5 and Refs. [88, 113–115], was considered briefly, but due to the lack experimental data, particularly for external ion injection, it was rejected. Since a residual magnetic field on the cathode generally has a stabilising effect on the electron beam a more conventional semi-immersed gun was chosen. To reach the required compression and current density the gun would be moved further out into the fringe field of the main magnet, and the nonadiabatic damping technique employed to reduce the beam ripple.

## 4.2.2 Electron gun design and simulation

For simulations of the electron gun we once again used *TRAK* [97]. Selected geometries have additionally been cross-verified with the help of *CST Particle Studio* [116], checking that both solvers converge on the same solution. The electron gun was placed into a model of the REX-EBIS main magnet, a 1.2 m long superconducting solenoid with an on-axis field of 2 T and a warm bore diameter of 150 mm, enclosed in a massive soft iron shield. The emission from the cathode followed the Child-Langmuir law. Since the time steps in the simulation need to be shorter than the cyclotron period of the electrons, the simulation effort increases the further the beam is tracked into the full field of the magnet. Due to memory and reasonable runtime limitations we have tracked the beam into a field of 1.7 T. As in the simulations for the conceptual investigations of nonadiabatic guns, we see an excellent agreement between simulations and theory and therefore expect that an analytical extrapolation of beam properties into the full field is justified and safe.

A Pierce-type geometry similar to that presented in Section 4.1 was selected for the electron gun. The final geometry is presented in Figure 4.10. With a cathode radius of 1 mm the simulated perveance of the gun amounts to 0.73  $\mu\text{A}/\text{V}^{3/2}$ . The nonadiabatic element is a passive soft iron ring (steel 1010).

### 4.2.2.1 Cathode plane flux density

As demonstrated above both the beam compression and the amplitude of the first radial excursion are very sensitive to the magnetic field in the electron gun. To determine a suitable flux density for the cathode, the electron gun was positioned in various positions in the fringe magnetic field and the nonadiabatic field modulation was optimised manually. The beam envelopes presented in Figure 4.11 demonstrate the beam behaviour as the electrons travel into

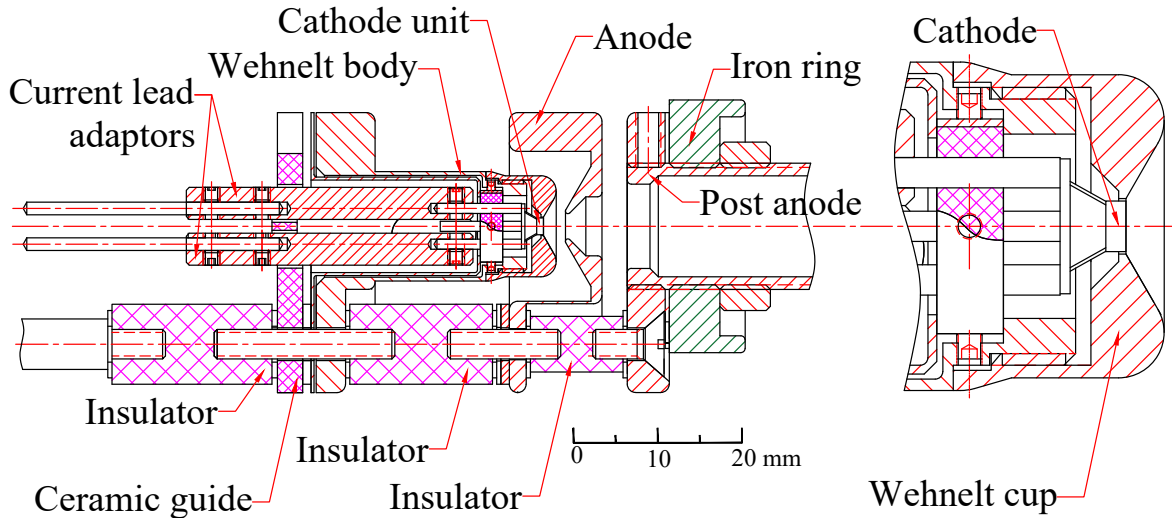


Figure 4.10: Mechanical drawing of the new electron gun for REXEBIS with an IrCe cathode and an iron ring acting as a passive nonadiabatic element. The section on the right shows a magnification of the cathode-mounting and Wehnelt electrode. Figure reproduced from Ref. [II].

the magnetic field. As the magnetic field increases, the beam is compressed and the cyclotron frequency increases. In all cases the beam ripple has been successfully dampened to fractions of the beam radius. Whereas a smaller cathode field results in better beam compression, there is a significant increase of the radial amplitude.

Of primary interest for operation is the current density of the compressed beam. The current density has been extracted from a number of *TRAK* and *CST* simulations for cathode flux densities ranging from  $\approx 35$  to  $75$  mT. In Figure 4.12 they are shown side by side with analytically predicted current densities, displaying excellent agreement. As pointed out, the simulations did not extend into the full field, so a projection of the peak current density is also provided.

Balancing current density-, acceptance-, thermal load- and beam stability-concerns, we have opted for a cathode flux density of  $70$  mT for the final design. As already demonstrated a beam current of  $500$  mA should be sufficient to maintain the acceptance of REXEBIS in this scenario. At the same time this still presents a considerable improvement in current density over the original electron beam, while maximising the chances of successful operation. If the new gun can be operated reliably long-term, the simulation results present an encouraging path for relatively simple future upgrades by retracting the gun into an even lower field.

#### 4.2.2.2 Beam current variation

In the conceptual discussion of the nonadiabatic damping technique it has become apparent that some degree of in-situ tuning is required to assert operability under non-optimal conditions. This

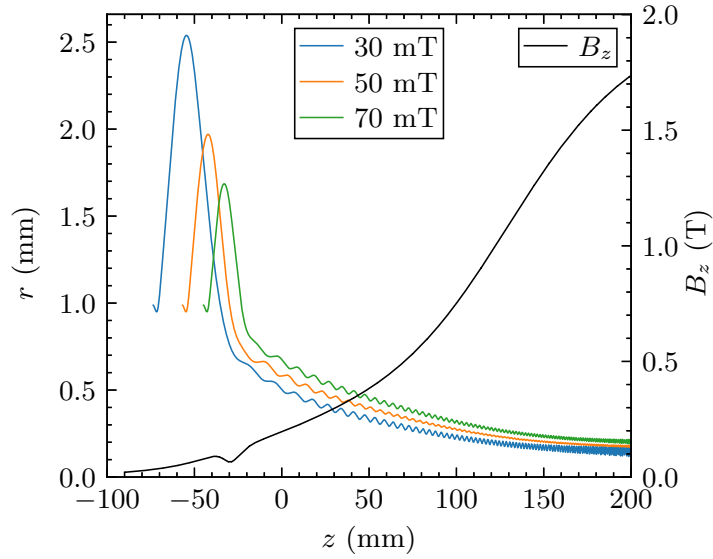


Figure 4.11: Comparison of 700 mA electron beam envelopes for three axial positions of the electron gun, resulting in different cathode flux densities and beam compression factors. NB: The magnetic field curve shows the nonadiabatic field depression as optimised for the 70 mT case. Figure reproduced from Ref. [II].

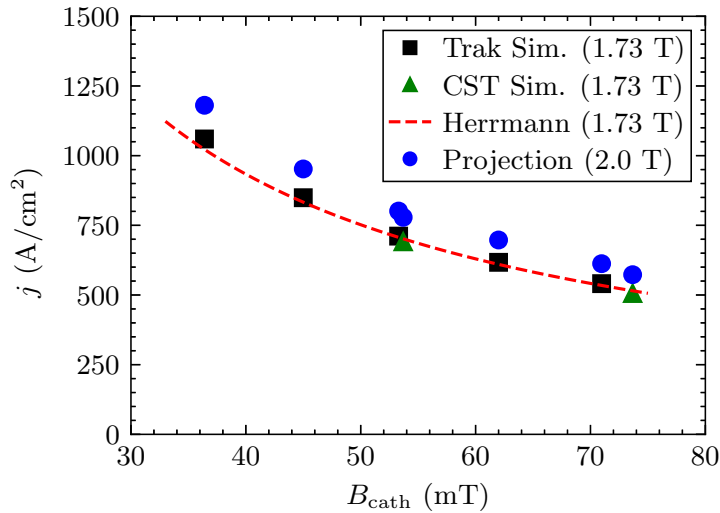


Figure 4.12: Variation of the current density as a function of the magnetic flux density in the cathode plane for an electron current of 700 mA. The simulation results (black squares, green triangles) have been evaluated at the end of the simulation domain in a field of 1.73 T. Theoretical values have been computed from the Herrmann formula and are shown in red. The blue dots display the current density extrapolated into the full field region of 2.0 T. Figure reproduced from Ref. [II].

is of course particularly important for a user-servicing machine. One major concern is the beam current, since incremental adjustments are expected for the commissioning phase. Moreover, cathode life-time concerns or thermally induced desorption in the electron collector could always mandate a current reduction. Beam current variations change the space charge forces, but more importantly the current is adjusted by tuning the voltage between cathode and anode (when operating in the Child-Langmuir regime), which also varies the forwards velocity of the beam.

Since the iron ring is a passive element its strength cannot be tuned on-line. Furthermore, positional adjustments are possible in principle but require a vacuum breach. We have instead opted to keep the anode short and follow it up with a separate “post anode” that can be biased to adjust the beam velocity and hence shift the descending slope of the first radial excursion with respect to the iron ring.

Figure 4.13 demonstrates both the increase of ripple amplitude for beams with varied currents and the mitigation by means of adjusting the post anode potential. The 500 mA curve presents the baseline scenario. For the 300 mA beam the voltage in the anode-cathode gap is reduced, and consequently the descending slope occurs too early. Providing an additional 3 kV bias on the post anode results in an amplitude reduction of  $\approx 16\%$ . The opposite behaviour is observed for the 800 mA scenario. Here, a bias of  $-1$  kV provides a reduction of  $\approx 46\%$ . In both cases the residual ripple accounts for less than 15 % of the total beam radius.

For a beam current of 500 mA the electron beam radius has been extrapolated to  $(187 \pm 1)$   $\mu\text{m}$  for a beam energy of 7.8 keV, corresponding to a current density of  $450 \text{ A/cm}^2$ . Even with the reduced cathode flux density the beam falls into the so-called “magnetised” regime, such that its radius is virtually independent of the current. For most of our experiments the real beam current was limited to 200 mA and 300 mA, or theoretical current densities of  $180 \text{ A/cm}^2$  and  $270 \text{ A/cm}^2$ , respectively.

#### 4.2.2.3 Axial shifts of the electron gun

Due to the construction of the gun, the position of the iron ring is fixed with respect to the cathode after installation. The whole gun assembly can still be moved in the axial direction, and hence to a non-optimised magnetic field. Shifts like this can be accidental, but a purposeful adjustment also presents a certain tuning range, and could in the future act as a stepping stone for exploring lower initial fields. A series of simulations was performed to verify the post anode’s ability to mitigate the ripple phase mismatch caused by such a shift. In Figure 4.14 we present the dependence of the ripple amplitude on the axial position (with respect to the target position) in a range of  $\pm 5$  mm. Similar to the results shown earlier in Figure 4.7, the ripple amplitude increases when deviating from the optimal conditions if the position of the descending envelope phase is not corrected. By adjusting the post anode bias the amplitude can be reduced significantly over the investigated range. Here, the coarse steps in the post anode

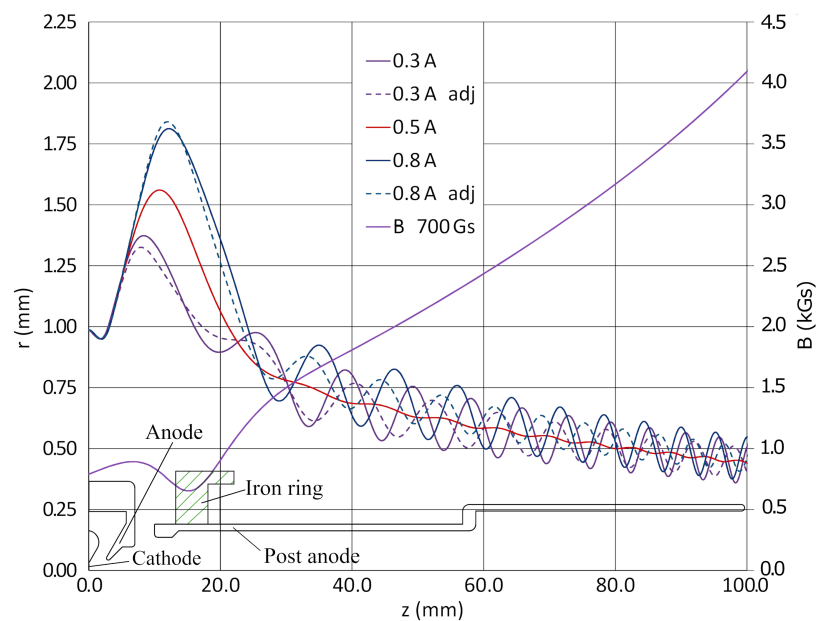


Figure 4.13: Electron beam envelopes for selected beam currents with the cathode located in a field of 70 mT. The magnetic field is optimised for 500 mA operation. The 300 mA and 800 mA beams are shown in their corrected (solid) and uncorrected form (dashed). For the optimised 300 mA beam the post anode was biased by 3 kV with respect to the anode, and by  $-1$  kV for the 800 mA beam. NB: The vertical dimensions of the machine geometry are not to scale. Figure reproduced from Ref. [II].

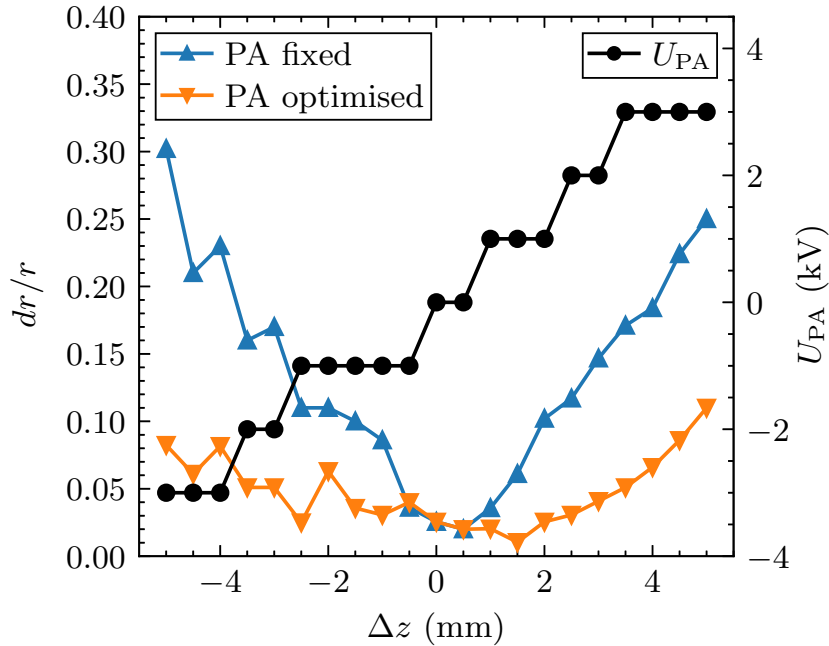


Figure 4.14: Variation of the beam ripple amplitude as a function of axial gun displacement. The blue curve shows the ripple without mitigation ( $U_{\text{PA}} = 0 \text{ kV}$ ), the orange curve shows the behaviour with an adjusted bias of the post anode (shown on the black curve). Figure reproduced from Ref. [II].

voltage are owed to simulation runtime. In reality, it could of course be tuned more carefully.

These simulation results provide confidence that the presented gun geometry, located at 70 mT, provides a safe yet promising upgrade path.

### 4.2.3 Mechanical design

The new electron gun (see Figure 4.10 and Figure 4.15) has been designed to require minimal modifications to the existing REXEBIS structure. To reduce the cathode field to 70 mT from the previous 200 mT the gun is retracted with the help of a new mounting base. An intermediate baseplate is mounted to a conventional CF63 flange with threaded rods, such that the axial position can be adjusted. The interface to the drift tube structure is provided with a ceramic adapter piece between the post anode and the first drift tube. Beyond this the internal structure of REXEBIS remains unchanged.

#### 4.2.3.1 Assembly and materials

The cathode is fixed to a ceramic base, that also acts as strain relief for the heating leads. This structure is inserted into a metallic cylinder referred to as the Wehnelt body. At the end of this

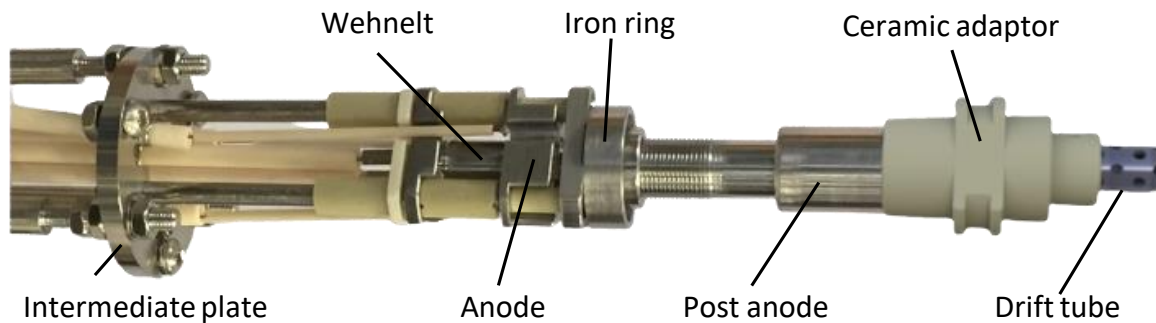


Figure 4.15: Photograph of the assembled electron gun from the intermediate mounting plate up to the first drift tube of the EBIS. Figure reproduced from Ref. [II].

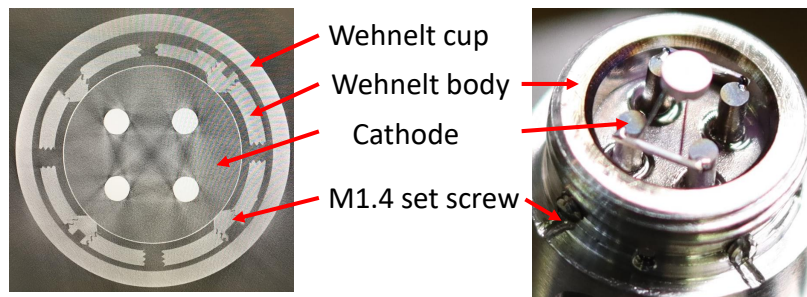


Figure 4.16: IrCe cathode mounted inside the Wehnelt body. The left image shows an x-ray tomography slice, the right image shows a photograph of the same assembly with the threaded Wehnelt cup removed. Two of the four rods on which the cathode is mounted also carry the heating current. Figure reproduced from Ref. [II].

cylinder set screws can be used to provide radial alignment of the cathode. This is necessary because x-ray tomography scans of the cathode assemblies revealed insufficiently tight tolerances (several hundred  $\mu\text{m}$ ) between the cathode itself and the base that it is mounted to in the factory. The radial alignment mechanism is shown in Figure 4.16; the concentricity with the Wehnelt cup can be better than  $30\ \mu\text{m}$ . Similarly, a shim between the mounting base of the cathode and the interior mating surface of the Wehnelt body is used to recess the cathode by approx 50 to  $100\ \mu\text{m}$  into the Wehnelt with the goal of reducing unwanted side emission from the cathode edges. Once the cathode has been aligned, the actual Wehnelt electrode surface (referred to as the cup) can simply be screwed onto the body. The Wehnelt is electrically isolated from the cathode such that it can be biased as a control electrode.

The iron ring is threaded onto the post anode and fixed in place with a locking ring. Afterwards, the anode and post anode are stacked onto the cathode / Wehnelt assembly via isolating stand-offs. The gun assembly is mating to the drift tube structure through a ceramic adaptor

piece with tight radial tolerances of approx 50  $\mu\text{m}$ . As the required heating power was estimated to amount to no more than 20 W and no considerable beam losses are expected inside the electron gun, water cooling was omitted.

The metallic pieces are manufactured from non-magnetic stainless steel (316LN), except for the iron ring made out of low carbon steel 1010. To improve the magnetic homogeneity of the ring it was annealed prior to installation. Steatite stand-offs provide isolation between the gun electrodes. Care was taken to provide sufficient sparking and creeping distances. The design accounts for up to 19 kV between cathode and anode, and another 11 kV between anode and post anode. This far exceeds the expected operating voltages. The adapter piece has been manufactured from alumina ( $\text{Al}_2\text{O}_3$ ). Stainless steel is an acceptable electrode material for the installed IrCe cathodes, but could carry a risk of surface poisoning of dispenser type cathodes. In case the cathode type is changed, the Wehnelt and anode should be made from molybdenum.

#### 4.2.3.2 Cathode

At a cathode radius of 1 mm, the target current of 500 mA amounts to an emission current density of about 16 A/cm<sup>2</sup>. For a cathode foreseen to operate continuously for up to 9 months a year this is a challenging value. The chemical composition of the LaB<sub>6</sub> cathodes originally used at REXEBIS had the excellent property of featuring only three stable isotopes: <sup>139</sup>La, <sup>10</sup>B, and <sup>11</sup>B. This limits the number of possible contaminants evaporating from the heated cathode. However, the long term thermal deterioration mentioned in the introduction limits the current that can be extracted from these cathodes to about 200 mA in continuous operation.

A possible alternative are IrCe alloy cathodes, which have previously been reported to deliver up to 20 A/cm<sup>2</sup> at a temperature of 1850 K while maintaining a low evaporation rate [117, 118]. Earlier tests at CERN could not confirm this emission density and peaked at 15 A/cm<sup>2</sup> [88]. But for lack of better alternatives it was decided to use IrCe cathodes for the initial version of the nonadiabatic gun. According to the manufacturer, cathodes of this type have successfully been operated continuously for more than 5000 h at emission currents from 500 to 600 mA [119]. With <sup>191</sup>Ir, <sup>193</sup>Ir, <sup>140</sup>Ce, and <sup>142</sup>Ce there are more problematic stable isotopes than for the old cathodes; hence, traces of these ions were searched for as part of the commissioning. The cathodes are mounted on a base made of an undisclosed pink-coloured material. No detectable outgassing could be found in a residual gas analysis.

For the future there is a prospect of installing a novel kind of dispenser-type cathode provided by Beijing University of Technology. These nanosized-scandium impregnated cathodes were demonstrated to operate at emission densities of 30 A/cm<sup>2</sup> at 1225 K for over 2000 h [120], but are not yet widely commercially available. They also potentially feature even more stable isotopes: <sup>45</sup>Sc, <sup>135</sup>Ba, <sup>136</sup>Ba, <sup>137</sup>Ba, <sup>138</sup>Ba, <sup>182</sup>W, <sup>183</sup>W, <sup>184</sup>W, and <sup>186</sup>W.

#### 4.2.4 Experimental setup

All tests and commissioning of the new electron gun were carried out at its final destination, REXEBIS. Only the EBIS itself was required for the pure electron beam commissioning. For charge breeding experiments, the full REX beam preparation stage, as shown in Figure 4.9, was exploited. While the EBIS is busy charge breeding, REXTRAP accumulates and cools the continuous stream of ions originating from ISOLDE or a local test ion source. Once the EBIS has expelled the preceding bunch, the accumulated ions are transferred from REXTRAP to REXEBIS via an electrostatic beam line (see also Fig. 9 in Ref. [III]). After a set charge breeding time, the now highly charged ions are expelled towards a Nier-type spectrometer to filter for a specific  $A/Q$  value [121]. Finally, the separated ions of interest are injected into the linear accelerator.

##### 4.2.4.1 REXEBIS

REXEBIS is an electron beam ion source built into a solenoidal 2 T warm-bore magnet. An overview of the most important components and operational parameters of REXEBIS is supplied in Figure 4.17. The gun has been installed at an axial position corresponding to a cathode flux density of 70 mT. It is followed by the drift tube structure which consists of a series of individually addressable tubes with an internal radius of 5 mm. At the far end of the machine, a water-cooled copper-made collector recycles the electron beam. The collector is preceded by a secondary electron suppressor and followed by an ion extraction electrode.

A pair of turbo-molecular pumps located at either end of the EBIS, provide a high pumping speed in proximity to the heat-loaded surfaces of the electron gun and collector. Arranged around the drift tubes are metallic strips coated with a non-evaporable getter (NEG) material that help to create an ultra-high vacuum in the trapping region at room temperature. Furthermore, the drift tubes are heavily perforated to increase the conductance between the trapping region and the NEG strips. During commissioning, the average pressure was approximately  $1 \cdot 10^{-10}$  mbar on the gun side and  $1 \cdot 10^{-9}$  mbar on the collector side.

The typical axial voltage profiles are also shown in Figure 4.17. The trap was predominantly controlled with the help of the outer barrier, which is pulsed between 600 V (at injection), 1300 V (during breeding), and 0 V (at extraction, 2 ms), unless specified differently. The gun bias voltage as well as the outermost drift tube, collector and suppressor electrode, were occasionally adjusted to minimise electron losses at different beam currents. For more detailed descriptions of the charge breeder, the reader is referred to references [14, 88, 100, 114].

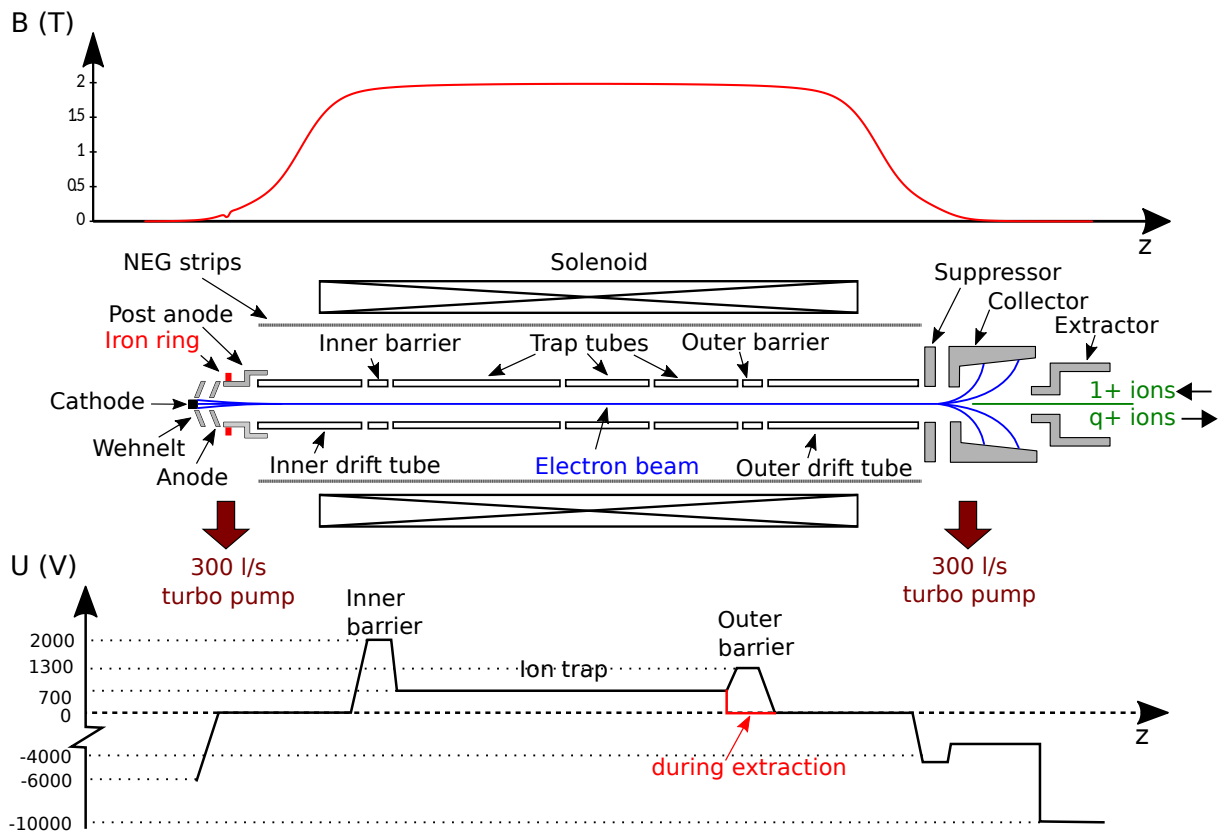


Figure 4.17: Schematic overview of REXEBIS in its new configuration with the nonadiabatic electron gun. The plots show the axial magnetic flux density and typical operational voltages applied to the EBIS electrodes. The latter are referenced to the EBIS platform potential. Figure reproduced from Ref. [II].

#### 4.2.4.2 Ion injection and charge breeding

For experiments involving ions, the particles could originate from a number of sources. A local surface ion source provides beam of  $K^+$  and  $Cs^+$  [122], whereas  $Li^+$ ,  $Na^+$ ,  $Sm^+$ , and  $Tl^+$  ions were available through the ISOLDE General Purpose Separator (GPS) line [102]. Neutral atoms of neon travel from REXTRAP into REXEBIS, providing a constant feed of fresh particles into the electron beam. Similarly, xenon could be injected through a precision leak valve located next to the electron gun. Generally, such constant sources run a risk of filling up the space charge well of the electron beam. In our experiments however, the residual gas pressure and the number of injected ions were sufficiently low that the space charge compensation remained below 2.5% in almost all cases. A maximum compensation of 7.5% occurred with xenon injection at a breeding time of 90 ms.

For singly charged ion injection, the REXTRAP parameters and beam transmission to REXEBIS were manually optimised for every ion species to guarantee the highest possible efficiency. Usually, the cycle time was varied from 600 ms (highest charge states of heavy elements) down to 20 ms (the time required for sufficient cooling in REXTRAP). Using the current measured with Faraday cups FC2 and FC4, cf. Figure 4.9, one can determine the single charge state and global efficiency of the EBIS

$$\eta_{\text{global}} = \frac{\sum_{Q=1}^Z I_{\text{FC4}}/Q}{I_{\text{FC2}}} \quad (4.10)$$

$$\eta_{\text{single}}(Q) = \frac{I_{\text{FC4}}/Q}{I_{\text{FC2}}}. \quad (4.11)$$

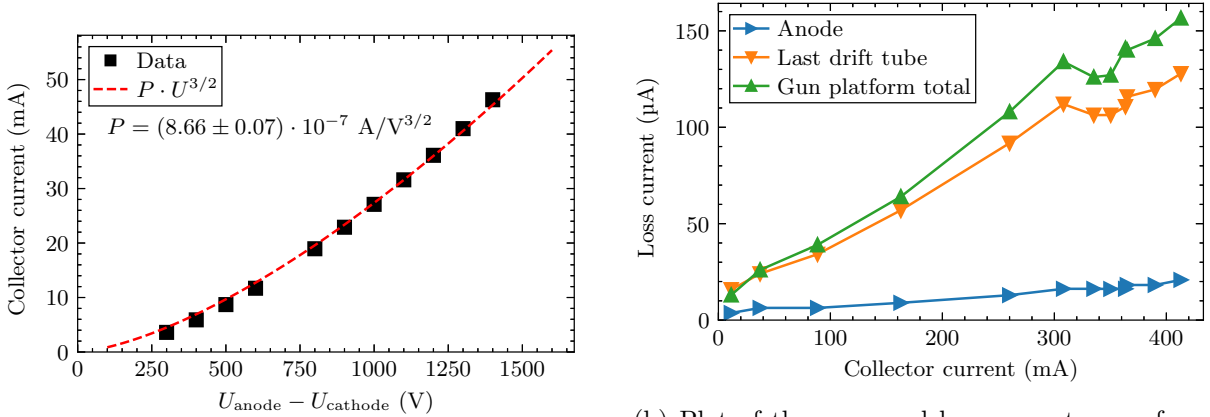
These efficiencies provide the ratio of ions available after charge breeding and filtering, respectively. The degree of space charge neutralisation at the end of the charge breeding cycle, can be determined from the total ion current leaving the EBIS (FC3)

$$\eta_{\text{neutralisation}} = \frac{I_{\text{FC3}} \cdot T_{\text{period}}}{L_{\text{trap}} I_e / u_e}. \quad (4.12)$$

Here,  $T_{\text{period}}$  denotes the period time of the entire REX stage cycle;  $L_{\text{trap}}$  is the length of the trapping region. The beam velocity  $u_e$  is computed as a self-consistent solution to Equations 2.27 and 2.40, assuming  $r_{\text{DT}} = 5$  mm,  $r_e = 187$   $\mu\text{m}$ ,  $\Phi_{\text{DT}} = 700$  V,  $I_e = 200$  to 300 mA, and  $\Phi_{\text{C}} = -6300$  to  $-5700$  V.

#### 4.2.5 Experimental methods & results

In the following, the relevant experimental results from the commissioning period are presented. Here, the various experiments and their results will be introduced successively for clarity. First, there is a collection of abridged results concerning the electron gun and beam, the charge breed-



(a) Plot of the electron beam current versus the cathode to anode voltage. The red line shows the best fit for the perveance law. Figure reproduced from Ref. [II].

(b) Plot of the measured loss currents as a function of the collector current. Beam energy and suppressor voltage have been retuned for currents exceeding 300 mA. Figure reproduced from Ref. [II].

Figure 4.18: Electron beam transmission results.

ing efficiency, and the purity of the machine vacuum and the resulting beam purity. Full discussions of these experiments can be found in the original publication [II]. Second, there is a detailed account of charge breeding performance measurements for determining the effective beam current density, as well as a survey of the axial energy distributions of ions extracted from REXEBIS.

#### 4.2.5.1 Gun perveance and electron beam losses

After the installation of the new electron gun, its perveance was measured by recording the electron beam current for cathode-to-anode voltages ranging up to 1400 V. Figure 4.18a contains the measurement data alongside a power law fit yielding a perveance value of  $(0.866 \pm 0.007) \mu\text{A/V}^{3/2}$ . The error for the perveance given here is the uncertainty of the fit parameter. The experimentally determined value exceeds this simulation prediction of  $0.73 \mu\text{A/V}^{3/2}$ . Likely reasons for this discrepancy are unwanted emission from the cathode edge or a slightly shorter than expected cathode to anode gap in the assembled gun. The perveance measurement was limited to low emission currents due to a combination of problems with loss currents and insufficient emission from the IrCe cathode. Especially the latter effect subdues the emission current below the value expected for Child-Langmuir emission and would distort the result. Throughout our experiments we generally used much higher currents of up to 420 mA, but in these situations the gun would practically operate in the thermionically limited regime.

Our simulations, carried out for Child-Langmuir emission, show an increased ripple as the beam current deviates from its optimised value of 500 mA. Regardless, we were able to transport

an electron beam with as little as a couple of mA, up to a maximum value of 420 mA without suffering prohibitive loss currents. Initially, loss currents were reduced by iteratively tuning electrode voltages and carefully adjusting the transverse position and alignment of the EBIS structure in the solenoid field. Once a good transverse alignment was attained, any further adjustments concerned applied electric potentials alone.

In Figure 4.18b, the dependence of loss currents on the total beam current is shown. The applied potentials were fixed for currents below 300 mA, with the cathode pulled to  $-6$  kV, anode, post anode and outermost drift tube fixed to ground, and the suppressor and collector set to 1.7 kV and 2.5 kV, respectively. For higher currents the suppressor voltage was lowered to 1.3 kV and the electron gun was biased to  $-7$  kV to reduce loss currents, which particularly affects the outermost drift tube.

The loss currents on the anode are sufficiently small over the full current range. Opposed to that, the last drift tube accounts for the majority of all loss currents, amounting up to 0.03 % of the beam current. Additional tests have shown, that a positive bias to the outermost drift tube can weakly reduce the loss current, whereas a negative bias leads to an increase in losses. If the suppressor voltage is lowered, less electrons hit the outermost drift tube. We therefore believe that a fraction of the current detected on the outermost drift tube is due to back-scattered or elastically reflected electrons from the collector. This effect is at odds with the observations for the biased drift tube though, which should see a reduction of collector-originating currents for negative voltage. Such a behaviour may also indicate the existence of loss current contributions that depend sensitively on the exact beam optics in the collector-preceding region.

#### 4.2.5.2 Charge breeding efficiency

As previously noted the charge breeding efficiency, i.e. ion survival rate, is of crucial importance for rare isotope beams. It can be expressed with the equations given above in Section 4.2.4. We have measured the charge breeding efficiency for a selection of isotopes ( ${}^7\text{Li}$ ,  ${}^{23}\text{Na}$ ,  ${}^{39}\text{K}$ ,  ${}^{152}\text{Sm}$ ,  ${}^{205}\text{Tl}$ ) spanning a large range of masses, in various charge states, and at two different electron beam currents of 200 mA and 300 mA. The ion transport from REXTRAP to REXEBIS and the injection into the electron beam were manually optimised for every configuration.

There are a number of uncertainty contributions related to these measurements. The ion injection quality in particular may vary across configurations as there is no way of measuring it in isolation. We have observed a sensitive response of the efficiency to the voltages applied to electrodes in proximity to the gun. Such adjustments can change the space charge profile in the collector region, which can in turn affect the ion injection due to changing beam optics. Finally, the Faraday cups suffer from relatively large uncertainties for ion beams with sub-pA average currents. Here, we assume a  $1\sigma$  uncertainty comprised of an absolute error of 0.1 pA and a relative error of 5 % of the measured current. As the sodium measurements suffer from an

erroneous measurement of the primary beam current, error bars for these measurements have been omitted.

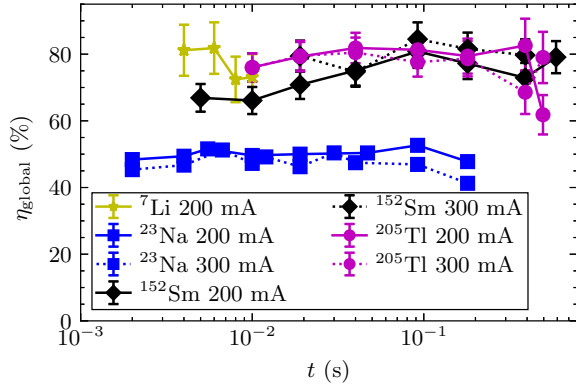
**Global efficiency** The results of the measurements of the global efficiency are collected in Figure 4.19a. With the exception of sodium, all data points range from approximately 65 to 85%. Importantly, there are no signs of a significant reduction of efficiency for long breeding times. This indicates that ion heating effects are not strong enough for ions to be lost from the trap for typical charge breeding times  $\lesssim 600$  ms. Furthermore, our data suggests that there is no significant mass trend. The discrepancy for sodium most likely roots in a problematic configuration of REXTRAP during the sodium measurements. Under unfortunate circumstances the injected primary beam can create Ne+ ions from the buffer gas which then hit the surrounding Faraday cups and produce inflated reference current readings.

**Single charge state efficiency** The global efficiency gives a good impression of losses during injection, charge breeding, and extraction of the ions, since it covers all charge states. In reality however, the linear accelerator will only be synchronous for a single selected A/Q ratio, i.e. charge state. Since the ions are spread over a range of charge states at any given time, this single charge state efficiency will always be smaller than the global efficiency.

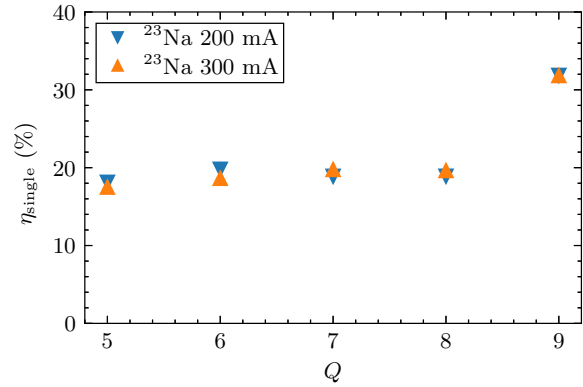
By measuring the current behind the separator magnet (FC4), the single charge state efficiency can be determined. The efficiency for each measured charge state was maximised by tweaking the charge breeding time. Single charge state efficiencies of all probed elements recorded at an electron beam current of 200 mA are given in Figure 4.19c.

The effect of closed-shell breeding is clearly visible in the plot. Several charge states, e.g. Li<sup>3+</sup> (bare ion), Na<sup>9+</sup> (He-like), and K<sup>9+,17+</sup> (Ne-like, He-like) show clear efficiency enhancement compared to their neighbours. Samarium has a 3*d* shell closure at charge state 34+ which has not been measured, but an increased abundance is noted for the 36+ state. Closed shell configurations typically create a stronger-than-usual drop in the ionisation cross sections, which leads to an accumulation of ions in the corresponding charge state since reaching the next higher charge state is much slower. The 3*d* orbital closure of Sm<sup>34+</sup> was not recorded explicitly, but the 36+ charge state still shows some enhancement. Potassium shows a particularly low efficiency for the 8+ charge state, which does not agree with simulation results but has been double-checked and confirmed on several occasions.

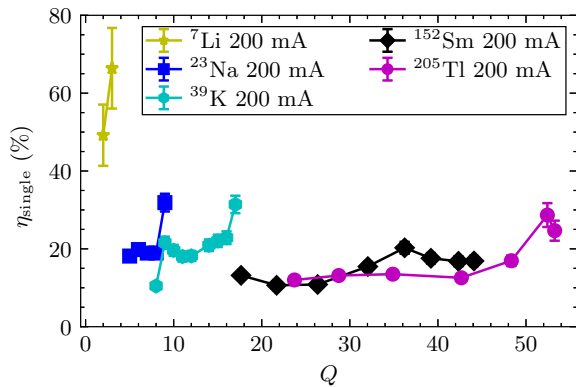
Opposed to the closed shell effect, the high charge states of thallium are best explained by the increasing ionisation energy. For instance, Carlson et al. lists an ionisation energy of 4854 eV [123] for Tl<sup>53+</sup>, which is a little smaller than the minimal binding energy of 5231 eV computed by Mertzig using *FAC* [35, 36, 87]. These thresholds are approaching the electron beam energy  $\leq 6.1$  keV, which leads to a strong reduction of the ionisation cross section, as previously discussed in Section 2.2.1. Since higher charge states are eventually impossible to



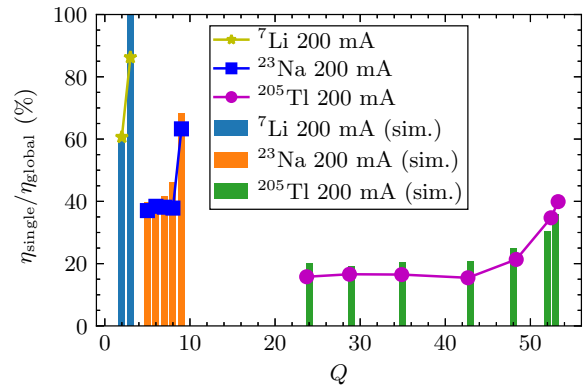
(a) Plot of the global EBIS efficiency as a function of breeding time for selected elements. Figure reproduced from Ref. [II].



(b) Comparison of the EBIS single charge state efficiency for sodium at electron currents of 200 mA and 300 mA. Figure reproduced from Ref. [II].



(c) Plot of the EBIS single charge state efficiency vs the charge state for selected elements. The data was recorded at an electron beam current of 200 mA. Figure reproduced from Ref. [II].



(d) Plot of the EBIS single charge state efficiency normalised by the global EBIS efficiency vs the charge state for selected elements. The bars indicate the relative abundance optima as computed with a charge breeding simulation. Figure reproduced from Ref. [II].

Figure 4.19: EBIS efficiency results.

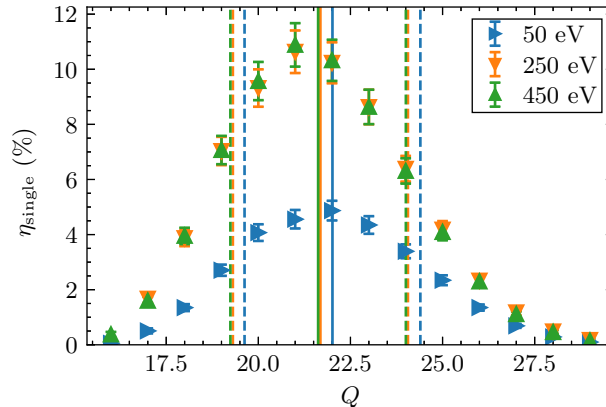


Figure 4.20: Plot of the EBIS single charge state efficiency of  $^{152}\text{Sm}$  after 10 ms in a 200 mA electron beam. The different curves were recorded for different ion injection energies, listed in the legend. The mean and standard deviations of the distributions are indicated with vertical lines. Figure reproduced from Ref. [II].

reach, the efficiency of the last reachable charge states is improved. The excellent efficiency for thallium demonstrates the holding capabilities of REXEBIS, even for long breeding times at relatively low beam currents.

In Figure 4.19d the single charge state efficiencies have been rescaled by the corresponding global efficiencies. The resultant values are compared to efficiencies predicted with basic model *ebisim* simulations, generally displaying a very good agreement. The strongly decreasing mass trend for the single charge state yield is well known and stems from the fact that the ions are spread out over more charge states at the same time.

Figure 4.19b provides a comparative measurement for sodium at an increased electron beam current. No significant changes in the single charge state efficiency are visible, which is in line with the global efficiency findings.

Finally, Figure 4.20 demonstrates the single charge state results for samarium recorded after 10 ms at different ion injection energies (that is their kinetic energy when entering the ion trapping region). Here, an energy of 250 eV presents the nominal case and should be compared to the depth of the potential well inside the electron beam, which amounts to approx 40 V for a 200 mA beam in the REXEBIS configuration. A strong dependence of the charge state spectrum on the injection energy is not observed, although a slight shift to higher charge states may be argued for in the 50 eV case. In the latter case however, significantly more ions are lost entirely.

**Discussion** In light of the acceptance formula (4.9) provided above, the insensitivity of the efficiency on the beam current is striking. One would expect a reduction of losses as the beam current is increased, unless the emittance of the injected beam is smaller than the acceptance. Past measurements of REXTRAP indicate however, that the ion beam emittance should exceed

the REXEBIS acceptance [106, 124]. Additionally, the injection energy does not show a large effect, except for a strong efficiency reduction in the 50 eV case. If the ion beam fits inside the EBIS acceptance, then this energy dependent drop would not be expected. We therefore conclude that, in the case of pulsed injection, the ion emittance can exceed the calculated EBIS acceptance while maintaining efficient capturing conditions, as long as the ions have sufficient energy to enter the trapping region. For an injection energy of 250 eV, the bunch length of ions originating from REXTRAP is typically around 10 cm, which should fit well within the 80 cm long trap, as long as the timing is correct.

If the ion energy exceeds the potential well of the electron beam significantly, it is possible for ions to encircle the electron beam for an extended time before getting ionised. Under such circumstances, the charge state spectrum is typically widened and shifted towards lower values. In the case of Figure 4.20 this effect is likely hidden by the already intermediate charge state, which is not as sensitive to early delays. Operational experience however, supports this assumption, and we have recorded potassium data (presented further below, cf. Figure 4.26) that agrees with this explanation.

#### 4.2.5.3 Vacuum quality and ion beam contamination

As ion beam purity is a major concern, we have carried out dedicated studies of the residual gas ion production. This involved a general survey across a large  $A/Q$  range, as well as a dedicated search for ions originating from the cathode material.

For common residual gases like e.g. oxygen and nitrogen, the ion current is large enough to measure with the Faraday cups along the beam line. We have measured both the total ion current and long range  $A/Q$  spectra for a selection of breeding times at an electron beam current of 200 mA. Since it is known that neon streams into REXEBIS from the cooling trap, these measurements were also repeated with the intermediate sector valve closed to eliminate any neon influx.

The rate of Ir and Ce ions extracted from REXEBIS is too low to detect with conventional means. Instead, the magnetic separator was set to specific  $A/Q$  values, at which such ions were expected to be found. The beam was then accelerated to a specific energy of 300 keV/u in the REX RFQ and sent onto a Passivated Implanted Planar Silicon (PIPS) detector. Calibrated attenuating grid were used to avoid pile-up in the detector. In this way, energy histograms of single ion impacts can be recorded and translated into mass spectra. More information on this procedure can be found in Ref. [125].

**Results** In Figure 4.21 the total residual gas ion current values are presented. After a relatively long breeding time of 300 ms the neutral gas ions (including neon) compensate the charge of the electron beam in the trapping region by  $\approx 17\%$ . Through the large difference between the

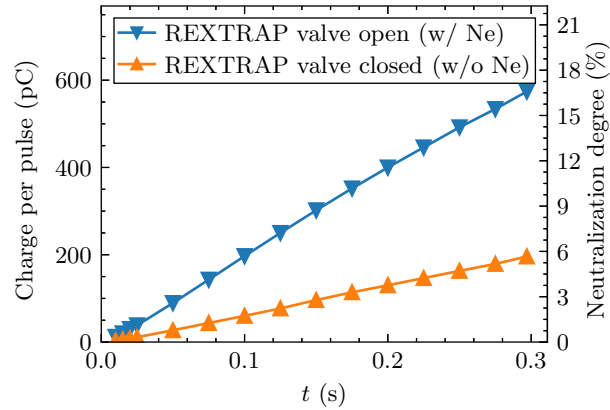


Figure 4.21: Plot of the extracted charge per pulse and equivalent electron beam compensation versus charge breeding time. The electron beam current was 200 mA at a nominal energy of 6.2 keV. With the valve to REXTRAP closed (open) the pressures recorded were  $1.2 \cdot 10^{-10}$  mbar ( $1.2 \cdot 10^{-10}$  mbar) at the electron gun and  $7.2 \cdot 10^{-10}$  mbar ( $7.7 \cdot 10^{-10}$  mbar) at the collector. Figure reproduced from Ref. [II].

curves, it is immediately visible that neon dominates the residual gas composition in the EBIS. This source is not linked to the new gun and therefore not of major concern. The data was recorded shortly after the installation of the gun; it is expected that the pressure continues to decrease over time, such that this can be seen as an upper limit for the compensation rate for the experiments carried out during the commissioning.

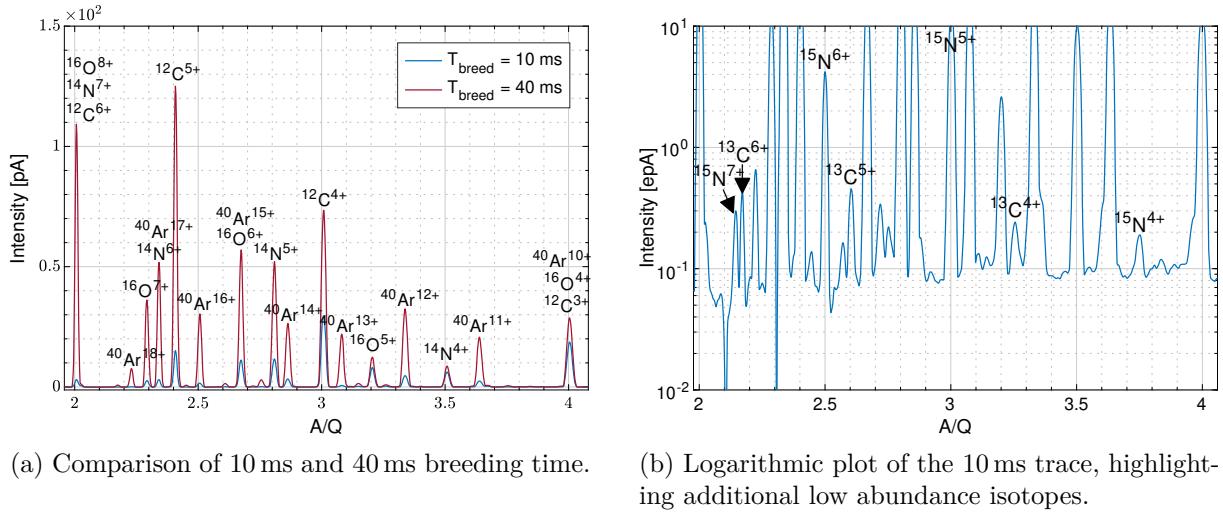
The charge-to-mass ratio surveys were carried out for breeding times from 5 to 50 ms; some examples with identified peaks are shown in Figure 4.22. Since many of the peaks are overlapping, the spectrum needs to be disentangled. This was achieved by fitting artificial spectra to the measured profiles.

The artificial spectra were generated by mixing the results of charge breeding simulations for a selection of elements with individual weights. Both the weights and the effective current density, determining the charge breeding speed, were free fit parameters. Here we assume a constant effective current density with the same value for all elements. From the fit we obtain  $j_{\text{eff}} = 180 \text{ A/cm}^2$ ; given the beam current of 200 mA this agrees perfectly with the electron beam radius predicted by the Herrmann formula.

To estimate the neutral atom density in the electron beam, one needs to determine the rate  $R_0$  at which new ions are created. Under the assumption that no particles are lost, this rate is the same as the increase of the total number of ions  $\sum_k N_k$ , which is provided by the fit result. The rate of ion creation through electron impact ionisation is conveniently independent of the

Table 4.1: Estimated residual gas densities in REXEBIS.

Element	Pressure (mbar)	$N_0(r \leq r_e)$
H	$3.9 \cdot 10^{-11}$	$8.4 \cdot 10^4$
C	$2.9 \cdot 10^{-12}$	$6.2 \cdot 10^3$
N	$5.2 \cdot 10^{-12}$	$1.1 \cdot 10^4$
O	$8.7 \cdot 10^{-13}$	$1.9 \cdot 10^3$
Ne	$1.9 \cdot 10^{-11}$	$4.1 \cdot 10^4$
Ar	$1.2 \cdot 10^{-12}$	$2.5 \cdot 10^3$
<b>Total</b>	$6.8 \cdot 10^{-11}$	$1.5 \cdot 10^5$


 Figure 4.22: Plot of long range  $A/Q$  scans recorded on FC4 at an electron beam current of 200 mA, without neon influx from REXTRAP. Figures reproduced from Ref. [II].

current density, and therefore one can relate

$$R_0 = \frac{d}{dt} \sum_k N_k = n_0 \frac{I_e}{e} L_{\text{trap}} \sigma_0^{\text{EI}}. \quad (4.13)$$

With this formula, one can determine the neutral atom density  $n_0$  for each element. Here, it is neglected that many common contaminants are actually molecules. Assuming a mono-atomic gas for simplification, an equivalent pressure at 300 K can be computed for easier comparability to the pressures read on the vacuum gauges. The corresponding results are collected in Table 4.1. The equivalent pressures are significantly lower than the readings at the gun and collector (cf. Figure 4.21). This is due to the NEG coated strips surrounding the drift tube structure that help to improve the vacuum conditions in the trapping region.

The results of the search for evaporated Ir and Ce from the cathode are provided in Figure 4.23.

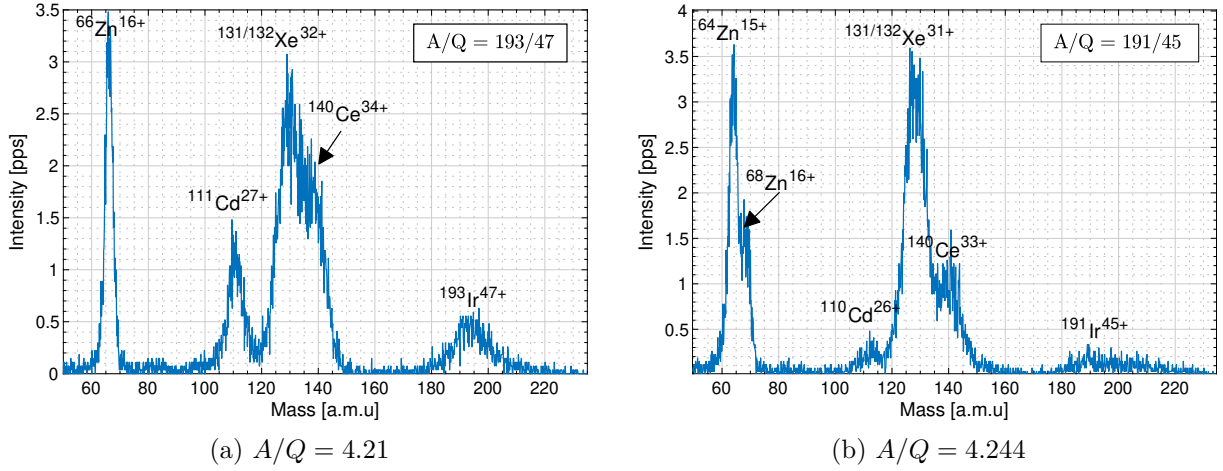


Figure 4.23: Spectra of low abundance ions recorded with a silicon detector behind the accelerating RFQ for two separate  $A/Q$  settings of the magnetic separator. Figures reproduced from Ref. [II].

Histograms show ions of various isotopes falling within a narrow  $A/Q$  range (the REX separator has a resolving power of  $\Delta(A/Q)/(A/Q) = 1/300$ ); the intensity has been corrected for the attenuation factors of the grids used during the measurement. Despite a cathode temperature of approximately 1900 K, required to provide a 300 mA beam, barely any Ir and Ce are detected. Their abundance is even smaller than that of other trace elements like e.g. xenon isotopes. At a rate of just a few particles per second they do not pose a risk of contaminating the extracted beam.

#### 4.2.5.4 Effective current density determination

One of the key figures for comparing the performance of EBIS-type charge breeders is the current density of the electron beam  $j$ , since it directly determines the charge breeding speed. While simulations yield the current density under perfect conditions, it is desirable to validate the performance of the actual hardware. Due to restrictions in the design of REXEBIS, and due to its crucial importance for the availability of the HIE-ISOLDE complex, direct current density measurements of the electron beam were impossible.

Instead, the effective current density was determined from the evolution of ion charge state spectra recorded during commissioning. This method provides an effective current density that quantifies the actual charge breeding performance. The effective current density can be written as the product of the true current density and an overlap factor  $j_{\text{eff}} = j f_{ei}$ , where the overlap factor  $0 \leq f_{ei} \leq 1$  carries the same meaning as that defined in Section 3.2. Generally, the overlap factor varies between elements, charge states, and with ion temperature and the degree of space charge compensation in the electron beam. At REX, the final  $A/Q$  values are usually

moderate, implying that heating effects such as Spitzer heating have only limited time to increase the temperature of the ion cloud and push the ions out of the electron beam. This raises the relative importance of a clean ion injection, since a poor overlap could cause an initial delay in the ionisation chain, increasing breeding times and reducing the prominence of individual charge state maxima.

**Methods** For this analysis we have recorded the charge state evolution of various elements, injected either as singly charged ions or in the form of a neutral gas, for electron beam currents ranging from 200 to 300 mA. The generated ion beams were scanned by charge state with the help of the separator magnet and the ion current was recorded on FC4, cf. Figure 4.9. In this manner charge state spectra were recorded for a range of element-specific charge breeding times.

In order to obtain an estimate for the effective current density, simulation-generated charge state distribution evolutions have been fitted to the recorded data. The artificial charge state spectra were generated with the basic simulation model of *ebisim* (Chapter 3), corresponding to Equation 2.11. This decision was taken since the inclusion of temperature effects introduces many additional unknown variables and therefore increases the general uncertainty. As this model implicitly assumes a perfect overlap between the ion cloud and the electron beam, the current density in the simulation should be interpreted as the effective current density in the experiment.

As charge exchange rates depend on the ion temperature, the effect is not included in the simulations. A brief estimate provides assurance that charge exchange is indeed negligible for the commissioning experiments. Charge exchange predominantly affects the most highly charged ions; hence, we consider the case of  $\text{Sm}^{49+}$ , the highest charge state recorded during the measurement campaign. Neon, the most abundant background gas, is chosen as the collision partner. Equation 2.9 yields a charge exchange cross section of  $2.8 \cdot 10^{-14} \text{ cm}^2$  for this process. Assuming a neon pressure of  $5 \cdot 10^{-11} \text{ mbar}$ , and an ion thermal velocity of  $1.27 \cdot 10^6 \text{ m/s}$  (corresponding to a relatively high temperature of  $k_{\text{B}}T = 10 \text{ keV}$ ) yields an approximate charge exchange rate of  $0.44 \text{ s}^{-1}$ . Conversely, the electron ionisation cross section of  $\text{Sm}^{48+}$  at an electron energy of approx. 6.5 keV is  $2.0 \cdot 10^{-21} \text{ cm}^2$ . With an electron current density of just  $200 \text{ A/cm}^2$  this results in an ionisation rate of  $2.5 \text{ s}^{-1}$ . Therefore, even in this most extreme case, ionisation outweighs charge exchange by a solid margin.

During the exploratory data analysis it became clear, that fitting a single constant current density to the recorded data would not be appropriate, as a large apparent variation was observed over time. A fitting procedure has therefore been developed in the following manner: Five geometrically spaced support points in time were selected between the shortest and longest recorded charge breeding times. The effective current density is fitted for these five sampling points, and linearly interpolated in between. This time dependent current density is fed into

the charge breeding model. Together with a sixth vertical scaling parameter, these values are optimised with the help of an ordinary least-squares method. The optimised parameter set provides an approximate time evolution of the effective current density as well as a scaling factor for the number of ions. For the analysis the data set has been normalised for the accumulation time in REXTRAP (proportional to the total injected ion count). As previously, the assumed ion current error is  $0.1 \text{ pA} + 5\%$  of the measured signal.

A lot of uncertainty remains in this model due to the insufficient knowledge about exact ionisation cross sections. To account for this uncertainty, the current density fits were repeated in a Monte Carlo fashion with randomised cross sections. Two sources of uncertainty were included. Firstly, the exact electron energy was sampled uniformly from a  $\pm 100 \text{ eV}$  interval around the space charge corrected experimental beam energy. The space charge correction for a  $6 \text{ keV}$ ,  $200 \text{ mA}$  ( $300 \text{ mA}$ ) beam with a radius of  $187 \text{ }\mu\text{m}$  inside an  $r_{\text{DT}} = 5 \text{ mm}$  drift tube amounts to  $305 \text{ V}$  ( $464 \text{ V}$ ), where  $40 \text{ V}$  ( $61 \text{ V}$ ) fall into the electron beam itself. The exact beam energy can imply large cross section variations for charge states with ionisation energies on the same order of magnitude as the beam energy. Secondly, the ionisation cross sections have been multiplied with random weights between  $0.7$  and  $1.3$  to account for the approximate errors reported by Lotz for his cross section model [31]. Every fit was repeated 200 times with shuffled cross sections and beam energy. Average charge state evolutions and standard deviations of the repeated runs have been computed to yield the final result.

**Results** With the method described above we have treated charge state spectra time series of  ${}^7\text{Li}$ ,  ${}^{23}\text{Na}$ ,  ${}^{39}\text{K}$ , and  ${}^{152}\text{Sm}$  (injected as singly charged ions), as well as  ${}^{22}\text{Ne}$  and  ${}^{129}\text{Xe}$  (released as neutral gases).

The current density fitting method is illustrated in Figure 4.24a, showing the example of sodium charge bred in a  $300 \text{ mA}$  electron beam. In the upper plot, the scatter points and error bars are the measured and normalised ion currents. The average and standard deviation of the Monte Carlo fitting results are reflected by the solid curves and the surrounding colour bands. A good agreement between measurement and simulation result can be observed. The lower plot shows the corresponding values of the fitted effective current density at each of the selected support points.

The data for all element and beam current combinations was analysed as shown for the example of sodium. The collective reconstructed current densities for all experiments are shown in Figure 4.24b. A large range of effective current densities is visible in the upper plot, ranging from  $100 \text{ A/cm}^2$  all the way up to  $800 \text{ A/cm}^2$ . In the lower plot the corresponding effective electron beam radii  $r_{\text{eff}} = \sqrt{I_e/\pi j_{\text{eff}}}$  are displayed. This presentation eliminates the actual beam current from the equation, which facilitates the comparison of the behaviour under different conditions. Clearly, the curves corresponding to equal elements show a good agreement with

each other in this normalised plot. Compared to that, clear differences remain between separate elements. All curves share a decreasing trend for the effective current density as the breeding time increases.

A closer look at the current densities also reveals a mass trend. Figure 4.25 contains a summary of effective current densities recorded for the 200 mA case. Here, the data points and their error bars correspond to averages over the five sampled values of the fitted current density. There is a very clear trend towards higher effective current densities for elements with a higher proton count  $Z$ . Additionally, the two gas injected species neon and xenon, appear to experience higher values than ions of similar mass that were injected from REXTRAP.

Charge spectra have been recorded for  $^{39}\text{K}$  ions at particularly short breeding times, recording even the lowest charge states in order to increase the sensitivity to effects linked to ion injection. This data is shown in Figure 4.26 alongside a simulated charge state evolution assuming a constant current density of  $200\text{ A/cm}^2$ . The experimental data features a prominent amplitude step at the  $8+$  to  $9+$  transition, which is not reproduced in the simulation output.

**Discussion** The result of the fitting procedure provided in Figure 4.24a demonstrate the general ability of the model to reproduce the experimental data. This is despite the strong simplifications of the model compared to the real conditions. The good agreement between data and model increases the confidence that the fitted current densities provide a good estimation of the practical effective current density.

Nevertheless, it remains difficult to deduce the actual current density of the electron beam from our results. Here, the most severe limitation is the lack of knowledge about the true overlap between electron beam and ions. In theory, the effective current density should be lower than the true current density, if a uniform beam profile is assumed. This could lead to an underestimation of the actual current density. Opposed to that the uncertainty about the exact value of the ionisation cross sections can affect the extracted current density value in either direction.

Evidence for both of these effects can be found in the charge state evolution of  $^{39}\text{K}$  in Figure 4.26. Compared to the predictions of the simulation, the lower charge states linger around significantly longer than expected. A likely explanation for this behaviour is a poor overlap of the injected  $1+$  ions with the electron beam. This will significantly reduce the ionisation rate in low charge states and the situation is better described as slow injection of singly charged ions into the electron beam over an extended amount of time. As new ions are provided over a range of time, the low charge states decay slower than they should. Besides that, one can observe a prominent step in amplitude at the  $8+$  to  $9+$  transition. Similar data has also recently been recorded for a thermal plasma in an ECR charge breeder where the same jump is observed [126]. Such steps can be caused by an abrupt increase in ionisation cross section, as is typical for

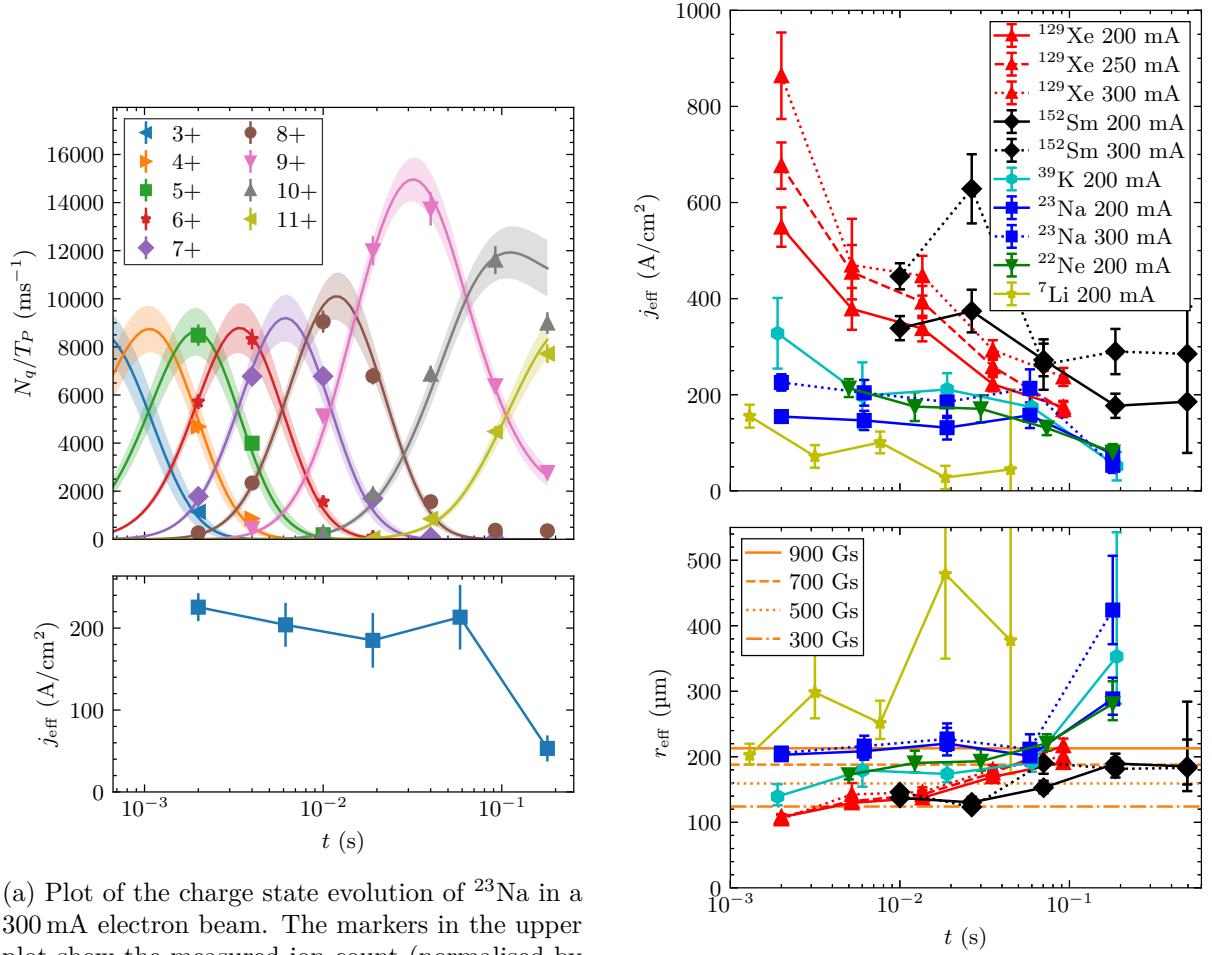


Figure 4.24: Results of the current density fitting method.

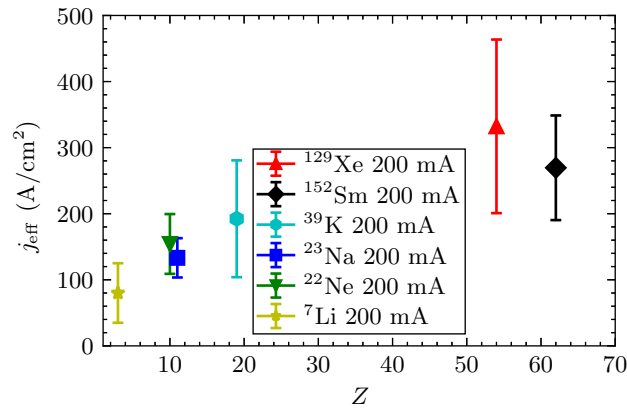


Figure 4.25: Plot of the range of deduced current densities for a 200 mA beam as a function of the nuclear charge. The markers and error bars show the average and standard deviation of the values presented in Figure 4.24b, respectively. Figure reproduced from Ref. [II].

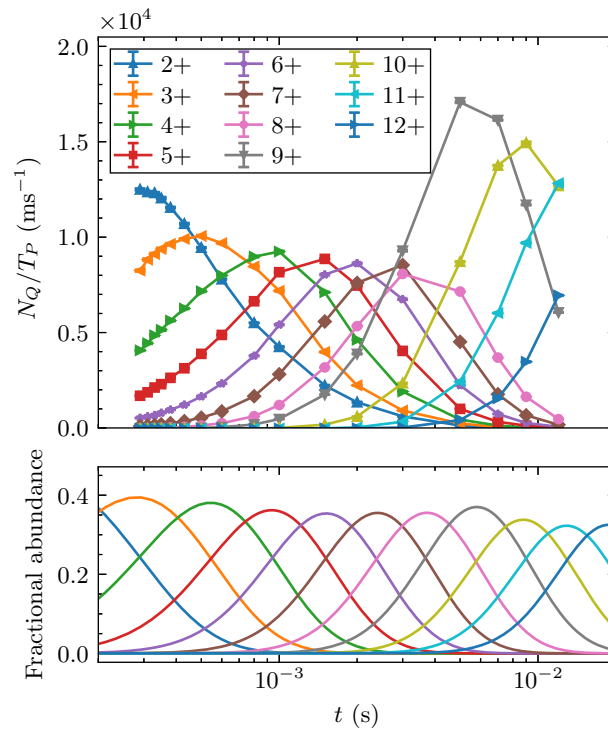


Figure 4.26: Plot of the charge state evolution of  $^{39}\text{K}$  for very short breeding times at a beam current of 200 mA. The upper plot shows data recorded at REXEBIS, the lower plot contains the result of a basic charge breeding simulation with an assumed current density of 200 A/cm<sup>2</sup>. Figure reproduced from Ref. [II].

closed shell configurations like  $K^{9+}$ . However, the simulation fails to reproduce the severity of this effect for potassium, which points to the Lotz formula being incapable of correctly modelling the ionisation cross sections for the present parameters. As visible in Figure 4.24a, the He-like shell closure of sodium does not present the same issues, underlining that the Lotz model does not generally present such large deviations.

The lower plot of Figure 4.24b contains reference lines indicating the theoretical electron beam radii for various cathode flux densities. At REXEBIS, the gun was installed in cathode field of 70 mT, with the error due to axial misalignment expected to be smaller than  $\pm 5$  mT. Effective radii exceeding the expected value are easily explained by a non-optimal overlap of ions and electrons. Ions outside the electron beam will not experience electron impact ionisation, leading to a reduction of the effective current density. Vice versa, this explanation is not applicable, since a reduction of the ion cloud radius, cannot push the apparent current density beyond that of the electron beam. Therefore, one would expect that a minimum effective radius emerges from the fitted data, which approximately agrees with the Herrmann predictions.

The existence of effective current densities significantly exceeding the theoretical maximum can hint at a non-uniform electron beam profile. The central current density of a bell shaped density profile may locally exceed the average current density of a uniform beam. If ions are constrained to sufficiently small radii they can truly witness an inflated current density.

The mass trend of the current density, cf. Figure 4.25, is expected as heavier, higher charged ions are confined more strongly to the electron beam. In the case of a bell-shaped beam, a sufficiently compressed ion cloud can benefit from the central current density, leading to apparent overlap factors larger than unity. The importance of a good overlap is further illustrated by xenon and neon that were leaking into the electron beam as a neutral gas. Since these ions are created within the electron beam their overlap factor is high right from the beginning, whereas externally injected ions may have to undergo one or more ionisations until the overlap with the electron beam improves. Compared to the injected ions, the gas species appear to have a slightly higher effective current density than close mass neighbours, which is coherent with the preceding explanation. The extremely high initial current densities for xenon may have been caused by the difficulty to define an accurate starting time for breeding from injected gas, generating additional uncertainty for short breeding times. Ions created before the nominal start of the charge breeding cycle will artificially inflate the average charge state, but their contribution becomes less important as time passes and many more ions are created.

The results of this analysis do not allow us to announce a definitive current density for the electron beam. However, paying respect to the clustering of values in Figure 4.24b, one may assume that the true beam radius is in the range of 150 to 190  $\mu\text{m}$ . This corresponds to a range of current densities from 176 to 283  $\text{A}/\text{cm}^2$  for a 200 mA electron beam, and from 265 to 424  $\text{A}/\text{cm}^2$  for a current of 300 mA. These values significantly exceed the current densities predicted in the

design simulations in Section 4.2.2. The practical charge breeding performance of an EBIS is determined by the current density of the electron beam, but also by its exact profile, the ion injection conditions, and thermal dynamics of the ion cloud. The effective current densities determined here provide a useful number of merit for performance comparisons.

#### 4.2.5.5 Axial energy distribution survey

In an attempt to provide more context to the current density results, the axial energy distribution of ions in REXEBIS was measured across a wide range of elements, charge states and breeding times. The axial energy distribution can provide some insight into the ion temperature, which is in turn expected to play a crucial role in determining the ion overlap with the electron beam. Whereas cold ions with small kinetic energy are well confined by the beam's space charge well, hotter ions can move far away from the electron beam and even leave it entirely. As outlined in Chapter 3, the main contributors (ignoring instabilities) to the energy balance in an EBIS are Spitzer (or Coulomb) heating, ionisation heating, and evaporative cooling. While we cannot measure them independently, recording the ion temperature allows for some consistency checks and can provide additional insight into the dynamics of the effective current density.

**Methods** The axial energy spectra were recorded with a method that had previously been implemented at REXEBIS in the context of slow ion extraction campaigns [23]. Conventionally, ions are extracted from REXEBIS by dropping the outer barrier tube from 1.3 kV to EBIS platform ground. Driven by their axial momentum the ions leave the EBIS as a bunch with a length of less than 100  $\mu\text{s}$ . To record the axial energy distribution the outer barrier was dropped to an intermediate voltage level for 0.5 ms, allowing only ions with sufficient axial momentum or energy to escape the trap. Subsequently, the trap was fully opened to evacuate all ions. In this measurement Faraday cup FC4 was gated to only record the ion current from the intermediate spill, such that the signal level is proportional to the number of ions with an energy exceeding the current intermediate barrier voltage. By scanning the intermediate voltage over many charge breeding cycles, an integrated spectrum is recorded. It should be noted that the energy acceptance of the REX separator magnet is sufficiently large to ensure transmission of all off momentum particles in this measurement, as this energy spread is inherently found in any bunch extracted from the EBIS under conventional operating conditions.

In order to extract quantifiable information from these spectra they were assigned characteristic temperatures by fitting theoretical energy distributions to the experimental data. Here, we use the energy distribution of particles obeying a Maxwell-Boltzmann distribution which is described by a Gamma( $k = n_D/2, \theta = k_B T$ ) distribution, where  $n_D$  is the number of degrees of freedom. The results presented below have been obtained for  $n_D = 3$  which shows a clearly superior goodness of fit over the  $n_D = 1$  case. A possible choice of  $n_D = 5$  is briefly refuted in

the discussion section.

For the axial energy measurements the ion escape current  $I_{\text{esc}}$  over the intermediate barrier is presented as a function of the barrier voltage  $U_B$ , such that it corresponds to the survival function  $S$  of the energy distribution [127]

$$I_{\text{esc}} = C \cdot S_{\text{Gamma}(k=n_D/2, \theta=k_B T)}(E) \quad (4.14)$$

$$= C \cdot \left[ 1 - \frac{1}{\Gamma(3/2)} \gamma \left( 3/2, \frac{E}{k_B T} \right) \right], \quad (4.15)$$

where

$$E = q(U_B - 700 \text{ V}) - E_0 \quad (4.16)$$

$$= q(U_B - 700 \text{ V} - U_0). \quad (4.17)$$

Here,  $\Gamma$  and  $\gamma$  denote the conventional and incomplete gamma functions, respectively.  $C$  is a scaling factor corresponding to the total current for a completely lowered barrier. The ion energy  $E$  depends on the charge of the ion as well as the barrier voltage with respect to the 700 V bias of the central trap drift tubes. An additional offset in the form of  $E_0$  or  $U_0$  was introduced to account for uncertainties in the exact drift tube voltages or non-thermal energy offsets. This function was fitted with a least-squares methods to every data set in order to obtain the best fit values for  $T$ ,  $C$  and  $E_0$  ( $U_0$ ).

The ion temperatures obtained in this way become more meaningful when they are related to the charge state and the potential well of the electron beam. In this manner the temperature is turned into a required equivalent trapping voltage that can be directly compared across charge states and elements. The potential well within the beam can be computed with the help of Equation 2.28, and – as stated above – amounts to approximately 40 (60 V) for a 200 mA (300 mA) beam.

**Results** For the axial energy studies, energy spectra of various elements have been recorded and analysed for a selection of charge states and breeding times. Figure 4.27 contains three typical examples of such energy distributions for  $\text{Sm}^{44+}$  in a 300 mA electron beam, together with the fitted 3D Maxwell-Boltzmann survival functions. Since the signal amplitude, corresponding to the total ion current, is of little interest for the energy studies, the data has been normalised by the fitted amplitude.

Information about the ion kinetic energy is obtained from the fitted values for  $E_0$  and  $k_B T$ . An example of the evolution of these parameters for  $^{152}\text{Sm}$  charge bred with a 300 mA electron beam is provided in Figure 4.28a. As expected the temperature is observed to grow over time, and this trend is confirmed in every data set recorded during the commissioning campaign. The

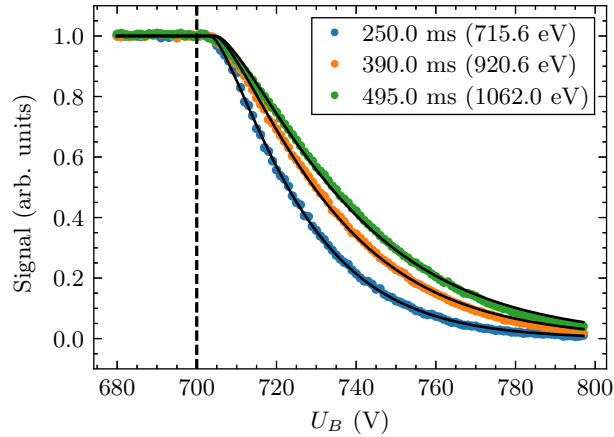


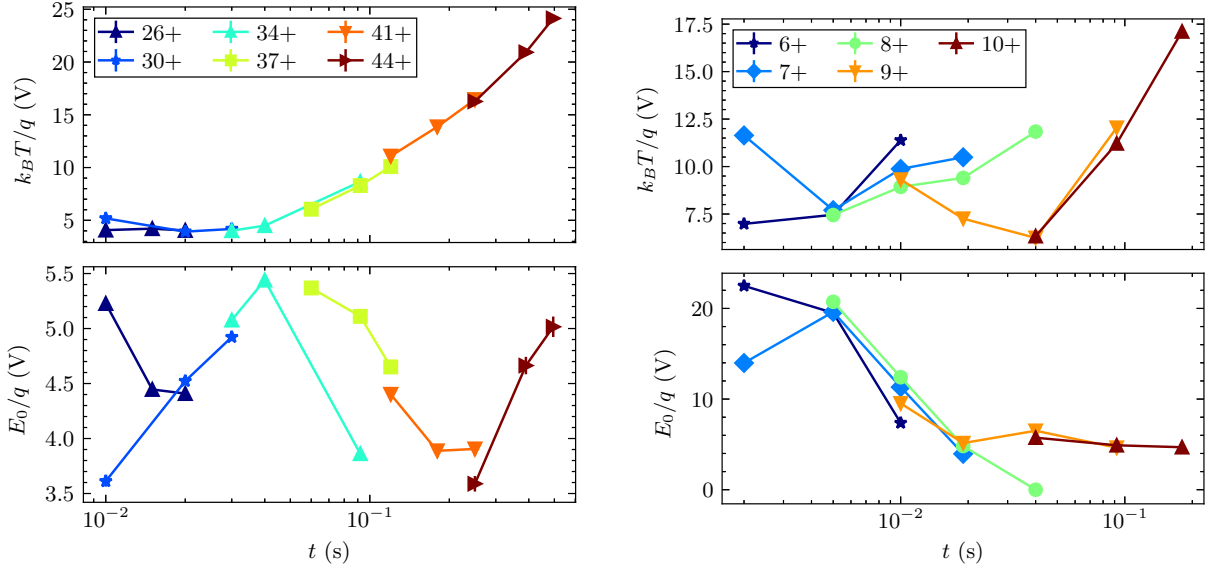
Figure 4.27: Example measurement of the axial energy distribution. The data shown here reflects the cumulative energy distribution of  $^{152}\text{Sm}^{44+}$  ions in a 300 mA electron beam for increasing breeding times. The black curves represent best fits of a Maxwell-Boltzmann energy distribution with 3 degrees of freedom; the best fit temperature is indicated in the legend. Figure reproduced from Ref. [II].

temperature is presented in its charge-normalised form such that it can be interpreted as an equivalent required holding voltage and provides better comparability between charge states.

With the same kind of charge-normalisation  $U_0 = E_0/q$  fluctuates in the range of 3 to 6 V. All but one dataset share this kind of behaviour for the offset energy. As can be seen in Figure 4.28b, the offset voltage for Na ions decreases from a value of more than 20 V at 2 ms ions before settling in the 3 to 6 V range after approximately 20 ms.

Figure 4.29 contains a collection of the temperature evolutions reconstructed for all recorded datasets. The temperature has been averaged over all measured charge states at a given breeding time, the error bars indicate the standard deviation across different charge states. Since neighbouring charge states were generally found to follow similar temperature evolutions, the temperature spread at any given time is not very large.

The upper plot of Figure 4.29 contains the temperatures fitted to the different measurements. The black curves provide a comparison of the temperature evolution for samarium ions exposed to two different electron beam currents. For sodium, one blue curve displays the temperature evolution in a conventional charge breeding set up, whereas the other curve contains the temperature evolution of a run in which xenon gas had accidentally been injected into the trapping region while processing the sodium ions. The sodium temperatures clearly evolve in unison at first, but after approximately 20 ms the temperature of the xenon mixture grows significantly quicker than that of the pure sodium curve. The green curve shows neon, representing a gas injected ion species. It starts out at a significantly lower temperature before approaching the evolution of the similar mass sodium ions.



(a)  $^{152}\text{Sm}$  ions in a 300 mA electron beam. Figure reproduced from Ref. [II].

(b)  $^{23}\text{Na}$  ions in a 200 mA electron beam. Figure reproduced from Ref. [II].

Figure 4.28: Plot of the best fit values for the ion temperature and energy offset. All values have been normalised by the charge state to yield more comparable equivalent voltages.

In the lower plot the temperatures have been normalised by the ion charge and by the depth of the electron beam space charge well for their respective beam currents. This compares the temperature to the ability of the electron beam to confine them. In this representation, the samarium curves follow each other closely. Relative to their charge, the temperature of the lighter sodium and neon ions is greater than that of samarium.

**Discussion** The increasing trend of the temperature in all measurements agrees with the notion that various heating processes constantly add heat to the ion cloud. Due to the thermal coupling of ions affected by different heating mechanisms to varying degrees, a proper extraction of isolated heating rates from the temperature evolution is not possible. However, we have compared the experimentally observed heating rates to the Spitzer heating rate as defined in Equation 3.29 as a sanity check.

For samarium the experimentally determined heating rates were smaller than the theoretical predictions by approximately 0 to 80 %. As a heavy ion, samarium benefits from cooling through collisions with lighter ions, which may explain this difference. The opposite behaviour is observed for neon and sodium; their measured heating rates partially exceeded the Spitzer rate by a factor of up to 3. Since these are relatively light ions, they are prone to suffer heat transfer from heavier ions, which are themselves more susceptible to heating. Moreover, ionisation heating, cf. Section 3.3.2.2, has a higher relative impact on lowly charged ions and can contribute to a

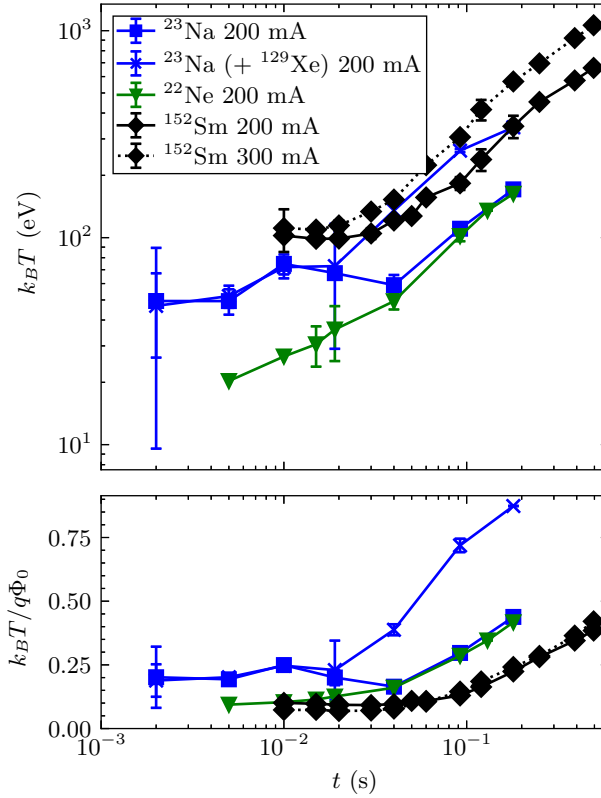


Figure 4.29: (Top) Plot comparing the ion temperature evolution in various charge breeding scenarios. Information about the element and electron beam current is provided in the legend. Every data point and its error bars represent the average and standard deviation of the temperature over several charge states at a given breeding time. (Bottom) The temperature has been rescaled by the charge  $q$  and the depth of the electron beam space charge well  $\Phi_0$ . Figure reproduced from Ref. [II].

fast temperature increase.

The equivalent holding voltage  $k_B T/q$  was smaller than 40 V in all experiments. This should be compared to the axial trap depth during the charge breeding cycle of 600 V and to the space charge depression created by the electron beam which typically exceeds 300 V. Under these circumstances it is justified to speak of a deep trapping potential, where thermal ion losses from the trap and hence evaporative cooling are expected to be largely suppressed. This explanation for a good ion confinement agrees well with the recorded EBIS efficiency that was found to be mostly constant over time.

Some interesting information can also be extracted from the offset energy  $E_0$  or voltage  $U_0$ . The widely observed fluctuation of  $U_0$  in the range of 3 to 6 V, is assumed to be caused by the analogue controlled power supplies used to bias the drift tubes. These can create small offsets and fluctuations between neighbouring drift tubes and appear to shift the energy distribution.

Currell and Fussmann presented the idea that the radial potential of the electron beam would introduce additional degrees of freedom, particularly for colder ions [28, 65]. Since the energy distribution is dominated by the exponential tail, the goodness of fit does not clearly favour a three or five dimensional model. When attempting to fit the energy distribution with an  $n_D = 5$  distribution,  $U_0$  would consistently show a decreasing trend over time. No physical explanation for this phenomenon comes to mind, as trap compensation by positive ion charges should act in the opposite direction. Therefore, it was decided to perform the fits with  $n_D = 3$  which results in the presented narrowly scattered values. It is important to note that this is no evidence for the actual dimensionality inside the trapping region, but that we find a 3D distribution to provide the best description of the escaping ions. Additional degrees of freedom that do not efficiently contribute to axial ion escape can still exist inside the EBIS.

The rapidly decaying offset energy observed during the  $^{23}\text{Na}$  measurement, cf. Figure 4.28b, can be linked to the ion injection process. Ions are conventionally injected with an excess energy of 200 to 300 eV, which requires some time to redistribute, especially when collision rates are low in a dilute plasma. This effect can also help to explain the early charge state evolution of potassium as shown in Figure 4.26. Since excess energy allows ions to leave the electron beam the initial overlap of ions and electron beam is poor, leading to the observed staggered launch of the ionisation chain.

Similarly, excess injection energy can explain the differences between the  $^{22}\text{Ne}$  and  $^{23}\text{Na}$  curves. As ions with almost identical mass and nuclear charge, one would expect them to behave similarly. While this is the case for longer breeding times, the neon temperature is significantly smaller initially. Since neon ions are created from a room temperature neutral gas inside the volume of the electron beam, they start out with a smaller initial kinetic energy than sodium ions injected from the outside. Once the extra energy carried by the sodium ions has thermalised and shrunk in significance compared to the total energy, the temperature evolution

of neon and sodium are almost indistinguishable. The accelerated heating of Na ions when mixed with xenon gas was shown in Figure 4.29; it supports the theory of energy transfer from strongly heated heavy ions to light ions.

The axial energy spectra were recorded with the goal of linking them to the observed dynamics of the effective current density. In line with the discussion in Section 3.2, the values shown in the lower plot of Figure 4.29 are expected to reflect the overlap of the ion cloud with the electron beam. Ignoring effects of the magnetic field, ions are expected to follow a Boltzmann distribution  $\sim \exp(q\Phi/k_B T)$  inside the space charge well. On a qualitative level, the increasing temperature is consistent with the observed decline of the effective current density. As ions are heated and driven out of the electron beam their ionisation is slowed down. Yet, we have not been successful in developing an electron beam model that can link the measurements in a quantitative manner. The fundamental difficulty is illustrated by neon and samarium. Both elements initially display very similar initial confinement factors. If the Boltzmann distribution model were correct, this should lead to them experiencing the same effective current density, regardless of the exact density profile of the electron beam. This is however not confirmed by the results of the current density reconstruction.

### 4.3 Conclusion

In this chapter a novel kind of electron gun for use in an EBIS charge breeder has been presented. Picking up earlier work started at BNL, charged particle tracking simulations have been employed to demonstrate the technique of using a short range modulation of the magnetic field to dampen radial oscillation of an electron beam. When extracting high currents from a small cathode located in a weak residual magnetic field, the space charge forces drive the beam apart, triggering an oscillation of the beam cross section along the magnetic field axis. A nonadiabatic field modulation can help to transfer an oscillating beam to its natural equilibrium radius, where focusing and defocusing forces are balanced, and the beam ripple is almost entirely eliminated.

The concept of nonadiabatic damping has been explored for electron beams in uniform magnetic fields in simulations. Both passive and active elements can in theory be used to provide the magnetic field modulation, and importantly it was shown that these elements can in principle be located further downstream as long as the beam remains sufficiently coherent before passing the nonadiabatic element. Under the right conditions the beam changes from a self-intersecting cyclotron oscillation to a more rigid beam rotation at a constant radius, as was shown in Figure 4.5.

In the next step a new electron gun, employing the nonadiabatic damping technique, was designed in order to upgrade the existing REXEBIS charge breeder. To our knowledge this is the first operational use of a nonadiabatic magnetically damped beam in an ion charge breeder,

that employs a dedicated adjustable damping element. The electron gun design is based on a Pierce geometry and has a baseline design current of 500 mA, extracted from a cathode of radius 1 mm which is located in a magnetic fringe field of 70 mT. During the commissioning campaign the gun perveance was measured to  $0.87 \mu\text{A}/\text{V}^{3/2}$ , which slightly exceeds the value predicted in simulations. However, emission insufficiencies of the IrCe cathode lead to the requirement for excessive heating power. For this reason the current was practically limited to 300 mA, but currents of up to 420 mA have been transmitted through the EBIS successfully for short periods.

As pointed out from the beginning, the high efficiency of the whole REX stage is crucial to providing the best possible conditions to the ISOLDE user community. In the context of the EBIS, both injection and extraction of ions, as well as their long term containment during the charge breeding, can suffer from losses. The data recorded in the commissioning phase, demonstrates an excellent efficiency of the upgraded REXEBIS, regardless of the time interval and despite the limited current provided by the IrCe cathode. Particularly high single charge state efficiencies have been recorded in electronic shell closure configurations and for very highly charged thallium ions, due to their increasing ionisation energy which is presenting an eventual limit to the ionisation chain.

The beam purity has been assessed with the help of wide range  $A/Q$  spectra characterising the ion beam composition as well as a careful search for ions that could be traced back to the cathode alloy. With the help of the time evolution of the  $A/Q$  spectra, approximate residual atom densities in the trapping region of the EBIS have been reconstructed. The rate of neutral gas ionisation was found to be comparable to that observed with the original electron gun, i.e. no deterioration has occurred. Ir and Ce ion rates were found to be at just a few particles per second behind the accelerating RFQ, which presents a largely negligible level of contamination.

In order to quantify the charge breeding capabilities of the new electron beam, effective current densities have been determined from measured charge state spectra by fitting them with the results of charge breeding simulations. The fitted current densities cover a large range, and generally show a decreasing trend as the breeding time increases, cf. Figure 4.24b. A beneficial effective current density trend can be identified for heavier elements. Due to the wide range of effective current densities, a confident estimation of the true current density of the electron beam is impossible. However, clustering of the data suggests an average beam radius of approximately  $(170 \pm 20) \mu\text{m}$ . The observation of apparent current densities exceeding the theoretical value significantly, suggests a non-uniform electron beam profile with an increased current density at its centre that is preferentially experienced by heavier, more highly charged ions. The fitting model is also sensitive to the assumed ionisation cross sections. As for example the potassium data suggests, the ionisation cross sections predicted by the Lotz formula are not always sufficiently accurate, distorting the simulated charge state spectrum with respect to reality.

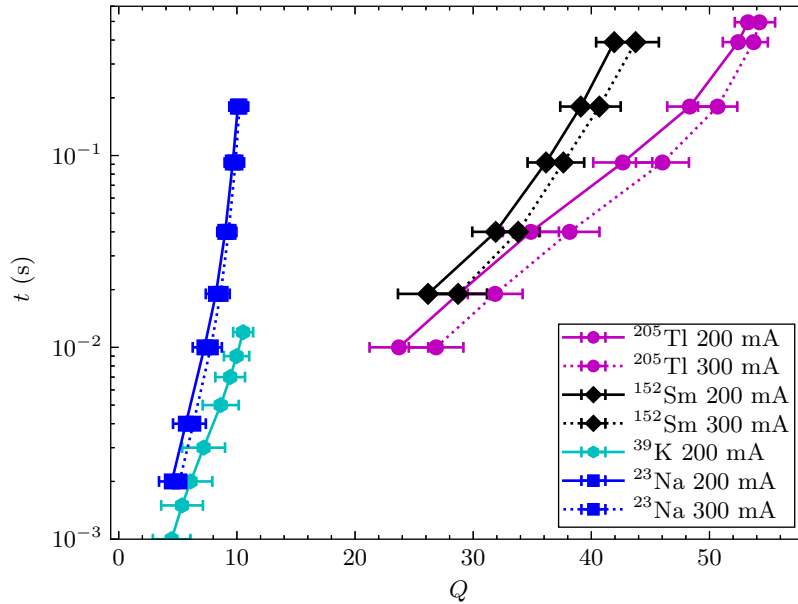


Figure 4.30: Plot of the charge state evolution of sodium, potassium, samarium, and thallium for electron beam currents of 200 mA and 300 mA. The data points and error bars represent the average and standard deviation of the charge state distribution at a given breeding time. Figure reproduced from Ref. [II].

The charge breeding performance for a number of elements is illustrated in Figure 4.30. Particularly the heavier elements display significant improvements in required charge breeding time over the original REXEBIS setup. This addresses the request for shorter charge breeding times and increased repetition rate. Since the end of the gun commissioning campaign, the first radioactive beam to be charge bred with REXEBIS was  $^{30}\text{Mg}^{11+}$  ions produced with an electron beam of 200 mA in 80 ms.

Axial energy scans have been carried out to estimate the ion temperature inside REXEBIS and to provide more context to the current density results. Fitting the recorded spectra with Maxwell-Boltzmann energy distributions showed excellent agreement and thus provides a procedure for assigning a temperature to the escaping ions. As expected the ion temperature increases over time; this is also qualitatively consistent with the reconstructed current densities, as hotter ions are expected to suffer from a worse overlap with the electron beam. Yet, we could not identify a model or mechanism that would support this correlation in a more quantitative fashion, as ions with similar normalised temperatures appear to experience notably different current densities.

The implied experimental heating rates are roughly comparable to those predicted by the Spitzer formula, which represents the most important heating mechanism for mid and highly charged ions. Furthermore, clear indications of energy transfer between ions were identified

(sodium / xenon mixture), and energy measurements suggest the prolonged existence of leftover injection energy (sodium vs. neon). Based on these initial findings it would be highly interesting to correlate the axial energy profiles with results of other independent methods such as e.g. x-ray emission spectrography. At present, REXEBIS does not permit such measurements as the machine geometry does not provide direct visual access to the trapping region.

As the beam current provided by the new electron gun was limited by cathode issues, there are plans to upgrade the gun with another cathode. A novel scandium-doped dispenser-type cathode is developed and promoted by Beijing University of Technology, that has previously been demonstrated to operate at high emission densities for an extended time [120]. An adapted cathode holder has been manufactured and is available for testing the new cathodes once the opportunity arises. Backed by the simulation results, it is expected that the new set up has the potential for operating at even higher current densities than presented in this work and future upgrades beyond the 500 mA at 70 mT baseline are in principle an option.



## CHAPTER 5

# MEDEGUN & TWINEBIS

Radiation therapy has become a valuable clinical tool, particularly in the field of cancer treatment. Owing to the characteristic well-defined stopping range of high energy ions in matter, i.e. the Bragg-peak phenomenon, ion beam therapy offers an option for particularly localised treatment. Studies suggest that certain cancer cells can be resilient against the irradiation with light ions like protons, but are more effectively treated with heavier projectiles as e.g. carbon nuclei [2, 128]. The size, complexity, and cost of the accelerators required to offer such therapy is often a prohibitive factor. There are proposals to develop linear accelerator based treatment facilities, which could offer a beneficial balance of treatment efficiency and cost, when compared to existing facilities [4, 22, 129]. Presently, there is a lack of suitable ion sources that could produce a beam of fully-stripped carbon ions in bunches of  $1 \cdot 10^8$  to  $1 \cdot 10^9$  ions with a length of  $\approx 1.5 \mu\text{s}$  at a repetition rate of 300 to 400 Hz, required by a treatment LINAC for efficient operation.

An EBIS is specialised in the production of highly charged ions and readily provides beam with pulse lengths on the microsecond scale, as the entire ion trap volume can be extracted at once by manipulating the axial trap potentials appropriately. The large ion production rates required for therapy exceed the capabilities of existing EBIS devices, but should be within reach if a sufficiently dense and intense electron beam can be provided [130]. This has been the motivation for the development of MEDeGUN, a Brillouin-type electron gun, that should provide a high current density ( $> 1 \text{ kA/cm}^2$ ) electron beam with parameters appropriate for operation in a medical context [88, 113].

This chapter presents the advances that were made in commissioning and characterising MEDeGUN at the TwinEBIS test stand. TwinEBIS, originally a close copy of REXEBIS, is a dedicated test bench for the development of EBIS charge breeders. It has been modified to accommodate a MEDeGUN prototype, in order to approach a proof-of-concept for an EBIS that serves as a high production-rate carbon ion source. This chapter contains a brief description of the test stand and the electron gun, as well as a selection of relevant experiments regarding the electron beam commissioning, and the charge breeding behaviour. Additionally, there is a sum-

mary of the design studies for a dedicated low energy ion beam line to be installed downstream of TwinEBIS, which is going to provide further instrumentation for the characterisation of ion beams, as well as preparing the injection into an accelerating RFQ that would present the next critical component in a LINAC treatment facility.

## 5.1 Description of MEDeGUN and the TwinEBIS test stand

All experiments concerning the operation of MEDeGUN were carried out at the TwinEBIS test stand. Initial electron beam tests were performed using just the EBIS itself, while charge breeding experiments saw ions extracted from the EBIS into a diagnostic line featuring a Faraday cup and a Time of Flight (TOF) ion spectrometer. This diagnostic setup presents the first step towards the installation of the full beamline described in the end of this chapter.

### 5.1.1 MEDeGUN

Driven by the charge breeding requirements for a treatment facility, it was decided to develop an electron gun that could provide electron beam current densities of  $\gtrsim 5 \text{ kA/cm}^2$  when compressed in a peak magnetic field of 5 T. Such an electron beam should in theory be able to provide fully stripped carbon ions at a repetition frequency of up to 400 Hz. Additionally, the electron beam needs to provide sufficient radial trapping capacity to confine approximately  $1 \cdot 10^9$  to  $1 \cdot 10^{10}$  positive charges. At the same time, the current emission density on the cathode should be kept at a minimum to maximise the cathode lifetime and reduce the necessity for interventions.

Balancing these constraints led to the definition of the MEDeGUN geometry, presented in Figure 5.1 [88, 113]. Its design is based on downscaled version of the so-called Magnicon gun [131], which was adapted slightly to increase the gun perveance to a value of  $1.0 \mu\text{A/V}^{3/2}$ . To obtain the most efficient beam compression, the gun is magnetically shielded and can generate an electron beam approaching the Brillouin density limit. The spherical gun is optimised to provide a strong electrostatic compression of the generated beam within the gun volume, before the beam is injected into the fringe-field of the EBIS main solenoid. The focal point is located 2 to 3 mm behind the anode aperture, to assure the electron beam is converging onto its waist when it enters the magnetic field.

Targeting an electron beam current of 1 A, the cathode was dimensioned to a radius of 6 mm (curvature radius 10.08 mm), which yields a cathode surface current density on the order of  $1 \text{ A/cm}^2$ . Such a low emission density allows operating the cathode at reasonably low temperatures of  $\approx 1300 \text{ K}$ , increasing their expected lifetime significantly. Assuming an electron beam of 1 A with an energy of 10 keV, one may estimate a Brillouin radius of  $r_B = 16.6 \mu\text{m}$  ( $41.5 \mu\text{m}$ ) in a focusing field of 5 T (2 T). Temperature effects inflate the actual beam radius to  $r_H = 53.3 \mu\text{m}$  ( $87.7 \mu\text{m}$ ). The heater coil inside the cathode can itself create a small axial magnetic field ex-

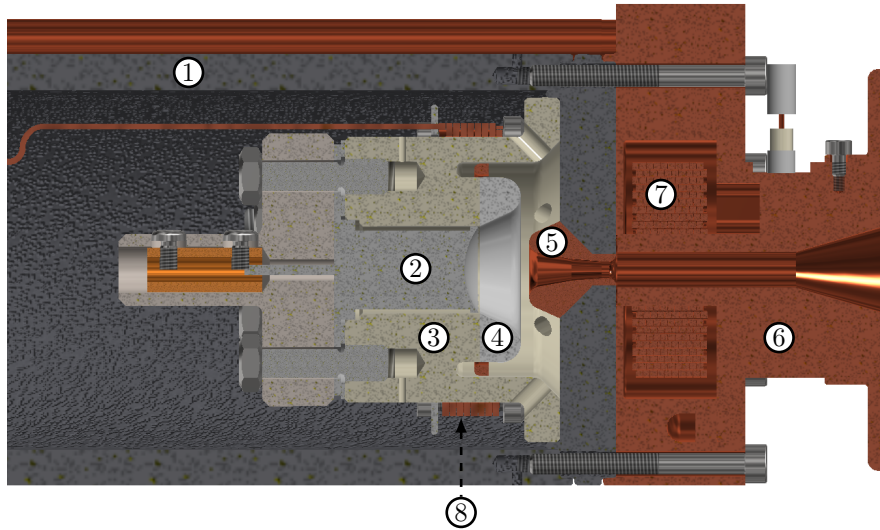


Figure 5.1: Overview of the MEDeGUN assembly. The numbers indicate: Iron shield (1), cathode (2), Shapal body (3), Wehnelt electrode (4), copper anode inset (5), anode extension (6), anode coil (7), and the cathode coil (8).

pected to amount to  $\leq 0.4$  mT under typical operating conditions [88]; this can further grow the beam radius to a value of  $64\ \mu\text{m}$  ( $104\ \mu\text{m}$ ). Under such conditions, the expected current density in the focal point of the electron gun is approximately  $87\ \text{A}/\text{cm}^2$ , and the beam should be injected into a residual magnetic field of about  $137\ \text{mT}$  to provide appropriate space charge balanced focusing at the handover point [88].

The MEDeGUN prototype assembly is illustrated in Figure 5.1. The gun is based on an M-type barium dispenser cathode fabricated by Heatwave Labs Inc [132]. It is inserted into a ceramic (Shapal) structure that mates with the anode plate which has appropriate mechanical registration features to assert that small mechanical tolerances are respected. Originally, the Wehnelt electrode was created by applying a thin coating of molybdenum to the front face of the Shapal structure. The ceramic was chosen both, for its good heat conductivity, and for having similar thermal expansion coefficients to the surrounding materials. This allows water cooling of the entire electron gun from the anode end. The anode plate is largely produced from ARMCO iron, and forms the cap of the iron shield. The anode electrode profile is machined into a small copper inset to reduce the risk of poisoning the cathode with sputtered iron ions. A small coil wound around the Shapal structure may be used to compensate residual magnetic fields created by the heating filament of the cathode which are expected to amount to a few  $0.1\ \text{mT}$ . A second coil located downstream of the anode allows adjustments of the initial magnetic field at the gun's focal point.

A first commissioning run performed prior to this work, had revealed significant damage to the coating forming the Wehnelt electrode and suggested some problems caused by trans-laminar

electrons emitted from the edge of the cathode [115]. Therefore, the coated Wehnelt electrode was replaced by a solid piece of molybdenum that was braised to a modified Shapal body. Using shims, the cathode was retracted approximately  $75\ \mu\text{m}$  into the Wehnelt to provide a better suppression of emission from the very edge of the cathode. Other than these modifications the mechanical layout remains largely identical to originally published concepts, and more detailed background information on the gun design may be found in Refs. [88, 113].

### 5.1.2 TwinEBIS

Due to its origin as a REXEBIS clone, TwinEBIS closely follows its mechanical design. An overview of the device is shown in Figure 5.2. The main solenoid is largely identical, featuring an iron shield, a 15 cm diameter warm bore, and a peak magnetic field of 2 T. Except for iron shields around the electron gun and collector, no further ferromagnetic materials are used inside the working volume of the EBIS.

MEDeGUN is mounted to its supporting flange on a long rigid arm. The flange is connected to the main vacuum structure through a flexible vacuum bellow, locked in place by three fine-threaded rods and nuts. By adjusting the length of the rods between the rigid parts of the vacuum structure, the electron gun can be moved with respect to the remainder of TwinEBIS. This allows fine adjustments of the gun position in operation, but also makes it possible to retract the gun and isolate it from the rest of the EBIS by closing a gate valve. The transverse position of the gun can be probed with the help of three mechanical fine-adjustable feed-throughs that short-circuit the otherwise isolated gun to ground when they make contact with the iron shield.

The water-cooled electron collector had to be adapted since the Brillouin beam produced by MEDeGUN is expected to display a faster radial expansion when exiting the solenoid than the immersed beams REXEBIS was originally designed for. Guided by simulations [88], the whole collector assembly including its iron shield, were pushed 2.5 cm closer towards the last drift tube compared to the REXEBIS reference. Within the iron shield, the secondary electron suppressor and the collector were moved several mm closer towards the last drift tube, to reduce the axial gaps between the electrodes, and avoid scraping of the expanding beam in the apertures.

The drift tube structure is manufactured from titanium and features a total of nine drift tubes with an internal radius of 5 mm. The lengths of the individual drift tubes are listed in Table 5.1. To improve the pumping speed the drift tubes are perforated and approximately 17 % transparent. All drift tubes can individually be biased to voltages of up to 3.0 kV. Specialised fast high voltage switches (Behlke GHTS-60) are installed to quickly pulse certain drift tubes (e.g. the outer trap barrier) between two bias levels with slew rates on the order of  $\text{kV}/\mu\text{s}$ . Alternatively, two precision high voltage amplifiers (HiVolt HA2B5-S) capable of voltages up to  $\pm 2000\ \text{V}$  with a driver current of up to 5 mA may be used to play arbitrary bias wave forms.

The first charge breeding experiments have been performed by introducing a working gas

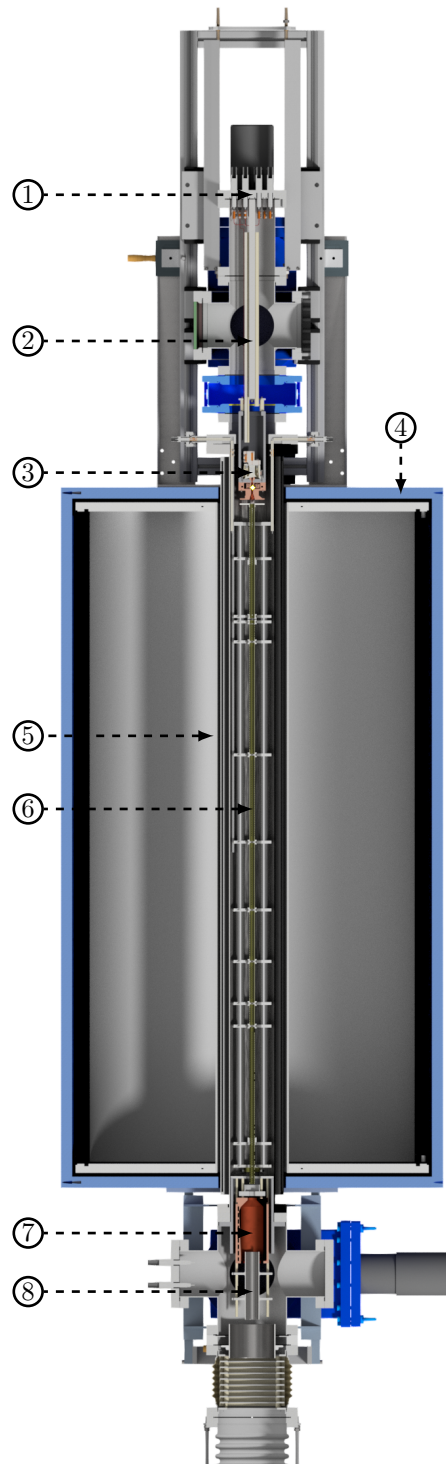


Figure 5.2: A schematic top view of TwinEBIS with installed MEDeGUN. The following elements are annotated: Gun mounting and feed-through flange (1), gun support arm (2), MEDeGUN (3), main magnetic shield (4), magnet bore / superconducting coil position (5), drift tube structure (6), collector (7), and the ion extractor (8).

Table 5.1: Length of the individual drift tubes in TwinEBIS listed from the electron gun towards the collector. Gaps between the drift tubes are approximately 2 mm wide.

Drift tube	Length (cm)
Gun side	25.4
Inner barrier	4.8
Trap 1	24.8
Trap 2	19.1
Trap 3	14.8
Trap 4	11.2
Trap 5	9.1
Outer barrier	4.8
Collector side	34.8

directly into the trap. For this purpose a primitive stainless steel feed line with an internal diameter of 4 mm was installed. Mounted parallel to the drift tubes at a distance of 2 cm, it runs from the high voltage feed-through flange of the drift tube structure on the gun side of the solenoid into the centre of the magnet. The last 2 cm of the pipe are bent towards the drift tubes at an angle of  $\approx 20^\circ$ . Gas can be released into this pipe through a needle valve that is fed from a small reservoir chamber equipped with a full-range vacuum gauge. Pressure simulations carried out with *Molflow* yield the expected pressure gradient inside the drift tube depending on the gas injection rate, an example is shown in Figure 5.3 [133, 134]. The molecular flow conductance of the gas injection line has been simulated to be  $\approx 0.0081/s$ , a value that is in good agreement with theoretical conductance models.

The backbone of the vacuum system are two turbo-molecular pumps located next to the gun and the collector. They are in turn connected to a backing pump supported by another turbo pump. Along the drift tube structure, metallic strips with a NEG powder pressed onto them aid in pumping the main working volume once they are activated during a vacuum bake-out. The pressures are reported by Penning gauges installed next to the gun and the collector. After a bake-out the vacuum pressure inside the EBIS is in the  $5 \cdot 10^{-11}$  mbar range, as long as the electron gun is not powered. During operation, the pressures climb into the  $1 \cdot 10^{-10}$  to  $1 \cdot 10^{-9}$  mbar range due to high temperatures in the gun and also the collector, and it may raise further if gas is injected into the trapping region. These values may not be an accurate representation of the pressure inside the trapping region, as there are many aperture restrictions impeding molecular flow towards the gauges. Before the installation of the ion diagnostic setup, during most of the electron beam commissioning experiments, the vacuum port at the collector side of TwinEBIS was closed with a vacuum window, that allowed visual access to the glowing cathode, such that its temperature could be measured using a pyrometer.

More information describing the original configuration of TwinEBIS may be found in Refs.

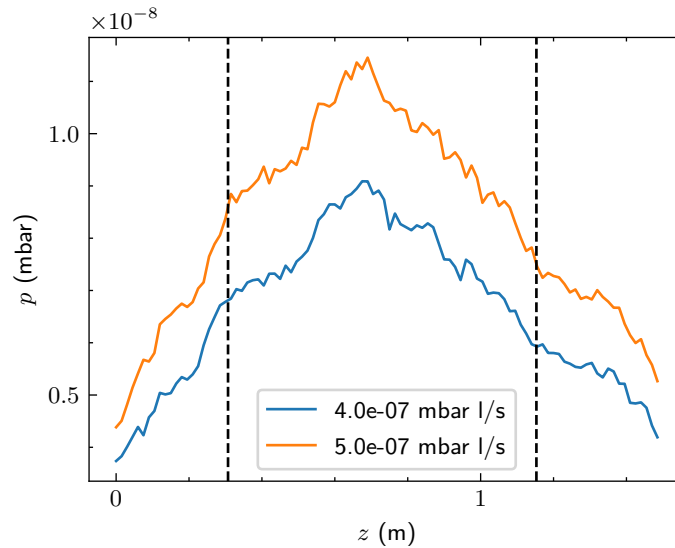


Figure 5.3: Pressure gradients (simulated with Molflow) for the injection of methane gas into the TwinEBIS trap volume, evaluated on the beam axis. The feed rates are given in the legend, the vertical dashed lines denote the axial extent of the drift tubes forming the ion trap. Data kindly provided by R. Taylor [134].

[88, 114].

### 5.1.3 Ion extraction and the Time of Flight spectrometer

After the initial electron beam commissioning tests, the TwinEBIS setup was extended to be able to analyse the generated ion beams. For the purpose of extracting ions into a dedicated beamline, the EBIS and all its supporting infrastructure are located inside a cage and electrically isolated from the laboratory earth with a conventional isolation transformer, cf. Figure 5.4. A single high voltage power supply (Heinzinger PNC 60000-3 pos) can then be used to bias the charge breeder setup with respect to the ion beamline which is tied to laboratory earth for easy and safe experimental access. The beamline is connected to the EBIS with a ceramic accelerating gap, as shown in Figure 5.5. To provide a uniform accelerating gradient the isolator houses ten evenly spaced stainless steel rings serially connected through  $10\text{ M}\Omega$  resistors. While the power supply is able to bias the EBIS by up to 60 kV, the physical isolation gaps and stand-offs of the setup are dimensioned for a maximum bias of 40 kV; during the commissioning experiments the actual accelerating voltage was typically in a range of 15 to 25 kV.

In this intermediate configuration, the ions would leave the extractor electrode with an energy of typically  $q_i \cdot 14\text{ keV}$ , and then be decelerated back to EBIS ground potential before entering the accelerating gap. Such a deceleration has the risk of causing a severe defocusing and blow-up of the ion beam. Therefore, an extender was installed on the extraction electrode to provide a more

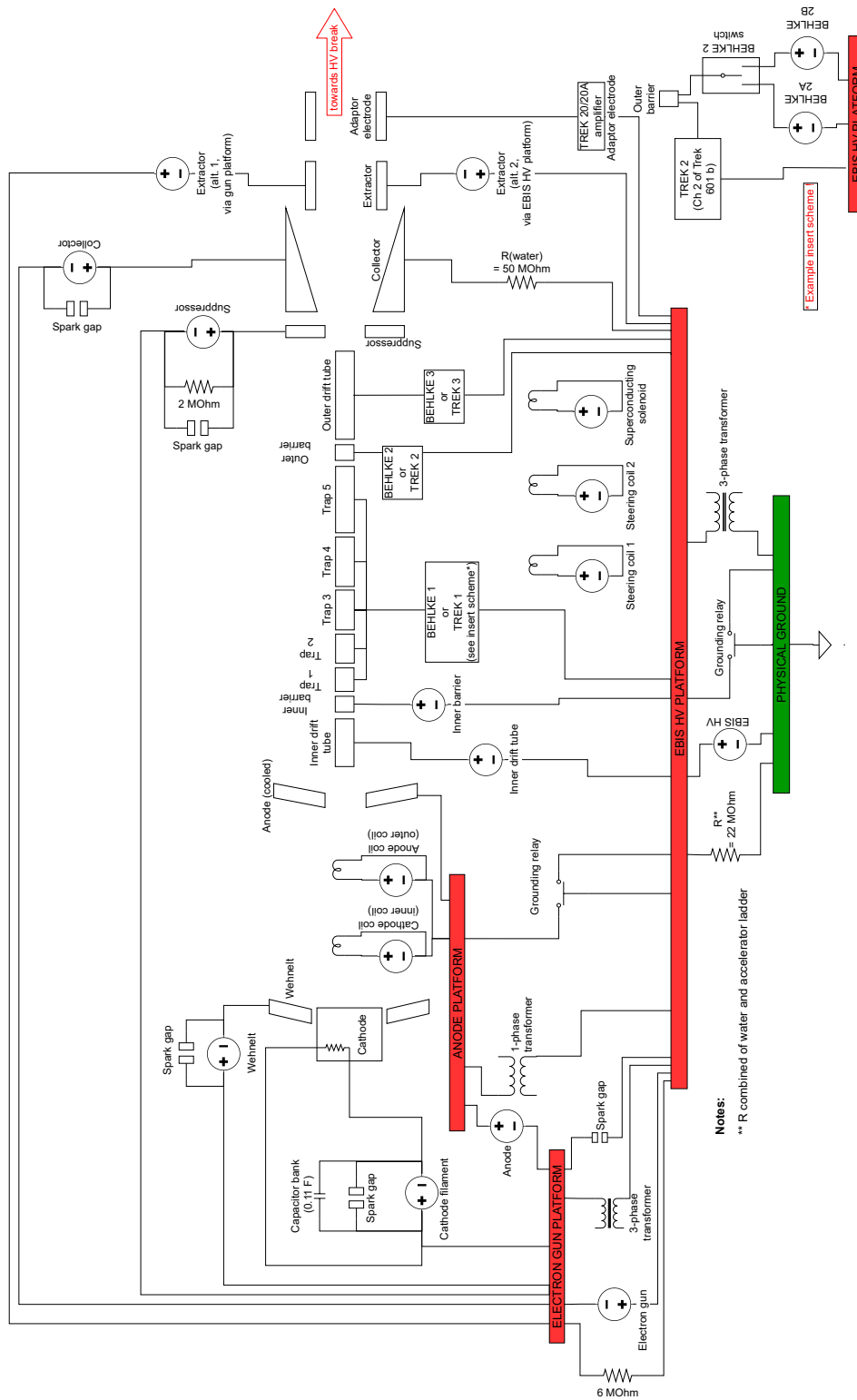


Figure 5.4: An overview of the high voltage platforms servicing TwinEBIS.

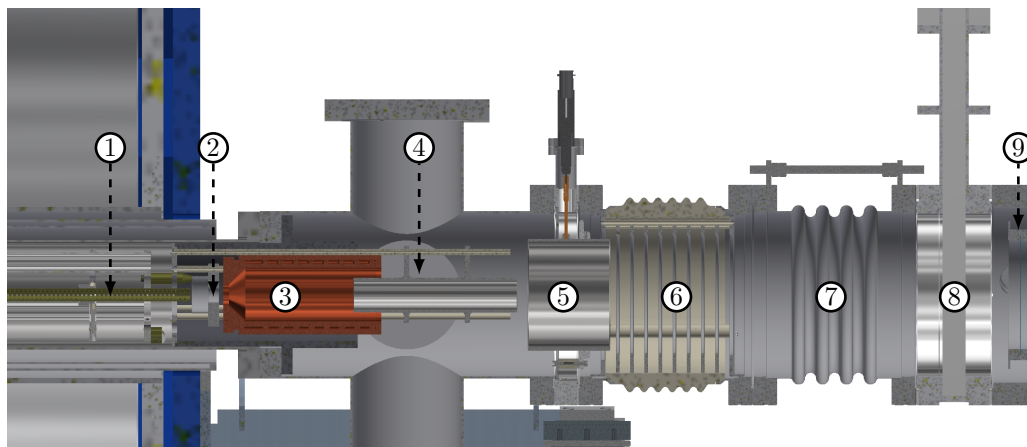


Figure 5.5: Illustration of the extraction section of the TwinEBIS setup. Visible are: Last drift tube (1), secondary electron suppressor (2), collector (3), ion extractor (4), adapter electrode (future design) (5), ceramic acceleration break with internal voltage ladder, vacuum bellow (7), gate valve (8), and the first gridded lens of the extraction line (9).

gentle transition by keeping the ions at the extractor potential for a longer time and shielding the field of the accelerating gap before releasing the ions into the final 5 cm of the accelerating gap. Here, the surrounding potential more closely matches typical energies of ions leaving the extractor electrode. Some initial experiments were however carried out without this extender, due to production delays. In the full ion beamline presented in Section 5.5, a dedicated adaptor electrode is foreseen to take over this task with even more fine grain control.

The accelerating gap is followed by a gridded electrostatic lens (cf. Section 5.5.4) for focusing the ion beam through a  $\approx 35$  cm drift space onto a Faraday cup, or the entrance to a time of flight spectrometer.

The Faraday cup consists of two isolated regions: the outer ring with a diameter of 10.5 cm is installed permanently and has a central opening of 2.5 cm diameter, while a central circular plate (paddle electrode) is located 0.5 cm downstream and can be retracted with the help of a pneumatic actuator, such that a focused ion beam may pass through the Faraday cup without being intercepted. Since the signals of both regions can be read out independently, this setup offers a comfortable way of asserting that the beam is appropriately focused. A suppressor electrode surrounds the Faraday cup, and is biased to  $\approx -800$  to  $-1000$  V, to make sure that ion beam current readings are not inflated by secondary electrons escaping from the electrodes of the Faraday cup. The signals are carried by low capacitance coaxial cables (60.0 pF/m, 75  $\Omega$ ) to reduce the  $RC$  time constant and measured via appropriate load resistors with the help of an oscilloscope.

**Time of Flight reflectron** If the beam passes through the central aperture of the Faraday cup, it can be analysed in a Time of Flight spectrometer (TOF). The spectrometer, depicted in Figure 5.6, is a so-called reflectron, as developed by Mamyrin et al. [135].

To fully benefit from the resolving power of the spectrometer, very short ion pulses on the ns timescale are required. Therefore, the beam enters the TOF through a Bradbury-Nielsen beam gate [136]. The gate consists of an array of channels formed by closely spaced parallel plates, where every other plate is biased with 1 kV. This causes a small deflection of ions passing the gate such that they get lost on the surrounding plates, hence blocking the beam from entering the spectrometer. A short high voltage pulse (generated by FIDTechnology FPG 1-0.1NMS) is then sent into the gate to compensate the DC bias, allowing a short pulse of ions to enter the TOF without being deflected. A fair amount of signal filtering is required to support electrode pulsing on this timescale without creating reflections and circuit ringing; a brief commissioning report [137] details the gate circuit, which supports pulse widths down to 6 ns.

After passing through the gate, the ion pulse may be gently deflected with a pair of diagonally bisected cylinder electrodes (as described in [15]), before entering the electrostatic mirror which characterises this type of TOF spectrometer. The mirror is formed by a set of 23 ring electrodes, configured with a resistor and capacitor ladder ( $5\text{ M}\Omega + 1\text{ nF}$  / gap). It should be noted that the first two rings of the mirror are both grounded which yields an effective mirror length of  $l_m \approx 33\text{ cm}$ ; the drift space ahead of the mirror has a length of  $l_d = 62\text{ cm}$ . A decelerating bias is applied to the final ring, which – by means of the resistor ladder – creates an electric field along the mirror that slows down the ions, and eventually forces them to turn around. By slightly tilting the mirror vertically, the reflected beam leaves the mirror with a small downwards angle where it hits a detector located in the same plane as the entrance gate.

The advantage of this geometry lies in the fact that it compensates well for an energy spread in the incoming beam, making use of so-called time focusing. Neglecting the vertical displacement, the time of flight from the gate to the detector can be written as

$$\Delta t = 2\sqrt{\frac{m_i}{q_i e}} \left( \frac{l_d}{\sqrt{2U_a}} + \frac{l_m \sqrt{2U_a}}{U_m} \right), \quad (5.1)$$

where  $U_a$  denotes the accelerating potential of the ion beam and  $U_m$  is the mirror bias voltage [135]. This formula illustrates how the time of flight is dispersed for different charge-to-mass ratios. Further, it is easily shown that

$$\frac{\partial}{\partial U_a} \Delta t \stackrel{!}{=} 0 \Rightarrow U_m = 2 \frac{l_m}{l_d} U_a. \quad (5.2)$$

This means that the time of flight is insensitive to the exact particle energy, as long as the mirror is tuned according to the nominal acceleration potential. At the test stand, ions are expected to

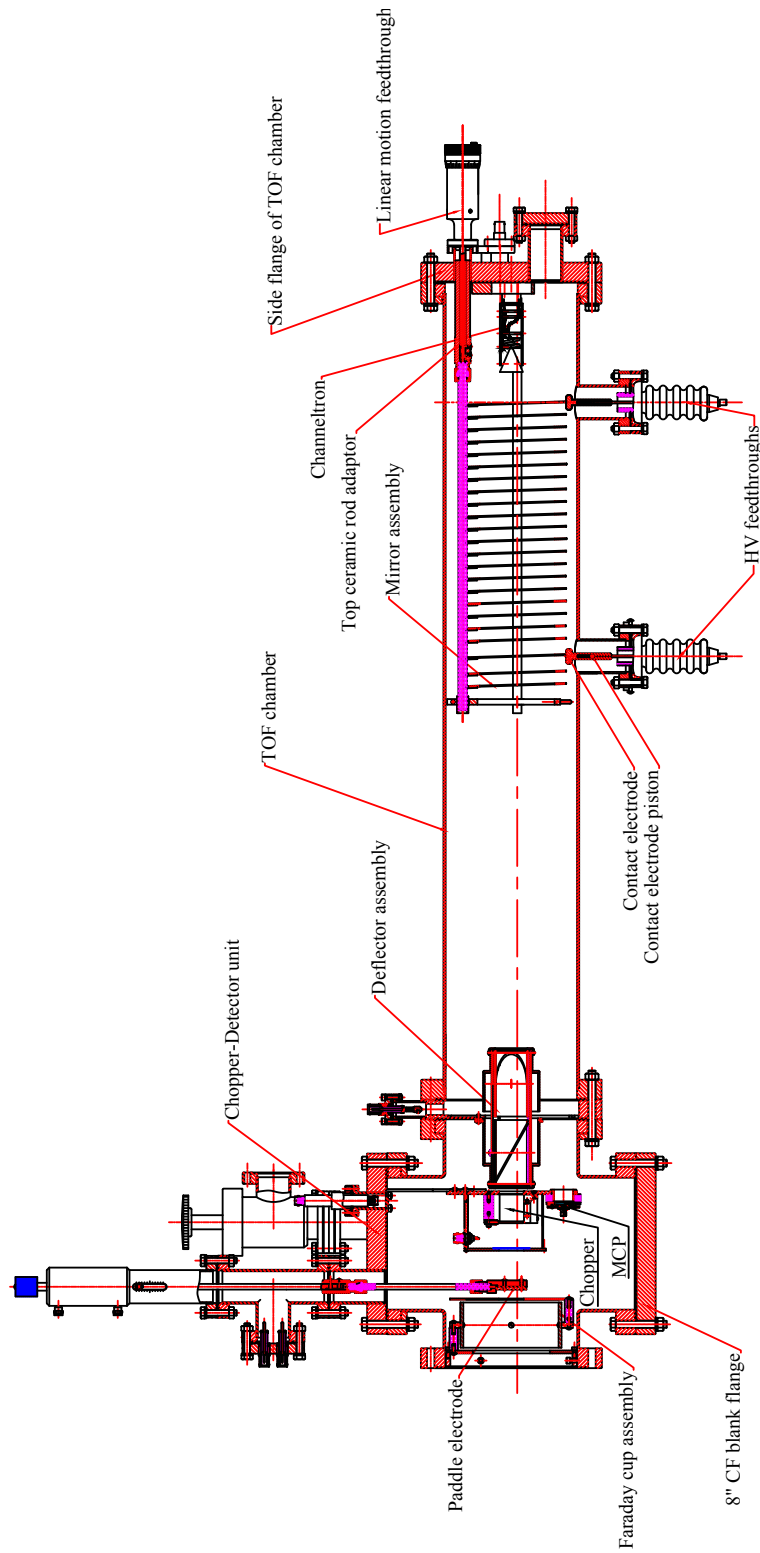


Figure 5.6: Drawing of the Time of Flight spectrometer.

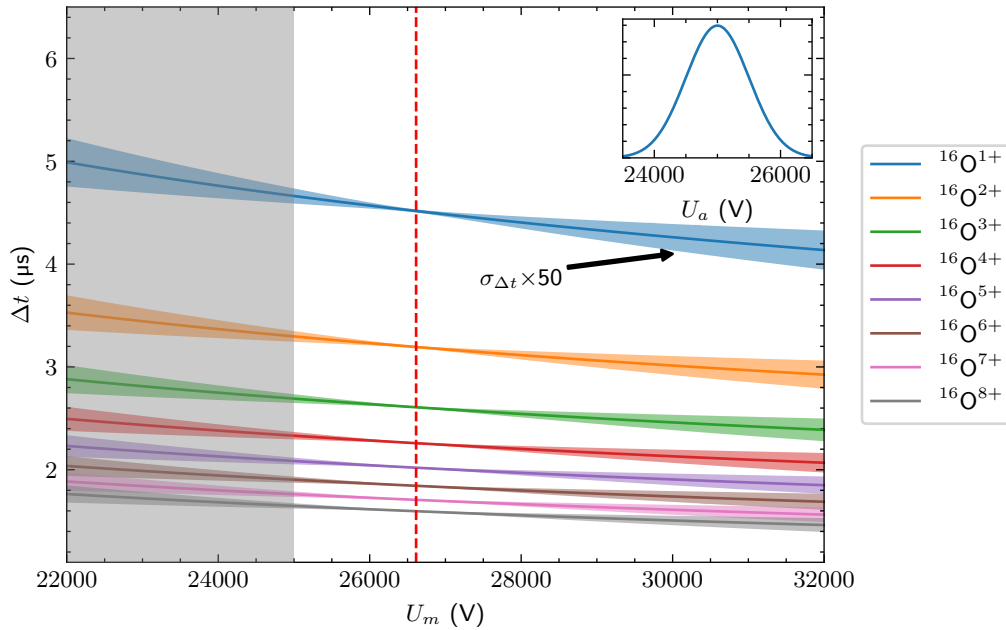


Figure 5.7: Plot illustrating the effect of time focusing of a reflectron-type TOF. The inset depicts the distribution of the particle acceleration potential (i.e. energy) distribution. The main plot shows the predicted time of flight and its uncertainty as a function of the mirror voltage. The confidence bands were inflated by a factor of 50 to improve visibility. The dashed red line corresponds to the theoretically optimal mirror voltage. In the shaded region the mirror voltage is too low to reflect the central beam energy, but the predicted values would apply for a longer mirror with the same field strength.

have a certain energy spread since they originate from a kinetic distribution trapped inside the EBIS. A faster ion is going to traverse the drift space in a shorter period of time, but will also fly further into the mirror, such that time of flight differences cancel out to first order. The effect of the mirror voltage on the  $\Delta t$  spread is illustrated in Figure 5.7 for the example of oxygen ions (the effect is of course more important for heavier ions with a denser spectrum). In practice good time focusing is still achieved even for non-perfect mirror voltages.

Chopping a ns slice from an EBIS pulse with an original length of tens of  $\mu\text{s}$ , as well as losses occurring in the reflectron, drastically reduce the pulse charge. Additionally, the mirror may disperse a single pulse over  $\geq 10 \mu\text{s}$ , resulting in very small ion currents impinging on the detector. In order to be able to record a signal, a charge-multiplying Microchannel Plate (MCP) is used, see e.g. Ref. [138]. Here we use a two-stage chevron-type MCP (Hamamatsu F4655-13). By tuning the MCP voltage up to 2500 V (split between the two plates with a resistor network), gain upwards of  $1 \cdot 10^6$  may be reached. The MCP is terminated with an effective impedance of  $50 \Omega$  by the manufacturer to facilitate reflection-free signal transport with a conventional coaxial cable. The cable lengths inside and outside the vacuum chamber were kept as short as possible,

to reduce the signal broadening due to capacitive time constants, and signals were recorded with a fast sampling  $\geq 1$  GS/s oscilloscope.

## 5.2 Experimental methods

The following section contains an overview of the procedures used during the MEDeGUN commissioning and performance tests. Prior to looking at the individual experiments it should be noted that the presented data was collected over a timeframe of multiple years during which the EBIS was partially rebuilt and modified several times. The pure electron beam studies were carried out prior to the installation of the ion extraction setup. The EBIS was then opened to install the ion beamline and first charge breeding experiments were carried out. Shortly after that a failed interlock caused severe damage to the electron gun when the cooling water flow was interrupted. The electron gun was rebuilt using a new cathode and anode coil piece / water cooling block. Due to a loose contact the Wehnelt electrode was found to be floating, effectively limiting the emission current to approximately 200 mA. Some further charge breeding tests were performed at this reduced current before the gun was removed from the vacuum chamber to fix the Wehnelt connection. TwinEBIS stayed in this final configuration for the remaining measurements. Whenever modifications were made to TwinEBIS or MEDeGUN, careful measurements of mechanical registration points were taken to reproduce the prior alignment to the best of our abilities, including high precision measurements of the gun assembly carried out by CERN's metrology service.

### 5.2.1 Electron beam commissioning

After the first installation of the electron gun, the transmission of the electron beam through the solenoid has to be optimised. Without this procedure the operation is quickly interrupted by loss currents on various electrodes, which can overpower the low current high voltage power supplies and cause thermal stress on the loss surfaces. Primary loss locations are the anode, the last drift tube, and the suppressor electrode in front of the collector. Typical losses recorded during the first commissioning run, can be found in Ref. [115].

The transmission was optimised by iteratively aligning the system and slowly increasing the electron beam current. Initially the vacuum chamber holding the drift tube structure was aligned parallel to the magnetic field axis. In the next steps the exact transverse positions of the vacuum chamber, and the gun within the vacuum chamber, were carefully adjusted for minimal beam losses. Losses on the collector side of the EBIS were found to depend also on the axial position of the collector with respect to the main magnet, which can be adjusted by a few mm. The electron beam current is controlled by means of the anode-to-cathode voltage, with the gun operating in the space charge limited emission regime. If the cathode heating power is too low,

Table 5.2: Potentials applied during the perveance measurements, expressed relative to the EBIS HV platform.

Element	Voltage (kV)
Cathode	-7.0
Anode	varied
Gun side & inner barrier DT	2.0
Remaining DT	0.0
Suppressor	-5.0
Collector	-4.7
Extractor	-11.0

and the current is pushed into the thermally limited regime, the beam quickly becomes unstable. Given a perveance of  $1.0 \mu\text{A}/\text{V}^{3/2}$ , an electron current of 1 A is expected for a voltage of 10 keV. The beam energy can be controlled independently of the beam current within a limited range by applying a bias voltage to the electron gun; transmission and loss currents are generally also energy dependent.

#### 5.2.1.1 MEDeGUN perveance

After the system was sufficiently well aligned to operate reliably for a wide range of beam currents, the perveance of the gun was determined by measuring the transmitted beam current as a function of the anode-to-cathode voltage. This process was repeated for a number of different cathode heating currents, and the beam current was raised until it would become too unstable for operation. At the same time the approximate cathode temperature was determined with the help of a pyrometer observing the glowing cathode through a vacuum window installed downstream of the ion extractor. Table 5.2 contains a listing of various settings for this measurement.

#### 5.2.1.2 Beam energy reduction & Bursian limit

There are a number of reasons for attempting to approach a relatively low electron beam energy. Firstly, the negative charge density increases as electrons are slowed down, which in turn increases the ion trapping capacity. Secondly, the EI cross section for  $\text{C}^{5+} \rightarrow \text{C}^{6+}$  peaks at around only 1.5 keV. The last reason is concerned with testing MEDeGUN at a reduced magnetic field of only 2 T: Compared to a 5 T case, the magnetic mirror reflection conditions are less strict. By reducing the axial velocity, the pitch angle of the electron trajectories with respect to the magnetic field is raised, to simulate reflection conditions closer to that for a higher energy beam in a 5 T magnet. For increasing magnetic fields, the pitch angle acceptance reduces as  $\sim 1/\sqrt{B_{max}}$  [49]; at the same time the trajectory pitch angles are expected to grow as the beam energy is reduced to first order as  $\sim 1/\sqrt{E_{kin}}$ . As MEDeGUN is designed to operate at 1 A and

Table 5.3: Operating parameters for the Bursian limit tests. Potentials expressed with respect to the EBIS platform unless indicated otherwise.

Cathode	varied
Wehnelt (fixed w.r.t. cathode)	-2 V
Anode (fixed w.r.t. cathode)	8.7 kV
Gun side & inner barrier DT	2.0 kV
Remaining DT	varied
Suppressor (fixed w.r.t. cathode)	3.0 kV
Collector (fixed w.r.t. cathode)	3.3 kV
Extractor	-13.0 kV
Cathode heater current	4.4 A
Max beam current	0.899 A

10 keV in a 5 T magnet, the goal has been set to transport the beam at  $\leq 4$  keV in the reduced 2 T field of TwinEBIS.

Due to the non-linear space charge feedback, the electron beam energy cannot simply be determined by computing the difference of the externally applied potentials. If the beam energy is lowered sufficiently, one may eventually run into the Bursian limit, cf. Equation 2.42, which yields a rough estimate of the actual space charge and resulting beam energy. In a fully choked scenario the entire electron beam would be lost, which is not sustainable in the TwinEBIS setup due to heat loading and current limited power supplies. But we may expect to observe an increase of loss currents as the Bursian limit is approached. These tests were performed such that the beam approaches its lowest energy in the central trap drift tubes. The tests were repeated for a number of different biases on the drift tubes to validate that any loss currents are linked to the beam energy reduction in the trap and not due to effects in other regions of the machine. Refer to Table 5.3 for a collection of the relevant machine settings.

### 5.2.2 Charge breeding experiments

Currently, the test stand does not provide an option for injecting singly charged ions into TwinEBIS from an external source. Therefore, all charge breeding experiments were performed by relying on gas ionisation in the central trap. This was either the residual gas inside the vacuum vessel, or a working gas was injected through the gas feed line. In the latter case either  $^{40}\text{Ar}$  or  $^{129}\text{Xe}$  were used. These noble gases are not efficiently pumped by the NEG strips around the drift tube structure, which is advantageous for intentional gas injection. Contrary, oxygen can permanently poison the NEG strips, and as such the use of oxides was ruled out.<sup>1</sup>

To load a new working gas into the feed line, the small reservoir chamber was first evacuated

<sup>1</sup>As no safety clearance for the use of flammable gases could be obtained, no carbohydrates have been used during these experiments either.

with a roughing pump and then filled with the working gas to above-atmospheric pressure. The overpressure reduces the risk of atmospheric contaminants leaking into the gas feed. The gas flow into the EBIS was regulated with the needle valve, and the full range vacuum gauge, installed between the valve and the entrance into the stainless steel tube, was used to monitor the injection pressure.

During ion extraction experiments, the trap drift tubes were biased to typically 1 to 1.5 kV, to provide an initial EBIS-internal acceleration potential to the ions when the trap is opened. The gun side barrier was set to 2 to 2.5 kV, while the collector side barrier was usually set to a slightly lower voltage. This causes evaporating ions to preferentially escape towards the extractor and prevents ion bombardment of the electron gun's cathode. To extract the ions, the outer barrier drift tube is quickly pulled to a potential lower than that of the trap (usually EBIS platform earth) with the help of a Behlke switch. This opens the trap virtually instantaneously. Keeping the trap open for 0.5 to 2 ms provides ample time for ions to escape from the trap due to their thermal velocities (with typical bunch lengths of tens of  $\mu\text{s}$ ) and be extracted into the beamline.

### 5.2.2.1 Space-charge trap compensation

For an initial test of the charge breeding capabilities of the MEDeGUN electron beam, the total ion charge produced in a single breeding cycle has been measured to ascertain whether the negative space charge of the electron beam can be compensated efficiently. The EBIS has been operated in a range of varying conditions while recording the integrated bunch charge with the Faraday cup. Initial compensation measurements have been carried out prior to the overheating electron gun incident, with  $^{40}\text{Ar}$  as a working gas. The charge output has been measured as a function of the breeding time for two injection pressures, and with a wide range of voltages applied to the outer barrier during the breeding phase. Critical experimental parameters are listed in Table 5.4.

To ensure that the ion beam was focused well onto the Faraday cup, the charge intercepted by the annular outer region and in the central region were recorded separately. It is then easy to tune the voltage of the gridded electrostatic lens until the ion signal on the ring vanishes and the beam is almost entirely measured on the central plate. Subsequently, the voltage of the secondary electron suppressor is increased until the measured charge stops decreasing and plateaus out. This indicates that secondary electrons can no longer escape from the Faraday cup and inflate the readings. The total charge readings reported below are the sum of signals on both regions of the Faraday cup.

As will become clear below, the charge output recorded during the initial experiments was far smaller than expected. Therefore, follow-up measurements have been carried out to investigate the effect of various settings on the charge production rate. The  $^{40}\text{Ar}$  studies were continued at a reduced beam current (due to the intermittent issues with the floating Wehnelt electrode).

Table 5.4: Operating parameters for the  $^{40}\text{Ar}$  bunch charge scan. (Voltages given with respect to the EBIS platform unless indicated otherwise.)

Cathode	−8.5 kV
Wehnelt (w.r.t. cathode)	−20 V
Anode (w.r.t. cathode)	10.5 kV
Gun side DT	2.0 kV
Inner barrier DT	2.7 kV
Trap DT	1.2 kV
Outer barrier DT	varied
Collector side DT	0.0 kV
Suppressor (w.r.t. cathode)	2.8 kV
Collector (w.r.t. cathode)	3.3 kV
Extractor	−13.0 kV
EBIS platform bias (w.r.t. beam line)	15.0 kV
Gridded lens bias (w.r.t. beam line)	−15.0 kV
Electron current	1.18 A
Low injection pressure	
Gas feed entrance ( $^{40}\text{Ar}$ )	$1.3 \cdot 10^{-5}$ mbar
Electron gun	$8 \cdot 10^{-10}$ to $10 \cdot 10^{-10}$ mbar
Electron collector	$1 \cdot 10^{-8}$ to $1.3 \cdot 10^{-8}$ mbar
High injection pressure	
Gas feed entrance ( $^{40}\text{Ar}$ )	$3.0 \cdot 10^{-5}$ mbar
Electron gun	$1.3 \cdot 10^{-9}$ to $1.6 \cdot 10^{-9}$ mbar
Electron collector	$1.1 \cdot 10^{-8}$ to $1.7 \cdot 10^{-8}$ mbar

Table 5.5: Operating parameters for the  $^{40}\text{Ar}$  / residual gas bunch charge scan with reduced beam current, see also Table 5.6.

Cathode	−9.5 to −9.7 kV
Wehnelt (w.r.t. cathode)	−21 V
Gun side DT	1.0 kV
Inner barrier DT	2.0 kV
Trap DT	1.0 kV
Outer barrier DT	1.3 kV
Collector side DT	0.0 kV
Suppressor (w.r.t. cathode)	3.0 kV
Collector (w.r.t. cathode)	3.3 kV
EBIS platform bias (w.r.t. beam line)	25.0 kV
Gridded lens bias (w.r.t. beam line)	−15.0 kV
Electron gun	$4.7 \cdot 10^{-10}$ to $5.4 \cdot 10^{-9}$ mbar
Electron collector	$1.3 \cdot 10^{-9}$ to $1.5 \cdot 10^{-9}$ mbar

Table 5.6: Run-specific parameters for the  $^{40}\text{Ar}$  / residual gas bunch charge scan with reduced beam current, see also Table 5.5.

ID	$U_{\text{Anode}}$ (kV)	$I$ (mA)	$U_{\text{Extractor}}$ (kV)	$p_{\text{gas}}$ (mbar)
A	3.5	209	−16.0	$4.16 \cdot 10^{-7}$
B	3.5	209	−17.0	$4.16 \cdot 10^{-7}$
C	3.5	209	−19.0	$4.16 \cdot 10^{-7}$
D	3.5	209	−19.5	$1.00 \cdot 10^{-6}$
E	3.0	164	−19.6	$1.04 \cdot 10^{-6}$
F	3.5	209	−15.5	$8.60 \cdot 10^{-8}$
G	3.5	209	−19.5	$8.60 \cdot 10^{-8}$

Here, the focus was put on assessing the influence of the ion extractor voltage on the recorded ion charge and determining the gas pressure in the trapping region. Machine settings are listed in Table 5.5 and Table 5.6.

After the broken Wehnelt electrode contact was fixed, additional studies were carried out at full electron beam current. The influence of the extractor and trap bias were investigated relying only on the residual background gas, without active gas injection. Table 5.7 contains a listing of the operating parameters.

Afterwards, the ion extractor was fixed to the beamline earth potential, while lifting the EBIS high voltage platform to create the required extraction voltage. This permits recording approximate values for ion losses on the extractor electrode by measuring positive current pulses via a load resistor, though it should be noted that the absolute value may be amplified by

Table 5.7: Operating parameters for the residual gas based extractor bias study.

Cathode	−8.9 kV
Wehnelt (w.r.t. cathode)	−16 V
Anode (w.r.t. cathode)	10.5 kV
Gun side DT	1.4 kV
Inner barrier DT	2.0 kV
Trap DT	1.0 kV   varied
Outer barrier DT (w.r.t. trap DT)	0.5 kV
Collector side DT	0.0 kV
Suppressor (w.r.t. cathode)	3.0 kV
Collector (w.r.t. cathode)	3.4 kV
Extractor	varied
EBIS platform bias (w.r.t. beam line)	20.0 kV
Gridded lens bias (w.r.t. beam line)	−9.8 to −11.2 kV
<hr/>	
Electron current	1.11 A
<hr/>	
Gas feed entrance (evacuated)	$3.4 \cdot 10^{-7}$ to $3.5 \cdot 10^{-7}$ mbar
Electron gun	$1.7 \cdot 10^{-9}$ to $2.0 \cdot 10^{-9}$ mbar
Electron collector	$3.1 \cdot 10^{-9}$ to $3.3 \cdot 10^{-9}$ mbar

secondary electrons emitted when ions hit the surface. These experiments were performed both with injected  $^{129}\text{Xe}$  and purely residual gas, cf. Table 5.8 for the machine settings.

### 5.2.2.2 Charge state spectrum and TOF measurements

When the central region of the Faraday cup is retracted, the beam may be detected with the TOF spectrometer. To simplify the setup of the spectrometer, the Bradbury-Nielsen gate and the MCP are initially turned off. This allows the full ion bunch to enter the spectrometer and be reflected towards the MCP. When not powered, the metallic front side of the MCP can be used just like a simple Faraday cup. The gridded lens, the transverse correctors in the TOF and the mirror tilt angle are then adjusted to maximise the ion signal on the MCP front side. Generally the beam is focused less tightly when operating the TOF, as the designated focal point is much further removed from the gridded lens. Due to the tight apertures in the beam gate, and beam defocusing in the mirror, the spectrometer is generally quite lossy, but several hundred pC/pulse are still routinely detected on the MCP in this manner. Then, the beam gate bias voltage is applied to block the beam such that the MCP can be powered on safely, as it must not be exposed to high primary signal levels to avoid permanent breakdown damage.

The ion extraction trigger signal is transferred from the EBIS high voltage platform via an optical fibre and used to trigger an adjustable delay generator which in turn controls the high voltage pulse generator that opens the beam gate for a few nanoseconds. In this manner the

Table 5.8: Operating parameters for the measurements of ion losses on the extractor electrode.

Cathode	−9.0 kV
Wehnelt (w.r.t. cathode)	−20 V
Anode (w.r.t. cathode)	10.5 kV
Gun side DT	1.4 kV
Inner barrier DT	2.0 kV
Trap DT	1.0 kV
Outer barrier DT	1.5 kV
Collector side DT	0.0 kV
Suppressor (w.r.t. cathode)	2.9 kV
Collector (w.r.t. cathode)	3.4 kV
Extractor	tied to lab earth
EBIS platform bias (w.r.t. beam line)	varied
Gridded lens bias (w.r.t. beam line)	−12.3 kV
<hr/>	
Electron current	1.1 A
<hr/>	
Gas feed entrance ( $^{129}\text{Xe}$ )	$5.1 \cdot 10^{-6}$ mbar   $< 3.4 \cdot 10^{-7}$ mbar
Electron gun	$6.0 \cdot 10^{-10}$ to $1.0 \cdot 10^{-9}$ mbar
Electron collector	$3.4 \cdot 10^{-9}$ to $7.3 \cdot 10^{-9}$ mbar

slice sampled by the beam gate can be selected freely over the ion bunch duration. If the leading edge of the bunch is sampled, signal contributions from slow ions are suppressed as they have not reached the beam gate by the time it opens. To get a representative spectrum, the sample should therefore be taken sufficiently late within the pulse. Generally the sampled spectrum was found to be stable a few  $\mu\text{s}$  after the leading edge. The oscilloscope is triggered by a copy of the HV pulse trigger signal to reduce jitter.

Here, the focus is going to be on two studies carried out using  $^{129}\text{Xe}$  as the working gas. In the first experiment, the evolution of the charge state spectrum has been recorded for increasing breeding times up to 100 ms. Additionally, the xenon flow rate was adjusted to three different levels with the help of the needle valve to assess the effect of the injection pressure on the charge breeding dynamics. The exact feeding pressure is regrettably obscured due to a malfunction of the injection pressure gauge, but the pressure gauges at the electron gun and collector show a clear response to adjustments of the flow rate. The experimental parameters, including the pressure gauge readings are listed in Table 5.9. In the following, the three measurements will simply be referred to by a high, medium, and low flow rate. For every configuration, the bunch charge is measured with the Faraday cup and on the extractor electrode.

In a next step, the TOF setup was used to implement a charge state resolved ion temperature measurement, similar to that described in Chapter 4. For this purpose, the outer barrier drift tube was connected to two independent power supplies selectable through a Behlke switch. This

Table 5.9: Operating parameters for the TOF  $^{129}\text{Xe}$  pressure studies.

Cathode	-7.5 kV
Wehnelt (w.r.t. cathode)	-10 V
Anode (w.r.t. cathode)	10.5 kV
Gun side DT	2.0 kV
Inner barrier DT	2.0 kV
Trap DT	1.0 kV
Outer barrier DT	2.0 kV
Collector side DT	0.0 kV
Suppressor (w.r.t. cathode)	2.9 kV
Collector (w.r.t. cathode)	3.4 kV
Extractor	tied to lab earth
EBIS platform bias (w.r.t. beam line)	18.0 kV
Gridded lens bias (w.r.t. beam line)	-5.5 kV
Electron current	1.1 A
Gas feed entrance ( $^{129}\text{Xe}$ )	n/a
Electron gun	$8.6 \cdot 10^{-10}$ , $8.0 \cdot 10^{-10}$ and $7.2 \cdot 10^{-10}$ mbar
Electron collector	$1.0 \cdot 10^{-8}$ , $8.1 \cdot 10^{-9}$ and $6.1 \cdot 10^{-9}$ mbar

configuration allows a rapid change of the barrier bias potential. At the end of the breeding cycle, the barrier is switched down to an intermediate bias, allowing the hottest ions to escape. A few instances later, the trap is opened fully, allowing the remaining ions to escape and a fresh breeding cycle to begin. The TOF acquisition was gated such that only ions from the pre-pulse have been measured. This is largely equivalent to the procedure used in the REXEBIS experiments, cf. Section 4.2.5.5, and by scanning the intermediate voltage level, the ion energy distribution can be determined. In conjunction with the TOF apparatus, this scan can be carried out for many charge states in parallel, opposed to the magnetic charge state separation used at ISOLDE.

## 5.3 Experimental results

Here, a selection of relevant experimental results are presented. A discussion of these results follows in the next section.

### 5.3.1 MEDeGUN perveance

The results of the electron gun perveance measurements are summarised in Figure 5.8. Figure 5.8a shows the electron current transmitted to the collector as a function of the anode voltage (expressed relative to the cathode potential) with different set points for the cathode

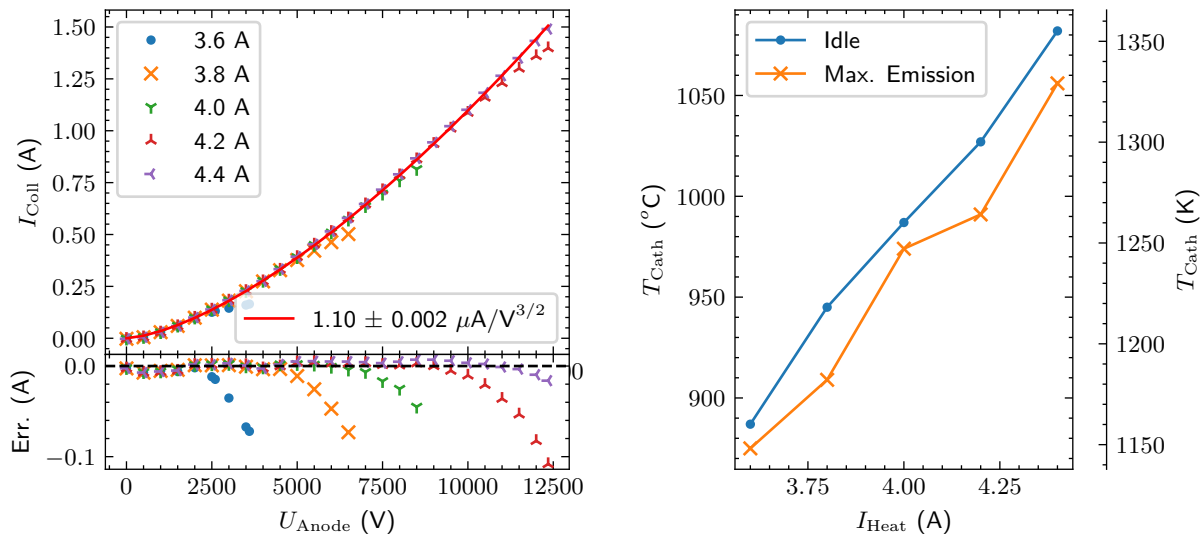
Table 5.10: Operating parameters for the TOF  $^{129}\text{Xe}$  temperature studies.

Cathode	−8.0 kV
Wehnelt (w.r.t. cathode)	−10 V
Anode (w.r.t. cathode)	10.5 kV
Gun side DT	1.9 kV
Inner barrier DT	1.9 kV
Trap DT	1.0 kV
Outer barrier DT	1.8 kV
Collector side DT	0.0 kV
Suppressor (w.r.t. cathode)	2.8 kV
Collector (w.r.t. cathode)	3.3 kV
Extractor	tied to lab earth
EBIS platform bias (w.r.t. beam line)	18.5 kV
Gridded lens bias (w.r.t. beam line)	−3.5 kV
Electron current	1.1 A
Gas feed entrance ( $^{129}\text{Xe}$ )	n/a
Electron gun	$6.0 \cdot 10^{-10}$ to $8.0 \cdot 10^{-10}$ mbar
Electron collector	$6 \cdot 10^{-9}$ to $7.5 \cdot 10^{-9}$ mbar

filament heater current. The red curve represents the result of a power law fit performed on the data for a heater current of 4.4 A. This yields a perveance of  $(1.100 \pm 0.002) \mu\text{A}/\text{V}^{3/2}$  for MEDeGUN. The lower section of the plot contains the differences between the measured currents and this fit, which illustrates distinct saturation points for the individual measurement series. As the heater current is increased, the saturation points shift towards higher anode voltages.

In addition to the transmitted current detected on the collector, there were minor losses on the last drift tube and the anode. Less than 1 mA was intercepted by the last drift tube at all times. The loss current on the anode generally falls from  $\approx 5$  mA to  $< 1$  mA as the anode voltage is increased from 0 V to 2 kV. It remains at this low level until the beam current starts to fall below the space charge limited emission current, then the anode losses increase again. At a level of 15 mA the anode power supply is current limited which leads to an anode voltage drop and generally unstable operating conditions. This is the main reason that the electron gun was not pushed further into the thermionically limited regime.

It is interesting to note that, for beam currents in the  $\approx 1$  A regime, significant power is required to provide the energy for overcoming the cathode work function. Therefore, the cathode cools down as the beam current increases, as is shown in Figure 5.8b. The two curves represent the approximate cathode temperature without current extraction, and at the highest emitted current before the emission becomes thermionically limited. The temperatures, which were determined with a manually operated pyrometer, have been corrected for a grey body surface emissivity of



(a) Perveance measurements for different cathode heating currents (cf. legend). The fit was performed for the data recorded at the highest heating current.

(b) Temperature of the cathode while idling, and at the maximum emitted current as a function of the cathode heater current.

Figure 5.8: MEDeGUN perveance results.

0.57 [139].

### 5.3.2 Beam energy reduction & Bursian limit

The perveance limit in the drift tube structure was investigated for an electron beam current of  $\approx 900$  mA. The beam energy was gradually reduced by changing the bias potential of the cathode, while recording the loss current on the anode (other losses were negligible and did not show a strong correlation with beam energy). The results of this scan are collected in Figure 5.9. To increase the confidence that the loss current was indeed correlated with the beam energy in the full magnetic field region, this measurement was repeated for drift tube voltages of 0 V, 500 V and 1000 V. The plot clearly shows that the anode loss currents in all situations depend only on the voltage difference between cathode and drift tubes, i.e. the net acceleration potential, and behave remarkably similar in all three cases. At the same time, the collector current was observed to reduce with a 1:1 correspondence to the increasing anode losses, indicating that a fraction of the beam current is reflected back towards the gun.

For the given machine settings and assuming a true beam energy of 2 keV, a beam radius of  $110 \mu\text{m}$  is predicted by the Herrmann formula. This value can be used to estimate the lower Bursian limit for the external accelerating gradient  $\approx 4540$  V, displayed by the red line in Figure 5.9, which appears to form an asymptote for the anode loss current data. To illustrate the stark discrepancy between the applied voltages and the actual beam energy as the limit is

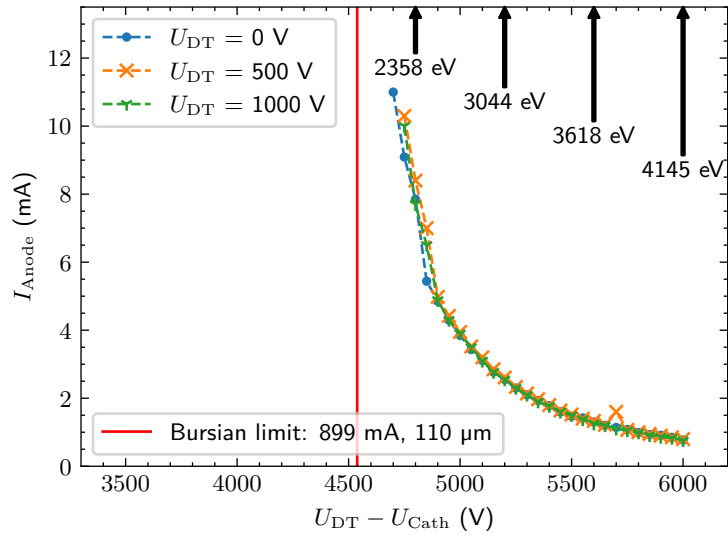


Figure 5.9: Electron loss current on the anode as a function of the local acceleration potential in the drift tube structure. The red line indicates the theoretical lower voltage limit for an electron beam with 899 mA and a radius of 110  $\mu\text{m}$  in a drift tube with radius 5 mm. The black arrows indicate approximate theoretical values for the space charge corrected beam energy.

approached, Equation 2.27 was used to estimate the space charge corrected energy, as indicated by the black arrows.

Throughout the electron beam commissioning phase various parameter regimes were explored. Figure 5.10 contains a selection of operational conditions with high current and low energy for which the electron beam was reliably transmitted to the collector with low overall loss currents ( $\leq 1$  mA). The estimated space charge-corrected beam energy is annotated in the plot for every scenario, suggesting that the true beam energy was successfully reduced to below 4 keV.

### 5.3.3 Space-charge trap compensation

**Argon injection at full beam current** The results of the initial charge breeding experiments carried out with argon as a working gas are collected in Figure 5.11. The plots show the bunch charge (integrated ion beam current) as detected on the Faraday cup  $Q_{\text{FC}}$  as a function of the barrier voltage  $U_{\text{Barrier}}$  (Figure 5.11a) or of the breeding time  $t$  (Figure 5.11b).

For sufficiently high barrier potentials and long breeding times, the detected charge saturates at approximately 1750 pC independently of the pressure at the entrance to the gas feed line ( $1.3 \cdot 10^{-5}$  mbar vs.  $3.0 \cdot 10^{-5}$ ). This value should be compared to the total amount of electronic charge inside the ion trap, which can be computed from the electron beam current and energy as  $Q_e = IL_t/u_e$ . Here,  $L_t = 80$  cm is the length of the trap. As the electron beam is compensated by ions, its velocity will increase but is generally expected to be limited by the externally applied

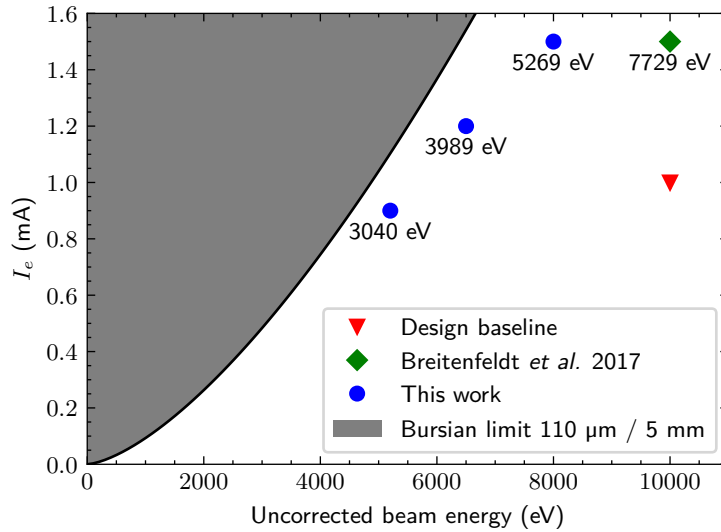


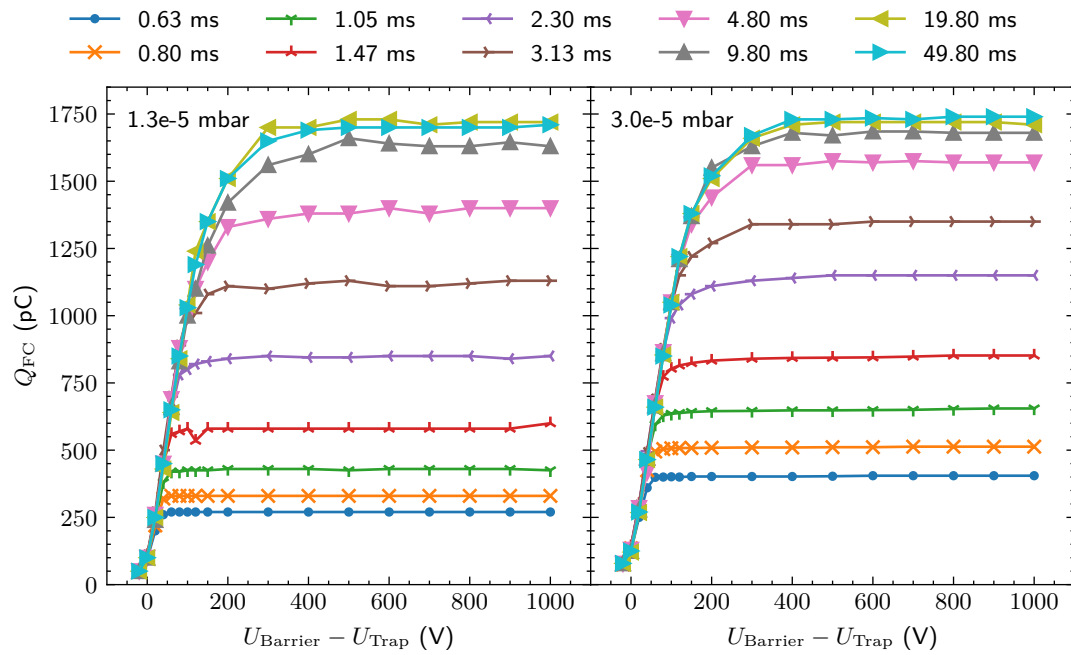
Figure 5.10: Plot illustrating a selection of stable operating conditions of MEDeGUN with total recorded loss currents  $< 1$  mA. Estimated space charge corrected energies and the Bursian limit exclusion zone are indicated for an assumed beam radius of  $110 \mu\text{m}$ . The plot also contains a data point from the initial gun commissioning run [115] for comparison.

potentials. The electron velocity is therefore computed neglecting space charge corrections. For the given machine settings (Table 5.4) this yields  $Q_e = 16\,160$  pC, which exceeds the detected ion charge by almost a factor ten.

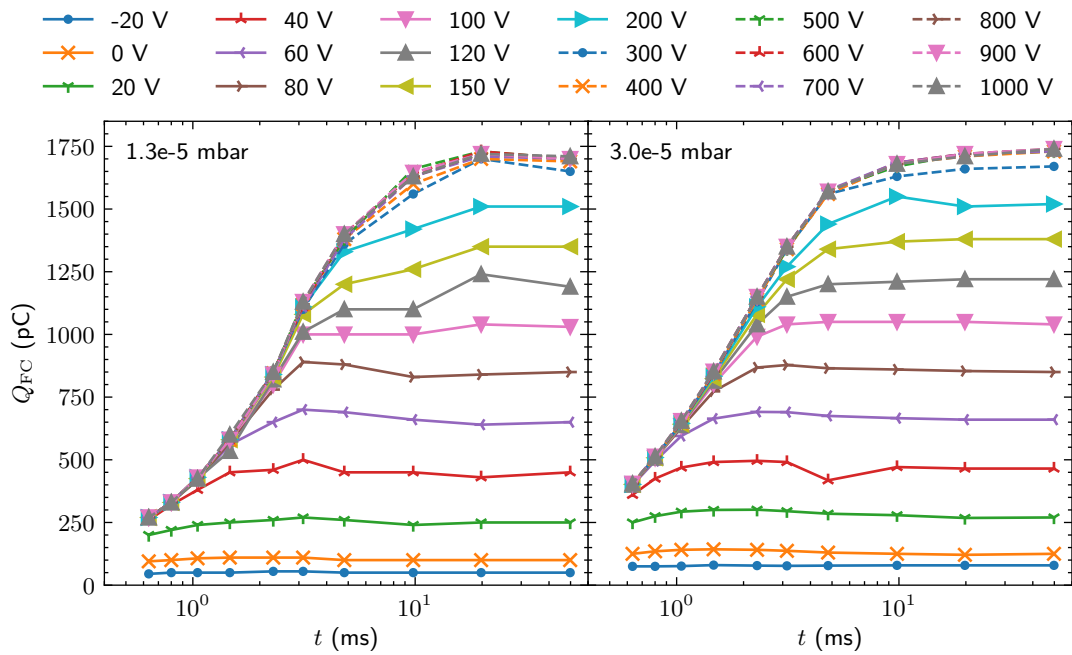
For either injection pressure, the detected charge appears to be independent of the axial trap depth for values  $\geq 300$  V. Similarly, the signals saturate for breeding times of 10 ms and longer. Comparing the two injection pressures, one may observe a faster charge build-up in the high pressure case, but beyond a breeding time of 10 ms the two measurements agree closely with each other.

**Argon and residual gas at reduced beam current** The next measurement series, recorded at an electron beam current of just 209 mA (164 mA), is visualised in Figure 5.12. The upper plot shows the extracted charge as a fraction of the total electron charge in the trap (computed as explained in the previous section). Absolute charge values are given in the lower plot, which also contains a graphical representation of linear functions that have been fitted to the data for breeding times less than 60 ms, which corresponds to the unsaturated range of the curves. While the absolute charge values are not starkly different from those presented in the previous section, the indicated relative compensation of the electron charges in the trap is much higher, ranging from about 30 to 90 %.

For measurements A, B, and C, the primary difference was the setting of the extractor bias ( $-16$  kV,  $-17$  kV, and  $-19$  kV, respectively). The data shows a strong dependence of the mea-



(a) Charge versus barrier height, breeding time indicated in legend.



(b) Charge versus breeding time, barrier height indicated in legend.

Figure 5.11: Extracted bunch charge for argon injection ( $1.3 \cdot 10^{-5}$  mbar |  $3.0 \cdot 10^{-5}$  mbar).

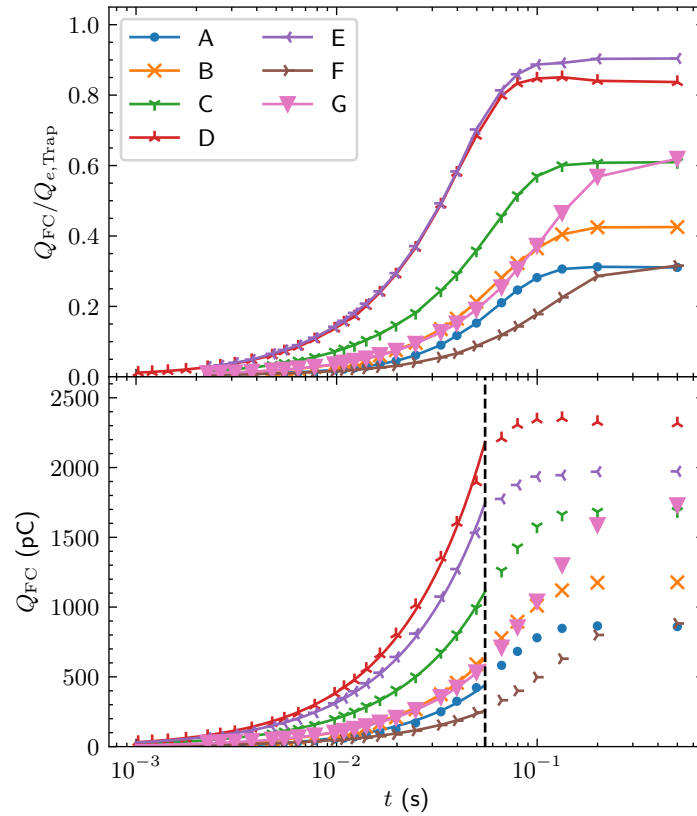


Figure 5.12: Results of the charge extraction studies performed at a reduced electron beam current. See Table 5.6 for run parameters. The upper plot shows the extracted charge as a fraction of the estimated electron charge within the trap. The lower plot contains the same data in absolute terms, including linear fits to the non-saturated section of each curve (results in Table 5.11).

sured charge on this parameter, suggesting significant ion losses for lower voltages. The gas injection pressure was doubled to  $1.0 \cdot 10^{-6}$  mbar and the extractor voltage was increased to  $\approx -19.5$  kV for measurements D and E. These runs provide the highest relative ion charge of all measurements in this run. In absolute terms, measurement E, with an electron beam current of just 164 mA, shows a reduced ion charge compared to run D. Runs F and G were recorded with a closed and evacuated gas feed system relying only on residual vacuum pressure for ion production. The detected charge grows slower as a function of breeding time but stabilises at a level similar to measurements A and C, from which these runs differ mostly in gas pressure while the remaining settings were similar.

The charge growth rate was determined by fitting a linear function to each measurement. The results are listed as  $\dot{Q}$  in Table 5.11. This quantity may be used to approximate the pressure in the trapping region. Assuming a stable pressure, new ions are created in the electron beam at a rate  $(j/e)\sigma_0 N_0$  (compare Equation 2.11), where  $\sigma_0$  and  $N_0$  are the ionisation cross section and number of neutral particles in the electron beam.  $N_0$  may be eliminated by making use of the ideal gas law  $pV = N_0 k_B T$  and observing that ionisation occurs within the electron beam volume such that  $jV = ILt$ . Adding the assumption that a representative mean ion charge state  $\bar{q}_i$  is quickly established, one may conclude

$$\dot{Q} = \bar{q}_i e \frac{j}{e} \sigma_0 \frac{pV}{k_B T} \Rightarrow \bar{q}_i p = \frac{\dot{Q}}{ILt} \frac{k_B T}{\sigma_0}. \quad (5.3)$$

Here we set  $T = 300$  K and assume  $\sigma_0 = 1 \cdot 10^{-17}$  cm<sup>2</sup> with a relative uncertainty of 33 %; this covers ionisation cross sections estimated using Lotz' formula for argon, oxygen and nitrogen at electron energies of about 10 keV. The resulting pressure estimates are listed in the final column of Table 5.11. Naturally, such an estimate is only meaningful if no ions are lost during the extraction process, which is clearly violated for measurements A, B, and F. Determining the actual pressure also requires knowledge of  $\bar{q}_i$ , such that the numerical values in Table 5.11 should be seen as an estimator. Depending on the gas mix,  $\bar{q}_i$  is expected to range from  $\approx 5$  to 15, and the pressure estimate should be scaled down accordingly.

**Extractor electrode bias scan** Motivated by the findings regarding the impact of the extractor voltage on the extracted charge, the effect was investigated more systematically while also returning to full electron beam current. During the following measurements the gas feed line was closed, but some residual xenon could have remained in the line, as xenon-evacuation after closing the valve was found to be very slow with the vacuum at the entrance to the feed line typically recovering slowly over many hours.

Figure 5.13 presents the ion charge measured on the Faraday cup as a function of the extractor voltage, and for a range of breeding times. The outer barrier was lifted 500 V above the trap

Table 5.11: Fitted charge production rates as displayed in Figure 5.12.

ID	$\dot{Q}$ (pC/s)	$\bar{q}_i \cdot p_{\text{trap}}$ (mbar)
A	$8384.88 \pm 257.66$	$(2.07 \pm 0.69) \cdot 10^{-9}$
B	$11\,752.50 \pm 164.54$	$(2.91 \pm 0.96) \cdot 10^{-9}$
C	$20\,206.30 \pm 93.44$	$(5.00 \pm 1.65) \cdot 10^{-9}$
D	$39\,869.00 \pm 399.71$	$(9.87 \pm 3.26) \cdot 10^{-9}$
E	$31\,778.50 \pm 297.80$	$(1.00 \pm 0.33) \cdot 10^{-8}$
F	$4683.33 \pm 77.00$	$(1.16 \pm 0.38) \cdot 10^{-9}$
G	$10\,657.70 \pm 48.61$	$(2.64 \pm 0.87) \cdot 10^{-9}$

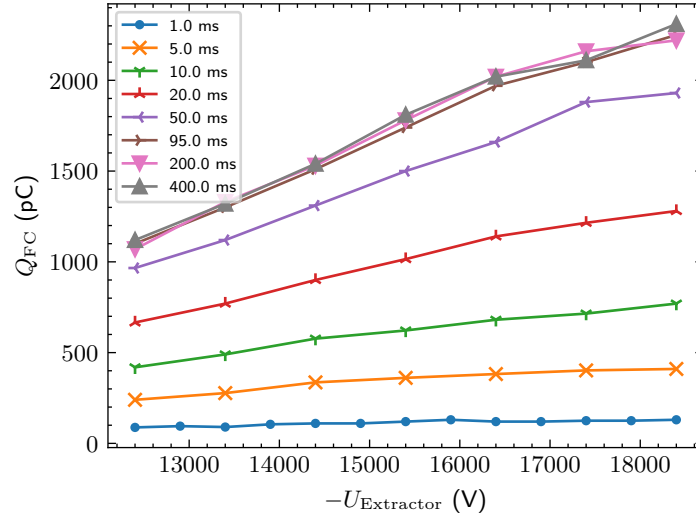


Figure 5.13: Plot of the measured bunch charge (no active gas injection, axial trap depth of 500 V) as a function of the ion extractor voltage for various breeding times (see legend).

during breeding. A strong correlation of the extraction voltage and the measured charge is clearly visible. In the experiments, the extractor voltage was practically limited to around  $-18.5$  kV due to high voltage breakdowns from neighbouring elements. This value was slightly lower than during the experiments with reduced beam current. Within the scanned range, there are no clear signs of eventual saturation for increased extraction voltages. In regard to breeding time, saturation is observed beyond approximately 100 ms.

In a second step the influence of the trap drift tube bias was tested in combination with varied extractor voltages. The breeding time was fixed at 200 ms, corresponding to the saturated regime of the previous measurement. The inner barrier was fixed at 2 kV while the outer barrier was varied in sync with the trap to keep the effective trap depth at 500 V. The detected extracted charge is presented in Figure 5.14. For all extractor settings, the recorded charge increases

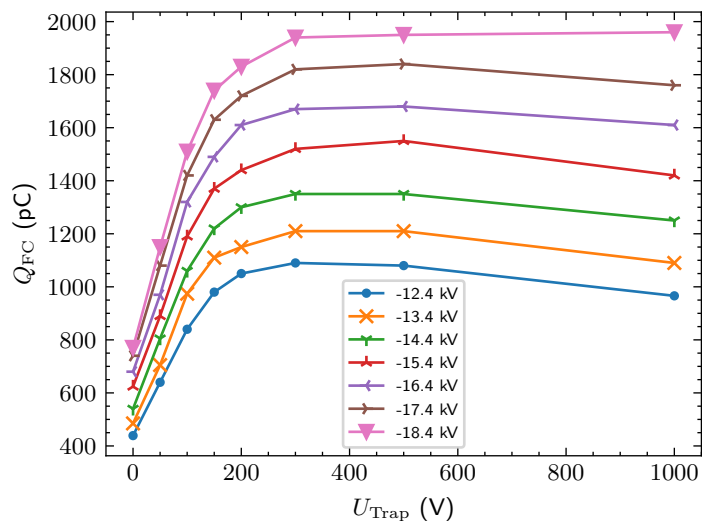


Figure 5.14: Plot of the measured bunch charge (no active gas injection, axial trap depth of 500 V) as a function of the trap bias voltage for various extractor settings (see legend).

strongly up to a trap bias of 300 V. Beyond that, the signal is decreasing, but this effect can evidently be mitigated by lifting the extractor voltage. For the highest possible extractor voltage, the curve stays flat all the way up to a trap bias of 1 kV.

**Ion loss currents on the extractor electrode** The previous results suggest that ions are lost in the extraction process. To investigate this effect further, loss currents on the extraction electrode have been recorded in parallel with the Faraday cup measurements. For this purpose the extractor was grounded via a load resistance, and the EBIS platform was raised to create an effective potential on the extraction electrode. Figure 5.15 contains the recorded data. The first dataset (Figure 5.15a) was recorded while injecting xenon at a pressure of  $5.1 \cdot 10^{-6}$  mbar, and a second reference measurement (Figure 5.15b) was performed 24 h after closing and evacuating the gas feed system.

The topmost plots in Figure 5.15 present the charge detected with the Faraday cup, and follow the previously observed scaling, with a signal increase as the extraction potential (indicated in the legend) is lifted. The central plots display the signal recorded on the extractor. Here, the measured charge is significantly higher than on the Faraday cup by up to a factor of  $\approx 8$  (xenon, 14 kV). It should be noted that the extractor reading may be inflated by the loss of secondary electrons depending on where the ions hit its surface, but we expect the effective gain to be  $< 2$ , based on years of experience with conventional Faraday cups. For both injection configurations, there is an inversion of the trend seen on the Faraday cup: as the voltage is increased, the charge intercepted by the extractor decreases. The bottom plots show the sum signal of Faraday cup and extractor.

For the xenon injection scenario, the measured charge levels are approximately four to five times higher than with a closed gas feed line. Moreover, saturation occurs after approximately 40 ms for the xenon rich measurement, whereas no definite saturation is observed when running with residual gas alone.

### 5.3.4 Charge state spectrum evolution

The time of flight spectra are recorded in the form of oscilloscope traces. One such trace is displayed in Figure 5.16a. To facilitate the interpretation of the measurement, it is helpful to extract the signal strength of every charge state of interest from the scope trace.

In a first step, the time of flight needs to be converted into an  $A/q$  ratio. For this purpose it is helpful to understand the structure of the spectrum. Towards the right (longer time of flight), one expects to find heavier and lower charged ions. Here, a collection of peaks with a shared envelope spanning a large range of the slow part of the spectrum is clearly visible – these are the  $^{129}\text{Xe}$  peaks. Towards the left, some more prominent and isolated peaks are identifiable, these result primarily from light ions created from other residual gases found in the EBIS. The leftmost and strongest peak represents protons; with an  $A/q = 1$  these are the fastest ions. It is followed by a much weaker peak at around  $2.2\ \mu\text{s}$ , which can be associated with  $A/q = 2$ .

The identification of just a few peaks is sufficient to begin establishing the calibration curve. From Equation 5.1 it is known that the time of flight scales as  $t \propto \sqrt{A/q}$ . Accounting for an arbitrary time offset, one can therefore fit a model of the form  $t = t_0 + b\sqrt{A/q}$  to the list of identified peaks. The fit provides a first calibration curve, that allows translating the spectrum to  $A/q$  ratios, and can aid in the identification of further signatures. This process can then be iterated for every newly identified peak to obtain a reliable calibration curve. The final calibration curve used for the evaluation of the pressure scan data is provided in Figure 5.17 and is the source for the secondary horizontal axis in Figure 5.16a.

With knowledge of the calibration curve and the ions mass, the expected locations of the xenon peaks can be computed easily. In Figure 5.16b, one can note a good agreement of the ticks on the second horizontal axis with the peak positions. To obtain a robust measure for the peak strength, every peak is fitted with a Gaussian profile. The area under the profile is then taken as the value for the peak strength. Here,  $^{129}\text{Xe}$  peaks that are overlapping or coinciding with other signatures, have been excluded from the analysis. Ranges with a high likelihood of contamination by residual gas ions are shaded in Figure 5.16b.

**$^{129}\text{Xe}$  injection pressure scan** For the injection pressure scan, a large number of spectra has been recorded at various breeding times and gas injection settings. These spectra have been processed according to the procedure described above to extract the intensity of all identifiable non-contaminated xenon peaks. The resulting charge state spectra are shown in Figure 5.18.

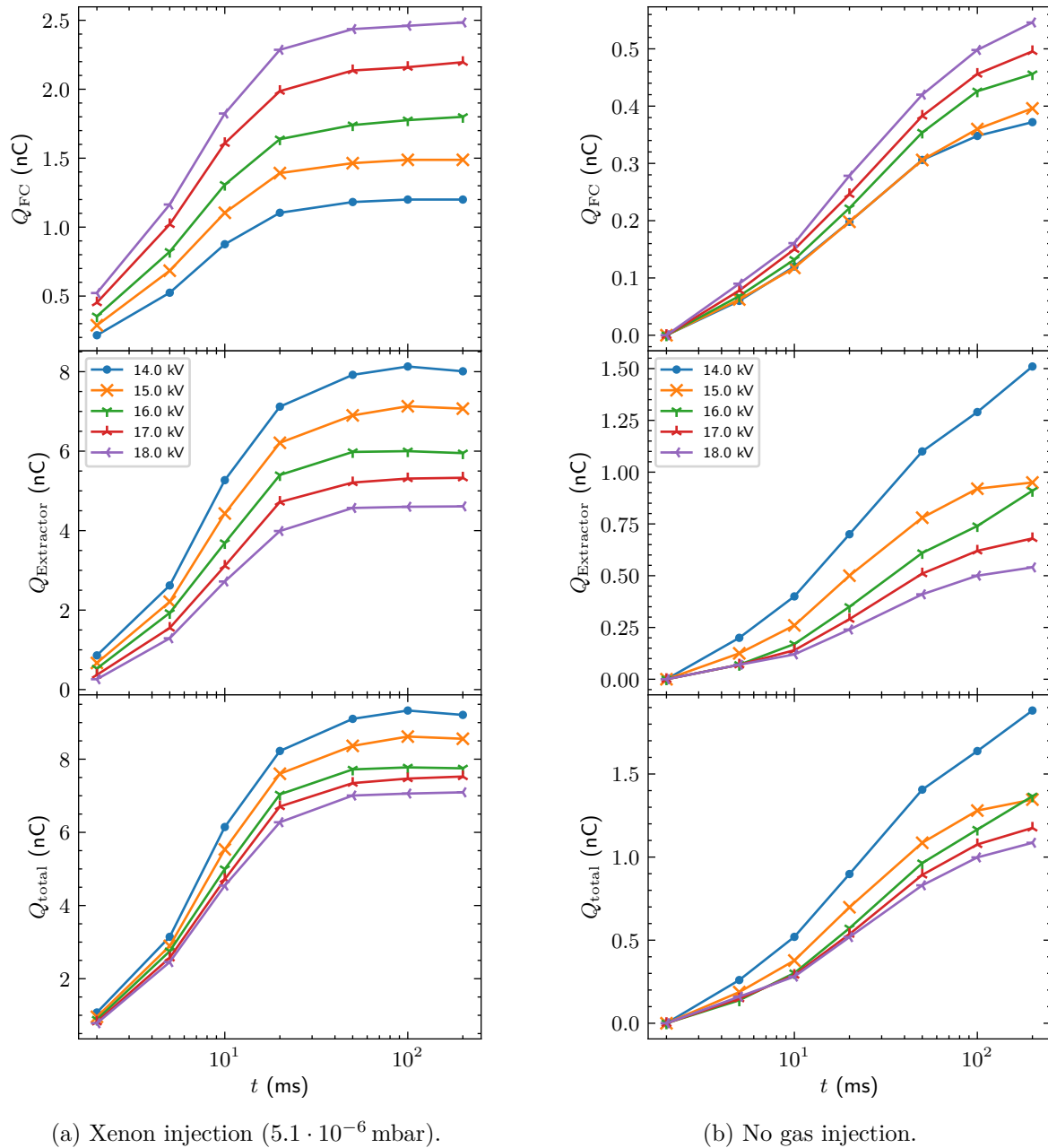
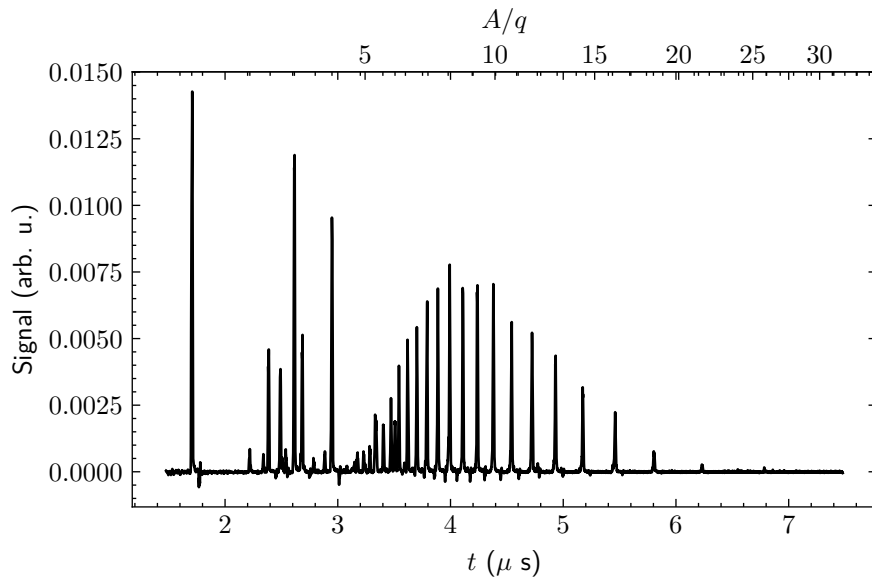
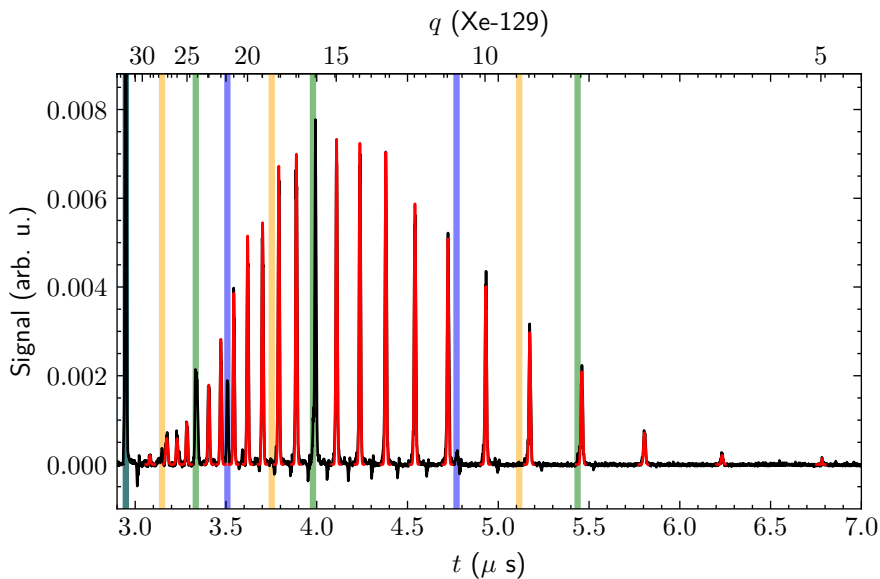


Figure 5.15: Extracted bunch charge as a function of breeding time for a selection of EBIS platform potentials (cf. legend). The upper plots display the charge recorded on the Faraday cup, the middle plots show charge measured on the extractor electrode, and the bottom plots contain the sum signal.



(a) Raw spectrum data, the upper horizontal axis indicates the  $A/q$  ratio corresponding to the time of flight given on the lower axis.



(b) Clipped section of the spectrum shown above, with Gaussian fits for the  $^{129}\text{Xe}$  peaks. The upper axis was scaled to reflect the charge states of  $^{129}\text{Xe}$ . The shaded bands indicate possible signal contamination by carbon (blue), nitrogen (orange), and oxygen (green).

Figure 5.16: Time of flight spectrum of the pressure scan at medium gas flow, 70 ms breeding time.

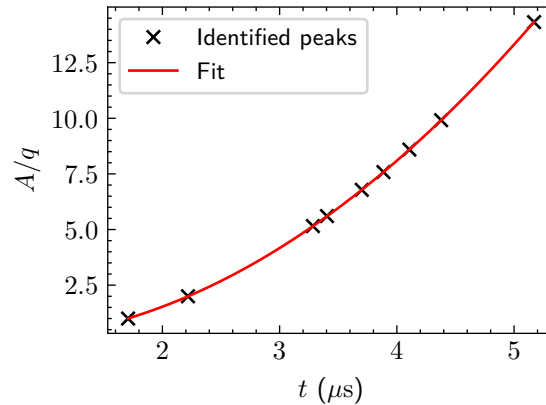


Figure 5.17: Plot of the calibration curve for the ToF spectra from the xenon pressure scan experiment.

Bunch charges that have been measured in parallel are graphed in Figure 5.19.

The spectra in Figure 5.18 are displayed on a common vertical scale. It is apparent, that the overall signal level grows fastest in the high gas flow case, followed by the medium and low scenarios, respectively. This observation is also consistent with the charge measurements in Figure 5.19, especially before saturation occurs at around 20 to 30 ms.

Moreover, it should be noted, that the whole distribution tends towards higher charge states, as the gas flow rate is reduced. In the strongest injection scenario, the spectrum stabilises with its peak at approximately  $q = 12$ , whereas  $q = 15$  and  $q = 20$  are reached under lower pressure conditions. On the contrary, there is no significant evolution of shape and centre of mass of the distribution as time progresses in all three scenarios. While a small shift may be observed for breeding times  $\lesssim 7$  ms, there is no discernible change beyond this point, other than a signal level increase which eventually saturates.

From the charge measurements, it can be seen that all scenarios saturate at approximately the same level. There is, however, a clear difference in the rate at which saturation is reached, with the low pressure curve growing notably slower than its two counterparts. The high pressure scenario shows a faster charge growth on the shortest timescales, but differences to the medium gas flow case quickly even out for longer breeding cycles. In all cases, the charge intercepted on the extractor accounts for about a quarter of the total charge, with the majority being measured on the Faraday cup.

**Ion temperature scan** Temperature scans have been performed for breeding times of 5 ms and 10 ms, with repeated measurement of the ion current extracted over an intermediate setting of the outer barrier drift tube. The extraction of the xenon peak strengths was performed in the same manner as for the pressure scan spectra. Subsequently, the data for every charge state

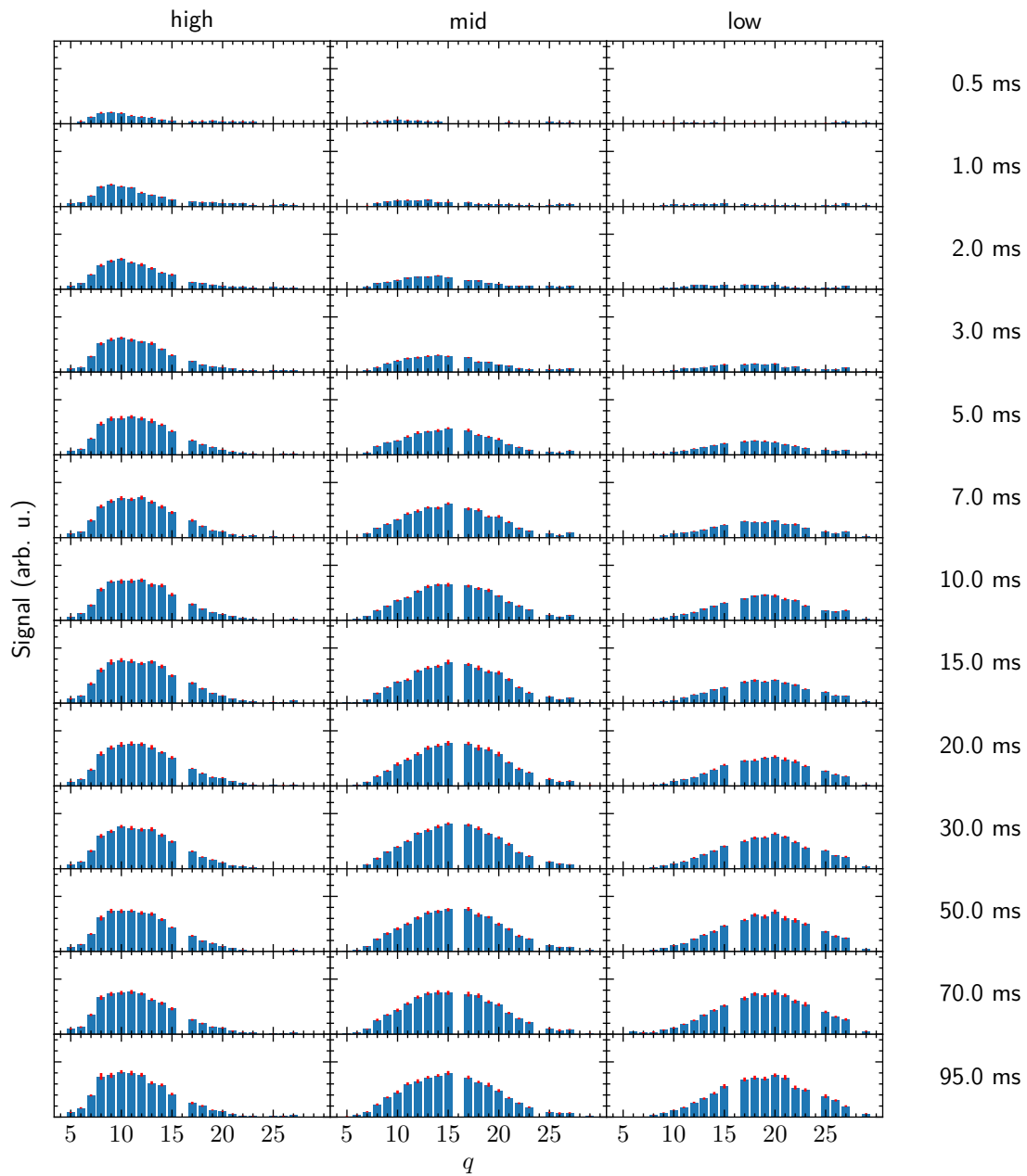


Figure 5.18: Collection of  $^{129}\text{Xe}$  charge breeding spectra as a function of breeding time and qualitative level of gas flow through the injection line.

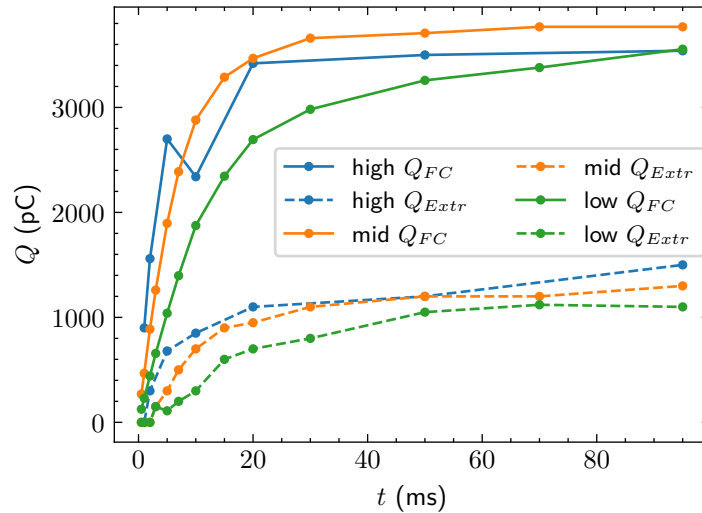


Figure 5.19: Plot of the charge detected on the Faraday cup and the extractor during the TOF pressure scan experiment (cf. Figure 5.18), as a function of breeding time.

is collected and fitted with the same model as used for the REXEBIS ion temperature studies (cf. Equation 4.14). Here, however, the constant  $U_0$  is absorbed into the trap bias voltage as the primary interest is on the equivalent temperature of the ion population.

The normalised and fitted data is presented in a stacked plot in Figure 5.20. Some fits had to be omitted as the signal level in the corresponding peaks was low, leading to very noisy data and hence poor fits. The fitted parameters for the remaining measurements are listed in Table 5.12. The temperatures presented therein have been normalised by the charge state for better comparability of the equivalent required holding voltage. For the 5 ms run, a gentle decreasing trend is present as the charge state increases. In the 10 ms case however, the normalised temperatures are much less correlated with the charge state, and generally less spread out.

With the 5 ms configuration, the charge detected on the Faraday cup when the trap is opened fully amounts to 2040 pC, whereas just 100 pC are detected on the extractor; for the 10 ms measurement the corresponding values are 3500 pC and 600 pC, respectively.

## 5.4 Discussion of experimental results

### 5.4.1 Electron beam measurements

Space-charge limited Child-Langmuir emission and the emerging perveance properties of electron guns operating in this regime are well understood. For MEDeGUN, we have measured a perveance of  $1.1 \mu\text{A}/\text{V}^{3/2}$  when operating at a cathode temperature of around 1050 to 1075 °C.

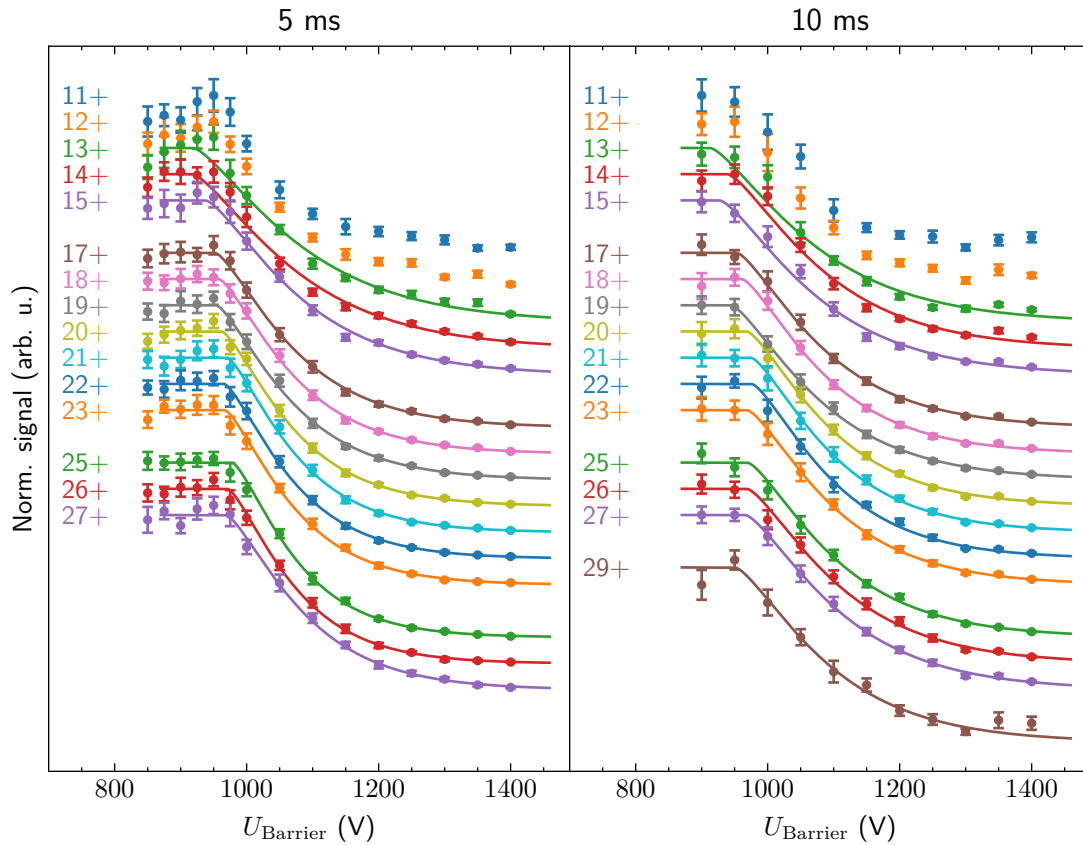


Figure 5.20: Stacked plot of normalised  $^{129}\text{Xe}$  charge state signals extracted from TOF spectra as a function of the barrier voltage during extraction for breeding times of 5 ms and 10 ms. The solid lines represent fitted Maxwell-Boltzmann energy spectra with three internal degrees of freedom. The corresponding fit parameters are listed in Table 5.12.

Table 5.12: Best fit parameters for the  $^{129}\text{Xe}$  ion energy distributions shown in Figure 5.20.

$q_i$	5 ms		10 ms	
	$k_{\text{B}}T_i/q_i$ (V)	$U_0$ (V)	$k_{\text{B}}T_i/q_i$ (V)	$U_0$ (V)
11	—	—	—	—
12	—	—	—	—
13	$120.83 \pm 4.88$	$918.49 \pm 12.26$	$117.69 \pm 5.32$	$912.47 \pm 16.67$
14	$117.73 \pm 3.92$	$917.45 \pm 10.21$	$108.78 \pm 4.44$	$939.08 \pm 13.71$
15	$106.93 \pm 3.39$	$937.59 \pm 9.18$	$111.49 \pm 3.80$	$926.91 \pm 13.99$
17	$90.17 \pm 2.79$	$951.93 \pm 6.92$	$99.46 \pm 3.19$	$952.98 \pm 9.30$
18	$85.39 \pm 2.06$	$957.45 \pm 6.08$	$95.07 \pm 3.09$	$960.78 \pm 9.09$
19	$86.36 \pm 2.39$	$953.50 \pm 6.14$	$103.26 \pm 3.26$	$944.10 \pm 11.14$
20	$81.15 \pm 1.98$	$961.91 \pm 5.32$	$94.87 \pm 2.65$	$968.29 \pm 9.16$
21	$77.88 \pm 2.14$	$970.13 \pm 6.33$	$92.57 \pm 2.61$	$974.76 \pm 9.25$
22	$78.14 \pm 2.29$	$965.60 \pm 5.96$	$92.13 \pm 2.86$	$975.67 \pm 8.49$
23	$78.21 \pm 2.12$	$966.57 \pm 5.42$	$98.06 \pm 3.16$	$968.93 \pm 10.06$
25	$72.55 \pm 1.78$	$977.79 \pm 4.68$	$100.57 \pm 2.84$	$969.27 \pm 9.29$
26	$75.27 \pm 2.27$	$970.92 \pm 5.36$	$104.43 \pm 3.44$	$968.49 \pm 9.90$
27	$87.13 \pm 3.14$	$968.51 \pm 7.23$	$107.13 \pm 3.82$	$966.11 \pm 9.53$
29	—	—	$105.82 \pm 7.63$	$950.39 \pm 15.34$

This operating temperature is well within the recommended limits for this type of cathode, promising a long life-time. The perveance value exceeds the documented baseline design value of  $1.0 \mu\text{A}/\text{V}^{3/2}$  [113]. More recent and careful simulations of the gun geometry performed with *CST*, however, have yielded a perveance of  $1.08 \mu\text{A}/\text{V}^{3/2}$  [140] which is in much better agreement with our measurement results. An excessive perveance could have otherwise pointed at current emission originating from additional surfaces as e.g. the outer rim of the cathode which could lead to increased loss currents and beam quality degradation.

We have further shown that insufficient cathode heating leads to unstable electron beam transmission with rising loss currents. This is likely caused by a transition into the thermionically limited emission regime. Because of the relatively large cathode surface, the surface temperature may not be homogeneous which then translates into a non-uniform current emission profile and space charge distribution, degrading the focusing force balance. This causes excessive current losses hindering machine operation. It is therefore important to ensure that the electron gun is provided with sufficient heating power during all experiments, while avoiding excessive heating of the cathode at the same time.

By reducing the electron beam energy for a fixed beam current, the system was brought close to the theoretical Bursian limit. The results demonstrate that a small but increasing fraction of the electron beam is reflected in the trapping region and lost on the anode as the beam energy

is lowered. The loss current increases slowly as the external voltage is decreased over a range of more than 1 kV before it jumps up more rapidly close to the theoretical perveance limit, cf. Figure 5.9. The slowly rising losses at energies well above the Bursian limit, may be explained by a fraction of electrons with particularly large initial pitch angles, that experience a more significant loss of forward momentum as the beam is compressed in the magnetic field ramp causing them to be reflected earlier.

The good agreement with the theoretical perveance limit increases the confidence that the electron beam dynamics follow theoretical expectations. Due to the intrinsic velocity spread of the beam electrons, however, the limiting threshold is blurred in practice, making it difficult to draw precise quantitative conclusions. In principle, Equation 2.43 links the limiting accelerating voltage to the electron beam radius, but the logarithmic dependence prohibits certain estimates. The relative uncertainty of the beam radius as a function of the limiting voltage may be evaluated by noting that  $(\partial r_e / \partial U) / r_e = -25.4 \mu\text{A} / \text{V}^{3/2} \cdot 3\sqrt{U} / (4I)$ . Taking  $I = 899 \text{ mA}$  and the limiting voltage  $U = 4540 \text{ V}$  and further assuming  $\sigma_U = 200 \text{ V}$  yields  $\sigma_{r_e} / r_e \approx 37.5\%$ , suggesting an electron beam radius in the range of 70 to 150  $\mu\text{m}$ , which is imprecise, but in good agreement with purely theoretical beam size predictions.

Despite the large uncertainty on the electron beam size, this experiment and others carried out during the commissioning phase illustrate that the beam can be operated reasonably close to the instability threshold without suffering from significant loss currents, cf. Figure 5.10. Additionally, the self-imposed goal of transmitting at least 1 A at a space-charge corrected beam energy below 4 keV has been achieved, increasing the confidence that this electron beam could successfully be used inside a stronger focusing field of 5 T without risking magnetic reflections of electrons with excessive pitch angles. In such a focusing field, a beam size of about 65  $\mu\text{m}$  is expected, which given the same current of 899 mA yields a Bursian limit of  $\approx 4900 \text{ V}$  for the externally applied acceleration voltage. This translates into a lower kinetic energy limit of 1630 eV, which is marginally higher than the ideal conditions for the production of fully stripped carbon ions.

#### 5.4.2 Trap compensation and ion extraction

**Argon injection at full beam current** Releasing argon gas into the electron beam and monitoring the extracted charge was intended to be a simple health and sanity check of the charge breeder after the electron beam commissioning had finished, and before the spectrometer was available. Continuous gas injection provides a constant supply of background gas which is then ionised and trapped by the electron beam, such that there is in principle an indepletable source of fresh ions. One would therefore expect, that the positive ion charge accumulates in the trap until the ions are either extracted, or sufficient positive charges have been collected to offset the negative space charge field created by the electrons, rendering further trapping

of additional particles ineffective. That is, given a sufficiently long breeding and accumulation time, the extracted ion charge should approach the absolute value of the total negative charge in the electron beam section that forms the ion trap.

As indicated in Section 5.3.3 and Figure 5.11, the ion charge detected on the Faraday cup saturates at about 1700 pC, regardless of the specific injection pressure ( $1.3 \cdot 10^{-5}$  mbar,  $3.0 \cdot 10^{-5}$  mbar). This amounts to only 10.5 % of the 16 160 pC of electrons forming the trap. While a perfect compensation is not expected, compensation levels exceeding 80 % or even 90 % are thought to be achievable in principle and have previously been demonstrated at other charge breeders.

Scaling laws from the simulation study carried out by Taylor et al. (focusing on methane) can be extrapolated to estimate the argon background pressure in the trap: Accounting for the conductance of the gas feed system, a gas pressure of  $3 \cdot 10^{-5}$  mbar is expected to translate to a flow rate of  $2.4 \cdot 10^{-7}$  mbar  $\cdot$  l/s. This should in turn result in an average pressure of approximately  $2.8 \cdot 10^{-9}$  to  $3.8 \cdot 10^{-9}$  mbar throughout the trapping region [134]. At this pressure, argon should dominate over any rest gas found in the trap, and sufficient gas should be available to quickly compensate the trap with ionic charges.

A fast growth of the detected ion charge can indeed be observed for the first 8 to 10 ms, but the curve then proceeds to saturate for longer breeding times up to 50 ms, without any notable further increase in detected charge. The saturation level is not affected by the specific injection pressure, but Figure 5.11b shows that a higher injection pressure slightly accelerates the charge production witnessed for short breeding times.

The final varied parameter in this experiment was the axial trap depth, regulated by the bias voltage applied to the outer barrier drift tube. As expected the accumulated charge tends towards zero as the axial trapping potential vanishes, in the other direction, however, charge saturation occurs at just 300 V of barrier voltage with no further gains beyond this value. The barrier voltage should be compared to the characteristic space charge potential drop of approximately  $\Phi_0 = 204$  V (intra-beam) or 1800 V (axis to drift tube wall) resulting from the machine configuration described in Table 5.4. This tells that the on axis potential can in principle perform a large sweep (approaching 1800 V) as the negative space charge is gradually compensated, eventually lifting it above the barrier. But it appears that charge saturation is witnessed at comparatively small axial barrier heights. It should, however, be noted, that the relation between compensation degree and the rise of on-axis potential is by no means expected to be strictly linear, since ions are allowed to stray far away from the electron beam, reducing the effective positive charge density.

To illustrate the expected charge production behaviour, a set of comparative simulations was set up using *ebisim*. The simulation parameters were chosen to represent the experimental set up as closely as possible, fixing the electron beam radius at 105  $\mu$ m. A background pressure of

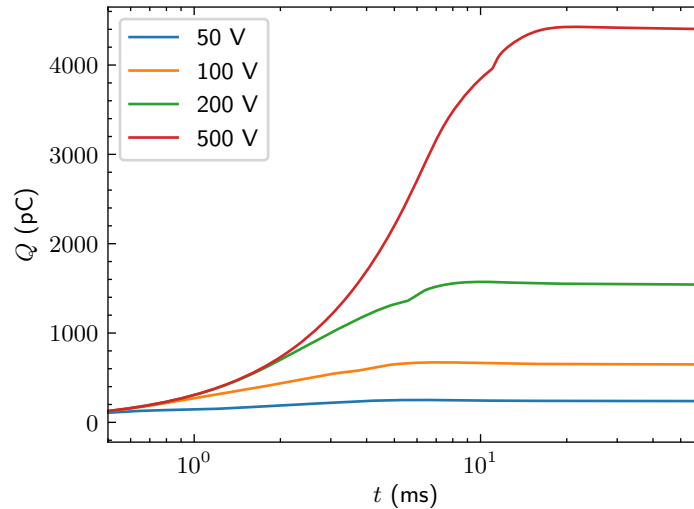


Figure 5.21: *Ebisim* simulation of total charge production with simulation parameters corresponding to the experiments presented in Figure 5.11, assuming a  $^{40}\text{Ar}$  background pressure of  $1 \cdot 10^{-9}$  mbar. The barrier height was varied between runs and is indicated in the legend.

$1 \cdot 10^{-9}$  mbar was chosen, which is expected to be roughly representative of the lower injection pressure run. The simulation results are presented in Figure 5.21. The general shape and trends of the presented curves agree well with the recorded measurement data, but as we can see the total charge output is not saturating for barrier voltages exceeding 300 V, instead the charge grows approximately linearly with the barrier height.

These measurements are the first indicator that the EBIS does not behave as expected, but the data does not provide sufficient information to draw early conclusions. The key observations from this run are that: there is a big discrepancy between the expected and detected amount of extracted positive charge, the injection pressure does not have an impact on the saturation level, but does vary the speed of the saturation, and that the axial trap appears to stop leaking even for relatively small trapping voltages.

**Argon and residual gas at reduced beam current** Forced by circumstance, experiments had to be continued with a reduced electron beam current of about 200 mA. This opportunity was used to take a second careful look at the unexpected compensation characteristics recorded at full beam current. Compared to the previous measurement the beam current is reduced by approximately a factor 6 to just 209 mA (164 mA), but also the gas injection pressure was lowered significantly to levels of  $4.16 \cdot 10^{-7}$  mbar,  $1.0 \cdot 10^{-6}$  mbar, and  $8.6 \cdot 10^{-8}$  mbar (closed needle valve), see also Table 5.6.

The most striking feature of this measurement series is the very high ion output compared to the full beam current scenario. With approximately 2300 pC Series D significantly exceeds

the charge output from the previous experiments, despite a significantly reduced current and injection pressure. The improvement becomes even more obvious when computing the relative compensation of the weaker electron beam as shown in the upper half of Figure 5.12. Here, Series D reaches a value of above 80 % but is still outperformed by Series E which manages to climb to just beyond the 90 % threshold. This further justifies the expectation of higher charge output set above for the full beam current experiments.

The second crucial finding is a strong sensitivity to the setting of the ion extractor. Series A, B, and C and Series F and G were recorded under identical conditions except for the extractor voltage. As the extractor voltage is increased within either group of related series, more ions are detected on the Faraday cup. Since the extractor is far removed from the trapping drift tubes, it is not expected to have any significant effect on the trapped ions and the charge breeding dynamics. Instead, this is a very strong indicator for the existence of extraction issues, i.e. one can be certain that not all the ions make their way from the EBIS to the detector. This is alarming, because it illustrates that the detected signal is not necessarily representative of the ion population trapped in the EBIS. It is in fact immediately obvious that Series A, B, and F are compromised in this way. Other series could be affected too, but as discussed below, they appear to behave much more coherently.

As explained in Section 5.3.3, fits of the charge growth rate can be used to roughly estimate the pressure conditions inside the trap, cf. Table 5.11. Under the given conditions the fitting results do indeed show a fairly linear correlation with experimental parameters. Series C and D vary mostly by a factor 2.5 in the injection pressure (as measured at the entrance to the feed line), with a small discrepancy in the extractor voltage. Comparing the fitted background pressure equivalent ( $\bar{q}_i \cdot p_{\text{trap}}$ ) we find a factor of close to 2 between these series. Considering the low conductance and slow reaction of the gas feed line, this is in good agreement with the measured pressure difference. In contrast to the full current experiments, one also sees a clear difference in absolute and relative saturation level for varying injection pressures, as is demonstrated by e.g. Series D and G, for which the remaining experimental parameters were equal.

Similarly, one can compare Series D and E which have been recorded at different beam currents. They clearly have different charge production rates, but after normalising for the electron beam current, we find that the pressure estimates are in excellent agreement with each other. After closing the entrance to the gas feed line entirely (Series G) the pressure estimator falls by half compared to Series C. However, a quantitative comparison may no longer be as appropriate, as the gas mix – and hence the mean charge state – is likely to shift notably when the argon supply is closed.

In summary, these experiments have taught us, that high compensation degrees are in fact achievable in an EBIS under the right circumstances. Furthermore, an important correlation of the extracted signal and the setting of the extractor voltage has been found. This tells us to

proceed with caution when drawing conclusions from this kind of measurement series, as they may not be fully representative of the charge breeding process. Additionally, this provides ample motivation for a closer look at ion losses and the role of the extractor electrode.

**Extractor electrode bias scan** After repairing the electron gun and returning to nominal beam current, the impact of the extractor potential has been investigated further whilst working without active gas injection. As evident in Figure 5.13, the detected charge increases almost linearly with the applied extractor voltage. There are no clear signs of saturation over the sampled range, suggesting that even more ions could be extracted if the extractor voltage had not been limited by discharges. As in the previous measurement, charge saturation is observed after approximately 100 ms of breeding time. This measurement confirms that the importance of the ion extraction optics holds also in the high electron current case. Despite the fact that the electron gun was rebuilt twice since the initial argon compensation measurements, this suggests that this first run suffered from the same issue, as the extractor voltage in that run had only been 13 kV, which corresponds to the low end in this data set.

In the second step, the breeding time was fixed at 200 ms, safely in the saturation regime, and the trap bias was varied in addition to the extractor bias. In contrast to the first experiment, this does not concern the height of the barrier but the trap as a whole, with the outer barrier constantly raised 500 V with respect to the trap. The trap is usually biased by approximately 1 kV, to provide an initial energy kick to the ions when the barrier opens and the bunch is extracted. This is important because the electron beam starts to decompress towards the end of the outermost drift tube, where the magnetic flux density begins to decrease. This in turn reduces the negative space charge, such that a longitudinal potential gradient can form along the exit region of the drift tube structure. Unless the ions are provided with a sufficient kick, they may not pass this barrier and end up getting caught in a parasitic trap. For a very conservative estimate one may assume that the electron beam radius has been inflated to 1000  $\mu\text{m}$ , compared to about 100  $\mu\text{m}$  in the charge breeding region; with the given experimental parameters this would translate to on-axis space charge corrections of  $\approx -1500$  V in the trap, and  $\approx -720$  V at the exit, providing an additional potential difference of around 780 V. The real gradient is expected to be smaller than this, but by biasing the trap to 1 kV one should be on the safe side.

In practice, see Figure 5.14, one can clearly recognize a signal suppression for trap biases below approximately 300 V, which is in line with the expectations laid out above. Beyond this threshold however, the signal actually starts to shrink again, as the bias is increased further. This behaviour is neither expected nor desirable. Raising the extractor voltage appears to mitigate this degradation, whilst also increasing the overall charge output, as seen previously. Neglecting small differences in beam energy, the trap bias is not expected to have any influence on the charge breeding process. The effect of different biases should only manifest from the point in

time when the barrier is opened, and the ions can escape with additional kinetic energy. As the extractor voltage can apparently mitigate issues related to the ion kinetic energy, this provides more evidence for serious problems with the ion extraction.

**Ion loss currents on the extractor electrode** To learn more about the extraction losses, the charge impinging on the extractor electrode was measured with the help of a load resistor connecting the electrode to ground, while the remainder of the EBIS platform was biased to provide the necessary potential gradient with respect to the extractor electrode. As shown in Figure 5.15, and explained in Section 5.3.3, this study revealed that a significant amount of ions is indeed intercepted by the extractor itself. Both with, and without, active injection of xenon, we find that the majority of the total signal is detected on the extractor and not on the Faraday cup. Since the extractor does not feature a secondary electron suppressor and is biased negatively compared to its immediate surroundings, these readings are most likely inflated. But we expect the signal gain to be  $\leq 2$  and there is no doubt that a significant fraction of the beam is lost on the extractor. Clearly, raising the extractor voltage shifts the balance in favour of successful extraction, with the intercepted charge decreasing while the Faraday cup signal grows at the same time.

Due to the unknown exact scaling factor of the extractor signal, a direct comparison of the signals detected on both surfaces is difficult. However, if we assume that ions are simply redistributed between the Faraday cup and the extractor, then we should be able to determine a common scaling factor for the extractor signal such that the sum signal becomes constant regardless of the extractor voltage. As this is not possible, we must assume that ions are also lost on other surfaces that are not accounted for. With this evidence no doubt remains, that TwinEBIS suffers from extraction problems when operating MEDeGUN at its nominal current of about 1 A and with insufficient extractor voltages. This means, that measurements with the Faraday cup will systematically underestimate the true degree of space charge compensation.

### 5.4.3 Charge breeding performance

Before looking at the TOF experiments in more detail, it should be noted that the beam energy in these following experiments was approximately 1 to 2 keV lower than during most of the compensation experiments. At the same time, the balance of charges detected on the Faraday cup and the extractor electrode appears to be flipped, with the majority of charges being measured on the Faraday cup. This trend inversion was noticed only in hindsight, and could not be followed up with more detail. A correlation of beam energy and losses during extraction could also relate to the effects observed during the variation of the trap bias, as this also introduces a beam energy variation. Yet, this does not invalidate any of the arguments made above. Variations of the beam energy also affect the effective potential of the collector and the suppressor electrode,

due to the high voltage platform scheme, contributing further to electric field changes in the extraction section.

As pointed out earlier, the pressure gauge for the gas feed line was broken, implying that no injection pressure readings are available. However, the detected charge is comparable to the values recorded during the loss current experiment with xenon injection. This leads us to believe that the injection pressure during the time of flight measurements has been on the same order of magnitude, i.e. in the regime of a few  $1 \cdot 10^{-6}$  mbar.

**<sup>129</sup>Xe injection pressure scan** The charge state spectra collected in Figure 5.18 are emblematic of performance issues that have persistently prevailed in all our charge breeding experiments. For all three injection pressure levels, some variation of the shape of the spectrum is seen for very short breeding times. But within just 7 ms, a stable envelope is established, and the peak of the distribution stops moving. After this, only the integrated signal level increases a little further before it, too, saturates. Figure 5.19 illustrates that charge saturation occurs within 20 ms for the high- and mid-pressure scenarios, while the low-pressure scenario displays a notably slower charge growth. Eventually, all total charge curves saturate at approximately the same level.

As indicated in Section 5.3.4, there are, however, striking differences between the three presented data sets. With increasing injection pressure, the peak of the distribution is located at significantly lower charge states, dropping from  $\approx 20+$  in the lowest pressure scenario to just  $\approx 10+$  for the highest pressure. In principle the electron beam has sufficient energy to reach charge states up to 44+ within the provided breeding time, however this does not appear to be practically achievable.

This is despite the fact, that the early evolution of the charge state distribution actually suggests rather high current densities. Whilst not easily visible in Figure 5.18 a look at the raw data reveals that the 20+ charge state is already well established after just 3 to 4 ms for the low pressure series. This can be compared to a simple charge breeding simulation to reveal that this early emergence requires an effective current density on the order of  $1600 \text{ A/cm}^2$ , which corresponds to about half of the theoretical current density of the electron beam  $3240 \text{ A/cm}^2$ . The plot also illustrates the charge state distribution one would expect to find after 95 ms if this performance could be successfully maintained throughout the breeding cycle.

The recorded spectra indicate that the charge breeding process does not just become slower over time, instead it appears to run into a virtually impassable threshold. Otherwise, there should be a more significant shift of the distribution after the 7 ms mark. The most likely explanation for such a behaviour is, that there is either a secondary process that acts counter to the electron impact ionisation, e.g. charge exchange with the background gas, or that the overlap between ion cloud and electron beam is degraded severely.

While the charge exchange mechanism could explain why the situation is worse in the high

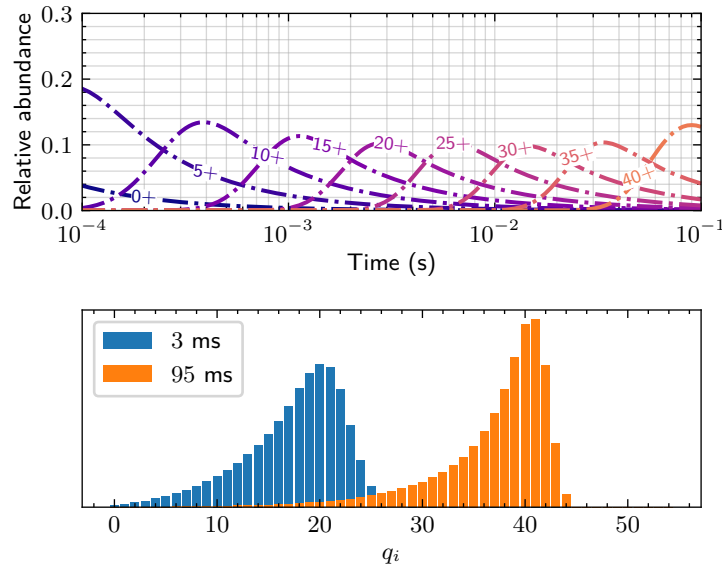


Figure 5.22: Basic model *ebisim* simulation of the charge breeding of xenon, with a fixed current density of  $1600 \text{ A/cm}^2$  and a beam energy of 7 keV. The evolution of all charge states is shown in the upper plot; the lower plot contains distribution snapshots after 3 ms and 95 ms.

pressure scenario, we can use the formulas provided in Section 2.2.4 and Section 3.3.1.3 to estimate which background pressure would be required to impede the charge breeding process so early on. Assuming an electron beam with a current density of  $1600 \text{ A/cm}^2$  at 7 keV, a xenon background pressure on the order of  $1 \cdot 10^{-7} \text{ mbar}$  would be required in order to have a charge exchange rate of  $10+ \rightarrow 9+$  that is comparable to the electron ionisation rate  $9+ \rightarrow 10+$ . This pressure value is quite excessive and should cause a notably elevated reading on the vacuum gauges at the gun and collector ports. Furthermore, simulation results presented in Figure 5.23 demonstrate that a background pressure on the order of  $1 \cdot 10^{-10} \text{ mbar}$  is sufficient to produce a total charge output comparable to the values recorded during the experiments, cf. Figure 5.19. This is three orders of magnitude less than would be required for significant charge exchange rates.

**Ion temperature scan** The ion temperatures determined in Figure 5.20 and Table 5.12 can be used to estimate the ion-electron overlap factors inside the trap without having in-situ access to the ion cloud. By making the simplifying assumptions that the total ion charge is dominated by xenon ions, and that the most significant charge states of xenon are included in the measurements, they can be viewed as representative of the ion population in the trap. One may then synthesize a spectrum with an arbitrary total charge value, that reflects the measured spectrum in relative intensities.

Such synthetic distributions can then be combined with the radial space charge well model

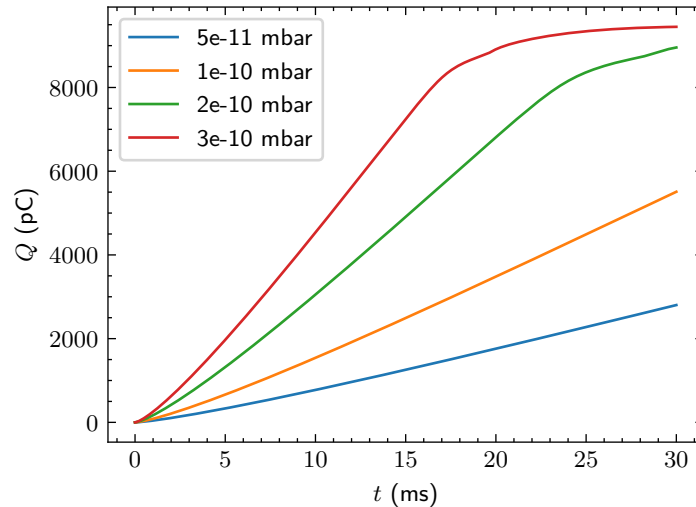
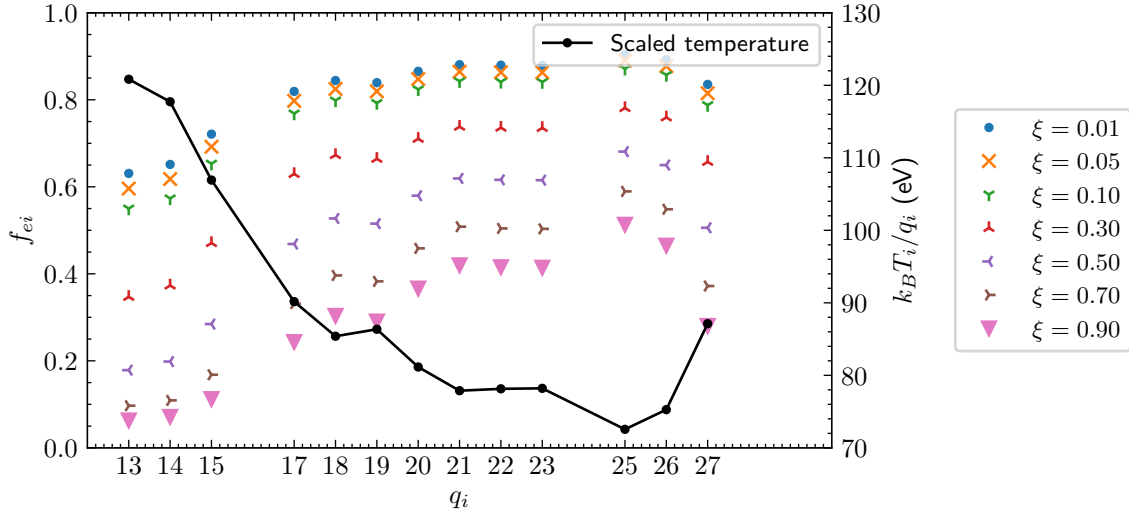


Figure 5.23: Total charge production extracted from an advanced model *ebisim* simulation of the charge breeding of xenon for varied background pressures, with machine parameters corresponding to the TOF spectrum pressure scans.

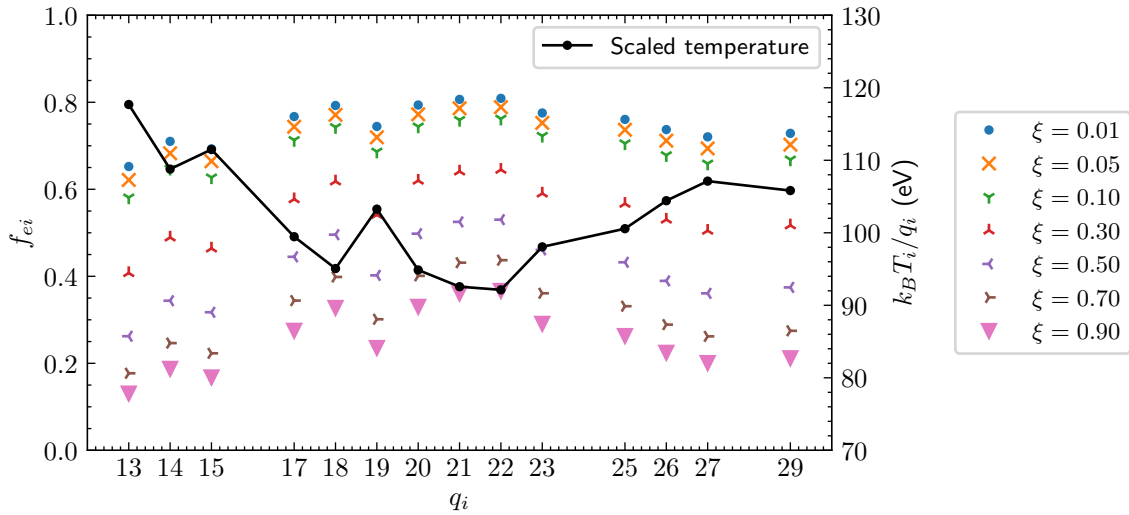
developed in Section 3.2 and Section 3.4.3. After finding the self-consistent solution to the Poisson equation, this provides the estimated ion overlap factors, as well as the net radial potential. As the exact compensation degree is unknown, the estimate can simply be computed for different compensation ratios  $\xi$ , the results of this procedure are gathered in Figure 5.24. A concrete example of the resulting radial distribution and overlap factors for the 10 ms measurement with an assumed compensation of 30% is presented in Figure 5.25. Given the measured total bunch charge of  $\approx 4100$  pC, this compensation factor appears appropriate. In this situation the overlap factors for ions in all charge states are close to  $1/2$ , which agrees well with the ratio between theoretical and apparent current density for short breeding times discussed in the previous section.

## 5.5 Studies of a low energy ion transport and measurement beamline

Prior to carrying out the experiments described above, plans for a versatile Low Energy Beam Transport (LEBT) beamline have been developed to extend the capabilities of the TwinEBIS test stand with regard to controlling and characterising ion beams. Regrettably, the parts for the beamline arrived too late to commission it within the scope of this thesis, due to long manufacturing delays. However, significant upgrades and additions have already been made in the TwinEBIS laboratory to provide the infrastructure required by the beamline, such as the installation of new high voltage power supplies and vacuum equipment as well as a full rebuild of



(a) Breeding time: 5 ms.



(b) Breeding time: 10 ms.

Figure 5.24: Plots of the fitted charge-scaled temperature for  $^{129}\text{Xe}$  ions as a function of the charge state. The scatter markers reflect the estimated overlap factors resulting from the fitted temperature and the assumed degree of neutralisation  $\xi$  of an electron beam with parameters that reflect the experimental setup.

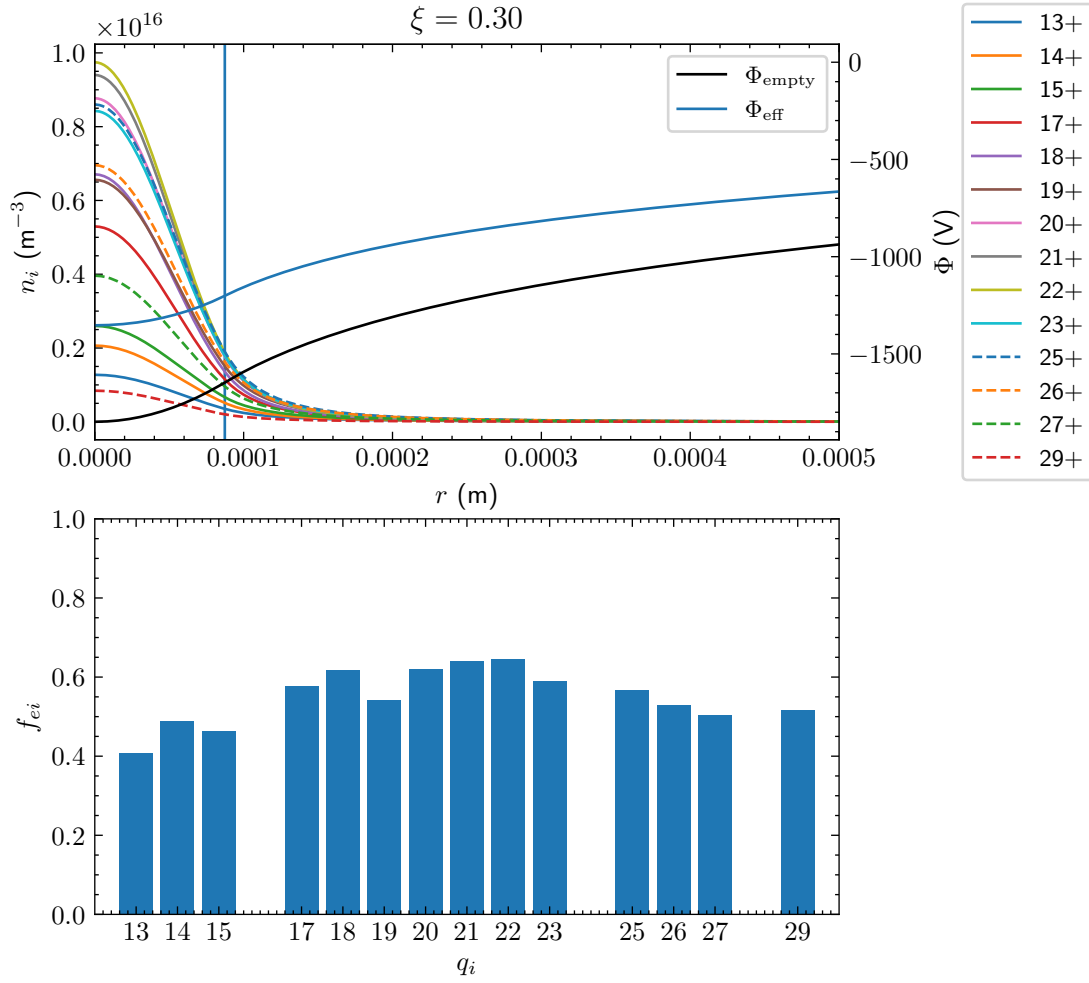


Figure 5.25: Plot of the simulated radial distribution for  $^{129}\text{Xe}$  ions after a breeding time of 10 ms, assuming a neutralisation degree of 30%. The lower plot shows the corresponding overlap factors.

the test stand's control system to accommodate the large number of added signals. Here follows a summary of the design studies for the LEBT which have been published in Ref. [IV].

The main purpose of the beamline is to provide the means for testing the injection of carbon ions extracted from a MEDeGUN-type electron beam into an accelerating RFQ. Such an RFQ would typically be the first element in the acceleration chain of a LINAC treatment facility, and an appropriate 750 MHz RFQ has already been designed [V, 141]. Since little is known about the actual quality and parameters of a carbon ion beam originating from a Brillouin electron beam, the beamline should also accommodate appropriate instrumentation for beam characterisation, such as Faraday cups and a pepperpot emittance meter, cf. Ref. [III]. Ultimately, sections of the beamline could also operate in the opposing direction to arrange for the injection of singly charged ions from an external source into TwinEBIS.

### 5.5.1 Overview

The design baseline for the LEBT assumes the transport of fully stripped  $^{12}\text{C}$  ion beams with a normalised RMS emittance of 0.02 mm mrad at a specific energy of 15 keV/u and with peak currents of up to 3 mA. At these parameters, space charge forces inside the ion beam are a concern as they may blow up the ion beam emittance prior to its injection into the RFQ. To mitigate these effects, the length of the beamline is kept at a reasonable minimum while providing large apertures to allow for an ion transport with a large beam radius. This is achieved by the use of purpose-tailored optical elements, such as strongly focusing gridded lenses and deflectors with optimised electrode profiles.

An overview illustration of the beamline is provided in Figure 5.26. In the forward direction the beamline is perfectly straight, such that the beamline and RFQ can be installed on the same axis as the electron beam inside the EBIS. This should facilitate the strongly constrained injection into the RFQ as only minimal corrections to the beam position and angle are expected to be necessary in this configuration. For added flexibility the beamline contains a switchyard with two additional ports at horizontal angles of  $\pm 20^\circ$ . These extension ports could host for example the TOF spectrometer and an external ion source or a magnetic spectrometer. Due to design constraints on the strong deflector, the side branches are expected to suffer from stronger ion optical aberrations than the main branch, as discussed in Section 5.5.3.

During operation, TwinEBIS is going to be biased by 30 kV with respect to the beamline. The voltage drops over an acceleration gap consisting of nine evenly spaced rings and an internal voltage divider. To flexibly ease the electric field gradient from the EBIS' extraction electrode into the acceleration gap and allow for tuning of the arising focusing fields, a ring shaped adaptor electrode is provided. Downstream, the beam encounters the first gridded lens, which acts as a collimating lens during ion extraction. After passing a vertical corrector the beam travels through the horizontal switchyard and into an Einzel lens, that offers some intermediate

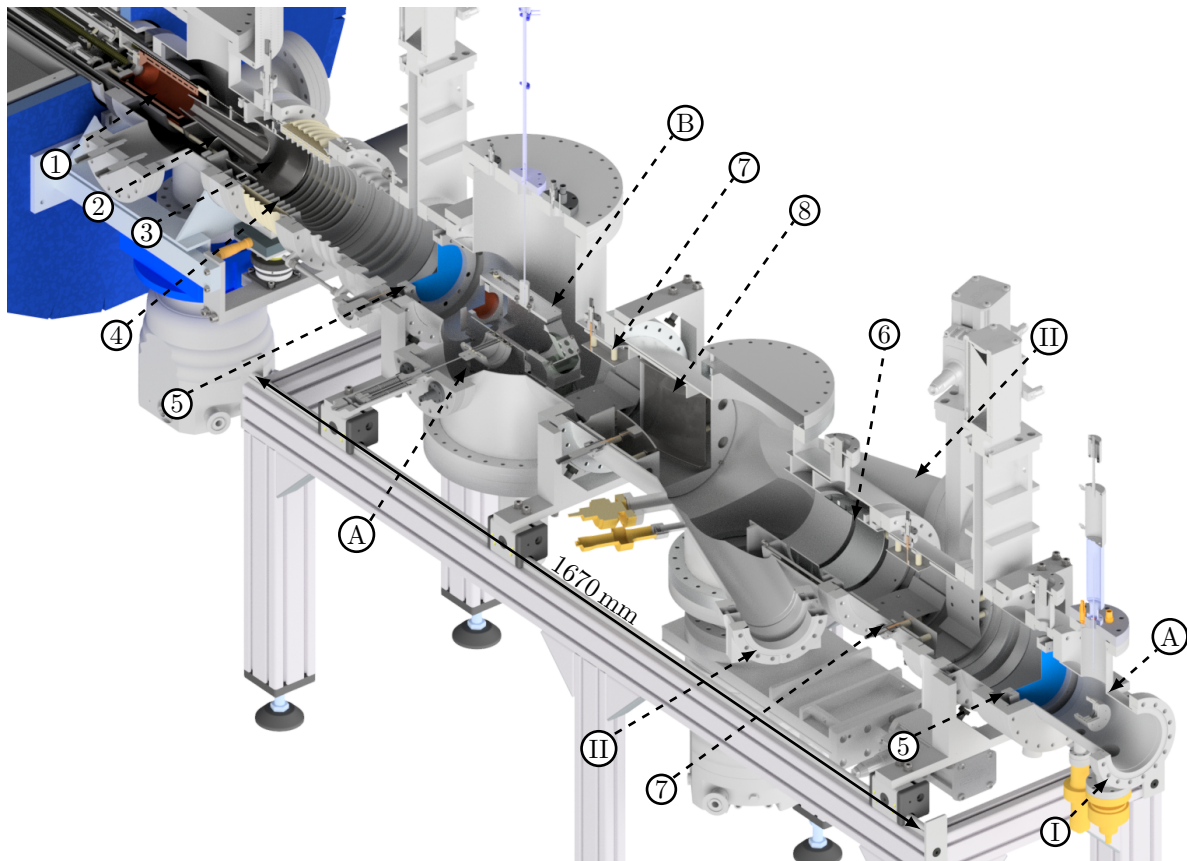


Figure 5.26: Section view of a 3D model of the ion beam line. Indicated elements are: Electron collector (1), extraction electrode (2), adaptor ring electrode (3), acceleration gap (4), gridded lenses (5), Einzel lens (6), small angle kickers (7), and the switchyard deflector (8). Port (I) in the forward direction will host the accelerating RFQ; the side ports (II) offer space for future extensions. Finally, there are two Faraday cups (A) and a pepperpot beam profiler (B). Figure reproduced from Ref. [IV].

Table 5.13: Acceptance characteristics of the accelerating RFQ assumed for the LEBT matching studies.

Specific kinetic energy	15 keV/u
Normalised acceptance	0.17 mm mrad
Twiss $\alpha_{x y}$	0.3
Twiss $\beta_{x y}$	0.01 mm/mrad

focusing to counteract space charge defocusing occurring as the ion beam travels forward. After passing a second pair of transverse correctors, the beam arrives at the second gridded lens, which is tasked with producing a tight focus into the entrance aperture of an accelerating RFQ. The smallest aperture in the beamline is the horizontal opening of the switchyard deflector with a width of 50 mm.

A chamber housing a Faraday cup and a pepperpot emittance meter is located upstream of the switchyard. Both devices are constructed in such a way that they can intercept beams travelling either from or towards the EBIS. Another Faraday cup is located just in front of the expected location of the RFQ aperture.

All beamline equipment from the EBIS up to and including the switchyard is expected to also be functional for ion beams getting injected into the electron beam. For all electrostatic elements this means that they need to be able to support fast switching, as beam optics may have to be changed between the injection and extraction phase of a single charge breeding cycle.

### 5.5.2 Beam optics

It is necessary to assert that the foreseen optical components are able to successfully focus, or match, the extracted ion beam into the RFQ acceptance (parameters listed in Table 5.13). Appropriate lens voltages were determined by means of space charge-aware particle tracking simulations. The details of the ion optics simulations will be strongly abbreviated here, and the reader is advised to refer to the original publication [IV] for an extended and more careful discussion. The ion optical matching has been performed assuming a worst-case beam current of up to 3 mA. Inside the beamline the ions travel with an energy of  $q_i \cdot 30$  keV.

Matching the beamline optics requires knowledge about reasonable initial conditions for the ion beam. These were obtained by simulating the extraction of ions from the electron beam in fully space charge consistent simulations with the help of *TRAK* [97]. Tracking ions and electrons from the full magnetic field trap is prohibitively computationally expensive.

Therefore, a simple model inspired by earlier work by Dickerson et al. [15] was used to model an ion distribution inside the last drift tube in a reduced magnetic field of 180 mT by relating them back to typical parameters in the charge breeding trap at 2 T. Taking the argument of

emittance conservation, it can be stated that

$$\epsilon \propto r_i \sqrt{E_{\perp i}} \Rightarrow E_{\perp i,T} r_{i,T}^2 = E_{\perp i,L} r_{i,L}^2, \quad (5.4)$$

where  $r_i$  and  $E_{\perp i}$  denote typical ion cloud radii and transverse energies in the trap and the last drift tube (subscripts  $T$  and  $L$ ). Further it is assumed that the characteristic transverse energy scales with the space charge potential drop within the ion beam  $\Delta\Phi$ , generated by the electron beam in different magnetic fields

$$\frac{E_{\perp i,T}}{E_{\perp i,L}} = \frac{\Delta\Phi_T}{\Delta\Phi_L}. \quad (5.5)$$

The space charge field of the electron beam can be estimated with the formulas presented in Chapter 2. Ion starting parameters inside the reduced magnetic field have been determined by solving the above equations for an electron beam of 1 A at 10 keV, and assuming an ion cloud radius of 150  $\mu\text{m}$ , corresponding to approximately 1.5 electron beam radii in the central trap. The transverse energy of the ions was estimated to correspond to the characteristic electron beam potential  $\Phi_0$  inside the trap (cf. Equation 2.28).

Ion distributions generated in this fashion have been tracked out of the TwinEBIS last drift tube together with the full electron beam using *TRAK*. Conveniently, the formed ion beam has a waist inside the EBIS extractor electrode. At this point the ion beam is fully separated from the electron beam, and inside a field free drift space, making it the perfect handover point for the LEBT simulations. The normalised ion beam RMS emittance resulting from the simultaneous tracking simulation is  $\approx 0.02$  mm mrad at the beam waist in the extractor with a 95 % beam radius of 2.5 mm.

From this point on the ion beam tracking was performed with the more efficient *Travel* code [142] using field maps generated with the help of *Superfish* [143] for a Gaussian beam with the starting parameters determined in the ion extraction simulations. By tuning the voltages of the adaptor electrode and the three lenses in the beamline, the matching is performed. After establishing a conventional telescopic optic, the transmission of ions into the RFQ acceptance was subsequently maximised in a parameter sweep. This has increased the injection efficiency from initially 55 % (telescopic) to 88 %.

The telescopic and optimised ion optics are illustrated in Figure 5.27 with the corresponding RFQ acceptance plots visible in Figure 5.28. The lens voltages for both optics are listed in Table 5.14. It should be noted that the simulations were performed with a modified conical extractor geometry, instead of the fixed width pipe that is currently in use. The non-Gaussian wings witnessed in the RFQ acceptance plane are attributed to a combination of space charge effects and aberrations occurring at the exit of the ion extractor electrode. The normalised ion beam emittance has grown to approximately 0.03 to 0.035 mm mrad at the end of the beamline, with a large fraction of the growth occurring at the extractor, upstream of the beamline, which

Table 5.14: Voltages of the focusing elements for a telescopic and optimised ion-optical setup.

Element	Telescopic (kV)	Optimised (kV)
Extractor (fixed)	17	17
Adaptor ring	23	23
Gridded lens 1	-8	-9
Einzel lens	9	13
Gridded lens 2	-25	-24.5

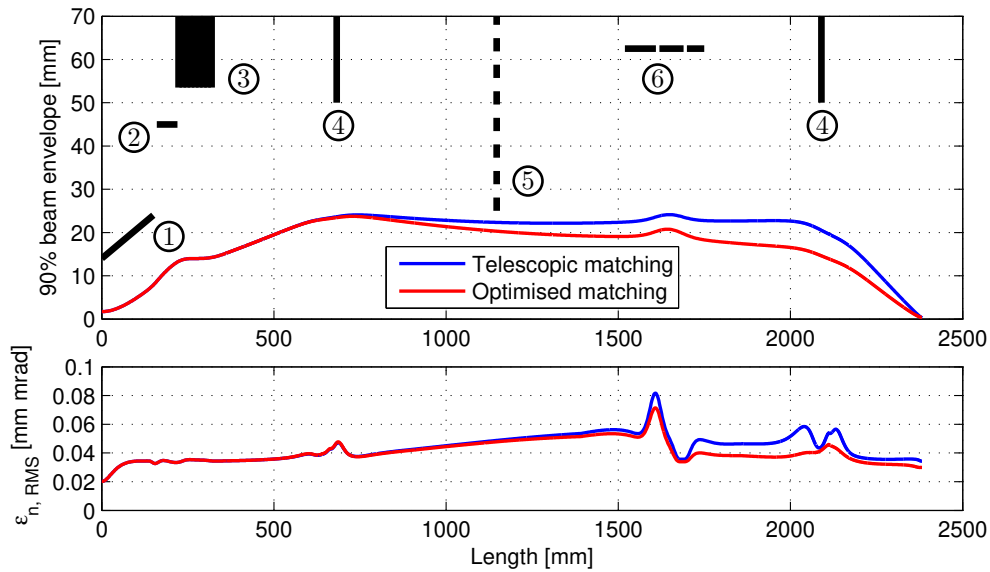


Figure 5.27: Plot of the beam envelope and the emittance for the two determined ion optics at an ion beam current of 3 mA. The balloons indicate: Extractor (1), adaptor (2), accelerating gap (3), gridded lenses (4), the horizontal entrance aperture of the switchyard (5), and the Einzel lens (6). Figure reproduced from Ref. [IV].

is readily explained by strong space charge defocusing in the tight beam waist at low energy. Critically, even under these pessimistic space charge conditions, the beam envelope only fills about half of the electrostatic lens apertures, reducing the influence of nonlinear focusing fields, and passes through the switchyard deflector without losses.

**Ion injection** Looking at a future option of ion injection from an external source, ion optical simulations have also been performed in the reverse direction. For the injected beam, space charge is assumed to be negligible and various ion distributions have been tracked starting from the diagnostic chamber into the outermost drift tube of the EBIS using a precomputed envelope and field of the undisturbed electron beam. Following the same formalism as for translating the extracted ion distribution, it was determined that the normalised RMS emittance of the injected

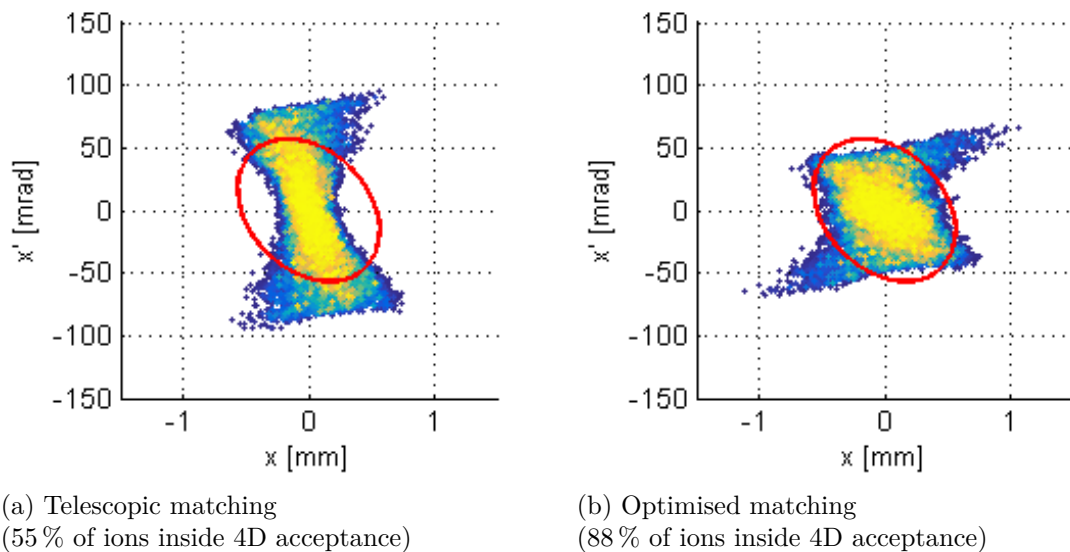


Figure 5.28: Acceptance plots for the RFQ entrance for the telescopic and optimised ion optics. Figure reproduced from Ref. [IV].

beam should not exceed  $0.012 \text{ mm mrad}$  in order to ensure efficient injection into the electron beam volume inside the charge breeding trap and not onto large orbits around it.

We will now take a closer look at the ion switchyard and the gridded lenses.

### 5.5.3 Three-way ion switchyard

The switchyard increases the flexibility of the LEBT and prepares it for future applications. However, its design was tightly constrained by ion optical, spatial, and budgetary concerns. The switchyard should be as short as possible and should not impact the forward beam path. Moreover, it has to maintain a low capacitance to allow for quick pulsing of the electrodes at several 100 Hz and should keep the required deflection voltage below 5 kV per plate for a  $q_i \cdot 30 \text{ kV}$  beam. This mostly rules out two component kicker / bender solutions and the use of resistor ladders for field shaping. The minimum entrance gap was chosen to be 50 mm to accommodate for large beams.

Out of a number of considered designs the most promising one was selected and is presented in Figure 5.29. It features cylindrical electrodes that are tangential to the design trajectories in the entrance and exit plane. This design keeps the deflected ions close to the attracting plate throughout the turn. A cage around the deflector reduces field leakage into the surrounding beamline. Similarly, small ledges at the vertical ends of the deflector plates work against the ground potential leakage from the surrounding structure, which reduces vertical components in the deflector field. Furthermore, the size of the vacuum chamber is increased to a diameter of 20 cm to aid in straightening the electric field in the active volume of the deflector by increasing

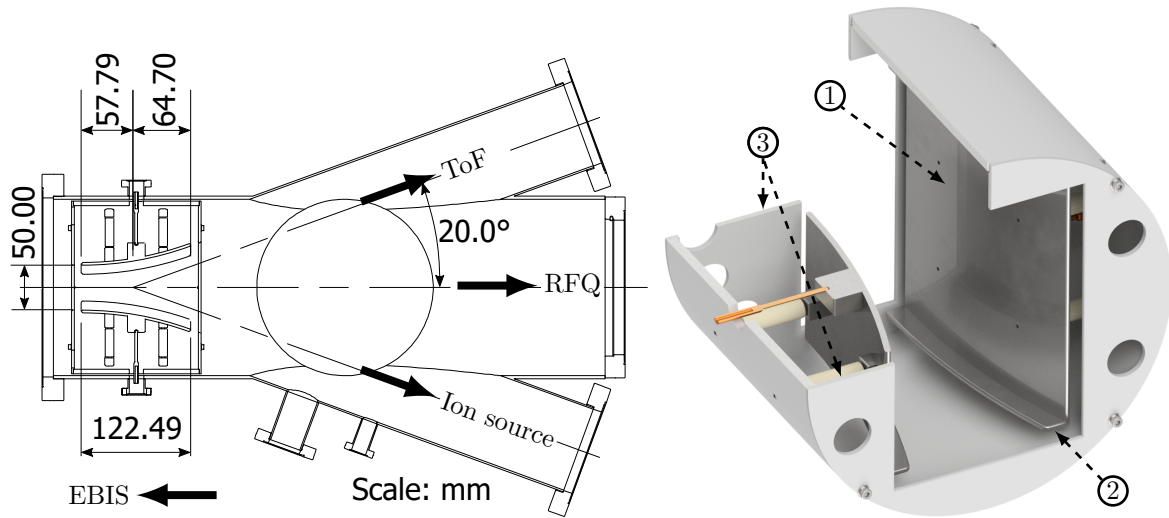


Figure 5.29: Drawing of the ion switchyard and 3D model of the deflector element. Balloons indicate the cylindrical deflector plates (1), with their field correcting rims (2), housed inside a field leakage limiting cage (3). Figure reproduced from Ref. [IV].

the distance to the walls.

There are two relevant scenarios when assessing the switchyard's impact on the beam quality. The first is injection from an ion source installed at a sidearm of the switchyard into the EBIS. Assuming a small emittance ion source, the incoming singly charged ion beam was modelled with a normalised RMS emittance of 0.004 mm mrad and a 90 % beam radius of 4 mm at an energy of 30 keV. The emittance growth after passing the deflector field was simulated with the help of *CST Particle Studio* and found to be below 5 % in all cases. This includes initial transverse beam offsets of up to 10 mm in any direction. Such a beam would still easily fit within the estimated EBIS acceptance of 0.012 mm mrad.

During extraction, the ion beam radius may be large compared to the dimensions of the deflector. In such situations the beam is much more susceptible to field imperfections as simulation studies prove. Using the example of a 180 keV beam of  $^{12}\text{C}^6$  ions, the emittance growth was studied for a selection initial emittances and beam sizes. The results of that scan are plotted in Figure 5.30. The data clearly illustrates the negative effect of beam size on the emittance growth in the horizontal deflection plane, that occurs as the deflecting fields are not uniform across the beam radius. The vertical plane stays largely unaffected by virtue of the suppressed vertical electric field components. As only the side ports of the switchyard are affected by this beam quality degradation, this effect is deemed acceptable. Instrumentation like the TOF spectrometer to be installed there is usually less sensitive to the beam quality than the accelerating RFQ installed in the forward direction. The chosen deflector presents a compromise between

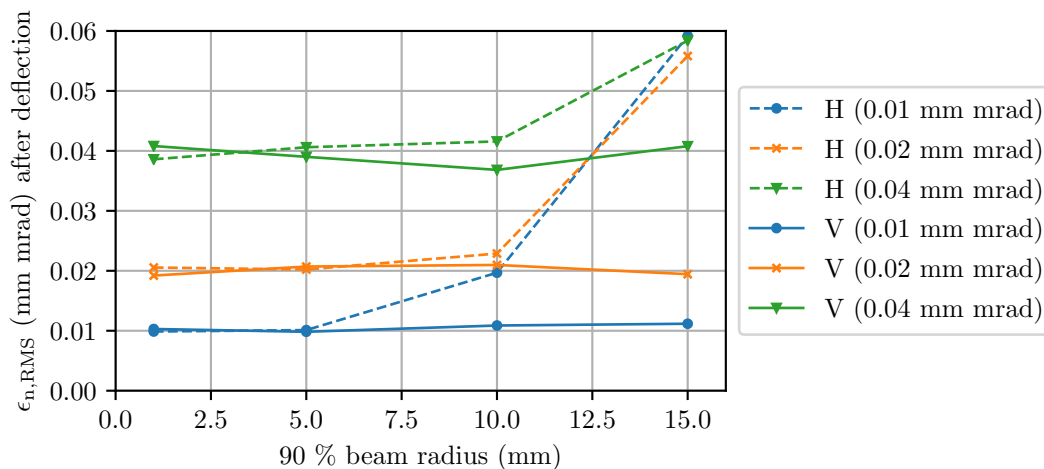


Figure 5.30: Emittance growth in the switchyard deflector as a function of beam size. The initial emittances for horizontal (H) and vertical (V) dimensions are provided in the legend. Figure reproduced from Ref. [IV].

beam quality demands and external constraints.

**Small angle correctors** The beamline features one horizontal and two vertical correcting kickers. These kickers are designed for providing small trajectory corrections and have electrode profiles that were manually optimised to shape a nearly homogeneous field inside a large aperture. The kicker design is shown in Figure 5.31. At a maximum operating voltage of  $\pm 500$  V per plate a deflection angle of  $1.27^\circ$  was determined for a  $q_i \cdot 30$  kV beam with the help of particle tracking simulations. At the same time, the ion emittance growth was negligible even with beam radii up to 15 mm.

#### 5.5.4 Gridded lenses

The focusing field of the gridded lenses (shown in Figure 5.32), is formed between a wire mesh oriented perpendicular to the beam, and the surrounding vacuum chamber by applying an accelerating bias voltage to the mesh. Compared to an Einzel lens of comparable radial dimensions, gridded lenses offer a very strong and linear focusing at relatively low operating voltages [144]. With the presented dimensions, a gridded lens provides a focal length of 530 mm at just  $-8$  kV (for a  $q_i \cdot 30$  kV ion beams). An Einzel lens consisting of 3 equal cylinders with a radius of 45 mm and a length of 80 mm each, separated by 10 mm gaps, would require a voltage of  $-35$  kV to obtain the same focal length.

The model in Figure 5.32 demonstrates how such a lens can be conveniently integrated into a double-sided CF160 flange. The presented design has been dimensioned for holding voltages of up to 35 kV in either polarity. As will be shown in the next section, fine wire meshes are

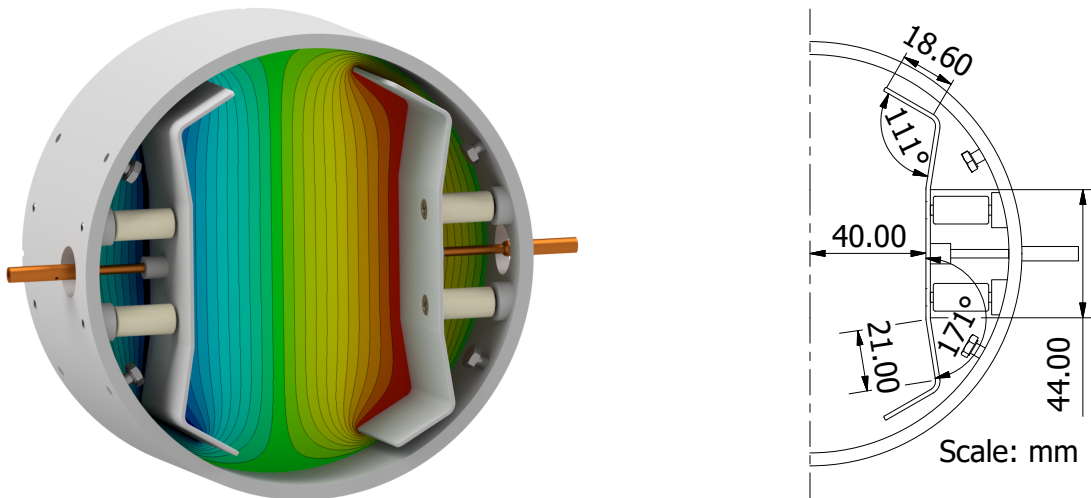


Figure 5.31: Model and drawing of the correcting kicker. Figure reproduced from Ref. [IV].

required for this application. A suitable mesh made up of  $30\ \mu\text{m}$  wires spaced at  $0.5\ \text{mm}$  with a resulting transparency of  $89\%$ , is commercially available. While sputtering by the ion beam is a concern, it has been estimated that these meshes should be resilient against significant damage for several years of continuous operation [145, 146] when considering average ion beam currents in the  $\mu\text{A}$  range.

#### 5.5.4.1 Micro-defocusing in mesh cells

Gridded lenses suffer from a particular optical imperfection generated by the mesh. When the lens is configured with a focusing bias voltage, the ion beam experiences a strong global focusing field. The near-field of every single wire mesh cell however, has a gentle defocusing effect on the beamlet that is passing it. This occurs due to a slight relaxation of the electrostatic potential in the empty mesh cell compared to the surrounding wires. Fine meshes are conventionally abstracted as transparent surfaces in particle tracking simulations, but by actually modelling out the mesh geometry it is possible to quantify the emittance growth at the expense of computational complexity, as was demonstrated in e.g. Ref. [147].

Using *CST Particle Studio* the lenses' impact on the low emittance beam produced by the EBIS has been assessed for various wire mesh pitches. The assumed wire diameter was chosen to be  $50\ \mu\text{m}$  in all cases, and the simulations also include a baseline for a lens modelled as a perfect transparent surface (corresponding to a wire spacing of  $0\ \text{mm}$ ). Ion beams with a range of initial emittances and a fixed  $90\%$  radius of  $15\ \text{mm}$  have been tracked through a lens biased to  $-8\ \text{kV}$ .

The results of these studies are presented in Figure 5.33 where they are also compared to the emittance increase inside the equivalent Einzel lens described above. For the baseline reference

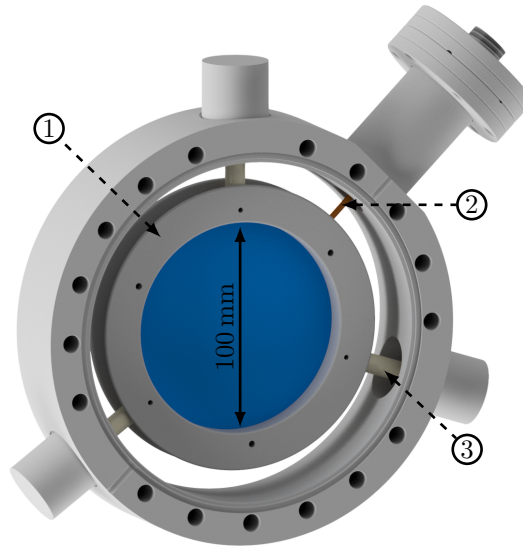


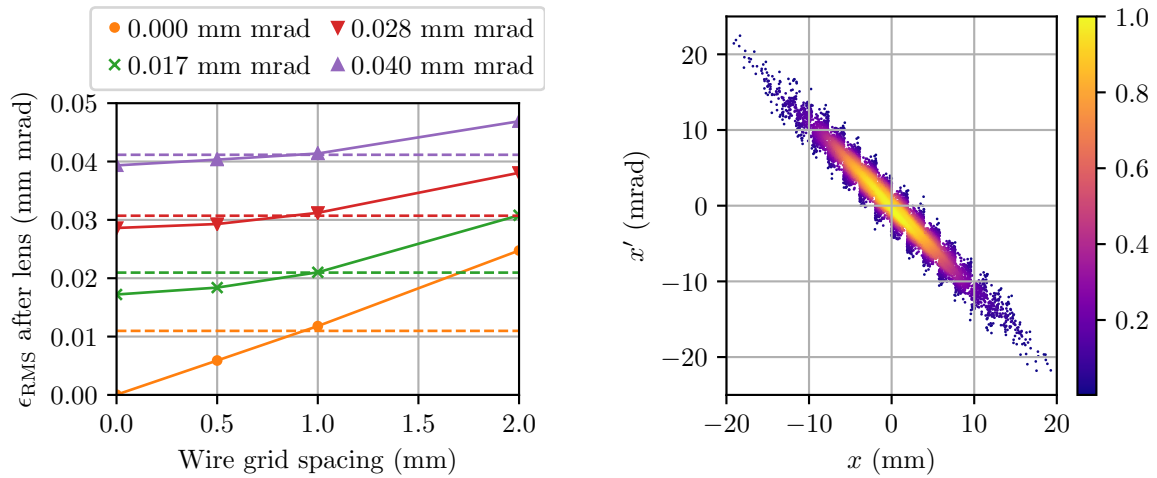
Figure 5.32: Model of a gridded lens integrated into a CF-160 vacuum flange with a thickness of 50 mm. The high voltage isolating supports (3) are retracted into cutouts to support grid bias voltages of up to 35 kV. The wire mesh is held by a clamping ring (1) and contacted with a spring-loaded pin (2). Figure reproduced from Ref. [IV].

of a perfectly flat gridded lens, the emittance growth is essentially zero, underlining the high field quality of the lens. For large mesh spacings, the beam emittance is increased by the micro-defocusing effect illustrated in the phase-space plot. Based on these results it has been decided that a mesh with a pitch  $\leq 1$  mm should be chosen for the TwinEBIS beamline in order to keep the emittance increase at an acceptable level.

#### 5.5.4.2 Secondary electrons

A fraction of the ion beam will collide with the wires making up the mesh. Besides sputtering of the wire material, these collisions can spray secondary electrons into the beamline. When operated in an ion-focusing configuration, the lens has a negative bias and will accelerate and defocus the electrons generated on its surface. Field non-uniformities around the wires make it difficult to predict where exactly electrons will be generated and on which surfaces they end up eventually. This is a concern with regard to the diagnostic equipment in the beamline which must not be negatively affected by intercepting secondary electrons in addition to the ion beam.

Since *CST Particle Studio* is unable to automatically generate secondary electrons for ions as primary particles, a custom procedure has been developed to estimate the distribution of electrons in the vicinity of the gridded lens. Firstly, the ion beam is tracked through the lens in a simulation model comparable to that described in the previous section. Afterwards the collision locations and respective surface normal vectors for every intercepted trajectory are evaluated with an external *Python* script making use of the *FreeCAD* project [78, 148]. These parameters



(a) Plot of the emittance growth. The initial emittance values are listed in the legend, dashed lines indicate the emittance growth in a comparable Einzel lens.

(b) Phase space plot of the 0.04 mm mrad beam after passing a lens with a wire spacing of 2 mm. The parallelogrammatic steps are caused by cell-wise micro-defocusing at the wire mesh.

Figure 5.33: Emittance growth for a gridded lens as a function of inter-wire distance. Figure reproduced from Ref. [IV].

are then fed into a simple model generating an initial distribution of secondary electrons which can be loaded back into the tracking simulation to determine the final electron distribution.

Generating an initial distribution of secondary electrons requires knowledge about the interaction of highly charged ions with the surface material onto which they impinge at an intermediate energy. A helpful review of this highly complex field is available in Ref. [149]. Simple scaling laws from this review and from Refs. [150–152] have been combined with measured electron yields for primary beams made up of carbon ions [153] to define a simple yet versatile generation model. The mean yield  $\langle\gamma\rangle$  of electrons scales with the incidence angle  $\Theta$  (measured with respect to the surface normal vector) as

$$\langle\gamma_{\Theta}\rangle = \gamma_0 / \cos \Theta. \quad (5.6)$$

Here, angles are clipped to a maximum of  $80^\circ$  to regularise the yield value. A comparable effect has been observed in multiple measurements [149].  $\gamma_0$  is a free scaling factor, that depends on the exact weight, charge and energy of the primaries. The mean yield is computed for every impact location, and subsequently the actual number of generated electrons is drawn from a Poisson distribution with the appropriate expectation value. The initial energy of the electrons follows a  $\Gamma$  distribution, with a free parameter  $\mathcal{T}_0$  fixing the mode. The electron emission direction is largely independent of the incidence angle. As such, the emission angle  $\vartheta$  follows a cosine

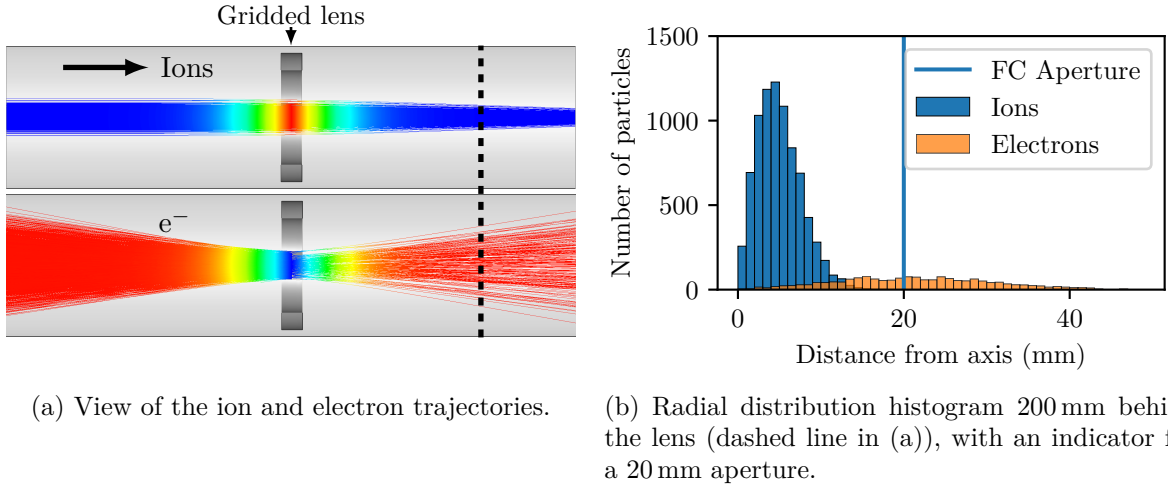


Figure 5.34: Secondary electron stream around a gridded lens. Figure reproduced from Ref. [IV].

distribution, with a uniform distribution of azimuthal angles  $\phi$  around the local surface normal

$$\vartheta \sim \cos \vartheta \text{ where } 0 < \vartheta < \pi/2 \quad (5.7)$$

$$\phi \sim U(0, 2\pi). \quad (5.8)$$

The wire mesh modelled for the simulation has a wire thickness of  $50 \mu\text{m}$  with a pitch of  $0.5 \text{ mm}$ . Resulting in a transparency of just  $81\%$ , this represents a pessimistic case in terms of primary beam losses on the gridded lens. Made up of  $^{12}\text{C}^{6+}$  ions, the primary beam had an energy of  $180 \text{ keV}$  and was directed at the lens biased to  $-8 \text{ kV}$ . With these impact parameters, literature suggests that reasonable values for the free parameters of the electron generating model are  $\gamma_0 = 9$  and  $\mathcal{T}_0 = 10 \text{ eV}$  [153].

Figure 5.34 contains a summary of the simulation results. Evaluating the collision locations of the primary beam results in an electron count exceeding the ions by a factor of approximately  $250\%$ . Most of these electrons are generated on the front face on the lens and are accelerated towards the source of the ion beam, where no active instrumentation would be expected. The remaining secondaries travel forward with the ion beam, but are quickly dispersed in the lenses defocusing field. The histogram shows an estimate for the particles arriving within a  $40 \text{ mm}$  aperture, located  $200 \text{ mm}$  behind the lens. Such an aperture could represent for example a Faraday cup. The total electron contribution within the aperture is found to be smaller than  $10\%$  of the total particle flux. Considering that the ions are in high charge states, the resulting error for a beam current measurement would be at an even lower level.

## 5.6 Conclusion

In this chapter the progress made in the MEDeGUN project has been presented. The MEDeGUN concept was originally developed under the design constraints set by the electron gun's intended use as the driver for an EBIS provisioning fully stripped carbon ion beams with parameters suitable for LINAC-based particle irradiation therapy applications. A summary of the MEDeGUN design, as well as modifications to the original concept, have been presented in the beginning of this chapter. Alongside it, a description of TwinEBIS, the test stand where the commissioning experiments were carried out, has been provided.

Initial tests were focused on the electron beam transmission through the EBIS apparatus. Our measurements have yielded a gun perveance of  $1.1 \mu\text{A}/\text{V}^{3/2}$ , provided that the cathode is heated sufficiently. This value is in line with measurements from the first commissioning run, and agrees well with recent computer simulations of the electron gun geometry. The electron gun is able to produce a stable electron beam at operating temperatures of around 1300 K, which is expected to result in a long cathode lifetime. While the cathode has been exchanged preemptively after the interlock failure, no cathode performance degradation was witnessed after multiple years of intermittent operation.

The electron beam energy has been lowered to demonstrate that the electron beam could successfully be transmitted even under the least favourable conditions. This test increases the confidence, that the beam produced by MEDeGUN does not feature excessive trajectory pitch angles and will be operable in the intended magnetic focusing field of 5 T without suffering from reflections in the field gradient. As summarised in Figure 5.10, the electron beam can approach the Bursian perveance limit closely over a large range of beam currents, while keeping the accumulated loss currents smaller than 1 mA, (corresponding to less than 1‰ of the total current). Purposefully approaching the Bursian limit has further confirmed that the beam behaviour agrees well with theoretical space charge models, and provides a rough confirmation of the theoretically expected beam radius of  $\approx 105 \mu\text{m}$ .

Continuing with first charge breeding experiments quickly revealed that the total charge extracted from the EBIS was lower than expected; which could not be mitigated with higher gas injection pressures or longer breeding times. Initial measurements with argon gas injected into the EBIS running at the nominal beam current level of around 1 A, have seen a total charge of just  $\approx 1700 \text{ pC}$  detected on the Faraday cup, which amounts to roughly a tenth of the total electron charge forming the space charge well in the trap. Injecting more gas would change the observed rate of charge production but not shift the saturation level.

Follow-up experiments carried out at just 200 mA beam current, have demonstrated that much higher degrees of space charge compensation in the trap are indeed achievable, with ion bunch charges amounting to a 90% equivalent of the electron charge successfully detected on the Faraday cup. Indeed, more charge could be extracted even in absolute terms in this config-

uration, with pulses approaching 2500 pC under the right conditions. This run also provided a first indication for significant ion losses in the extraction process and a strong sensitivity to the extractor electrode potential.

Further investigations at the nominal beam current have confirmed that the charge detected on the Faraday cup increases as the extractor voltage is ramped up. This suggests that the EBIS is not necessarily failing to produce the expected levels of bunch charge, but that the ions cannot be extracted from the electron beam and transferred into the beam line efficiently. Rearranging the extractor wiring and installing a load resistor, has made it possible to detect positive current spikes and to measure that a significant amount of ions is indeed lost on the surfaces of the extractor itself. This experiment (and the following TOF experiments) suggest that the beam energy, or cathode potential, are also linked to the extraction efficiency. In summary, our observations reveal, that there are undoubtedly problems relating to the ion beam extraction, and that the losses are strongly correlated with the potentials inside the collector / extractor region.

The extraction process was investigated further with the help of dedicated computer simulation studies carried out by Woudenberg [140]. The results of these studies suggest, that ion losses on the extractor surface are not easy to provoke, unless there is a significant misalignment or tilt of components on the collector-side of the EBIS (e.g. a shift of the drift tube structure) or if the ion cloud starts out significantly wider than the electron beam. Furthermore, the existence of space charge induced lensing was considered. The suspicion that a virtual cathode may be forming in the suppressor electrode (where the beam is particularly slow) could not be confirmed for typical operation conditions. However, the extracted ions are much slower than the electrons in the beam, boosting their resulting charge density. To rule out that this has a negative effect on the extraction, it was suggested to carry out comparative studies with slow ion extraction in the future.

These findings have since triggered a redesign of the collector led by A. Pikin, aiming to improve the vacuum separation between collector and trap, and to reduce the likelihood of elastically reflected electrons returning from the collector back to the drift tubes. This is achieved by constricting the collector entrance to the smallest practical diameter and using an auxiliary coil to compress the beam while it traverses the aperture. Additional magnetic shielding helps to accelerate electron beam divergence inside the collector. The extractor was shortened slightly to reduce the risk of scraping an expanding ion beam. The issue of reflected electrons had already been considered in the original MEDeGUN design study [88, 115] and resurfaced during the investigations of Woudenberg. One suspicion is, that the collector was unknowingly misaligned during the electron beam commissioning, as this can reduce the amount of reflected electrons reaching the anode, which appears favourable when looking at the electron beam in isolation. This would then be reflected in extraction problems when starting to work with ions.

Beyond the extraction issues, the TOF spectrometry of the extracted ion bunches has revealed that the charge breeding process is facing unexpected problems, too. In the xenon breeding experiments presented above (and other measurements that could not be included in this document) a fast onset of charge breeding followed by a rapid stagnation of the mean charge state development is observed consistently. The early evolution  $\lesssim 10$  ms of the charge state spectra supports effective current densities in excess of  $1500 \text{ A/cm}^2$ . However, this performance level cannot be maintained, and the charge state distribution appears to freeze, with only the integrated signal level continuing to increase until charge saturation is reached. There is a clear correlation of the injection pressure and the attainable charge state, with the charge state decreasing as the pressure rises. While this is a typical indicator for the occurrence of charge exchange which can counteract the electron impact ionisation, our estimates suggest that unrealistically high background pressure levels would be required in order for this effect to manifest as early as observed.

Another possible explanation for the poor charge breeding performance is a degraded overlap of the electron beam and ion cloud. As shown above, the results of the axial energy scans can be used to estimate the overlap factors under a number of assumptions. The modelling yields estimated overlap factors close to 0.5 after a breeding time of 10 ms. This estimate agrees well with the ratio between the observed effective current density of  $\approx 1600 \text{ A/cm}^2$  and the theoretically achievable value of around  $3100 \text{ A/cm}^2$  for a perfect electron beam and perfect ion overlap. Usually, for gas injection, one would expect the ions to have a good overlap, since they are created inside the beam, resulting in a good radial confinement. As time progresses the ions are heated and the space charge well is compensated by the accumulating positive charge. In this situation the ion cloud can grow considerably, which in the worst case scenario can drive the overlap factor close to zero, as the electron beam occupies only about 2% of the drift tube diameter. The existence of extraordinary heating mechanisms like the emergence of plasma instabilities suspected by some authors [26, 27, 154–157] can neither be confirmed nor rejected with the collected data, but could serve as an explanation for a rapid increase of the ion temperature. An extended ion cloud with poor beam overlap is also in line with the findings for possible reasons explaining the extraction losses noted above.

For its use as a carbon ion source, the EBIS should be able to hold  $1 \cdot 10^9$  to  $1 \cdot 10^{10} \text{ C}^{6+}$  ions (accounting for some loss margin), which corresponds to an upper limit of 9600 pC. The theoretical capacity of the TwinEBIS / MEDeGUN setup amounts to approximately 16 000 pC, and charges of up to 3500 pC have been extracted onto the Faraday cup, with additional ions lost on e.g. the extractor. That provides some confidence that the required capacity and charge output is within reach. Our experiments further show that current densities of  $1600 \text{ A/cm}^2$  are achievable for short periods. For pulsed ion injection, 80% of the injected carbon ions are expected to be fully stripped of electrons within 7 ms at this current density. In principle,

however, the achievable current density should be even higher in the 2 T test magnet, but the data presented above illustrates that even the effective density of  $1600 \text{ A/cm}^2$  cannot be maintained for extended breeding cycles. To progress, it is important to understand the nature of the underlying effects that cause the performance degradation.

At the time of writing, the TwinEBIS test stand is being prepared for another run with MEDeGUN. The components for the ion beamline described in the last section of this chapter have arrived at CERN and the installation of the line and its infrastructure is finished. The EBIS as well as the electron gun, have been equipped with precision metrology markers, that allow CERN's survey team to perform highly accurate alignment measurements of the assembled system. A dedicated 5-axis alignment stage has been acquired to improve control over the electron gun position, and the new collector / extractor system has been installed. Together these modifications are expected to significantly improve the confidence about the alignment of the individual components, and the beamline provides additional instrumentation to characterise the extracted ion beam. For the next commissioning run it will be crucial to determine whether the observed performance degradations are rooted in mitigable design, assembly and operational errors, or whether there are fundamental physical limitations that destabilise the non-neutral plasma column in the EBIS. Additionally, it would be desirable to test the charge breeding of a carbon-containing gas to benchmark the electron gun against its intended use case. Providing a sufficient feed rate of carbon particles into the electron beam can provide its own challenges as the work of Taylor et al. [134] has shown, and alternative injection mechanisms like the use of a gas cell, molecular beam, or external ion injection may have to be explored.



# CHAPTER 6

## SUMMARY & OUTLOOK

In the field of particle acceleration, electron beam ion sources serve as charge breeders producing beams of highly charged ions, which couple more strongly to the electric fields used for acceleration and hence maximise the attainable energy gain in a given structure. This thesis presents recent advances made towards improving the charge breeding performance of EBIS devices and facilitating the simulation-based interpretation of their performance characteristics.

**Charge breeding simulations** Contrary to EBIT apparatuses, electron beam ion sources rarely feature extensive diagnostic instrumentation and usually offer no means of carrying out measurements within the primary working volume of the source. Therefore, characterisation measurements are mainly limited to secondary witness signals – typically the ion beam current and composition – recorded outside the EBIS, after a charge breeding cycle has concluded. Additionally, a high repetition rate of the source is often desirable, which implies that a typical breeding cycle is dominated by transient behaviour and will commonly end before an equilibrium or stationary state is reached, limiting the applicability of explicit analytical models. In this situation, modelling and simulating the charge breeding process numerically can shed additional light on the hidden processes acting out inside the ion trap and link them to measurement data.

Chapter 3 contains a review of the established expressions commonly used to describe the charge breeding process with a set of coupled rate equations and details the implementation of a simulation toolbox in a custom *Python* package dubbed *ebisim*. The terms forming the rate equations are rooted in elastic and inelastic collision rates, and their computation requires knowledge of the associated interaction cross sections. A simple charge breeding model can be limited to tracking the charge state distribution of an initial ion population over time, its evolution driven only by electron impact ionisation, resonant and non-resonant recombination, and charge exchange. Such a model, introduced alongside the charge state changing interactions and their cross sections in Chapter 2, is mathematically more tractable and allows for very fast numerical integration, which makes it suitable for purposes like fitting, or parameter optimisation.

More comprehensive modelling introduces the concepts of collisional heating, ion temperature, and related effects, as presented and discussed in Chapter 3. A finite temperature allows ions to spread out in the trapping potential created by the electron beam and naturally leads to questions about the radial ion density distribution and the degree of overlap between the electron beam and the ion cloud, which has a direct impact on charge breeding performance. Determining these transverse properties, requires finding a self-consistent solution to the Poisson equation for electrons and ions simultaneously. Thermal coupling and temperature equilibration introduce meaningful interactions between all ions, regardless of the element they represent. Heavy ions can transfer heat to lighter collision partners, that are lost from the trap more easily due to their reduced charge state, resulting in a removal of excess heat in a process known as evaporative cooling. While the temperature rates can be expressed similarly to the terms for the inelastic processes, they increase the total number of equations, introduce a full coupling between all species and charge states, and require the solution to the nonlinear Poisson equation. This results in a much more powerful, but also computationally expensive simulation.

The *ebisim* package, created in the scope of this thesis, provides the function implementations and data resources required to perform charge breeding simulations based on the presented modelling approaches. Notably, it includes a custom specialised solver for the Poisson problem, allowing for a fast computation of the transverse distribution on every time step, and hence eliminating the need for performance-degrading intra-time step density corrections. To improve robustness, *ebisim* works with temperature rate equations, as expressed in Chapter 3, instead of the more commonly used energy density rate equations. Distributed freely and built on top of established and well-known scientific computing tools, the code is written to provide a simple interface but to also be extensible by its users, if the provided models or data tables are insufficient for a specific scenario. Components of this package have been used to aid in the analysis and interpretation of charge breeding data presented in Chapter 4 and Chapter 5. Additionally, a web-based graphical user interface, that exposes basic features of *ebisim* and enables clients to run simplified simulations without the need to install software locally, has been deployed at CERN and sees regular use by machine operators and researchers.

The capabilities of the simulation code have been illustrated by comparing simulation results to experimental data recorded at the REXEBIS setup. For the demonstration experiment the electron beam energy was scanned over the approximate range (2400 to 2900 eV) that allows for driving of KLL-type dielectronic recombination resonances of  $^{39}\text{K}$ . Both, experiment and simulation, show that the resonant recombination transitions possess sufficiently large cross sections to shift the charge state balance of the extracted ions. Being able to deactivate individual processes in the simulation and to freely tune initial conditions has proven helpful in highlighting their importance and contribution to the heavily coupled system, providing motivation for the additional modelling and computational effort. With adequate parameter tuning, a single con-

---

figuration can predict reasonably well the abundance of multiple charge states over an extended breeding time window of up to a full second and across a range of resonant recombination cross section peaks. The best reproduction of the experimental data is achieved by the inclusion of a small amount of neon background gas, which is known to be present in the real REXEBIS setup. It acts as a coolant for potassium ions, but also contributes to compensating the space charge and changing the net energy of the relatively weak electron beam along the cycle.

Access to a flexible simulation tool has proven valuable throughout the studies presented in this document and has repeatedly helped to understand and interpret experimental results. However, there are known limitations and stability issues with the presented formulas and implementations, especially when the charge breeder system approaches extreme conditions. Particularly shallow traps and hot ion populations for example, implicitly violate the assumption that ions follow a thermal distribution, as the high energy tail would not be contained by an insufficient trapping potential. In practice this can result in the computation of non-physical loss rates and invalidate the simulation. Similar problems can occur when small collision rates numerically suppress ion losses and paired with a steady influx of new ions eventually allow for an overcompensation of the trap. Moreover, a proper inclusion of the magnetic field contribution to radial ion trapping is not easily possible in the presented formalism. Extreme operational regimes can be interesting when investigating high performance charge breeders or dealing with extended breeding time experiments where the compensation degree grows fast or very high, or when attempting to model ion clouds with extraordinarily high temperatures. There is therefore ample motivation for a continued development of improved simulation tools for the EBIS and EBIT community. With an overall improved reliability would also come the option to more confidently benchmark differing models against measurements in order to determine the most appropriate formulation, as for example alternative ion loss rate expressions or ionisation cross section models.

**Nonadiabatic electron gun for REXEBIS** At the ISOLDE rare isotope beam facility, REXEBIS operates as a charge breeder preparing beams of highly charged exotic ions for injection into the REX/HIE post accelerator. After many years of successful operation with its original electron gun, performance limitations linked to the utilised LaB<sub>6</sub> cathodes meant that the EBIS was deserving of an upgrade. Susceptibility to thermal stress damage had imposed a practical beam current limit of typically 200 mA, and with a cathode immersion field of 200 mT peak current densities of just around 100 A/cm<sup>2</sup> could be reached in the trap. An improved current density reduces the charge breeding time and allows for a faster cycling of the REX beam preparation stage. This is reflected in reduced peak currents and pile up events in the experiments. Moreover, it can unlock experiments with short-lived isotopes that are at risk of decaying during beam preparation.

The development and the commissioning of the new electron gun as well as the characterisation of the upgraded charge breeder are presented in Chapter 4. Because a working charge breeder is critical for the operation of the HIE ISOLDE complex, a low risk upgrade path was chosen by sticking to an immersed electron gun design and limiting the foreseen beam current to 500 mA for regular operation. These choices help to ensure that the high injection efficiency of REXEBIS is maintained and that beam induced vacuum degradations are kept to a minimum, factors that are particularly important when working with rare isotope beams.

To obtain the required improvement in beam compression, the cathode would be retracted from the main magnet, reducing the immersion field experienced by the cathode. An iterative design process settled on a Pierce-type electron gun featuring a cathode with radius 1 mm, positioned in a magnetic flux density of 70 mT. For typical beam energies of a few keV the predicted Herrmann beam radius is 187  $\mu\text{m}$  inside the 2 T focusing field, corresponding to a current density of around 450 A/cm<sup>2</sup> given a beam current of 500 mA. These specifications require a considerable emission current density of up to 16 A/cm<sup>2</sup> on the cathode surface. Faced with a limited selection of materials able to provide such current densities under quasi-permanent operation, IrCe alloy cathodes were chosen based on claims of the successful operation of such devices at densities of up to 20 A/cm<sup>2</sup> over periods exceeding 5000 h.

The high emission current density and low beam energy are at odds with the reduced magnetic field at the cathode. Large transverse space charge forces are not met with a sufficient focusing force, causing a rapid divergence of the beam and large amplitude oscillations of the beam cross section. Without further mitigation efforts this puts the electron beam at the risk of being scraped by small apertures inside of and close to the gun. The transverse oscillations continue as the beam is adiabatically compressed, and can create a longitudinal modulation of the space charge field, which can cause parasitic trapping of ions or unstable beam transmission in extreme cases. Any immersed beam necessarily performs such radial oscillations but a proper matching of the beam size and convergence angle to the magnetic focusing field can reduce the amplitude significantly.

Studies at BNL had shown some success in reducing radial beam ripple by using a ferromagnetic insert inside the gun's anode that creates a strong and short scale modulation of the magnetic field. Such a field modulation breaks the common assumption of adiabaticity, as the momentum vector of charged particles cannot follow the magnetic field lines as closely as in slow field gradients. There, the beam can behave in ways that are not easily linked to the equations for space charge balanced flow. In systematic simulations, presented in Chapter 4 we have shown that the nonadiabatic damping (and excitation) technique can be decoupled from the electron gun and hence be of interest for various electron beam applications. An appropriately tuned short-range depression of the magnetic field can be aligned with any converging section of a coherently oscillating beam to provoke a damping of large amplitude oscillations. The transition

---

region appears to stitch together two valid solutions to the beam envelope equation with different amplitudes found on either side of the nonadiabatic element. In practice, the depression can be created for example by a small passive iron ring placed around the magnetic field axis.

This solution was adopted for the new REXEBIS gun, allowing for small positional adjustments of the ring by threading it onto a dedicated adapter piece located between the gun and the drift tube structure. Additionally, it is possible to vary the beam velocity in the adapter to shift the descending slope of the beam envelope along the field axis. Particle tracking simulations were used to confirm that the nonadiabatically damped beam is operable over an extended current and energy range and can compensate for small installation errors.

First tests of the new gun quickly revealed that approaching the desired current of 500 mA, transfers the cathode in the thermionically limited emission regime, despite the use of excessive heating. As this effect is commonly accompanied by decreased beam stability and increased loss currents, the current is rarely pushed beyond 350 mA. This also protects the cathode from over-temperature damage. In this configuration, the total detected loss currents amount to well below 1 mA. The gun perveance was measured at low emission currents to be  $0.87 \mu\text{A}/\text{V}^{3/2}$ , which is a little higher than the simulated value of  $0.73 \mu\text{A}/\text{V}^{3/2}$ .

The reduction of the beam current could affect the acceptance for injected ions, and diminish the efficiency of the charge breeder, but in practice we have not observed such a degradation. Commonly, 70 to 80 % of the injected ions are successfully extracted from the charge breeder after the breeding cycle, which is an excellent value. Even after filtering for a single charge state, end-to-end conversion efficiencies of up to 35 % were recorded in favourable cases. The achievable charge state purity agrees well with *ebisim* simulation predictions. At the same time there was no significant increase of background current with respect to the original electron gun, suggesting that the excellent vacuum in the EBIS is maintained. Trace amounts of ions originating from the cathode alloy were found to be negligible in a high sensitivity measurement.

To gauge the charge breeding performance, various elements were injected into the EBIS either as singly charged ions or in neutral gas form and processed at varying beam currents. The measured charge state evolution was then fitted with a charge breeding model built on *ebisim* to estimate the effective current density required to drive the charge state evolution at the experimentally observed pace. The current density estimates cover an unexpectedly large range and in some cases far exceed the theoretical current density of the electron beam. For a beam current of 300 mA, the fits produce current densities ranging from 265 to 424 A/cm<sup>2</sup>. On average, the electron beam appears to show slightly higher effective densities than expected, which helps to compensate for the reduced beam current. Our studies have also uncovered significant discrepancies between the simulated and measured charge state evolution of potassium, which indicate limitations of the Lotz ionisation cross section model.

In all experiments the charge breeding appears to slow down over time at a rate faster than

explained by the shrinking cross sections, which means that the efficient current density is decreasing. Despite the large range covered by the fitting results, similar behaviours are observed for ions of similar proton number and mass. As expected, accelerated breeding is observed early on for gas injection, and heavy elements appear to consistently experience higher effective current densities than lighter ones. A possible explanation is that the beam density profile is not uniform but peaks on axis. Heavy ions tend to be confined closer to the beam axis, making them more sensitivity to locally inflated current densities. As time progresses the overlap of ions and electron beam shrinks due to heating effects and the effective current density drops.

The charge state evolution experiments have been complemented with axial energy measurements, that employ an energy-selective extraction scheme to measure the kinetic energy distribution of ions inside the EBIS, and enable the association of a temperature value through the fit of a Maxwell Boltzmann distribution. The implied ion heating rates are roughly comparable to predictions of the Spitzer heating model. Qualitatively, the behaviour of the ion temperature increasing over time agrees with expectations and matches the observation a decaying effective current density, which could be explained by a shrinking overlap factor. However, attempts of quantitatively linking both measurements were not successful.

At present, REXEBIS, featuring the new electron gun, is in routine operation with electron beam currents of typically 250 mA. The increased robustness and life-time of the IrCe cathodes has significantly reduced the need for interventions on the apparatus and increased the overall reliability of the system. It continues to operate with performance characteristics similar to those recorded during the commissioning and provides significantly accelerated charge breeding compared to the old electron gun, particularly for heavy elements. Recently, the option of breeding into higher charge states has proven helpful in mitigating for a degradation of the accelerating fields in the HIE linear accelerator that limits its acceptance to  $A/Q < 4$ . Since the commissioning run, single charge state efficiencies of up to 55 % have been recorded for  $^{39}\text{K}^{17+}$ , and  $\text{U}^{61+}$  ions were produced at a level of 20 % in 395 ms. As REXEBIS satisfies the facility and user requirements, no immediate further upgrade is planned. However, our design studies suggest multiple upgrade paths such as increasing the beam current, or further reducing the cathode magnetic field. A scandate-impregnated dispenser cathode and the required assembly hardware are ready for testing if higher beam currents are required.

**MEDeGUN** The requirements set by concepts for next generation ion beam irradiation therapy facilities have motivated the development of a high-throughput charge breeder. There is a demand for an ion source capable of providing beams of fully stripped carbon ions in bunches of  $1 \cdot 10^8$  to  $1 \cdot 10^9$  with pulse lengths on the microsecond scale at repetition rates of 300 to 400 Hz. These requirements align well with the capabilities of an EBIS, but considerable progress in charge breeding speed and throughput capacity is needed to meet the needs of therapy applica-

---

tions.

MEDeGUN, discussed in Chapter 5, is a prototype for a high current, high compression electron gun designed to drive an EBIS capable of generating a carbon ion beam with the required intensity parameters. Aiming to achieve the highest possible current densities, while minimising the cathode's emission density in an attempt to maximise its lifespan, the gun is designed to produce a Brillouin type electron beam, with close to zero magnetic field penetrating the cathode surface. An M-type barium dispenser cathode with 6 mm radius is able to provide the design current of 1 A at temperatures of just around 1300 K, and a design gun perveance of  $1 \mu\text{A}/\text{V}^{3/2}$ . In the 2 T focusing field available at the TwinEBIS test stand, the final electron beam radius is expected to be  $\approx 105 \mu\text{m}$  at a beam energy of 10 keV translating to a theoretical current density of  $2900 \text{ A}/\text{cm}^2$ . Eventually the gun is envisioned to run with a 5 T focusing field, resulting in a beam radius of  $65 \mu\text{m}$  or a current density in excess of  $5000 \text{ A}/\text{cm}^2$ . Save for small modifications, the gun design has remained unchanged with respect to the first electron beam test run carried out prior to this thesis. Numerous commissioning experiments were carried out with MEDeGUN at the TwinEBIS test stand.

Electron beam tests have confirmed the previously measured gun perveance of  $1.1 \mu\text{A}/\text{V}^{3/2}$ , which agrees well with the latest computer simulations. Multiple factors motivated exploring the lower beam energy limits: The space charge capacity of the EBIS increases when the electron beam is slowed down, and the cross section for the final ionisation step of carbon peaks at just around 1.5 keV. Additionally, decelerating the beam increases the sensitivity to trans-laminar electron trajectories with excessive pitch angles with respect to the magnetic field, which could result in loss currents due to magnetic reflections when stronger focusing fields are used. We have repeatedly approached closely the Bursian perveance limit – where space charge effects dramatically reduce the beam energy – for beam currents  $\geq 1 \text{ A}$ , while keeping the integrated loss currents below 1 mA, including the set target of transmitting 1 A at less than 4 keV after space charge corrections. This demonstrates a good beam quality and stability even under unfavourable conditions. Pushing even further towards the Bursian limit has demonstrated a sudden energy-dependent jump of loss currents close to the theoretical limit. These observations indicate that the beam propagation aligns well with theory and provide a loose confirmation of the expected beam size.

Initial charge breeding experiments were focused on determining the total charge production rate and storage capacity of the EBIS. First measurements recorded bunch charges limited to below 2000 pC, amounting to just about a tenth of the integrated negative charge of the electron beam in the 80 cm long trapping region of TwinEBIS. Follow-up experiments revealed that significantly higher relative compensation degrees, exceeding 80 %, could be recorded when running with just 200 mA, and that the charge reaching the Faraday cup was strongly correlated with the voltage bias applied to the ion extractor electrode. Subsequent investigations were able

to confirm the suspicion that losses in the extraction process contribute to the low reading on the charge detector and that a significant fraction of the beam is indeed lost on the extraction electrode itself, with additional ions likely lost on other unmonitored surfaces. Our measurements suggest that the severity of losses is sensitive to the beam current and the relative voltages between elements in the collector region of the EBIS. Simulation studies indicate a large initial ion cloud radius or a misalignment of electrodes with respect to the magnetic field as possible root causes for poor extraction efficiencies [140].

The charge state composition of extracted bunches was analysed with the help of a TOF spectrometer. As exemplified by the charge breeding of xenon at different pressures, these experiments reveal a very inconsistent charge breeding performance. Whilst charge breeding proceeds very quickly for short intervals  $\leq 10$  ms indicating an effective current density on the order of  $1500 \text{ A/cm}^2$ , the process virtually comes to a standstill for longer breeding times. The integrated charge can keep growing, but the relative distribution of charge states no longer changes significantly. Charge states of around  $40+$  should be achievable with the given electron beam, but the charge stabilises at just  $10+$  to around  $20+$ , depending on the injection pressure. The observed stagnation of the charge breeding cannot be explained by charge exchange alone, as the background gas pressure is not sufficiently high.

By combining the TOF spectrometer with the energy-selective extraction scheme also previously used at REXEBIS, charge state resolved ion temperature measurements were carried out. The information about the charge state distribution was used to generate artificial ion distributions corresponding to varying degrees of space charge neutralisation. Pairing these with the ion temperatures and using the self-consistent transverse ion density model introduced in Chapter 3, allows approximating the expected ion overlap factors. While no excessive ion temperatures were recorded, the ion overlap factors can be diminished notably if the electron beam's space charge is strongly compensated by positive ions. As our measurements suggest several tens of percent of charge compensation may be reached within 10 to 30 ms, providing a possible contribution to the poor charge breeding performance. This phenomenon could also result in a large ion cloud, which was named as one of the possible reasons for extraction losses.

Chapter 5 also contains a summary of the design study for an ion beamline that will extend the TwinEBIS test stand. The beamline contains ion-optical elements capable of accommodating a large ion beam diameter and space-charge driven beam divergence to enable matching of the extracted ion beam into the acceptance cone of an accelerating RFQ, which will be required in future development steps. The line may also be used to inject a beam of singly charged ions originating from a secondary source into the EBIS. Besides this the beamline hosts instrumentation such as Faraday cups, a pepperpot beam profile monitor and emittance meter, and the TOF detector to permit a comprehensive characterisation of the extracted ion beams. The three-way ion switchyard and gridded lenses have been studied in particle tracking simulations to ensure

---

that they do not deteriorate the beam quality through aberrations beyond an acceptable level. Furthermore, the distribution of secondary electrons created on the surface of the gridded lens wires was simulated with particle tracking simulations and the help of a custom secondary emission model to verify that they are not expected to interfere with the measurement devices in the beamline.

The results of the MEDeGUN commissioning experiments indicate that the operation of an electron gun meeting the requirements for carbon beam therapy applications is feasible. However, we do not yet witness the charge breeding performance that would be expected from this electron beam and further studies are required to understand what causes both, the stagnation of the charge breeding at low and intermediate charge states and the observed ion losses during extraction. A combination of strong space charge compensation and elevated ion temperatures could be the reason for an increased ion cloud size that slows down breeding and impedes successful extraction. Such effects could put important limits on a high throughput charge breeder, especially when fed from background gas, and understanding the relationship between trap compensation the charge breeding efficiency is crucial for gauging the feasibility of the targeted beam production rates. TwinEBIS has been equipped with a new collector and the installation of the beamline has concluded. The system is now under preparation for further MEDeGUN experiments. For this next run it would be interesting to complement the charge breeding measurements with lighter elements, ideally of course with carbon, to see if the lower average charge state and decreased space charge compensation improve the breeding and extraction efficiency and to measure the actual breeding time required for the production of fully stripped ions. An additional plan is to extract ions slowly to determine whether the peak ion current has an impact on the extraction efficiency. In parallel, collaborators are carrying out theoretical studies to identify potential susceptibilities to plasma instabilities that could result in extraordinary ion heating and the expulsion of ions from the electron beam.



# PUBLICATIONS

- [I] A. Pikin, H. Pahl, and F. Wenander, “Method of controlling the cyclotron motion of electron beams with a nonadiabatic magnetic field”, [Physical Review Accelerators and Beams](#) **23**, 103502 (2020),  
Heavily referenced in Chapter 4.
- [II] H. Pahl, N. Bidault, G. Khatri, A. Pikin, and F. J. C. Wenander, “Nonadiabatic electron gun at an electron beam ion source: Commissioning results and charge breeding investigations”, [Physical Review Accelerators and Beams](#) **25**, 013402 (2022),  
Heavily referenced in Chapter 4.
- [III] J. Pitters, M. Breitenfeldt, S. D. Pinto, H. Pahl, A. Pikin, A. Shornikov, and F. Wenander, “Pepperpot emittance measurements of ion beams from an electron beam ion source”, [Nuclear Instruments and Methods in Physics Research Section A: Accelerators, Spectrometers, Detectors and Associated Equipment](#) **922**, 28–35 (2019),  
Mentioned in Chapters 4 and 5.
- [IV] H. Pahl, V. Bencini, M. Breitenfeldt, A. G. Costa, A. Pikin, J. Pitters, and F. Wenander, “A low energy ion beamline for TwinEBIS”, [Journal of Instrumentation](#) **13**, P08012–P08012 (2018),  
Heavily referenced in Chapter 5.
- [V] V. Bencini, M. Breitenfeldt, J. Lallement, A. Lombardi, H. Pahl, J. Pitters, A. Pikin, and F. Wenander, “High Frequency RFQ Design and LEBT Matching for the CERN TwinEBIS Ion Source”, [10.18429/JACoW-LINAC2018-TUP0016](#) (2018),  
Mentioned in Chapter 5.
- [VI] J. Pitters, M. Breitenfeldt, H. Pahl, A. Pikin, and F. Wenander, “Challenges in 11c charge breeding”, [Nuclear Instruments and Methods in Physics Research Section B: Beam Interactions with Materials and Atoms](#) **463**, 198–200 (2020),  
No explicit references.
- [VII] A. Pikin, V. Bencini, H. Pahl, and F. Wenander, “Electron gun producing beams with controllable current density”, [Journal of Physics: Conference Series](#) **2244**, 012103 (2022),  
No explicit references.



## REFERENCES

- [1] J. M. Poate and J. S. Williams, eds., *Ion Implantation and Beam Processing* (Elsevier, 1984).
- [2] H. Tsujii and T. Kamada, “A Review of Update Clinical Results of Carbon Ion Radiotherapy”, [Japanese Journal of Clinical Oncology](#) **42**, 670–685 (2012).
- [3] A. Garonna, U. Amaldi, R. Bonomi, D. Campo, A. Degiovanni, M. Garlasché, I. Mondino, V. Rizzoglio, and S. V. Andrés, “Cyclinac medical accelerators using pulsed C 6+ /H 2 + ion sources”, [Journal of Instrumentation](#) **5**, C09004–C09004 (2010).
- [4] U. Amaldi, S. Braccini, and P. Puggioni, “High Frequency Linacs for Hadrontherapy”, [Reviews of Accelerator Science and Technology](#) **02**, 111–131 (2009).
- [5] M. A. Blessenohl, “Fine-structure investigations in highly charged ions using spectroscopy in the vacuum ultraviolet regime”, PhD thesis (Heidelberg University, Heidelberg, 2020).
- [6] S. Kühn, C. Cheung, N. S. Oreshkina, R. Steinbrügge, M. Togawa, S. Bernitt, L. Berger, J. Buck, M. Hoesch, J. Seltmann, F. Trinter, C. H. Keitel, M. G. Kozlov, S. G. Porsev, M. F. Gu, F. S. Porter, T. Pfeifer, M. A. Leutenegger, Z. Harman, M. S. Safronova, J. R. C. López-Urrutia, and C. Shah, “New Measurement Resolves Key Astrophysical Fe XVII Oscillator Strength Problem”, [Physical Review Letters](#) **129**, 245001 (2022).
- [7] M. G. Kozlov, M. S. Safronova, J. R. Crespo López-Urrutia, and P. O. Schmidt, “Highly charged ions: Optical clocks and applications in fundamental physics”, [Reviews of Modern Physics](#) **90**, 045005 (2018).
- [8] S. A. King, L. J. Spieß, P. Micke, A. Wilzewski, T. Leopold, E. Benkler, R. Lange, N. Huntemann, A. Surzhykov, V. A. Yerokhin, J. R. Crespo López-Urrutia, and P. O. Schmidt, “An optical atomic clock based on a highly charged ion”, [Nature](#) **611**, 43–47 (2022).
- [9] E. D. Donets, V. I. Ilyushchenko, and V. A. Alpert, “Ultra-high Vacuum Electron Beam Source of Highly Stripped Ions”, in *First international conference on ion sources*, edited by Anatole Abragam and A. Lévy-Mandel, 3 (1969), pp. 635–642.

- [10] J. Alessi, E. Beebe, D. Graham, A. Kponou, A. Pikin, K. Prelec, J. Ritter, and V. Zajic, “Design of an EBIS for RHIC”, in [Proceedings of the 2003 bipolar/bicmos circuits and technology meeting \(ieee cat. no.03ch37440\)](#), Vol. 1 (2003), pp. 89–91.
- [11] M. Levine, R. Marrs, J. Bardsley, P. Beiersdorfer, C. Bennett, M. Chen, T. Cowan, D. Dietrich, J. Henderson, D. Knapp, A. Osterheld, B. Penetrante, M. Schneider, and J. Scofield, “The use of an electron beam ion trap in the study of highly charged ions”, [Nuclear Instruments and Methods in Physics Research Section B: Beam Interactions with Materials and Atoms](#) **43**, 431–440 (1989).
- [12] M. A. Levine, R. E. Marrs, C. L. Bennett, J. R. Henderson, D. A. Knapp, and M. B. Schneider, “EBIT: Electron beam ion trap”, in [AIP conference proceedings](#), Vol. 188 (1989), pp. 82–101.
- [13] D. Habs, O. Kester, T. Sieber, A. Kolbe, J. Ott, G. Bollen, F. Ames, D. Schwalm, R. von Hahn, R. Repnow, H. Podlech, A. Schempp, U. Ratzinger, L. Liljeby, K.-G. Rensfelt, F. Wenander, B. Jonsson, G. Nyman, P. Van Duppen, M. Huyse, A. Richter, G. Shrieder, G. Walter, and R.-I. Collaboration, “The REX-ISOLDE project”, [Nuclear Instruments and Methods in Physics Research Section B: Beam Interactions with Materials and Atoms](#) **139**, 128–135 (1998).
- [14] F. J. C. Wenander, “Charge breeding and production of multiply charged ions in EBIS and ECRIS”, PhD thesis (Chalmers University of Technology, 2001).
- [15] C. Dickerson, B. Mustapha, A. Pikin, S. Kondrashev, P. Ostroumov, A. Levand, and R. Fischer, “Simulation and design of an electron beam ion source charge breeder for the californium rare isotope breeder upgrade”, [Physical Review Special Topics - Accelerators and Beams](#) **16**, 024201 (2013).
- [16] R. C. Vondrasek, C. A. Dickerson, M. Hendricks, P. Ostroumov, R. Pardo, G. Savard, R. Scott, and G. Zinkann, “Charge breeding of radioactive isotopes at the CARIBU facility with an electron beam ion source”, [Review of Scientific Instruments](#) **89**, 10.1063/1.5013140 (2018).
- [17] F. Ames, R. Baartman, B. Barquest, C. Barquest, M. Blessenohl, J. R. C. López-Urrutia, J. Dilling, S. Dobrodey, L. Graham, R. Kanungo, M. Marchetto, M. R. Pearson, and S. Saminathan, “The CANREB project for charge state breeding at TRIUMF”, in [AIP conference proceedings](#), Vol. 2011, September (2018), p. 070010.
- [18] M. A. Blessenohl, S. Dobrodey, C. Warnecke, M. K. Rosner, L. Graham, S. Paul, T. M. Baumann, Z. Hockenbery, R. Hubele, T. Pfeifer, F. Ames, J. Dilling, and J. R. Crespo López-Urrutia, “An electron beam ion trap and source for re-acceleration of rare-isotope ion beams at TRIUMF”, [Review of Scientific Instruments](#) **89**, 052401 (2018).

- 
- [19] A. Lapierre, S. Schwarz, K. Kittimanapun, J. Rodriguez, C. Sumithrarachchi, B. Barquest, E. Berryman, K. Cooper, J. Fogleman, S. Krause, J. Kwarsick, S. Nash, G. Perdikakis, M. Portillo, R. Rencsok, D. Skutt, M. Steiner, L. Tobos, W. Wittmer, G. Bollen, and D. Leitner, “Commissioning results of the ReA EBIT charge breeder at the NSCL: First reacceleration of stable-isotope beams”, *Nuclear Instruments and Methods in Physics Research Section B: Beam Interactions with Materials and Atoms* **317**, 399–401 (2013).
- [20] A. Lapierre, “Electron-beam ion source/trap charge breeders at rare-isotope beam facilities”, *Review of Scientific Instruments* **90**, 10.1063/1.5127203 (2019).
- [21] H.-J. Son, A. Lapierre, A. C. Villari, A. Henriques, C. Supangco, C. Knowles, D. Crisp, S. Nash, and E. N. Beebe, “Progress of the High-Current EBIS Charge Breeder for the FRIB”, *Journal of Physics: Conference Series* **2244**, 012018 (2022).
- [22] S. Verdu-Andres, U. Amaldi, and A. Faus-Golfe, “CABOTO, a high-gradient linac for hadrontherapy”, *Journal of Radiation Research* **54**, i155–i161 (2013).
- [23] N. Bidault, J. A. Rodriguez, M. Lozano, and S. Sadovich, “Slow extraction of charged ion pulses from the REXEBIS”, in *AIP conference proceedings*, Vol. 2011, 1 (Sept. 2018), p. 070009.
- [24] A. Lapierre, “Time-dependent potential functions to stretch the time distributions of ion pulses ejected from EBIST”, *Canadian Journal of Physics* **95**, 361–369 (2017).
- [25] M. Vella, “Physics of the high current density electron beam ion source (EBIS)”, *Nuclear Instruments and Methods in Physics Research* **187**, 313–321 (1981).
- [26] C. Litwin, M. Vella, and A. Sessler, “Linear electrostatic instability of the electron beam ion source”, *Nuclear Instruments and Methods in Physics Research* **198**, 189–192 (1982).
- [27] L. Jacquet and M. Tagger, “Ion-electron two-stream instability in EBIS ion sources”, *Nuclear Instruments and Methods in Physics Research Section A: Accelerators, Spectrometers, Detectors and Associated Equipment* **369**, 1–10 (1996).
- [28] F. Currell and G. Fussmann, “Physics of electron beam ion traps and sources”, *IEEE Transactions on Plasma Science* **33**, 1763–1777 (2005).
- [29] W. Lotz, “An empirical formula for the electron-impact ionization cross-section”, *Zeitschrift für Physik* **206**, 205–211 (1967).
- [30] W. Lotz, “Electron-impact ionization cross-sections and ionization rate coefficients for atoms and ions from hydrogen to calcium”, *Zeitschrift für Physik* **216**, 241–247 (1968).
- [31] W. Lotz, “Electron-impact ionization cross-sections for atoms up to  $Z=108$ ”, *Zeitschrift für Physik* **232**, 101–107 (1970).
-

- [32] V. P. Shevelko and H. Tawara, “Semiempirical formulae for multiple ionization of neutral atoms and positive ions by electron impact”, *Journal of Physics B: Atomic, Molecular and Optical Physics* **28**, L589–L594 (1995).
- [33] Y. S. Kim and R. H. Pratt, “Direct radiative recombination of electrons with atomic ions: Cross sections and rate coefficients”, *Physical Review A* **27**, 2913–2924 (1983).
- [34] L. Meitner, “Über den Zusammenhang zwischen  $\beta$ - und  $\gamma$ -Strahlen”, *Zeitschrift für Physik* **9**, 145–152 (1922).
- [35] M. F. Gu, “Recombination X-Ray Line Formation of Iron L-Shell Ions in Low-Temperature Plasmas”, *The Astrophysical Journal* **593**, 1249–1254 (2003).
- [36] M. F. Gu, “The flexible atomic code”, *Canadian Journal of Physics* **86**, 675–689 (2008).
- [37] A. Müller and E. Salzborn, “Scaling of cross sections for multiple electron transfer to highly charged ions colliding with atoms and molecules”, *Physics Letters A* **62**, 391–394 (1977).
- [38] B. M. Penetrante, J. N. Bardsley, D. DeWitt, M. Clark, and D. Schneider, “Evolution of ion-charge-state distributions in an electron-beam ion trap”, *Physical Review A* **43**, 4861–4872 (1991).
- [39] F. Wenander, “Charge breeding of radioactive ions with EBIS and EBIT”, *Journal of Instrumentation* **5**, C10004–C10004 (2010).
- [40] C. D. Child, “Discharge From Hot CaO”, *Physical Review (Series I)* **32**, 492–511 (1911).
- [41] G. R. Brewer, “High-Intensity Electron Guns”, in *Focusing of charged particles v2* (Academic Press New York and London, 1967) Chap. 3.2, pp. 23–72.
- [42] J. R. Pierce, “Rectilinear Electron Flow in Beams”, *Journal of Applied Physics* **11**, 548–554 (1940).
- [43] I. Langmuir and K. B. Blodgett, “Currents Limited by Space Charge between Concentric Spheres”, *Physical Review* **24**, 49–59 (1924).
- [44] C. J. Davisson and C. J. Calbick, “Electron Lenses”, *Physical Review* **42**, 580–580 (1932).
- [45] H. Busch, “Berechnung der Bahn von Kathodenstrahlen im axialsymmetrischen elektromagnetischen Felde”, *Annalen der Physik* **386**, 974–993 (1926).
- [46] G. R. Brewer, “Focusing of High-density Electron Beams”, in *Focusing of charged particles v2* (Academic Press New York and London, 1967) Chap. 3.3, pp. 73–95.
- [47] L. Brillouin, “A Theorem of Larmor and Its Importance for Electrons in Magnetic Fields”, *Physical Review* **67**, 260–266 (1945).
- [48] G. Herrmann, “Optical Theory of Thermal Velocity Effects in Cylindrical Electron Beams”, *Journal of Applied Physics* **29**, 127–136 (1958).

- 
- [49] R. Post, “The magnetic mirror approach to fusion”, [Nuclear Fusion](#) **27**, 1579 (1987).
- [50] M. V. Nezlin, *Physics of Intense Beams in Plasmas*, Series in Plasma Physics and Fluid Dynamics (Taylor & Francis, 1993).
- [51] R. C. Davidson, *Physics of Nonneutral Plasmas* (Imperial College Press, 2001).
- [52] D. Noll, “Investigations on the Transport of High-Intensity Beams Using Particle-in-Cell Simulations”, PhD thesis (Goethe Universität Frankfurt, 2016).
- [53] E. Hairer, S. P. Nørsett, and G. Wanner, *Solving Ordinary Differential Equations I*, Vol. 8, Springer Series in Computational Mathematics (Springer Berlin Heidelberg, Berlin, Heidelberg, 1993).
- [54] E. Hairer and G. Wanner, *Solving Ordinary Differential Equations II*, Vol. 14, Springer Series in Computational Mathematics 4 (Springer Berlin Heidelberg, Berlin, Heidelberg, July 1996), p. 439.
- [55] L. Zhao and J.-S. Kim, “Numerical simulation of ion charge breeding in electron beam ion source”, [Review of Scientific Instruments](#) **85**, 02B706 (2014).
- [56] Y. F. Liu, K. Yao, R. Hutton, and Y. Zou, “Numerical simulations using an improved calculational scheme for ion charge state distribution and ion temperature evolution in an EBIT”, [Journal of Physics B: Atomic, Molecular and Optical Physics](#) **38**, 3207–3216 (2005).
- [57] G. Fussmann, C. Biedermann, and R. Radtke, “EBIT: An Electron Beam Source for the Production and Confinement of Highly Ionized Atoms”, in *Advanced technologies based on wave and beam generated plasmas*, edited by H. Schlüter and A. Shivarova (Springer Netherlands, Dordrecht, 1999).
- [58] R. Radtke, C. Biedermann, P. Bachmann, G. Fussmann, and T. Windisch, “Sawtooth oscillations in EBIT”, [Journal of Physics: Conference Series](#) **2**, 84–93 (2004).
- [59] I. V. Kalagin, D. Küchler, V. P. Ovsyannikov, and G. Zschornack, “Modelling of ion accumulation processes in EBIS and EBIT”, [Plasma Sources Science and Technology](#) **7**, 441–457 (1998).
- [60] C.-Z. Cheng and G. Knorr, *The Integration of the Vlasov Equation in Configuration Space*, tech. rep. (University of Iowa, Iowa City, 1975).
- [61] C. K. Birdsall and A. B. Langdon, *Plasma Physics Via Computer Simulation* (Taylor & Francis Group, London, United Kingdom, 1991).
- [62] D. Kuchler, “Beiträge zur Simulation und Diagnostik von Elektronenstossionenquellen”, PhD thesis (Technische Universität Dresden, 1999).

- [63] R. Becker, “EBIS/EBIT: Electron Beam Ion Source/Trap”, in *Handbook of ion sources*, edited by B. H. Wolf (1995) Chap. 2.11, pp. 157–182.
- [64] X. Lu, H. Watanabe, and F. Currell, “Numerical simulation of the charge balance in an EBIT”, [Nuclear Instruments and Methods in Physics Research Section B: Beam Interactions with Materials and Atoms](#) **205**, 234–238 (2003).
- [65] X. Lu and F. J. Currell, “Numerical simulation of the charge balance and temperature evolution in an electron beam ion trap”, [Physical Review Special Topics - Accelerators and Beams](#) **12**, 014401 (2009).
- [66] M. Gryziński, “Classical Theory of Atomic Collisions. I. Theory of Inelastic Collisions”, [Physical Review](#) **138**, A336–A358 (1965).
- [67] M. Gryziński, “Two-Particle Collisions. II. Coulomb Collisions in the Laboratory System of Coordinates”, [Physical Review](#) **138**, A322–A335 (1965).
- [68] L. Spitzer, “Equations of Motion for an Ideal Plasma”, [The Astrophysical Journal](#) **116**, 299 (1952).
- [69] L. Spitzer, *Physics of Fully Ionized Gases : Second Revised Edition* (Dover Publications, New York, United States, 2006).
- [70] P. Helander and D. J. Sigmar, *Collisional Transport in Magnetized Plasmas*, Cambridge Monographs on Plasma Physics (Cambridge University Press, 2005).
- [71] A. S. Richardson, “2019 NRL Plasma Formulary”, Plasma Physics (2019).
- [72] L. Spitzer and H. Shapley, “The Stability of Isolated Clusters”, [Monthly Notices of the Royal Astronomical Society](#) **100**, 396–413 (1940).
- [73] L. Spitzer and R. Härm, “Transport Phenomena in a Completely Ionized Gas”, [Physical Review](#) **89**, 977–981 (1953).
- [74] V. Pastukhov, “Collisional losses of electrons from an adiabatic trap in a plasma with a positive potential”, [Nuclear Fusion](#) **14**, 3–6 (1974).
- [75] M. N. Rosenbluth, W. M. MacDonald, and D. L. Judd, “Fokker-Planck Equation for an Inverse-Square Force”, [Physical Review](#) **107**, 1–6 (1957).
- [76] R. Marrs, “Self-cooling of highly charged ions during extraction from electron beam ion sources and traps”, [Nuclear Instruments and Methods in Physics Research Section B: Beam Interactions with Materials and Atoms](#) **149**, 182–194 (1999).
- [77] H. Pahl, *Ebisim*, version v0.2.0, (Sept. 2021) <https://doi.org/10.5281/zenodo.5293487>.
- [78] *Python.org*, <https://www.python.org/> (visited on 10/30/2020).

- 
- [79] C. R. Harris, K. J. Millman, S. J. van der Walt, R. Gommers, P. Virtanen, D. Cournapeau, E. Wieser, J. Taylor, S. Berg, N. J. Smith, R. Kern, M. Picus, S. Hoyer, M. H. van Kerkwijk, M. Brett, A. Haldane, J. F. del Río, M. Wiebe, P. Peterson, P. Gérard-Marchant, K. Sheppard, T. Reddy, W. Weckesser, H. Abbasi, C. Gohlke, and T. E. Oliphant, “Array programming with NumPy”, *Nature* **585**, 357–362 (2020).
- [80] P. Virtanen, R. Gommers, T. E. Oliphant, M. Haberland, T. Reddy, D. Cournapeau, E. Burovski, P. Peterson, W. Weckesser, J. Bright, S. J. van der Walt, M. Brett, J. Wilson, K. J. Millman, N. Mayorov, A. R. J. Nelson, E. Jones, R. Kern, E. Larson, C. J. Carey, Í. Polat, Y. Feng, E. W. Moore, J. VanderPlas, D. Laxalde, J. Perktold, R. Cimrman, I. Henriksen, E. A. Quintero, C. R. Harris, A. M. Archibald, A. H. Ribeiro, F. Pedregosa, and P. van Mulbregt, “SciPy 1.0: fundamental algorithms for scientific computing in Python”, *Nature Methods* **17**, 261–272 (2020).
- [81] J. D. Hunter, “Matplotlib: A 2D Graphics Environment”, *Computing in Science & Engineering* **9**, 90–95 (2007).
- [82] L. F. Shampine and M. W. Reichelt, “The MATLAB ODE Suite”, *SIAM Journal on Scientific Computing* **18**, 1–22 (1997).
- [83] S. K. Lam, A. Pitrou, and S. Seibert, “Numba”, in *Proceedings of the second workshop on the llvm compiler infrastructure in hpc - llvm ’15* (2015), pp. 1–6.
- [84] S. K. Lam, A. Pitrou, S. Archibald, M. Florisson, S. Seibert, G. Markall, T. A. Anderson, V. Haenel, Rjenc29, J. Bourque, Luk-f-a, A. Meurer, G. Leobas, T. E. Oliphant, Densmirn, njwhite, E. Pronovost, S. Seefeld, H. Grecco, P. Peterson, E. Wieser, I. Virshup, M. G, J. Bourbeau, A. Malakhov, U. Laserson, P. M. Maries, E. Totoni, M. Collison, and R. Sanjay, *numba/numba: Version 0.52.0*, Dec. 2020.
- [85] *The LLVM Compiler Infrastructure Project*, <https://llvm.org/> (visited on 10/12/2020).
- [86] H. Pahl, *ebisim 0.2.0 documentation*, <https://ebisim.readthedocs.io/en/latest/> (visited on 03/10/2021).
- [87] R. Mertzig, *Project Ion Potentials*, (2015) <http://project-ionpotentials.web.cern.ch/> (visited on 11/10/2020).
- [88] R. Mertzig, “Modelling and Design of High Compression Electron Guns for EBIS / T Charge Breeders”, PhD thesis (2016).
- [89] H. Sundqvist and G. Veronis, “A simple finite-difference grid with non-constant intervals”, *Tellus* **22**, 26–31 (1970).
- [90] S. D. Conte and C. de Boor, *Elementary Numerical Analysis: An Algorithmic Approach 3rd ed.* (1980).

- [91] L. Brieda, *Nonlinear Poisson Solver*, <https://www.particleincell.com/2012/nonlinear-poisson-solver/> (visited on 03/09/2020).
- [92] S. Milewski and J. Orkisz, “In search of optimal acceleration approach to iterative solution methods of simultaneous algebraic equations”, *Computers and Mathematics with Applications* **68**, 101–117 (2014).
- [93] J. Barroso and C. Stellati, “A design study of non-adiabatic electron guns”, in 1994 international conference on plasma physics (1994), pp. 265–268.
- [94] I. Spassovsky, R. Correa, J. Barroso, and I. Yovchev, “High-quality electron beam with nonadiabatic electrostatic pumping”, *IEEE Transactions on Electron Devices* **41**, 1451–1455 (1994).
- [95] A. Pikin, J. G. Alessi, E. N. Beebe, D. Raparia, and J. Ritter, “Analysis of magnetically immersed electron guns with non-adiabatic fields”, *Review of Scientific Instruments* **87**, 113303 (2016).
- [96] A. Pikin and D. Raparia, “Generation of magneto-immersed electron beams”, *Review of Scientific Instruments* **89**, 052002 (2018).
- [97] Field Precision LLC, *TRAK Charged Particle Toolkit 8.0*, (2017) <https://www.fieldp.com>.
- [98] S. Humphries Jr., *Finite-element Methods for Electromagnetics* (2010), pp. 1–324.
- [99] L. Samuel J, J. Sanny, and B. Moebs, *Magnetic Field of a Current Loop*, 2016.
- [100] F. Wenander, B. Jonson, L. Liljeby, and G. H. Nyman, *REXEBIS the Electron Beam Ion Source for the REX-ISOLDE project*, tech. rep. (CERN, Geneva, Dec. 1998).
- [101] F. Wenander, J. Cederkäll, B. Jonson, L. Liljeby, G. Nyman, K.-G. Rensfelt, Ö. Skeppstedt, and B. Wolf, “REXEBIS, design and initial commissioning results”, in *AIP conference proceedings*, Vol. 572 (2001), pp. 59–73.
- [102] E. Kugler, “The ISOLDE facility”, *Hyperfine Interactions* **2000 129:1 129**, 23–42 (2000).
- [103] D. Habs, O. Kester, T. Sieber, H. Bongers, S. Emhofer, P. Reiter, P. G. Thirolf, G. Bollen, J. Aystö, O. Forstner, H. Ravn, T. Nilsson, M. Oinonen, H. Simon, J. Cederkall, F. Ames, P. Schmidt, G. Huber, L. Liljeby, O. Skeppstedt, K. G. Rensfelt, F. Wenander, B. Jonson, G. Nyman, R. Von Hahn, H. Podlech, R. Repnow, C. Gund, D. Schwalm, A. Schempp, K.-U. Kühnel, C. Welsch, U. Ratzinger, G. Walter, A. Huck, K. Kruglov, M. Huyse, P. Van Den Bergh, P. Van Duppen, L. Weissman, A. C. Shotton, A. N. Ostrowski, T. Davinson, P. J. Woods, J. Cub, A. Richter, G. Schrieder, and R.-I. Collaboration, “The REX-ISOLDE project”, *Hyperfine Interactions* **129**, 43–66 (2000).

- 
- [104] F. Ames, J. Cederkäll, T. Sieber, and F. J. C. Wenander, *The REX-ISOLDE Facility: Design and Commissioning Report*, CERN Yellow Reports: Monographs (CERN, Geneva, 2005).
- [105] J. A. Rodriguez, W. V. Delsolaro, W. Andreatza, J. M. Bibby, N. Bidault, E. Bravin, J. C. Broere, E. D. Cantero, R. Catherall, V. Cobham, M. Elias, E. Fadakis, P. Fernier, M. A. Fraser, F. Gerigk, K. Hanke, Y. Kadi, M. L. Benito, E. Matli, S. Sadovich, E. Siesling, D. Valuch, F. Wenander, and P. Zhang, “Beam commissioning of the HIE-ISOLDE post-accelerator”, in [Ipac 2016 - proceedings of the 7th international particle accelerator conference](#) (2016), pp. 2045–2047.
- [106] F. Ames, G. Bollen, P. Delahaye, O. Forstner, G. Huber, O. Kester, K. Reisinger, and P. Schmidt, “Cooling of radioactive ions with the Penning trap REXTRAP”, [Nuclear Instruments and Methods in Physics Research Section A: Accelerators, Spectrometers, Detectors and Associated Equipment](#) **538**, 17–32 (2005).
- [107] B. Wolf, J. Cederkäll, O. Forstner, F. Wenander, F. Ames, K. Reisinger, L. Liljeby, Ö. Skeppstedt, B. Jonson, and G. Nyman, “First radioactive ions charge bred in REXEBIS at the REX-ISOLDE accelerator”, [Nuclear Instruments and Methods in Physics Research Section B: Beam Interactions with Materials and Atoms](#) **204**, 428–432 (2003).
- [108] F. Wenander, P. Delahaye, R. Scrivens, and R. Savreux, “The REX-ISOLDE charge breeder as an operational machine”, [Review of Scientific Instruments](#) **77**, 03B104 (2006).
- [109] F. Wenander, “Charge state breeders: On-line results”, [Nuclear Instruments and Methods in Physics Research Section B: Beam Interactions with Materials and Atoms](#) **266**, 4346–4353 (2008).
- [110] F. J. C. Wenander and K. Riisager, “Isotope toolbox turns 10”, [CERN Courier](#) **52**, 33–36 (2012).
- [111] N. Warr, J. Van de Walle, M. Albers, F. Ames, B. Bastin, C. Bauer, V. Bildstein, A. Blazhev, S. Bönig, N. Bree, B. Bruyneel, P. A. Butler, J. Cederkäll, E. Clément, T. E. Cocolios, T. Davinson, H. De Witte, P. Delahaye, D. D. DiJulio, J. Diriken, J. Eberth, A. Ekström, J. Elseviers, S. Emhofer, D. V. Fedorov, V. N. Fedosseev, S. Franchoo, C. Fransen, L. P. Gaffney, J. Gerl, G. Georgiev, R. Gernhäuser, T. Grahn, D. Habs, H. Hess, A. M. Hurst, M. Huyse, O. Ivanov, J. Iwanicki, D. G. Jenkins, J. Jolie, N. Kesteloot, O. Kester, U. Köster, M. Krauth, T. Kröll, R. Krücken, M. Lauer, J. Leske, K. P. Lieb, R. Lutter, L. Maier, B. A. Marsh, D. Mücher, M. Münch, O. Niedermaier, J. Pakarinen, M. Pantea, G. Pascovici, N. Patronis, D. Pauwels, A. Petts, N. Pietralla, R. Raabe, E. Rapisarda, P. Reiter, A. Richter, O. Schaile, M. Scheck, H. Scheit, G. Schrieder, D. Schwalm, M. Seidlitz, M. Seliverstov, T. Sieber, H. Simon, K.-H. Speidel, C. Stahl, I. Stefanescu, P. G. Thirolf, H.-G. Thomas, M. Thürauf, P. Van Duppen, D. Voulot, R.

- Wadsworth, G. Walter, D. Weißhaar, F. Wenander, A. Wiens, K. Wimmer, B. H. Wolf, P. J. Woods, K. Wrzosek-Lipska, and K. O. Zell, “The Miniball spectrometer”, *The European Physical Journal A* **49**, 40 (2013).
- [112] F. Wenander, “EBIS as charge breeder for radioactive ion beam accelerators”, *Nuclear Physics A* **701**, 528–536 (2002).
- [113] R. Mertzig, M. Breitenfeldt, S. Mathot, J. Pitters, A. Shornikov, and F. Wenander, “A high-compression electron gun for C6+ production: concept, simulations and mechanical design”, *Nuclear Instruments and Methods in Physics Research, Section A: Accelerators, Spectrometers, Detectors and Associated Equipment* **859**, 102–111 (2017).
- [114] M. Breitenfeldt, R. Mertzig, J. Pitters, A. Shornikov, and F. Wenander, “The TwinEBIS setup: Machine description”, *Nuclear Instruments and Methods in Physics Research Section A: Accelerators, Spectrometers, Detectors and Associated Equipment* **856**, 139–146 (2017).
- [115] M. Breitenfeldt, F. di Lorenzo, A. Pikin, J. Pitters, and F. Wenander, “MEDeGUN commissioning results”, in *AIP conference proceedings*, Vol. 2011, 1 (Sept. 2018), p. 040004.
- [116] Dassault Systemes Deutschland GmbH, *CST Studio Suite 2020 SP7*, (2020) <https://www.cst.com>.
- [117] G. Kuznetsov, “High temperature cathodes for high current density”, *Nuclear Instruments and Methods in Physics Research Section A: Accelerators, Spectrometers, Detectors and Associated Equipment* **340**, 204–208 (1994).
- [118] G. I. Kuznetsov, “IrCe cathodes for EBIS”, *Journal of Physics: Conference Series* **2**, 35–41 (2004).
- [119] ISTOK, Moscow Russia, Private communication, 2020.
- [120] W. Liang, Y. Wang, J. Wang, W. Liu, and F. Yang, “DC Emission Characteristic of Nanosized-Scandia-Doped Impregnated Dispenser Cathodes”, *IEEE Transactions on Electron Devices* **61**, 1749–1753 (2014).
- [121] R. Rao, O. Kester, T. Sieber, D. Habs, and K. Rudolph, “Beam optics design of the REX-ISOLDE -separator”, *Nuclear Instruments and Methods in Physics Research Section A: Accelerators, Spectrometers, Detectors and Associated Equipment* **427**, 170–176 (1999).
- [122] A. Ghalambor Dezfuli, R. Moore, and P. Varfalvy, “A compact 65 keV stable ion gun for radioactive beam experiments”, *Nuclear Instruments and Methods in Physics Research Section A: Accelerators, Spectrometers, Detectors and Associated Equipment* **368**, 611–616 (1996).
- [123] T. A. Carlson, C. Nestor, N. Wasserman, and J. McDowell, “Calculated ionization potentials for multiply charged ions”, *Atomic Data and Nuclear Data Tables* **2**, 63–99 (1970).

- 
- [124] I. Podadera-Aliseda, *New developments on preparation of cooled and bunched Radioactive Ion beams at ISOL facilities: the ISCOOL project and the rotating wall cooling*, 2006.
- [125] N. Bidault, M. Lozano, and J. Rodriguez, “Residual Gas Ions Characterization from the REXEBIS”, [Proc. 9th International Particle Accelerator Conference \(IPAC’18\)](#), 784–786 (2018).
- [126] J. Angot, M. Luntinen, T. Kalvas, H. Koivisto, R. Kronholm, L. Maunoury, O. Tarvainen, T. Thuillier, and V. Toivanen, “Method for estimating charge breeder ECR ion source plasma parameters with short pulse 1+ injection of metal ions”, [Plasma Sources Science and Technology](#) **30**, 035018 (2020).
- [127] R. V. Hogg, A. T. Craig, and J. W. McKean, *Introduction to Mathematical Statistics, 8th edition* (Pearson Higher Education & Professional Group, 2019).
- [128] H. Eickhoff and U. Linz, “Medical Applications of Accelerators”, in [Reviews of accelerator science and technology](#) (WORLD SCIENTIFIC, Dec. 2008), pp. 143–161.
- [129] A. Peeters, J. P. Grutters, M. Pijls-Johannesma, S. Reimoser, D. De Ruyscher, J. L. Severens, M. A. Joore, and P. Lambin, “How costly is particle therapy? Cost analysis of external beam radiotherapy with carbon-ions, protons and photons”, [Radiotherapy and Oncology](#) **95**, 45–53 (2010).
- [130] A. Shornikov and F. Wenander, “Advanced Electron Beam Ion Sources (EBIS) for 2-nd generation carbon radiotherapy facilities”, [Journal of Instrumentation](#) **11**, T04001–T04001 (2016).
- [131] Y. V. Baryshev, I. V. Kazarezov, E. V. Kozyrev, G. I. Kuznetsov, I. G. Makarov, O. A. Nezhevenko, B. Z. Persov, M. A. Tiunov, V. P. Yakovlev, and I. A. Zapryagaev, “A 100 MW electron source with extremely high beam area compression”, [Nuclear Inst. and Methods in Physics Research, A](#) **340**, 241–258 (1994).
- [132] HeatWave Labs Inc., *TB-117 Emission Characteristics of “M Type” Dispenser Cathodes*.
- [133] R. Kersevan and M. Ady, “Recent Developments of Monte-Carlo Codes MOLFLOW+ and SYNRAD+”, [10.18429/JACoW-IPAC2019-TUPMP037](#) (2019).
- [134] R. Taylor, F. Wenander, G. Khatri, and H. Pahl, *Simulations of methane gas injection into TwinEBIS*, tech. rep. (2019).
- [135] B. A. Mamyrin, V. I. Karataev, D. V. Shmikk, and V. A. Zagulin, “The mass-reflectron, a new nonmagnetic time-of-flight mass spectrometer with high resolution”, [Sov. Phys. JETP](#) **37**, 45–48 (1973).
- [136] N. E. Bradbury and R. A. Nielsen, “Absolute Values of the Electron Mobility in Hydrogen”, [Physical Review](#) **49**, 388–393 (1936).
-

- [137] R. Taylor, G. Khatri, and F. Wenander, *Chopper testing for the TwinEBIS time of flight-mass spectrometer*, tech. rep. (2019).
- [138] J. Ladislav Wiza, “Microchannel plate detectors”, *Nuclear Instruments and Methods* **162**, 587–601 (1979).
- [139] D. F. Simmons, C. M. Fortgang, and D. B. Holtkamp, “Using multispectral imaging to measure temperature profiles and emissivity of large thermionic dispenser cathodes”, *Review of Scientific Instruments* **76**, 44901 (2005).
- [140] N. van Woudenberg, “Investigation of Ion Extraction Anomalies at TwinEBIS”, Master thesis (2023).
- [141] V. Bencini, H. W. Pommerenke, A. Grudiev, and A. M. Lombardi, “750 MHz radio frequency quadrupole with trapezoidal vanes for carbon ion therapy”, *Physical Review Accelerators and Beams* **23**, 122003 (2020).
- [142] A. Perrin, J.-F. Amand, T. Mütze, and J.-B. Lallement, *TRAVEL v4.07 User Manual* (2007).
- [143] R. F. Holsinger, K. Hallbach, and Los Alamos Accelerator Code Group, *Poisson Superfish*, 2013.
- [144] A. Pikin and A. Kponou, “Correction of spherical aberration for an electrostatic gridded lens”, *Review of Scientific Instruments* **79**, 123303 (2008).
- [145] J. F. Ziegler, M. Ziegler, and J. Biersack, “SRIM – The stopping and range of ions in matter (2010)”, *Nuclear Instruments and Methods in Physics Research Section B: Beam Interactions with Materials and Atoms* **268**, 1818–1823 (2010).
- [146] N. Matsunami, Y. Yamamura, Y. Itikawa, N. Itoh, Y. Kazumata, S. Miyagawa, K. Morita, R. Shimizu, and H. Tawara, “Energy dependence of the ion-induced sputtering yields of monatomic solids”, *Atomic Data and Nuclear Data Tables* **31**, 1–80 (1984).
- [147] G. N. Kropachev, N. N. Alexeev, A. I. Balabin, T. V. Kulevoy, and V. I. Nikolaev, “Numerical simulation of gridded electrostatic lens”, *Review of Scientific Instruments* **83**, 02B907 (2012).
- [148] The FreeCAD Team, *FreeCAD*, (2017) <https://www.freecad.org/> (visited on 12/11/2017).
- [149] D. Hasselkamp, H. Rothard, K.-O. Groeneveld, J. Kemmler, P. Varga, and H. Winter, *Particle Induced Electron Emission II* (Springer Berlin Heidelberg, 1992).
- [150] E. Cantero, A. Sosa, W. Andrezza, E. Bravin, D. Lanaia, D. Voulot, and C. Welsch, “Design of a compact Faraday cup for low energy, low intensity ion beams”, *Nuclear Instruments and Methods in Physics Research Section A: Accelerators, Spectrometers, Detectors and Associated Equipment* **807**, 86–93 (2016).

- [151] E. Ebrahimibasabi and S. Fegghi, “Design and construction of a secondary electron suppressed Faraday Cup for measurement of beam current in an electrostatics proton accelerator”, [International Journal of Mass Spectrometry](#) **386**, 1–5 (2015).
- [152] F. Hamme, U. Becker, P. Hammes, and C. S. T. Gmbh, “Simulation of secondary electron emission with CST Particle Studio TM”, in Proceedings of icap 2006 (2006), pp. 160–163.
- [153] R. Decoste and B. H. Ripin, “Secondary-electron emission by energetic ions incident on metal surfaces”, [Journal of Applied Physics](#) **50**, 1503–1505 (1979).
- [154] M. A. Levine, R. Marrs, and R. W. Schmieder, “Measurement of instabilities and ion heating in an electron beam ion source”, [Nuclear Instruments and Methods in Physics Research Section A: Accelerators, Spectrometers, Detectors and Associated Equipment](#) **237**, 429–440 (1985).
- [155] A. Hershcovitch, “Review of electron beam macroinstabilities and other EBIS related stability and issues”, [Review of Scientific Instruments](#) **69**, 668–670 (1998).
- [156] A. Shornikov, R. Mertzig, M. Breitenfeldt, A. Lombardi, F. Wenander, and A. Pikin, “Parametric study of a high current–density EBIS Charge Breeder regarding Two Stream plasma Instability (TSI)”, [Nuclear Instruments and Methods in Physics Research Section B: Beam Interactions with Materials and Atoms](#) **376**, 361–363 (2016).
- [157] C. Thakur, S. Kumar, N. Jakhar, S. Kashyap, J. Sharma, M. K. Kashyap, H. Pahl, and F. Wenander, “Beam driven plasma instabilities in electron beam ion sources”, To be published. (2024).



# ACKNOWLEDGEMENTS

I would like to express my gratitude to Prof. Dr. José Crespo López-Urrutia for accepting me as his doctoral student and acting as my academic supervisor throughout this project. Despite us not having met previously and me planning to carry out my work mostly externally, I was welcomed without hesitation, and I appreciate the trust implied in that decision. He has also presented me with repeated cherished opportunities to visit, join, and learn from him and his group at the Max Planck Institute for Nuclear Physics.

I would like to extend my recognition to Prof. Dr. Yury Litvinov for serving as the second referee to this thesis and to Prof. Dr. Mark Ladd and Prof. Dr. Maurits Haverkort for completing the examination committee.

The majority of this work has been carried out within the EBIS team at CERN, under the supervision of Dr. Fredrik Wenander. I simply cannot thank him enough for the opportunities he has provided me with and his seemingly unlimited respect, trust, and patience towards me. Thank you for always having my back.

Further, I want to thank Dr. Alexander Pikin for offering me the privilege of learning from his vast pool of experience with electron beam-driven devices. Naturally, I extend my gratitude to all of my wonderful colleagues throughout the past years for our stimulating and friendly discussions on physics and beyond whilst jointly trying to master an at times temperamental and fickle experimental setup: Martin Breitenfeldt, Johanna Pitters, Gunn Khatri, Rebecca Taylor, Niek Van Woudenberg – it has been a joy. Niels Bidault has been a great sparring partner and companion on our journeys into the arcane depths of EBIS theory, and Jørgen Steen is not only to thank for the working of the TwinEBIS control system but for many good times outside the lab and office. Of course, the list goes on, and there are – as usual – too many people involved to name them all, but I want to thank everyone in the Accelerator and Beam Physics Department at CERN with a dedicated mentioning of the technical staff for their support. I also want to thank Bernhard Holzer, who, through friendly but persistent nagging, has ensured that this document eventually made it past the finish line, and Alexander Huschauer and Bettina Mikulec for their understanding and support when the thesis forced me to divert some attention from my regular tasks.

My visits to the group for highly charged ion dynamics at the Max Planck Institute for Nuclear Physics in Heidelberg have granted me an alternative perspective on the field of highly charged

ions, and I have much enjoyed the possibility to work with the skilful and welcoming members of the group and the institute as a whole. There are, once again, too many people to do them all justice, but I would like to take the time to acknowledge the help of Stepan Dobrodey, Michael Blessenohl, Michael Karl Rosner, and Christian Warnecke for showing me the ropes in the beginning and many fruitful discussions thereafter.

Additionally, I acknowledge the financial support of the Wolfgang Gentner scholarship programme of the German Federal Ministry for Education and Research, which has provided me with three years of funding for my doctoral student position; the thesis simply could not have happened without this generous support.

Last but not least, I want to thank the people who may have had to show more patience than anyone else. Julia, thank you for your positive outlook and for keeping me sane. To my family, and especially my parents: None of this would have ever been possible without your unconditional and unwavering support. Thank you.

# ABBREVIATIONS & ACRONYMS

<b>BNL</b>	Brookhaven National Lab
<b>CERN</b>	European Organization for Nuclear Research (former: Conseil européen pour la recherche nucléaire)
<b>CX</b>	Charge exchange
<b>DR</b>	Dielectronic recombination
<b>DT</b>	Drift tube
<b>EBIS</b>	Electron beam ion source
<b>EBIT</b>	Electron beam ion trap
<b>ECR</b>	Electron cyclotron resonance
<b>EI</b>	Electron (impact) ionisation
<b>FAC</b>	Flexible Atomic Code
<b>GPS</b>	General Purpose Separator (Magnetic spectrometer at ISOLDE)
<b>HCI</b>	Highly charged ions
<b>HIE</b>	High Intensity and Energy (upgrade of REX)
<b>HV</b>	High voltage
<b>ISOL</b>	Isotope separation on-line
<b>ISOLDE</b>	Isotope Separator On-line Device (RIB facility at CERN)
<b>LEBT</b>	Low energy beam transport
<b>LINAC</b>	Linear accelerator
<b>MCP</b>	Micro channel plate

## *References*

---

<b>NEG</b>	Non-evaporable getter
<b>PIPS</b>	Passivated implanted planar silicon
<b>RHIC</b>	Relativistic Heavy Ion Collider
<b>RIB</b>	Rare isotope beam
<b>REX</b>	Radioactive beam EXperiment (part of ISOLDE)
<b>RF</b>	Radio frequency
<b>RFQ</b>	Radio frequency quadrupole
<b>RR</b>	Radiative recombination
<b>SC</b>	Space charge
<b>TOF</b>	Time of flight
<b>TRIUMF</b>	Canada's national particle accelerator centre (former: TRI-University Meson Facility)

# SYMBOLS

## Natural constants

Boltzmann constant	$k_B = 1.380\,648\,52 \cdot 10^{-23} \text{ J/K}$
Electron charge to mass ratio	$\eta = e/m_e$
Electron mass	$m_e = 9.109\,383\,56 \cdot 10^{-31} \text{ kg}$
Elementary charge	$e = 1.602\,176\,620\,8 \cdot 10^{-19} \text{ C}$
Fine structure constant	$\alpha = 0.007\,297\,352\,564\,3$
Reduced Planck constant	$\hbar = 1.054\,571\,817 \cdot 10^{-34} \text{ Js}$
Rydberg energy	$Ry = 13.605\,693\,122\,990 \text{ eV}$
Vacuum permittivity	$\varepsilon_0 = 8.854\,187\,817\,6 \cdot 10^{-12} \text{ As/(Vm)}$

## Others

Brillouin radius	$r_B$
Cathode potential	$\Phi_C$
Charge exchange cross section	$\sigma^{CX}$
Charge density	$\rho$
Current	$I$
Current density	$j$
Debye length	$\lambda_D$
Dielectronic recombination cross section	$\sigma^{DR}$
Drift tube potential	$\Phi_{DT}$
Electric field	$\mathbf{E} = (E_x, E_y, E_z) \text{ or } (E_r, E_\theta, E_z)$

## References

---

Electron beam energy	$E_e$
Electron beam velocity	$u_e$
Electron ionisation cross section	$\sigma^{\text{EI}}$
Herrmann radius	$r_{\text{H}}$
Larmor frequency	$\omega_{\text{L}} = \eta B/2$
Magnetic field	$\mathbf{B} = (B_x, B_y, B_z)$ or $(B_r, B_\theta, B_z)$
Magnetic flux	$\psi$
Magnetic vector potential	$\mathbf{A} = (A_x, A_y, A_z)$ or $(A_r, A_\theta, A_z)$
Plasma frequency (electrons)	$\omega_{\text{p}} = \sqrt{\eta \rho /\varepsilon_0}$
Radiative recombination cross section	$\sigma^{\text{RR}}$
Space charge potential	$\Phi_{\text{SC}}$
Temperature	$T$